Investigation of Interfacial Effects in Ferromagnetic Thin-Films

TOKAC, MUSTAFA

Investigation of Interfacial Effects in Ferromagnetic Thin-Films

Mustafa Tokaç

Department of Physics
University of Durham

This dissertation is submitted for the degree of
Doctor of Philosophy

Ustinov College

September 2016

DEDICATED TO MY FAMILY & NIHAN

Declaration

I hereby declare that the work contained in this thesis is my own and has not been submitted for examination for any other degree at any University. The work of collaborators is acknowledged as appropriate. The magnetic thin-films presented in this work were deposited by Dr. A.T. Hindmarch and Dr. M. Wang at Nottingham University. Magnetic characterization of Co thin-films presented in Chapter 5 were made by the author at Nottingham University. Magnetic characterization of CoFeB:Ta thin-films presented in Chapter 6 were made by S. Horry (Durham University) and Dr. C.J. Kinane at Rutherford Appleton Laboratories, R53 Materials Characterization Lab. Analysis of magnetization data was performed by S. Horry which has been repeated by the author. Neutron scattering experiments were performed at CRISP beamline at ISIS in Oxfordshire along with Dr. C.J. Kinane, Dr. A.T. Hindmarch and Richard Rowan-Robinson. The analysis of the results was performed by the author. The structural analysis of thin-films were made at Rutherford Appleton Laboratories, R53 Materials Characterization Lab by Dr. C.J. Kinane and analyzed by the author. Ferromagnetic resonance experiments were performed using vector network analyzer at University of Porto by the author along with Professor D.S. Schmool, Professor G.N. Kakazei and Dr. S. Bunyaev. Analysis of magnetization data was performed by the author.

Mustafa Tokaç
September 2016

Acknowledgements

At this point I would like to take this opportunity to thank the many people who have supported and contributed in many ways to this work. I am indebted to the Ministry of National Education of Turkey for a financial support of my PhD. I could not have achieved any of this without its support.

I must first express my sincere gratitude to my supervisors, Professor Del Atkinson and Dr. Aidan T. Hindmarch. Not only for providing me with the excellent opportunity to continue my studies, but for providing me with help and support throughout the years we have worked together. Their guidance helped me in all the time of research and writing of this thesis. Also, I would like to extend this gratitude to the wider physics department at the Durham University for providing a friendly and engaging work environment.

I am very grateful to Dr. M. Wang, Dr. A. W. Rushorth, and Prof. B. L. Gallagher who have collaborated in the sample preparation and characterization. Also, I would like to thank Dr. C. J. Kinane and Dr. T. Charlton at ISIS for their assistance during experiments and with the lengthy analysis and interpretation of the PNR data. These would not have been possible without the many support staff involved in running these laboratories. I gratefully acknowledge Dr. S. Bunyaev and Prof. G. N. Kakazei from University of Porto and Prof. D. S. Schmool from University of Perpignan for providing me an opportunity to use their facilities, as well as the support and time devoted to my work in a very friendly collaboration climate.

I would like to thank my fellow labmates in room 12: D. Burn, E. Arac, M. Sultan, J. King, A. Webb, S. Dempsey, R.R. Robinson, S. Jaiswal, S. Azzawi and O.O. Inyang, in for the stimulating discussions, for the sleepless nights we were working together in beamlines, and for all the fun we have had in the last four years.

Tüm çalışmalarım boyunca desteklerinden dolayı arkadaşlarım, Malik, Mustafa Onur, Mehmet, Selime ve Çiǵdem'e, bu meşakatli ve uzun yolda senelerdir birlikte yürüdüǧümüz Hatice Büber'e, Durham'da doktora yapmama vesile olan Dr. Erhan Araç'a, sohbetlerinden her daim memnuniyet duyduǧum Hatice & Bünyamin çiftine, sevgili dostlarim Samet & Saliha çiftine, doktoraya beraber baslayıp bitirdiǧim, bu süre zarfında çok eǧlenceli vakitler geçirdiǧim meslektaşım Murat Aydemir'e teşekkürü bir borç bilirim.

Eǧitim hayatım boyunca maddi ve manevi yardımlarını esirgemeyen aileme ve sıkıntılarımı paylaşıp sevgi ve hoşgörüsünü hiçbir zaman eksik etmeyen çok kıymetli hayat arkadaşım, eşim Nihan Tokaç'a en içten duygularımla teşekkür ederim.

Abstract

The magnetic behaviour in thin-film structures has attracted considerable interest and also has importance for wide ranging technological applications. As the dimension of magnetic films reduce, they are able to exhibit different electrical and magnetic properties, where interfacial magnetism become more important. This thesis is centered on the interfacial effects in ferromagnetic thin-film structures with various adjacent materials. Within this framework, the ferromagnetic materials Co and CoFeB:Ta alloy have been investigated.

A detailed investigation of the structural, magnetic and anisotropic magnetoresistance (AMR) properties of Co thin-films with Cu and Ir overlayers as a function of Co thickness was performed. Magnetic characterization of thin-films was performed to determine possible magnetic dead layer formations in these thin-films, where no magnetic dead layers were found to be present within these structures. Electrical resistivity measurements showed that the AMR is dependent upon on Co film thickness, where it decreases with decreasing of Co thickness, and it tends toward zero for Co thicknesses below 6 nm. The contribution to the AMR from a single Co/Ir interface is presented where the AMR is shown to vary inversely proportional to the Co film thickness with a Co/Ir interface.

Interface magnetism and magnetic dead layers in amorphous CoFeB:Ta alloy thin-film multilayers were studied using polarized neutron reflectometry. Temperature dependent variations in the effective magnetic thickness of the film are found, and correlated with structural intermixing at interfaces. At the interface between ferromagnetic film and capping-layer the structurally graded interface appears to cause a concomitant grading of the local Curie temperature, and at the interface between ferromagnetic film and GaAs(001) substrate local interfacial alloying also creates a region where a magnetic dead-layer forms. The thickness of the magnetic dead layer at the ferromagnet-semiconductor interface is shown to

be temperature dependent, which may have significant implications for room-temperature operation of hybrid ferromagnetic metal-semiconductor spintronic devices.

Enhancement of Gilbert damping in Co thin-films of various thicknesses with Cu or Ir overlayers is studied under ferromagnetic resonance to understand the role of local interface structure in spin-pumping. Structural analysis indicates that Co films less than 6 nm have fcc(111)-dominated texture while thicker films are dominated by hcp(0001) structure. The intrinsic damping for Co thicknesses above 6 nm is weakly dependent on Co thickness for thin-films with both overlayers, and below 6 nm the Ir overlayers show higher intrinsic damping enhancement compared to Cu overlayers, as expected due to spin-pumping. The interfacial spin-mixing conductance is significantly enhanced in structures where both Co and Ir have fcc(111) structure in comparison to those where the Co layer has subtly different hcp(0001) texture at the interface.

List of Publications

Chapter 5 contains work partially summarized in the following journal article:

M. Tokaç, S. Jaiswal, M. Wang, A.W. Rushforth, B.L. Gallagher, D. Atkinson and A.T. Hindmarch, *"Interfacial Origin of Thickness-Dependent In-Plane Anisotropic Magnetoresistance"*, AIP Advances 5, 127108, 2015

Chapter 6 contains work partially summarized in the following journal article:

M. Tokaç, C.J. Kinane, D. Atkinson and A.T. Hindmarch. *"Temperature Dependence of Magnetic Dead Layers in Ferromagnetic Thin-Films"*, Journal of Physics: Condensed Matter, Under Review, 2016

Chapter 7 contains work partially summarized in the following journal article:

M. Tokaç, S.A. Bunyaev, G.N. Kakazei, D.S. Schmool, D. Atkinson and A.T. Hindmarch, *"Interfacial Structure Dependent Spin-Mixing Conductance in Polycrystalline Cobalt Thin-Films"*, Physical Review Letters, 115, 089901, 2015

Related work which has been co-authored by the candidate during the period of doctoral study has appeared in the following peer-reviewed publications:

S. Azzawi, A. Ganguly, **M. Tokaç**, R.M. Rowan-Robinson, J. Sinha, A.T. Hindmarch, A. Barman, and D. Atkinson, *"Evolution of Damping of Ferromagnetic / Nonmagnetic Thin Film Bilayers as a Function of Nonmagnetic Layer Thickness"*, Physical Review B, 93, 054402, 2016

Table of contents

List of figures

List of tables

1

Introduction

Magnetism and magnetic phenomena are not only interesting for fundamental research, but also relevant for applications. Since the starting points of Feynman's [1] famous talk in 1959, where he described a process in which researchers can manipulate and control individual atoms and molecules, much progress has been made in the understanding of nanotechnology. Spintronics, or spin-electronics, where the idea is to control and manipulate the spin of conduction electrons, aims for the exploitation of the spin degree of freedom rather than the electron's charge as in conventional charge-based electronic devices being used today.

In recent decades, an increasing number of developments in technological applications in data storage technology from magnetic sensors, magnetic domain wall racetrack memory [2], and magnetic random access memory (MRAM) [3], featuring high write endurance, high read and write speeds and low power consumption, are now reaching the commercial market for non-volatile solid state devices. Research in this field resulted in the discovery of new physical phenomena such as giant magnetoresistance (GMR) [4, 5] and tunnel magnetoresistance (TMR) [6]. The interest in MRAM increased significantly after the recent developments in the spin transfer torque (STT) induced switching of magnetization [7–9] and fast dynamic magnetization excitation in Co/Cu/Co systems [10, 11], after theoretical proposals by Berger [12] and Slonczewski [13].

Ferromagnetic thin-films with perpendicular magnetic anisotropy (PMA) designed for MRAM and other nanoscale spintronics devices have been important in spintronics, for

applications of increased data storage density. PMA devices were demonstrated to have great advantages over in-plane magnetized devices, including strong thermal stability and low critical switching current density [14, 15]. These fundamental phenomena gave rise to the contemporary research interest in the field of spintronics.

To achieve a better understanding of the physical processes governing the discovered effects, a clear understanding and control of all effects at the interfaces between ferromagnetic and non-magnetic materials is very important. A precise characterization of ferromagnetic thin films is necessary for the performance and reliability of spintronics devices. Magnetic thin-films are important due to their use in most spintronic devices. In addition, thin-films are of interest because as the thin-film dimensionality reduces, they demonstrate novel physics. The progress in thin-film preparation techniques under ultra high vacuum (UHV) has made it possible to fabricate very thin-films of different materials on top of each other with monolayer precision. Ultra-thin magnetic films, consisting of only a few atomic monolayers, have been employed in spintronics devices and studied in low dimensional systems. As magnetic films become thinner in these systems, the interfaces play a crucial role where the electrical and magnetic properties of interface atoms show different behaviour from those in the bulk due to reducing the dimensionality of the system and symmetry breaking at the interfaces. Therefore, the detailed understanding of interfacial effects in magnetic materials is a significant challenge.

The general aim of the work presented in this thesis is to develop a deeper understanding of the mechanisms for some of the interfacial effects in ferromagnetic thin-films. This study provides structural, magnetic and magnetoresistance behaviour of polycrystalline Co thin-films to understand the interfacial contribution to anisotropic magnetoresistance from a single designed electrically opaque (less transparent) interface for conduction electrons. The magnetic properties of thin-films are influenced by interfacial effects. As the dimensions of thin-film devices are reduced, thermal stability becomes an important issue, which affects the performance of spintronic devices. Thus, understanding of interface magnetism and magnetic dead layers are of critical importance for thin-film magnetic devices. The study also includes an investigation of temperature dependence of magnetic dead layers in ferromagnetic thin-films. Furthermore, structural characterization of polycrystalline Co thin-films was investigated to understand the nature of the crystal structure, which is significant in determining the magnetic properties of thin-films and the structure at the interface. By studying the ferromagnetic (FM) layer thickness dependence of ferromagnetic resonance, the influence of both non-magnetic (NM) layers and the role of local interface structure in

spin-pumping mechanism was studied for a deeper understanding of the dynamical magnetic properties of the thin-films.

This thesis begins with the theoretical background necessary for the understanding of magnetism and interfacial effects in ferromagnetic thin-films. This chapter establishes an understanding of the relationship between atomic magnetic moments and the magnetization behaviour of ferromagnetic materials. A brief introduction of interfacial magnetic dead layers in thin ferromagnetic films is discussed. Then, electronic transport properties of metallic thin-films are introduced. After a brief summary of the physics of ferromagnetism and the underlying interactions, the fundamental equation of the magnetization dynamics, the Landau-Lifshitz-Gilbert equation is discussed, which describes the time evolution of the magnetization in the nanosecond scale. Finally, the fundamental principles of the spin-pumping effect are reviewed and a phenomenological description of the process is presented.

Chapter 3 describes the wide range of experimental techniques used within this thesis to characterize structural and magnetic properties of thin-films. This chapter includes the physics behind thin-film material structures and methods for their growth. SQUID magnetometry is introduced for magnetic characterization of thin-films and for structural analysis of these samples x-ray reflection and diffraction techniques are introduced. The production of neutrons and polarized neutron reflectometry are explained for neutron scattering experiments and the 4-point probe technique is introduced for magnetoresistance measurements of thin-films. Finally, a comprehensive overview of ferromagnetic resonance measurements using a vector network analyzer is given. The theory of scattering for x-rays and neutrons are given in Chapter 4. In particular, details of the scattering process from magnetic thin-films and multilayers, and scattering on non-ideal interfaces are provided. The physical principles of x-ray diffraction are also introduced briefly. Afterwards, a brief introduction of neutron scattering, including the data fitting procedure are presented.

Chapter 5 presents the structural and magnetic characterization of polycrystalline Co thin-films with Cu and Ir overlayers to develop an explanation of anisotropic magnetoresistance behaviour of Co thin-films as a function of thickness. In Chapter 6, the structural and magnetic characterization of amorphous CoFeB:Ta thin-films deposited on Si/SiO_2 and GaAs(001) substrates are investigated to explain temperature dependence of magnetic dead layer formations in thin-films using polarized neutron reflectometer. Chapter 7 presents the crystal structure of Co thin-films, and enhancement of intrinsic damping in these thin-films of various thicknesses are investigated to understand the role of local interface structure in spin-pumping. Finally, the thesis concludes with a summary of the key results obtained in this investigation.

2

Theoretical Background

This chapter introduces the theoretical background of magnetism and interfacial effects which are required to understand the present work. The discussion starts with the basic concept of the magnetic moment and the angular momentum associated with the electron spin, and orbital motion. In the following section, materials are classified according to their magnetic response to an applied magnetic field. Afterwards, the basic concepts of ferromagnetism with underlying magnetic interactions are described. The physical principles of electrical transport in ferromagnetic (FM) thin-films are discussed which includes the general theory of electronic transport in bulk materials as well as a model which describes the size effect of low-dimensional systems.

The different contributions to the magnetic free energy are presented to introduce the total internal magnetic field which acts on the magnetic moments. The fundamental principles of magnetization dynamics are discussed, and the Landau-Lifshitz-Gilbert (LLG) equation describing the precessional motion of the magnetization in an applied field is derived. The ferromagnetic resonance (FMR) condition and the basic principles of the spin-pumping process are introduced. The origin of intrinsic damping due to spin-orbit interaction (SOI) and the extrinsic contribution to the damping are also discussed. This chapter finishes with discussions of the formation of magnetically dead layers (MDL) in FM thin-films.

2.1 Atomic Magnetic Moments

In atomic theory, magnetism observed in bulk matter arises from two kinds of motion of the electrons. The orbital motion of electron around the nucleus which produces an orbital magnetic dipole moment and rotation of electrons around their own axis known as spin which produces spin magnetic moment. Fig. 2.1 shows simplistically the relationship between magnetic moments, and orbital and spin motion of an electron.

The movement of electrons in orbits around the nucleus can be considered as an electric current flowing in a closed loop with zero resistance. When an electron with mass m_e and charge $-e$ orbiting around the nucleus with velocity v and radius r gives rise to the orbital magnetic moment, which points perpendicular to the plane of the orbit. It is defined as $\mu_L = \gamma_L L$, where L is the total orbital angular momentum which points in the opposite direction to the orbital magnetic moment. In 1925, Uhlenbeck and Goudsmit [16] postulated that the electron possesses an intrinsic angular momentum which causes a magnetic moment in the electron that would interact with an external magnetic field. The electron spin and its magnetic moment are quantized such that there are only two possible discrete values (spin-up and spin-down). The spin magnetic moment, due to the rotation about its own axis is defined as $\mu_S = \gamma_S S$, where S is the total spin angular momentum, and $\gamma_{L,S}$ is the gyromagnetic ratio which describes the frequency of the orbital motion of the electron, and

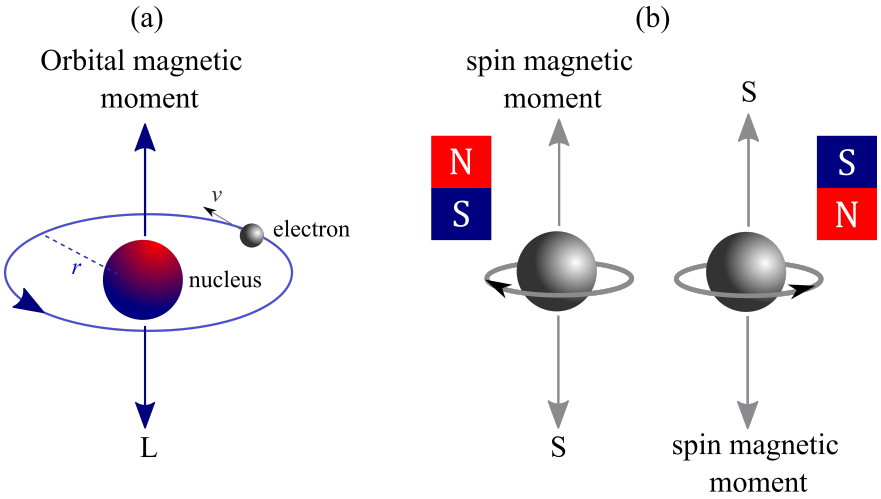

Fig. 2.1 Schematic representation of (a) orbital motion about the nucleus gives rise to an orbital magnetic moment with associated angular momentum, L (b) spin of the electron about its own axis resulting in a spin magnetic moment with associated angular momentum, S.

is given as $\gamma_{L,S} = g\mu_B/\hbar$ [17]. Here g is the dimensionless Landé g-factor, $\hbar$ is the Planck's constant, and $\mu_B = (e\hbar)/(2m_e) = 9.27 \times 10^{-24}$ A/m^2 is the basic unit of magnetic moment known as the Bohr magneton. The general expression to define the total magnetic moment, μ_m of the atoms including spin and orbital angular momentum is;

$$\mu_m = -\frac{g\ \mu_B}{\hbar}\ J \tag{2.1}$$

where $J = L + S$ is the total angular momentum, given by Hund's rules [18], The Landé g-factor is given by;

$$g = 1 + \frac{J(J+1) + S(S+1) - L(L+1)}{2J(J+1)} \tag{2.2}$$

where Landé g-factor takes values between 1 and 2. For atoms with total angular momentum $J = 0$, there is no permanent magnetic moment. If the spins cancel out $S = 0$, $J = L$ and $g = 1$ which gives the orbital contribution [17]. If there is no net orbital contribution to the moment $L = 0$, $J = S$ and $g = 2$ which gives the spin contribution. The exact free electron value for g-factor $g = 2.00232$ can be obtained by quantum electrodynamics [19].

2.2 Magnetization Behaviour of Metals

In order to explain the different types of magnetic behaviour, it is required to describe the magnetic response of a material in the presence of external magnetic field. The magnetic behaviour of materials may be broadly classified into five groups: diamagnetism, paramagnetism, ferromagnetism, antiferromagnetism and ferrimagnetism. The first two groups are known as non-magnetic, where they exhibit a weak response to an applied field. The last three group of materials, show long range order below T_C.

Diamagnetism is based on the interaction of electrons with the applied magnetic field. It is a fundamental property of all materials in which the magnetization opposes the external magnetic field. The magnetic susceptibility of a diamagnetic material is negative, hence the material gets weakly magnetized opposing the external field.

In paramagnetic materials, there are unpaired electrons in unfilled orbital shells resulting in a non-zero magnetic moment in response to an applied magnetic field. In the absence of applied field, the magnetic moments in the material are randomly oriented because the magnetic moments interact very weakly with neighbouring atoms. When a magnetic field is

applied to a paramagnet, the magnetic moments tend to align parallel to the external magnetic field, but the interaction of magnetic moment with the applied field is weak.

Materials which have a large spontaneous magnetization even in the absence of an applied field are known as FM materials [17]. Importantly, these materials exhibit long range ordering of the magnetic moments which causes the unpaired electron orbitals aligning along a single direction. The atoms have magnetic moments due to unfilled electronic orbitals, leading to a spontaneous magnetization which has a maximum value at $T \rightarrow 0$ K and disappears at a certain temperature which is called the Curie temperature, T_C. Ferromagnetic materials become paramagnetic in the presence of an applied field at temperatures above T_C where the susceptibility is expressed by the Curie-Weiss law;

$$\chi = \frac{C}{T - \theta} \tag{2.3}$$

where C is the Curie constant, T is the temperature and θ is the Weiss constant. The divergence of the susceptibility at $T = \theta$ corresponds to the phase transition to the spontaneously ordered phase. Fig. 2.2 (a) shows temperature dependent magnetization and susceptibility curves of a single ferromagnetic domain below and above the T_C.

The theory of ferromagnetism was first postulated by Weiss [20], who assumed the existence of large internal field in a FM material that acts to align the neighbouring moments parallel to one another. This field is sufficient to magnetize the FM material to saturation. The origin of these huge effective fields remained a mystery until Heisenberg introduced the concept of the exchange interaction in 1928 [21]. At low-temperature, the magnetic moments can be aligned even without external applied field. As the temperature increases, thermal energy begins to destroy the spontaneous alignment of the magnetization, and at $T = T_C$, the magnetic order will be destroyed. Increasing temperature leads to a phase transition, and the material becomes paramagnetic above T_C.

The irreversibility and demagnetization behaviour of FM materials in the presence of an applied field is plotted as a hysteresis loop, as shown in Fig. 2.2 (b). When a strong field is applied to a FM material, the magnetic moments are aligned uniformly in the direction of the applied field until the magnetization no longer increases. This state is known as saturation magnetization, M_S. When the magnetic field is removed, the magnetization decreases to the remanent magnetization, M_r, where there are partial alignments between magnetic moments even in the absence of applied field. To remove this remanent magnetization, a reversed field is required to reduce the magnetization to zero which is known as the coercive field, H_C. As the magnetic field increases in the opposite direction, the same saturation magnetization occurs in the opposite direction. Materials with low coercivity are called magnetically soft,

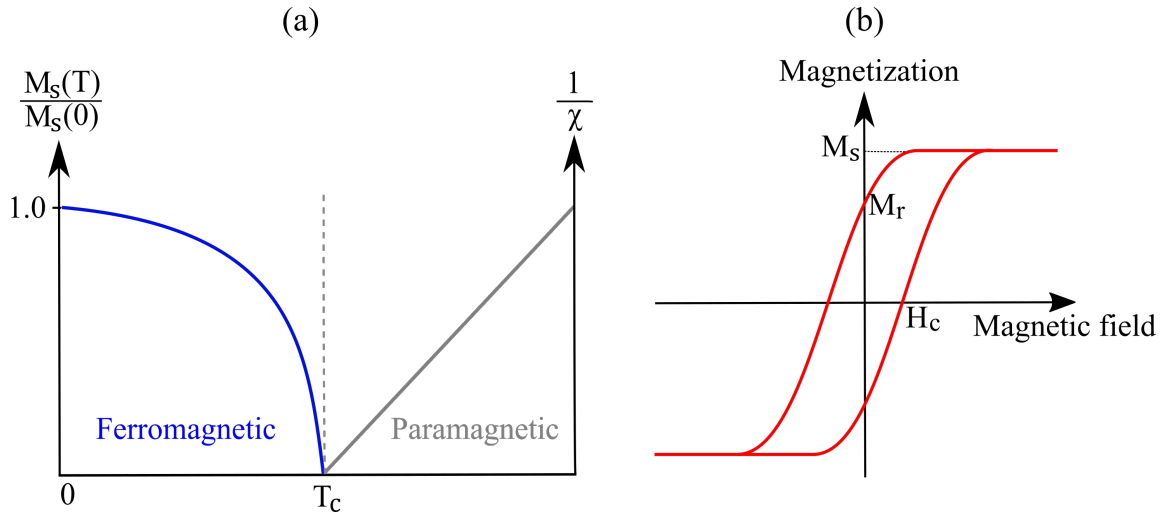

Fig. 2.2 (a) Magnetization and susceptibility curves of a single ferromagnetic domain below and above the T_C. (b) Schematic view of a typical hysteresis loop for a ferromagnetic material. The magnetization reaches the saturation magnetization, M_S, at high fields, retains a remanent magnetization, M_r, when the field is removed and requires a coercive field, H_C, to remove the net magnetization.

such as permalloy $Ni_{81}Fe_{19}$. However, materials which possess large coercivity are called hard materials, such as FePt, CoIr etc.

In antiferromagnetic materials, the magnetic moments align in a regular pattern, but unlike a ferromagnet, the neighbouring spins of electrons display a preference in opposite directions. Antiferromagnetic materials behave similar to ferromagnetic materials, but the anti-parallel alignment of the magnetic moments are seen due to the exchange interaction between neighbouring atoms. In the presence of a magnetic field, these materials can be weakly magnetized in the direction of the applied field because the exchange interactions work against the magnetic field.

Ferrimagnetic materials have magnetic moments aligned opposing to another magnetic moments, similar to antiferromagnetism. Normally, the opposite ordering of magnetic moments cancels out the overall magnetic field of the sample, but these opposing moments are unequal in ferrimagnets, resulting in a non-zero spontaneous magnetization.

2.3 Band Theory

Band theory is a general theory of the electronic structure of solids, which is valid for metals, semiconductors and insulators. The applications of band theory to magnetic materials were first made by E.C. Stoner and J.C. Slater [22, 23] to explain the origin of the non-integer effective Bohr magneton values of the FM transition metals at $T = 0$ K. The effective number of Bohr magnetons, provides the number of the unpaired spins per atom, is $n_{\text{eff}} = M_{\text{S}}(0)/(n\mu_{\text{B}})$, where M_{S} is the saturation magnetization at T= 0 K, and n is the number of atoms per unit volume. The values of n_{eff} for Fe, Co and Ni are 2.22, 1.72 and 0.60 μ_{B} per atom, respectively.

The electrons in atoms, which are located at large distances from each other, occupy certain energy levels according to the Pauli exclusion principle, which states that no two electrons in an atom can occupy the same quantum state. Each energy level contains a maximum of two electrons; one electron has spin-up and the other has spin-down. When n atoms are brought close together to form a solid, each energy level of the free atoms begin to overlap, and split into n sub-levels because the Pauli exclusion principle applies to prevent them from having, for example, a single 1s level. Instead of this, the 1s level must split into n levels, and each have two electrons [17].

The spin-resolved density of states for a non-ferromagnetic and ferromagnetic materials are compared in Fig. 2.3. Non-ferromagnetic transition metals have a valence configuration of the form $d^n s^1$, where both d and s states are at the Fermi level. In FM transition metals, the valence configuration is of the form $d^{n\uparrow} d^{n\downarrow} s^1$. They have both s and d states at the Fermi level, and the densities of spin-up and spin-down d states are not equal [24].

The filling of atomic energy levels continues regularly from hydrogen up to argon, but when heavier elements are considered, there are some complications for 3d and 4s levels which have nearly the same energy. 3d electrons, which are carriers of the magnetism, are located relatively far from the nucleus, and instead of being localized to an individual atom, they are considered to be moving among the atoms. The outermost electrons of the transition elements are 3d and 4s which are the first to overlap and form energy bands. The narrow 3d band has a higher density of states at the Fermi level, but the 4s band is broad, and it has a low density of states at the Fermi level. When the inter-atomic distance z has decreased to z_0, as indicated in Fig. 2.4 (a), 3d levels are spread into a band from B to C, and the 4s levels are spread into a band from A to D, much wider than 3d levels, because the 4s electrons are less strongly bound to the nucleus. Lower levels; 1s and 2s, are closer to nucleus, hence the

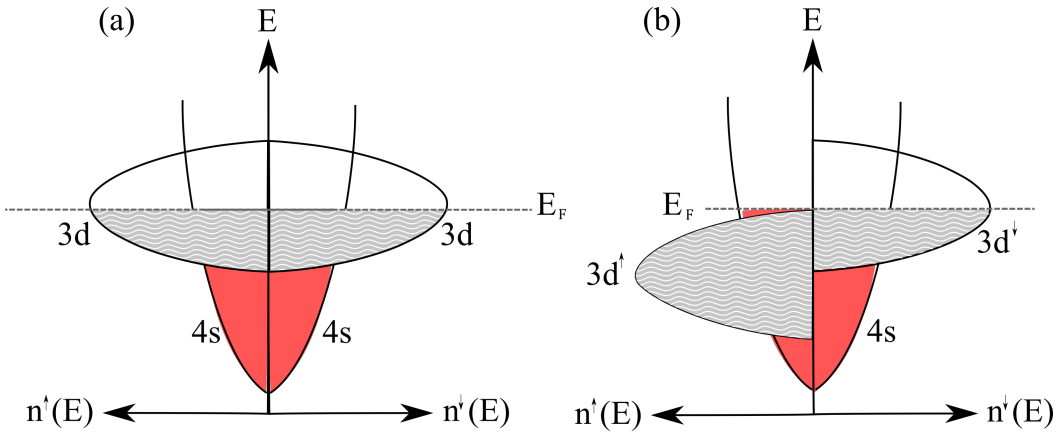

Fig. 2.3 Schematic to show the electronic band structure and density of states for (a) non-ferromagnetic and (b) ferromagnetic transition metals which shows 3*d* band splitting in spin-up and spin-down states.

corresponding energy levels exhibit a smaller splitting. The energy difference between these levels is the density of levels, which is a function of the energy E in the band. The product of the density $N(E)$, and any energy range gives the number of levels in that range. Therefore $N(E)dE$ gives the number of energy levels between the energies E and $E+dE$. In Fig. 2.4 (b), the density of states curves of 3*d* and 4*s* bands are drawn side by side because these bands overlap in energy. The density of 3*d* levels is greater than the density of 4*s* levels, because the 3*d* band has a maximum occupancy of 10 electrons in every atom. Thus 3*d* levels have a high electron density [17].

The extent to which these levels are occupied (dotted line - Fermi Energy) would depend on the total number of $(3d+4s)$ electrons in the atom. Let n represent the number of $(3d+4s)$ electrons per atom, and x represent the number of 4*s* electrons per atom, and the number of 3*d* electrons per atom is represented by $(n-x)$. The spin imbalance, n_{eff} is given by;

$$n_{\text{eff}} = [5-(n-x-5)]\mu_B \;=\; [10-(n-x)]\mu_B. \tag{2.4}$$

Due to the overlap between 3*d* and 4*s* bands, the valence electrons partially occupy each of these bands. When the electronic structure of Ni is considered, the exchange interaction displacement is very strong such that one 3*d* sub-band is completely filled with 5 spin-up electrons, and $(n-x-5)$ electrons have spin-down, and the measured value of n_{eff} is 0.60 μ_{B}. Inserting these values into Eq. 2.4, x is found as 0.6 which is proportional to number of 4*s* electrons below the Fermi level. This result shows that 9.4 electrons are in the 3*d* band, and 0.6 electrons in the 4*s* band; the corresponding distribution in the free atom is 8 electrons in 3*d* band and 2 electrons in 4*s* band. This is the reason why the Fermi level for Ni is drawn

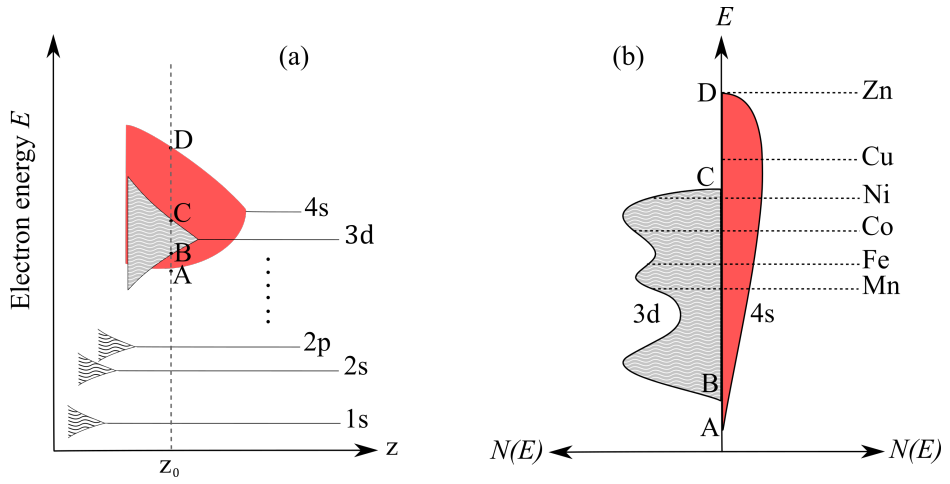

Fig. 2.4 (a) A schematic view of splitting of electron energy levels when the inter-atomic distance decreases. (b) Density of levels in the $3d$ and $4s$ bands. Both figures are reproduced from [17].

below the top of $3d$ band. Inserting the number of valence electrons for Fe, Co and Ni in the given equation, the spin imbalance is found to be, 2.6 μ_B, 1.6 μ_B and 0.6 μ_B, respectively.

This model is useful to demonstrate why the later transition metals, Cu and Zn, are not ferromagnetic. For Cu, the Fermi level is above the $3d$ band. It has a total of 11 $(3d+4s)$ electrons, so its $3d$ sub-bands are completely filled, and $4s$ band is half full. Zn has 12 electrons, hence $3d$ and $4s$ bands are full, so do not contribute a magnetic moment. For lighter transition metals, such as Mn, the exchange interaction is less strong, and the band energy is larger, hence ferromagnetism is not observed because these metals do not meet Stoner criterion. The existence of ferromagnetism is governed by the Stoner criterion; $I\,N(E_F) > 1$ where I is the exchange parameter and $N(E_F)$ is density of states at the Fermi energy [22]. Since the value of exchange interaction $I \cong 1eV$ being similar for all $3d$ transition metals, the condition for ferromagnetic ordering depends on the density of states $N(E_F)$ at Fermi energy.

2.4 Spin-Orbit Interactions

The spin-orbit interaction (SOI) is a well-known phenomenon which can be understood by considering the effects of an electron's orbital motion with respect to its spin. Within its rest frame, an electron is traveling through an electric field, it sees the proton around it. As its name already implies, SOI results from the interaction of the electron's spin with

the magnetic field from the orbital motion around the nucleus. The magnitude of the SOI is a function of the atomic number Z^4 [25]. The current generated due to the circulating of a larger nucleus around the electron is much stronger for a larger nuclear charge. This means SOI increases rapidly with atomic number. In recent years, SOI in FM multilayers has become a significant field of study in spintronics due to possible technological applications.

In solid state systems, the SOI along with structural asymmetry gives rise to more interesting phenomena such as Rashba and Dresselhaus SOI, where the total SOI is the sum of these different sources. The SOI due to the impurities in the conduction layer is the main source of SOI in many metallic systems. The SOI due to lack of crystal inversion symmetry is known as Dresselhaus SOI. This type of SOI is seen in most III-V semiconductors, such as GaAs. They have a zinc-blende structure where the lattice does not have inversion symmetry. The SOI due to lack of structural inversion symmetry in a heterostructure is known as Rashba SOI. This effect enables to control the spin states of electrons through an electric field rather than magnetic fields. In FM heterostructures, the Rashba SOI has become an interesting topic due to the technological applications, where the spin Hall effect with the Rashba SOI provides the opportunity of switching the magnetization just by a charge current [26].

2.5 Magnetic Dead Layers

Magnetically dead layers (MDL) may arise at the interfaces in FM thin-films with length scales of the order of a few monolayers. These MDLs may form during the deposition processes due to interfacial diffusion, causing magnetic moment loss in the FM layer over a distance of the order of a few monolayers. However, some theoretical calculations contradict this explanation, and showed this non-magnetic layer formation is an experimental artifact, for example, due to the incorporation of H atoms into Ni layer [27]. The formation of MDLs and their thicknesses depend on the FM material, deposition conditions, and the material interface [28, 29]. The terminology of magnetic dead layers in the literature is sometimes misleading. Even though this layer is non-ferromagnetic in nature, it may be paramagnetic or antiferromagnetic.

The early studies of dead layer formation are observed at room-temperature for Fe film deposited on a Cu substrate [30], where Fe film has two magnetically dead layers. Later, they investigated the temperature dependence of the MDL for Ni film, and they found 2 and 4 dead layers at 0 K and at room-temperatures, respectively. The dead layer formation at 0 K is attributed to a transfer of electrons from *s* band to the *d* band in the neighbouring surface [31],

which means *s* electrons fill the *d* orbital that reduce the properties of ferromagnetism of Ni film. The magnetization of the film in the presence of magnetically dead layers can be written as;

$$M = M_{\text{bulk}} - \alpha/D \tag{2.5}$$

where M_{bulk} is the bulk magnetization of the FM film, α is proportional to the number of non-magnetic dead layers, and D is the number of atomic layers in the thin-film.

It is very important to precisely determine the thickness of any dead layer formation in FM thin-films because the MDLs do not contribute to the magnetic volume. This can have consequences for spintronics systems which rely on interfacial magnetism such as magnetic tunnel junctions and spin-injection devices [32, 33]. It is significant to understand the formation of MDL in the film structure as the MDL modifies not only the magnetic volume but also the magnetic anisotropy [34]. Theoretical calculations indicated that the magnetic behaviour of Ni films with a few-monolayer thickness grown on Cu layer depends strongly on the crystal direction [35]. They have shown that a single layer of Ni at 0 K is magnetically alive when the film is deposited onto Cu(100) and Cu(110) surfaces, but magnetically dead on the Cu(111) surface [35] where these conclusions are based on the idealized surfaces without considering atomic intermixing at the interface.

2.6 Electronic Transport in Metals

The transport of electric charges in metallic films can be understood by starting with the simple model for free electrons which was proposed by Paul Drude in 1900 [36]. In this model, the electrons are treated as point-like objects that do not interact with each other. Hence, in the absence of externally applied electric field, each electron is taken to move uniformly in a straight line between collisions, without interactions with other electrons or ions. However, in the presence of an external field, each electron is taken to move according to Newton's laws of motion.

In metals, the electrons which contribute to electrical conduction are in energy levels close to the Fermi level. Conductivity is determined by the scattering of the conduction electrons in the material, which is related to the mean free path between scattering events. The electrical conductivity of a material, σ, is expressed as;

$$\sigma = \frac{1}{\rho} = \frac{ne^2\tau}{m^*} \tag{2.6}$$

where n is the volume concentration of free carriers, m^* is the effective mass of the charge carriers, ρ is the electrical resistivity, and τ is the relaxation time between scattering events. This is given by, $\tau = v_F \lambda$, where v_F is the Fermi velocity and λ is the mean free path of the conduction electrons, which is the distance traveled by an electron before it scatters [17]. The electrical resistivity is an intrinsic property of a material which determines how a material opposes the flow of the current. The resistivity of a conducting material is proportional to its cross-sectional area, A, and calculated from measured resistance $R = V/I$;

$$\rho = \frac{\mathrm{R} \times \mathrm{A}}{\mathrm{L}} \tag{2.7}$$

where L is the length of the thin-film. To understand electrical conductivity in FM metals, a description in terms of the two-current model was first suggested by Mott [37], who proposed that at temperatures below T_C, the conduction electrons in a ferromagnet can be classified into two, having spins parallel or anti-parallel to the magnetization [38]. Magnetization of the material causes the $3d$ band to split into two different sub-bands representing the different spin orientations. Spins parallel to the magnetization direction is energetically more favorable than the other, therefore preferentially filled and resulting in the parallel aligned sub-band being entirely below the Fermi level while the anti-parallel channel is only partially occupied. The scattering of $4s$ electrons to the $3d$ band is possible when the $3d$ band is not completely occupied.

The movement of the conduction electrons is influenced by the film thickness where some physical effects arise due to this geometrical limitation which is imposed by the film boundaries. In thin-films, the film thickness is comparable in magnitude with the mean free path. As the film thickness decreases additional scattering mechanisms arise associated with the interfaces, which increases the resistivity of the system.

In 1901, J.J. Thomson [39] proposed a size effect theory where the thin-metal film boundaries might influence the system's resistivity to explain the high electrical resistivity of thin-metal films, compared with the same metals in bulk. Later on, a more accurate size effect theory for a free electron, model based on the Boltzmann transport equation, was developed by Fuchs [40], and extended by Sondheimer [41]. Several assumptions were made by Thomson to develop the theory for the conduction in thin-films: The first assumption states that the electron mean free path in a metal is constant, and it is the same for all conduction electrons. The second assumption is that if an electron collides with the film surface the probability of scattering is independent of the initial and final directions of motion of the electron.

Fig. 2.5 (a) shows the Thomson model for inelastic scattering of conduction electrons from a film surface with thickness t which is less than the bulk mean free path λ_0. Consider an electron that begins its motion from a point P at some distance z from the surface and moves at an angle θ with the z-axis, the average mean free path is;

$$\lambda = \frac{1}{2t}\left(\int_0^t dz \int_0^\pi \lambda_0 \sin\theta d\theta\right) = \frac{t}{2}\left(\log\left(\frac{\lambda_0}{t}\right) + \frac{3}{2}\right) \tag{2.8}$$

where λ_0 is the mean free path of the bulk material. As the conductivity is proportional to the mean free path, Thomson's formula can be obtained as below;

$$\frac{\sigma}{\sigma_0} = \frac{\rho_0}{\rho} = \frac{t}{2\lambda_0}\left(\log\left(\frac{\lambda_0}{t}\right) + \frac{3}{2}\right) \tag{2.9}$$

where σ_0/ρ_0 are the conductivity/resistivity of the bulk material. Here, as film thickness t decreases, λ decreases, and ρ increases; and there is an obvious size effect. Note that this model is based on an assumption that all surface scattering events are inelastic. According to Fuchs, the assumptions used in deriving Thomson's formula are incorrect for the following reasons. First, mean free paths of the electrons starting on the film surface are neglected. Second, the statistical distribution of the mean free path about λ_0 was not taken into account, and finally, to get the mean free path, all electrons should be taken into account in the metal at a given moment, and their mean free paths averaged [40]. The schematic view of Fuchs-Sondheimer model is shown in Fig. 2.5 (b). They derived an approximate formula to model the experimental results;

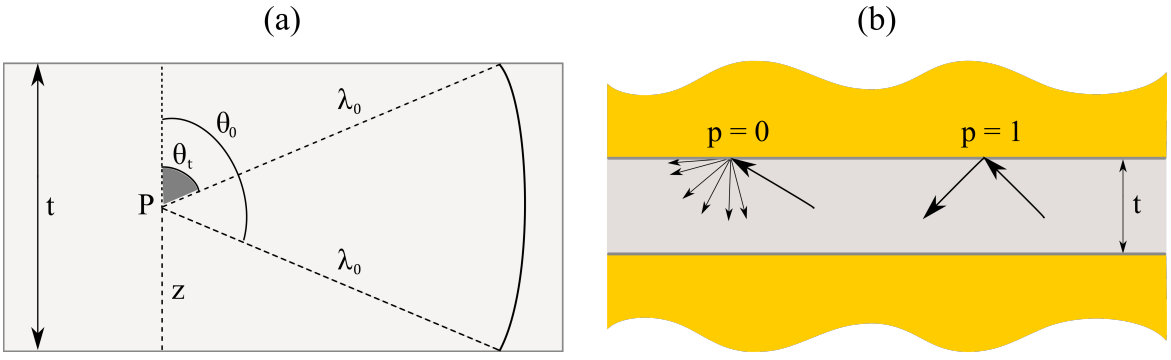

Fig. 2.5 (a) A schematic view of Thomson model for inelastic scattering of conduction electrons from film surface with film thickness t, less than the bulk mean free path λ_0. Reproduced from [39]. (b) An illustration of Fuchs-Sondheimer model for a thin-film with thickness t. If the specularity parameter $p = 0$, all electrons scatter diffusely, and if $p = 1$ all electrons scatter speculary at the layer surfaces.

$$\frac{\sigma_0}{\sigma} = \frac{\rho}{\rho_0} = 1 + \frac{3\lambda_0}{8t}(1-p) \tag{2.10}$$

for sufficiently thick films ($t >> \lambda_0$)

$$\frac{\sigma_0}{\sigma} = \frac{\rho}{\rho_0} = \frac{4(1-p)}{3(1+p)}\frac{\lambda_0}{t\ \ln(\lambda_0/t)} \tag{2.11}$$

for very thin-films ($t << \lambda_0$). The increase of resistivity for thin-films can be described by the reduction of the average mean free path of electrons. When the electrons are accelerated by the external field, they lose momentum by scattering if they hit the film surface. If the momentum is parallel to the surface, the effect of scattering on the mean free path vanishes which is called a mirror reflection. If the scattering process is random, the scattering effect on the mean free path is the largest. The probability of mirror reflection is defined by the specularity parameter p, which describes the conservation of momentum parallel to the surface or interface. If the specular parameter $p = 0$ that means all electrons scatter diffusely at the rough surface, which causes a higher resistivity of the film. However, in the case of $p = 1$, all electrons scatter from a perfect surface. This theory is based on the assumption that the value of specularity parameter p is constant for both surfaces.

2.6.1 Magnetoresistance Behaviour of Metals

In normal metals, electrons move through a material in straight lines between scattering events when there is no applied field. In the presence of the applied magnetic field, there is a change in resistance due to the Hall effect, which deflects moving charges from the direction of current. When a charge carrier starts to orbit around the applied field due to the Lorentz force, it makes a reduced contribution to the current density. After a scattering event, the conduction electron travels further with an initial velocity around applied field. Hence, the resistance in the presence of applied field is larger than the resistance without applied field. This mechanism is known as the ordinary magnetoresistance effect which is described by Kohler's rule;

$$\frac{\Delta\rho}{\rho} \propto \left(\frac{H}{\rho}\right)^2 \tag{2.12}$$

where $\Delta\rho$ is the change in resistivity, ρ is the film resistivity, and H is the applied magnetic field. The change in resistivity is positive for both magnetic field directions, and it has a maximum/minimum value when the applied magnetic field, and the electric current are perpendicular/parallel to each other [24]. The magnetoresistance is described as transverse

or longitudinal depending on the direction of the applied field either perpendicular or parallel to the direction of the electrical current, respectively. For FM materials, the Kohler rule can be generalized as;

$$\frac{\Delta\rho}{\rho} \propto a\left(\frac{H}{\rho}\right)^2 + b\left(\frac{M}{\rho}\right)^2 \tag{2.13}$$

where the first term describes the ordinary magnetoresistance, and the second term is the spontaneous or anisotropic magnetoresistance.

2.6.2 Anisotropic Magnetoresistance in Ferromagnets

Anisotropic Magnetoresistance (AMR) is a transport mechanism arising from the interaction of the electron spin with the orbital moment of the atom [42, 43]. This effect depends on the angle between the magnetization vector **M** and the direction of the applied current **J** for a FM film, as illustrated in Fig. 2.6. This dependence of the resistance on the applied field was first reported in 1857 by William Thomson [44]. The AMR ratio can be defined [43] as the ratio of the resistivity change, $\Delta\rho$ to the perpendicular resistivity as;

$$\text{AMR Ratio} = \frac{\Delta\rho}{\rho_\perp}. \tag{2.14}$$

The change in resistivity is $\Delta\rho = \rho_\parallel - \rho_\perp$. The resistivity for current flowing in the material parallel to the magnetization direction ($\theta = 0$) is longitudinal resistivity, $\rho_\parallel$. The resistivity for current flowing perpendicular to the applied field ($\theta = 90$) is transverse

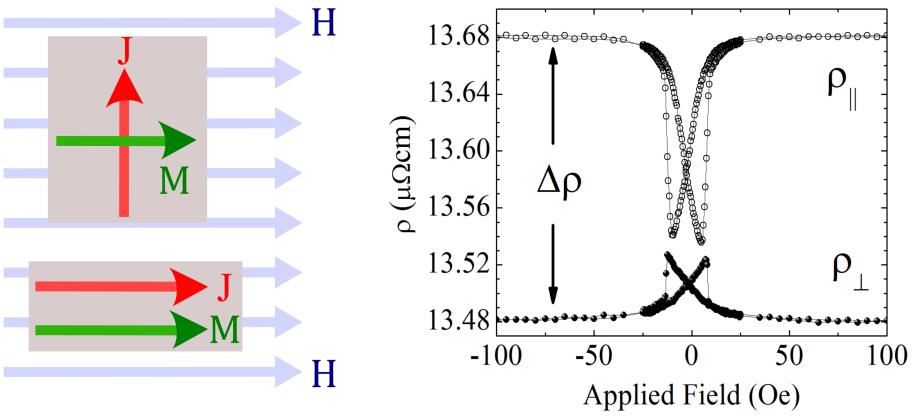

Fig. 2.6 Example of the anisotropic resistance in Co thin-film taken at room-temperature with corresponding schematics to show the orientation of the magnetization **M** and the current density **J** in the presence of saturation magnetic field **H**.

resistivity, $\rho_{\perp}$ [43]. As the direction of the magnetization vector rotates, the $3d$ electron cloud for each nucleus deforms, hence the scattering probabilities of the conduction electrons are changed due to this deformation [17, 42, 43]. When the magnetization direction is oriented perpendicular to the current, the unfilled electronic orbitals are in the same plane of the current, then the cross section for scattering is reduced. This results in the low resistance state. Conversely, in the case when the magnetization direction is parallel to the current direction, the unfilled electronic orbitals are perpendicular to the current, the cross-section for scattering is increased, yielding a high resistance state. For a FM material subjected to a saturating magnetic field the angular dependent resistivity, $\rho(\theta)$, [43];

$$\rho(\theta) = \rho_{\perp} + \Delta\rho cos^2(\theta) \tag{2.15}$$

where θ is the angle between the current density $\mathbf{J}$ and magnetization $\mathbf{M}$. The magnitude of the change in resistance due to the magnetization is up to a few per cent at room-temperature. The magnitude of the AMR in thin-films depends on the thickness, grain size and film surface conditions [45–48].

The microscopic origin of AMR was first proposed by Smit [42] as a basis of his results of magnetoresistance in ferromagnets. He proposed that this effect can only arise due to the SOI which causes different directional scattering of spin-up and spin-down electrons. Smit argued that to observe the AMR where $\rho_{\parallel} > \rho_{\perp}$, spin-flip scattering must occur because the AMR ratio tends to zero as temperature increases towards T_{C}. In this model, it is assumed that the SOI provides mixing of spin-up and spin-down states, thus $s^{\uparrow}$ electrons can be scattered into empty $d^{\downarrow}$ states. Since this mixing is anisotropic, and the scattering probability is larger for electrons travelling parallel to the direction of the magnetization, it can be concluded that $\rho_{\parallel}$ is larger than $\rho_{\perp}$.

2.7 Energy Contributions in Ferromagnets

The total energy of a ferromagnetic system is given by summing up the different free energy contributions which govern the magnetic system behaviour;

$$\varepsilon_{\mathrm{tot}} = \varepsilon_{\mathrm{ex}} + \varepsilon_{\mathrm{dem}} + \varepsilon_{\mathrm{mc}} + \varepsilon_{\mathrm{ze}} \tag{2.16}$$

where $\varepsilon_{\mathrm{ex}}$ is exchange energy, $\varepsilon_{\mathrm{dem}}$ is demagnetization energy, $\varepsilon_{\mathrm{mc}}$ is magnetocrystalline anisotropy energy, and $\varepsilon_{\mathrm{ze}}$ is Zeeman energy. The total energy allows the introduction of

the total internal magnetic field H_{eff} acting on the magnetic moments inside a material. This field is the derivative of the free magnetic energy over the direction of the magnetization as;

$$H_{\text{eff}} = -\frac{1}{\mu_0}\frac{d\varepsilon}{dM} \tag{2.17}$$

and represents the combination of exchange, anisotropy, demagnetization and applied field in a single precession. Total energy calculations show that even in the absence of an external field there is an effective field present and acting on the magnetization. In the case of an applied magnetic field, depending on the internal and external forces, different equilibrium configurations for the magnetization are obtained where it is a consequence of the minimum energy state. The magnetization precession will be introduced using H_{eff} in the next section. The following subsections describe these interactions and corresponding energy contributions.

2.7.1 Exchange Energy

The quantum mechanical exchange interaction is the strongest magnetic interaction which gives rise to the parallel (ferromagnetic) or anti-parallel (antiferromagnetic) spin alignment between neighbouring magnetic moments in a material. It is very strong interaction, but acts only between neighbouring moments, and drops very rapidly with increasing distance, hence it is very weak at large distances. For ferromagnetism when the angle between neighbouring spins becomes zero the exchange energy is minimized and gives parallel alignment of the spins. This interaction leads to the spontaneous magnetization which occurs in FM material. It is responsible for the establishment of magnetic ordering in the material, and it is based on the Coulomb interaction between charges and the Pauli exclusion principle. The exchange interaction between two neighbouring spins S_i and S_j can be described as;

$$\varepsilon_{\text{ex}} = -2\, J_{\text{ex}} \sum_{ij} S_i S_j \cos(\phi_{i,j}) \tag{2.18}$$

where ϕ is the angle between neighbouring spins, and J_{ex} is the exchange constant which is a measure of the strength of the interaction, and its value depends on the distance between interacting spins. In the case of ferromagnetic ordering, a positive value of J_{ex} are necessary resulting in a lower energy configuration for parallel spin alignment ($\cos\phi$ = 1). When J_{ex} is negative ($\cos\phi$ = -1), it causes to anti-parallel spin alignment, resulting antiferromagnetic ordering [17]. Inter-atomic distances determine the exchange integral J_{ex}, which is non-zero if the electrons are close enough for their wave functions to overlap.

2.7.2 Demagnetizing Energy

For a uniformly magnetized FM material, the magnetization within the sample creates magnetic free poles that appear on the surface, creating a magnetic field outside and inside of the material. The magnetic field inside the material is in the opposite direction to the magnetic moments, resulting in a demagnetization field, H_{dem}. The energy associated with the H_{dem} is termed the demagnetizing energy given by;

$$\varepsilon_{\text{dem}} = -\frac{\mu_0}{2}(MH_{\text{dem}}). \tag{2.19}$$

Here the demagnetizing field for a uniformly magnetized ellipsoid is described as $H_{\text{dem}} = -\overline{N}\,M$ where $\overline{N}$ is the demagnetizing tensor. If the magnetization points along a principle axis of the ellipsoid then $\overline{N}$ is diagonal and can be written as;

$$\overline{N} = \begin{bmatrix} N_X & 0 & 0 \\ 0 & N_Y & 0 \\ 0 & 0 & N_Z \end{bmatrix}$$

When the magnetization lies uniformly in the plane of the film, magnetic charges are avoided, leading to the lowest energy configuration. In this case the demagnetization factors are $N_X = N_Y = 0$ and $N_Z = 1$.

2.7.3 Zeeman Energy

The interaction of magnetic moments with an external magnetic field leads to an energy term known as the Zeeman energy. This energy is minimum when the magnetic moments are aligned parallel to the external magnetic field. Zeeman energy is expressed as;

$$\varepsilon_{\text{ze}} = -\mu_0 \int_V M\, H_{ext}\, dV. \tag{2.20}$$

2.7.4 Magnetocrystalline Anisotropy Energy

The magnetization in a FM material has an energetic preference for certain crystallographic directions which are called easy axes, along which small applied magnetic field is sufficient to reach the saturation magnetization. The directions along which it is most difficult to saturate the sample inside a crystal are called hard axes, along which large applied magnetic field is required to reach the saturation magnetization. This dependence of free energy on the preferential alignment of magnetization along the specific crystallographic

axes in the material is known as magnetocrystalline anisotropy [17]. This anisotropy is caused by the SOI of the electron; the spin of the electron in the orbit is strongly coupled to the lattice. If the magnetic moments in a FM material is oriented towards one certain axis, this material have uniaxial anisotropy, but if the moments have equivalent minima along all three directions, it will have a cubic anisotropy. Usually this anisotropy energy is smaller than the exchange energy. In the absence of an external applied field, the direction of the magnetization is determined by the anisotropy, but the exchange interaction tries to align the magnetic moments regardless of their direction. For a ferromagnetic single crystal Co, the magnetization curves with the applied field along the easy and hard axes is shown in Fig. 2.7.

The magnetization curves of Co at room-temperature measured with the field along different crystallographic axes is illustrated in Fig. 2.7. Each material has different easy axes [18], for example, the easy axis of hexagonal close-packed (hcp) Co is [0001], and the hard axis is [1000] direction. In hexagonal crystals the weak ferromagnetism lies in the *c*-axis, which is the easy axis of magnetization. All directions in the basal plane are very difficult to flip the magnetization out of the *c*-axis. The energy required to rotate the magnetic moments in a FM material from easy axes of magnetization to the hard axis is known as magnetocrystalline anisotropy energy [17]. This energy is usually small in comparison to the exchange energy. However, the magnetization direction can be determined only by the anisotropy, because the exchange interaction tend to align the magnetic moments parallel to each other no matter in which direction. For uniaxial crystals, the magnetocrystalline anisotropy energy is given by,

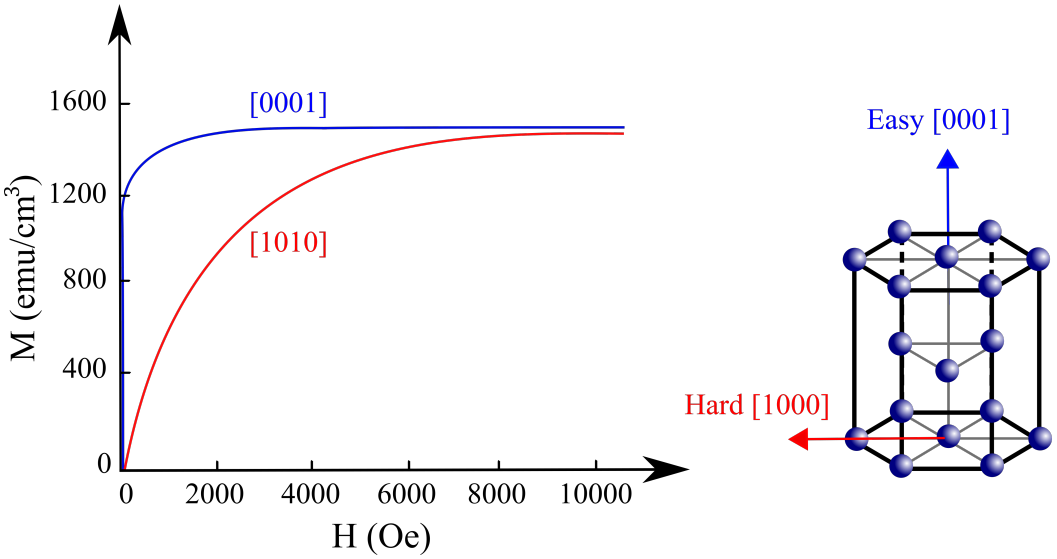

Fig. 2.7 Magnetization curves for the principle crystallographic axes of single crystal Co.

$$\varepsilon_{mc} = K_1 \sin^2\theta + K_2 \sin^4\theta + ... \tag{2.21}$$

where $K_1 = 45 \times 10^4$ J/m^3 and $K_2 = 14.5 \times 10^4$ J/m^3 [17] are first and second order uniaxial anisotropy constants in the case of hcp Co, and θ is the angle between the easy axis and the magnetization.

2.8 Magnetization Dynamics

In the last section the total static energy of a magnetic thin-film at equilibrium, and from that the effective field was defined. The fundamental principle of the magnetization dynamics is based on precession of magnetic moments under the influence of external and internal magnetic fields. This precessional motion of the magnetization in an effective field was proposed by Landau and Lifshitz (LL) and represent by;

$$\frac{dM}{dt} = -\gamma\Big(M \times H_{\text{eff}}\Big). \tag{2.22}$$

This equation explains the precession of magnetic moment around the static field at a constant angle θ, but does not reach the equilibrium position. This is in a contradiction to experimental observations in which the magnetic moment reach equilibrium after a finite time. Hence, an additional term is needed which points toward the effective field in order to support experimental observations. The Landau-Lifshitz equation of motion with addition of a damping term is [49];

$$\frac{dM}{dt} = -\gamma\Big(M \times H_{\text{eff}}\Big) - \frac{\lambda}{M_{\text{S}}^2} M \times \Big(M \times H_{\text{eff}}\Big) \tag{2.23}$$

where $\lambda = 1/\tau$ is a phenomenological damping frequency which is the inverse of the relaxation time τ. This equation of motion causes very fast precession in the case of very large damping which does not correctly describe the behaviour of magnetization in the large damping case. This time-dependent Landau-Lifshitz (LL) equation was reformulated by Gilbert, introducing a viscous damping term to form the famous Landau-Lifshitz-Gilbert (LLG) equation [50];

$$\frac{dM}{dt} = -\gamma\Big(M \times H_{\text{eff}}\Big) + \frac{\alpha}{M_{\text{S}}}\Big(M \times \frac{dM}{dt}\Big). \tag{2.24}$$

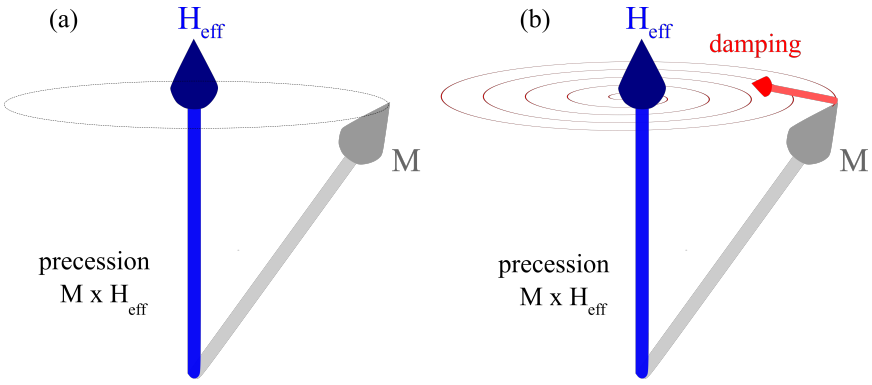

Fig. 2.8 Uniform precession of magnetization vector around an effective field direction (H_{eff}) governed by (a) precessional torque and (b) damping effects which acts perpendicular to the direction of motion to move the magnetization toward H_{eff}.

The first term in Eq. 2.24 corresponds to a uniform precession of the magnetization, where there is no damping in the system as shown in Fig. 2.8 (a), and the second term is the phenomenological damping term with dimensionless damping parameter α which is known as Gilbert damping parameter. Damping acts perpendicular to the direction of motion of the magnetization M, and makes the system relax toward the effective field H_{eff} as shown in Fig. 2.8 (b). The magnetization follows a helical trajectory as time passes until it becomes aligned with the applied field due to the damping term. In this case, all torques acting on the magnetization vanish. In the case of small damping, $\alpha \ll 1$, both the LL and the LLG equations can be shown to be identical.

2.8.1 Ferromagnetic Resonance

Ferromagnetic resonance (FMR) is a very powerful technique to probe the magnetization of a material. It involves precessional motion of magnetization of a FM material around an externally applied magnetic field. In FMR experiments, a microwave field is applied to the sample to excite the magnetization with a fixed frequency f, and a magnetic field is applied at the same time in plane of sample to change the precessional frequency. The physical process of FMR is fulfilled when the microwave frequency is matched with the precessional frequency at a given effective field. The FMR condition in a FM film is related to the demagnetizing field, hence the FMR equation depends also on the shape of the FM film [51]. The resonant condition for a thin-film magnetized in the film plane in an applied field is expressed by the Kittel Law [51];

$$\left(\frac{2\pi f}{\gamma}\right)^2 = H_{\text{res}}\left(H_{\text{res}} + 4\pi M_{\text{eff}}\right). \tag{2.25}$$

where f is the resonance frequency, H_{res} is the magnetic field at the resonance condition, and M_{eff} is the effective magnetization which includes the saturation magnetization and other anisotropy contributions. The effective demagnetization field $4\pi M_{\text{eff}}$ for a continuous film is given by;

$$4\pi M_{\text{eff}} \;=\; 4\pi M_{\text{S}} + \left(\frac{2K_{\text{S}}}{M_{\text{S}}\, t}\right) \tag{2.26}$$

where M_{S} is the saturation magnetization. The surface uniaxial anisotropy field, H_{S}, originates from interface [52] is given by;

$$H_S \;=\; \frac{2K_{\text{S}}}{M_{\text{S}}\, t}. \tag{2.27}$$

The expression of the Kittel equation for crystals with cubic anisotropy can be found elsewhere [51]. FMR measurements provide useful information about magnetic damping through the study of the linewidth of the microwave absorption. The full-width-half-maximum (FWHM) gives the resonance linewidth, $\triangle H_{\text{res}}$, and it is obtained from the peak-to-peak linewidth of the derivative of the absorption curve, which is the field between two inflection points, using the relation $\triangle H_{\text{pp}} = (1/\sqrt{3})\triangle H_{\text{res}}$.

2.8.2 Magnetization Damping

A clear description of the Gilbert damping mechanism in metallic films is still under debate, and there are many possible phenomena, which might have a contribution to it. In this section several of those possible contributions to magnetic damping are discussed. In metallic ferromagnets, contributions to the magnetic relaxation are broken down into intrinsic and extrinsic effects. Intrinsic effects originate from the interactions of magnetic and non-magnetic modes of a system which are intrinsic to the material. These effects are unavoidable, such as scattering of electrons by phonons and magnons in the lattice, and operate even within 'perfect' material. The extrinsic effects are avoidable and would be absent for a perfect material. These effects result from two-magnon scattering due to structural defects, sample inhomogeneities and surface roughness, which can lead to a broadening of the resonance peak. Both these effects determine the Gilbert damping coefficient which was introduced in Eq. 2.24 as a phenomenological description of the magnetization relaxation. In the following subsections, the physical concept of these relaxation mechanisms are discussed with respect to their relevance to FM thin-films.

In metallic thin-films, the precession of magnetization induces *eddy currents*, leading to a contribution to the magnetic relaxation [53]. Eddy currents are electric currents which

are induced in a conductor in response to a changing magnetic field. In FM materials, the eddy currents are induced by the local magnetic field fluctuating due to the magnetization precession. Eddy currents are characterized by the skin depth which is defined as the depth below the conductor surface where the current flows with a uniform density in a layer. For samples thinner than the skin depth the eddy current contribution to magnetization relaxation can be evaluated by integrating Maxwell's equations across the film thickness t. For films thicker than the skin depth, the influence of eddy currents on the magnetization precession is entirely negligible. The amount of damping depends on the square of the film thickness, hence the eddy current contribution to relaxation is reduced by using thin-samples. This mechanism becomes important when the film thickness is comparable to the skin depth, but it is in the range of one micrometre at 10 GHz for a typical transition metal [54].

Another relaxation mechanism for thin-films is *phonon-magnon* scattering. Thermally excited phonons can lead to a damping contribution to the material at finite temperature. This mechanism was first predicted by Suhl [55], who presented calculations for damping resulting from phonon-magnon coupling, and was verified experimentally by Heinrich *et al.* [56]. Suhl indicated that this contribution to magnetization relaxation is significantly smaller than experimentally observed values and stated that there are two paths for degradation of the uniform mode; (i) energy flows from the uniform mode into lattice motion (phonons) and (ii) energy flows into the non-uniform magnetic mode (magnons), where these modes decay to the lattice. In the second case, a delay is expected for the lattice motion (phonons), called phonon drag. Both these modes eventually decay to the lattice. This mechanism does not appear to contribute significantly to the magnetization relaxation in comparison to the effective Gilbert damping constant.

The most significant contribution to the damping mechanism in FM thin-films is caused by *itinerant electron* interactions. This model was proposed by Heinrich *et al.* [56] which is based on the exchange interaction between $s-p$ like electrons (itinerant) and localized d electrons. A schematic illustration of coherent scattering process between a magnon with energy $\hbar\omega_q$ that collides with an itinerant electron with energy $\varepsilon_{k,S}$ is given in Fig. 2.9. There are two processes which contribute to magnetic relaxation. In the first process, a magnon with energy $\hbar\omega_q$ collides with an itinerant electron of energy $\varepsilon_{k,S}$, where s denotes the spin state. This results in the annihilation of the magnon and the creation of an electron-hole pair with energy $\varepsilon_{k+q,S'}$. As the $s-d$ exchange interaction conserves the total angular momentum in the collision the itinerant electron has to flip its spin $s=-s\prime$ during scattering with the magnon [53]. The electron-hole pair needs to be scattered incoherently by thermally excited magnons or phonons to cause relaxation of magnetization. For metals the spin-

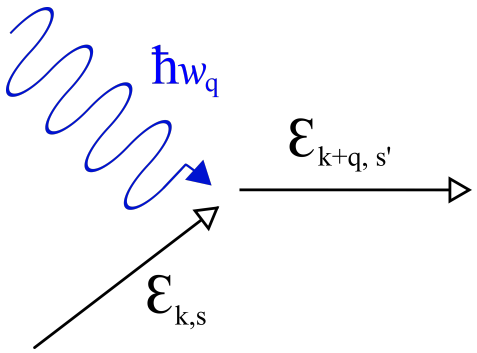

Fig. 2.9 A schematic illustration of coherent scattering process between a magnon with energy $\hbar\omega_q$ collides with an itinerant electron with energy $\varepsilon_{k,S}$, which results changing its spin and energy to $\varepsilon_{k+q,S'}$.

flip time, τ_{sf} of an electron-hole pair is related to the orbital relaxation time, τ_{orb}, where $\tau_{flip} = \tau_{orb}/(g-2)^2$ [57]. The contribution to the magnetic relaxation is proportional to the rate of spin-flip ($1/\tau_{flip}$). This proportionality shows the importance of spin-orbit coupling for magnetic damping in metallic films where the g-factor depends on the spin and the orbital angular momentum ratio [58].

In the previous model, the Fermi surface was assumed to be independent of the external magnetic field. However, the shape of the Fermi surface changes in FM materials when the direction of the magnetization is changed [59]. In the presence of an external magnetic field, the Fermi surface of a FM thin-film is influenced by the dipole, Zeeman and SOI energies. When the magnetization precession evolves in time and space, it results in a periodic variation of the Fermi surface due to spin-orbit coupling, referred as the "breathing Fermi surface". This is the second mechanism for the contribution to the magnetic damping that depends on the spin-orbit coupling, and it is proportional to $\tau_{orb}/(g-2)^2$ [59]. The proportionality to τ_{orb} corresponds to the sample conductivity which is in contrast to the first case, explained above. This contribution to intrinsic damping depends on the conductivity of the material, hence is dominant at low-temperatures.

In summary, these two processes contribute to Gilbert damping. However, these mechanisms do not necessarily contribute equally to the magnetic relaxation, depending on the temperature as the first process is proportional to the resistivity, while the second process is proportional to the conductivity. This was demonstrated in a study where the temperature dependence of the relaxation was examined, and the orbital relaxation time, τ_{orb}, was shown to be temperature dependent [60].

Structural inhomogeneities and defects can play an important role in magnetic relaxation. The extrinsic contribution to the damping which results from structural defects and is usually

referred to as *two-magnon scattering*. Inhomogeneous properties of magnetic materials can result in scattering of magnons. In this process, a uniform precession magnon ($k = 0$) is scattered to another magnon, corresponding to a nonuniform precession ($k \neq 0$), at the surface and/or interface of a FM thin-film, leading to an additional contribution to the linewidth. Since this is a spin-spin process the total number of magnons remains the same. Due to energy conservation, the uniform precession magnon ($k = 0$) can only scatter into another magnon with the same frequency. However, the magnon momentum conservation, the conservation of wave vector q, is not required due to the loss of translational invariance (due to sample inhomogeneities). Two-magnon scattering makes a significant contribution to the magnetic relaxation in thin-films magnetized in the film plane. However, this mechanism is absent in thin-films magnetized perpendicular to the film plane because the wavevectors of spin waves are constrained to be in the thin-film plane. If the magnetization of a sample is perpendicular to the film, the extrinsic linewidth vanishes since this mechanism does not work.

In ultra thin-films, if the magnetization is perpendicular to the film plane, the extrinsic linewidth vanishes because the wave vector of the spin waves are constrained in the film plane. This mechanism was proposed in order to explain the extrinsic FMR line broadening in YIG samples [61] and in metallic thin-films [62]. Recently, a theory was developed by Arias and Mills [63] for the two-magnon scattering in thin-films in the parallel FMR configuration. In this theory, they indicated that lateral variations in the perpendicular uniaxial interface anisotropy field, due to the interface roughness, are a source of the two-magnon scattering [53]. The frequency dependence of the FWHM allows the definition of the zero frequency linewidth, $\triangle H_0$, as;

$$\triangle H(f) \;=\; \triangle H_0 \;+\; \alpha \frac{2\pi f}{\gamma}. \tag{2.28}$$

The FMR linewidth is expected to vary linearly with the resonant frequency, but there is a non-zero intercept. The zero frequency linewidth, $\triangle H_0$, is usually considered to be an extrinsic contribution to the FMR linewidth which depends on the film quality. Hence, $\triangle H_0$ approaches zero for the highest quality films [52]. The Gilbert damping parameter can be obtained by a linear fit when the linewidth is plotted as a function of the excitation frequency.

2.8.3 Spin-Pumping Mechanism

A pure spin-current can be generated by several mechanisms, including spin Hall effect, spin-pumping and spin Seebeck effect [64–70]. For detecting a pure spin-current, the most widely used method is the inverse spin Hall effect [64, 71, 72], where the pure spin-

current in a metal with strong SOI generates a charge current and charge accumulation in the transverse direction. The phenomenon in which a spin-current is generated from the precession of the magnetization of a FM metal and is driven into an adjacent metal is called spin-pumping [66, 67]. The mechanism behind the enhanced damping is due to a spin-current injected from the FM into the non-magnetic (NM) layer [66]. This pumping of spin-current, which is associated with the loss of angular momentum from precessing M, flows perpendicular across the FM/NM interface. A schematic of the spin-pumping mechanism is shown in Fig. 2.10.

The precessing magnetization creates an unbalanced chemical potential between the two spin channels (spin-up and spin-down electrons) in the FM layer which is an effect usually called spin accumulation. This leads to a transfer of spin angular momentum between the FM and the NM layer, creating a leakage of spin-current from FM into NM layer where its magnitude depends on the combination of materials at the FM/NM interface. Due to this spin accumulation in the adjacent NM layer, the injected spin-current, J^S_{pump}, (i) is either fully relaxed in the adjacent NM layer (by spin-flip scattering), (ii) fully diffuses back to the FM layer, J^S_{back}, (iii) or is partially absorbed and partially diffuses back to the FM layer. For NM metals with a fast spin-flip relaxation time, the injected spins can be balanced by spin-flip relaxation, hence spin-current crossing over the FM/NM interface is quickly absorbed in the NM metal, and $J^S_{\text{back}} = 0$. This type of NM metals, such as heavy metals (Pd and Pt) act as a spin sink. These metals have short spin-flip relaxation times due to their strong SOI, and have been used in many experiments due to their effective spin sink properties [73, 74]. When the thickness of the NM layer is larger than the spin diffusion length,($\lambda^{\text{Pt}}_{\text{sd}} \sim 1$ nm [75]),

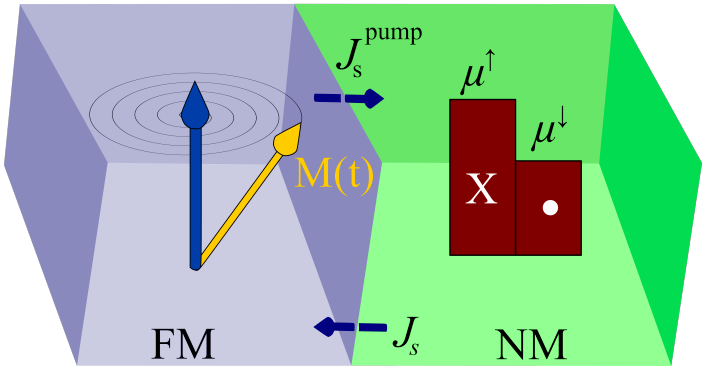

Fig. 2.10 A schematic illustration of the spin-pumping process. The magnetization precession in a FM layer injects a spin-polarized current J_S into the adjacent NM layer. The inset in NM layer shows the chemical potential for spin-up ($\mu^{\uparrow}$) and spin-down ($\mu^{\downarrow}$) electrons in the structure.

the NM layer acts as a perfect spin sink for the injected spin-current. However, if the NM thickness is below the spin diffusion length, the injected spin-current flows back to the FM layer causing spin accumulation. Hence, no spin-pumping is observed and consequently, there is no enhancement of the damping. Lighter NM metals, such as Cu and Al, have a long spin-flip relaxation time in comparison to heavy metals. For thickness below spin diffusion length ($\lambda_{\mathrm{sd}}^{\mathrm{Cu}} \sim 350$ nm [76]), the injected spin-current can not be dissipated quickly, thus spin accumulation arises at the FM/NM interface. Accumulation of spins prevents further transfer of spins, so no enhancement of the damping factor is expected. This is consistent with many experimental studies [74]. Due to their long spin-flip lifetimes, these lighter NM metals are called poor spin sinks [73, 74].

Spin-pumping was originally proposed by Berger [77], and the theory was further studied in detail by others [67, 78, 79]. The pure spin-current, J^S_{pump}, generated from the time dependent magnetization direction, flows perpendicular to the FM/NM interface, and its direction from FM layer into the NM layer is shown in Fig. 2.10. The NM layer is assumed as a perfect spin sink, i.e., all spins pumped from FM into NM layer are dissipated with in the NM layer, and there is no back-flow of spin-current into the FM layer. Hence, spin-current emitted from FM into the NM metal layer is given by [78];

$$J^S_{pump} = \frac{\hbar}{4\pi} g^{\uparrow\downarrow} \left(\hat{m} \times \frac{d\hat{m}}{dt} \right) \tag{2.29}$$

where $g^{\uparrow\downarrow}$ is a interfacial spin-mixing conductance. This is a material parameter which determines how much spin-current is passed through the FM/NM interface. The electrical conductivity is the ability of a material to allow passing charge currents through them. In spin-current transport, the conductivity is dependent on spins of electrons. This spin dependence of conductivity is described in terms of the spin-mixing conductance in FM/NM heterostructures. The spin-current (I) for FM/NM structure can be written in terms of a potential difference (ΔV) created by spin accumulation which is generated in the NM layer near the FM interface, and a conductance matrix: $I = \Delta V g^{ss}$. This can be written as;

$$g^{ss} = \begin{pmatrix} g^{\uparrow\uparrow} & g^{\uparrow\downarrow} \\ g^{\downarrow\uparrow} & g^{\downarrow\downarrow} \end{pmatrix} \tag{2.30}$$

where $g^{\uparrow\uparrow}$ and $g^{\downarrow\downarrow}$ are the spin-dependent conductances which are used for collinear cases, i.e. when the spin-current transferring across FM/NM interface are parallel or antiparallel to the local spin accumulation in the NM layer. $g^{\uparrow\downarrow}$ and $g^{\downarrow\uparrow}$ are used when the spin accumulation in the NM layer is not collinear with the spin-current. The emission of spin-current is

associated with angular momentum loss in the FM layer, thus it acts as a source of damping within thin-films which is consistent with Gilbert damping [67]. The total spin S is related to the total magnetization of the film M via,

$$S = \frac{\mathrm{M}}{\gamma} = \frac{M\hat{m}}{\gamma}. \tag{2.31}$$

Using the spin conservation law [80], the contribution of Gilbert damping constant due to spin-pumping can be described as;

$$\frac{d\hat{m}}{dt} = \triangle\alpha\left(\hat{m} \times \frac{d\hat{m}}{dt}\right) \tag{2.32}$$

where α is the Gilbert damping constant which is given by;

$$\triangle\alpha = \frac{g\mu_B G^{\uparrow\downarrow}}{4\pi M}. \tag{2.33}$$

By substituting $g^{\uparrow\downarrow} = G^{\uparrow\downarrow}/A$ and using $M_{\mathrm{S}} = M/V$, where A is the interface area and V is the total volume, Eq. 2.33 can be written as;

$$\triangle\alpha = \left(\frac{g\mu_B}{4\pi M_S}\right)\frac{g^{\uparrow\downarrow}}{t} \tag{2.34}$$

where t is the FM layer thickness. The intrinsic damping under the influence of spin-pumping is related to the total effective spin-mixing conductance [67, 81];

$$\alpha_{\mathrm{eff}} = \alpha_0 + \frac{g\mu_B}{4\pi M_S t} g^{\uparrow\downarrow}. \tag{2.35}$$

The Gilbert damping constant can be substituted by the effective Gilbert damping parameter $\alpha_{\mathrm{eff}} = \alpha_0 + \triangle\alpha$, where α_0 is the bulk Gilbert damping, and $\triangle\alpha$ is the contribution due to the spin-pumping effect which can be derived from the conservation of the total angular momentum [80].

3

Investigative Techniques

This chapter presents the variety of investigative techniques that were employed in this thesis to fabricate and characterize thin-film samples. In the first part the thin-film growth modes are described during the thin-film deposition. The sputter deposition technique used for the fabrication of the studied thin-films in an ultra-high vacuum (UHV) system is introduced. Following this, a description of the SQUID magnetometry is discussed for magnetic property measurements of thin-films. The details of x-ray reflectivity and diffraction techniques are discussed for the structural characterization of the magnetic thin-films. For the neutron analysis, experimental details of CRISP reflectometer used to study the amorphous CoFeB:Ta thin-films are presented to understand temperature dependence of magnetic dead layers formation. Magneto-transport properties of polycrystalline Co thin-films were carried out using a room-temperature magnetoresistance measurement system. This chapter ends with a basic description of the vector network analyzer ferromagnetic resonance technique (VNA-FMR) to introduce magnetization dynamics of Co thin-films.

3.1 Thin-Film Deposition

Thin-film deposition techniques are essential for the development of spintronic devices. This section describes the method of different growth modes that can observe during the deposition of metallic thin-films. These methods are divided into two categories: (i) vapor-phase deposition, such as sputtering, thermal evaporation, molecular beam epitaxy, and (ii) liquid-based deposition, such as electrochemical deposition and Langmuir-Blodgett films. Thin-film deposition involves various processes such as evaporation, adsorption, nucleation and desorption on growth surfaces.

Thin-films, which are deposited on a substrate surface, can be grown in three different growth modes [82], as shown schematically in Fig. 3.1. The Volmer-Weber growth mode (island growth) occurs when the vaporized atoms bond to each other more strongly than to the substrate surface. This strong bonding leads to the formation of islands that join to form a continuous thin-film. The Frank-Van der Merwe growth mode occurs when the vaporized atoms have stronger bonding with the substrate surface than with each other. In this mode, a complete monolayer is formed, and then deposition of the second layer begins on the top of the first layer. This growth mechanism requires a lattice matching, hence it is considered an ideal growth mode. Frank-Van der Merwe growth is also known as layer-by-layer growth, which is in contrast to the Volmer-Weber growth. The final growth mechanism is the combination of both layer-by-layer and island growths, known as the Stranski-Krastanov growth mode. At the initial stage, layer-by-layer growth takes place to cover the substrate surface with a monolayer, and then the island growth mode is preferred to form three dimensional islands [83]. While the Frank-Van der Merwe and the Volmer-Weber growth modes lead to stress-free films; significant stresses are induced in the Stranski-Krastanov growth mode because the interface energy increases when the layer thickness increases, hence this layer is strained to fit the substrate [84]. These growth modes are expected to induce to different surface structures [85].

In the following sections, the preparation of SiO_2 and GaAs(001) substrates for the deposition of thin-films are discussed in order to produce high quality thin-films. A brief description of amorphous CoFeB:Ta alloys and polycrystalline Co thin-films used in this thesis are then given. The amorphous CoFeB:Ta thin-films and polycrystalline Co thin-films were deposited by A.T. Hindmarch and M. Wang using a similar deposition system at Nottingham University. This section ends with the basic principles of sputtering, and the properties of the system used to fabricate the thin-films.

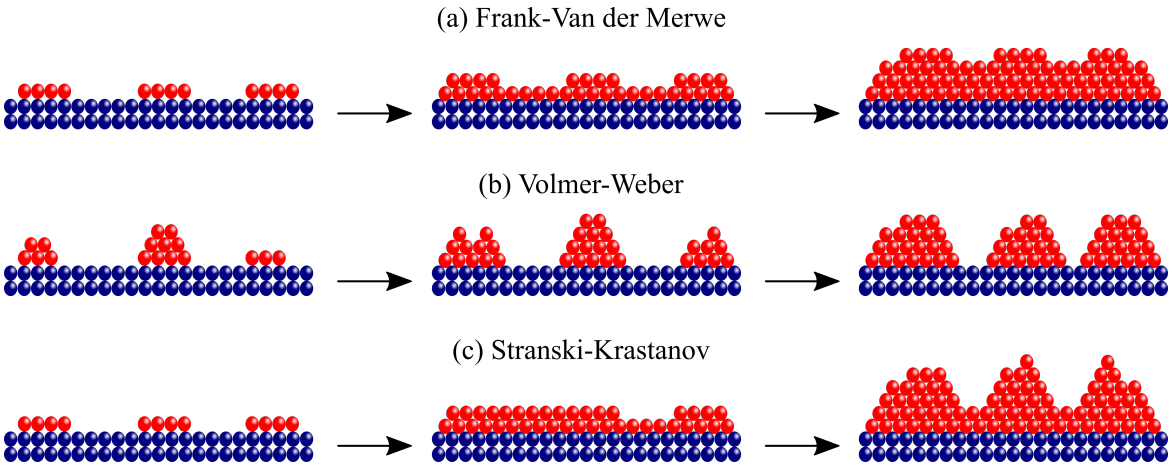

Fig. 3.1 Schematic illustration of thin-film growth modes including (a) Frank-Van der Merwe layer-by-layer growth, (b) Volmer-Weber island growth and (c) Stranski-Krastanov layer-plus-island growth.

3.1.1 Preparation of Substrates

The quality of a substrate surface is important in relation to the good quality of the thin-films produced. The preparation of substrates, prior to loading them into the load-lock chamber of the magnetron sputtering system is critical. In this work, thin-films were deposited onto both Si/SiO_2 and GaAs(001) substrates.

Single crystal silicon wafers, topped with $\sim$ 100 nm thick amorphous thermally-grown oxide layer were used. This oxide layer acts as an electrically insulating layer to prevent conduction through the substrate when making electrical measurements. These wafers were diced, using a diamond tipper scribe, into square chips of approximately 25 mm^2 for neutron scattering experiments and elongated strips of approximately 15 mm$\times$2 mm for magneto-transport and magnetization dynamics measurements. The cleanliness of the substrate is extremely important for proper film adhesion. Once cut, each piece of wafer was washed with acetone for a few minutes to remove grease and dust, and then in isopropanol for further minutes to remove any traces of the acetone, prior to film deposition. Each cleaning processes were performed using ultrasonic agitation in order to enhance the cleaning. Each wafer was then dried using dry N_2 gas applied at a glancing angle.

Amorphous CoFeB:Ta thin-films were deposited onto commercially available epi-ready GaAs(001) crystal surfaces for neutron scattering experiments. 2 inch diameter GaAs(001) wafers were cut into quarter segments. Each chip was chemically etched in dilute hydrochloric acid (HCl) to remove the native oxide layer from the substrate. After etching, it is necessary to rinse the wafer in deionized water to stop the surface etching, and dry it using a nitrogen gas.

After the cleaning procedure, the substrates were annealed at 600 °C for an hour to remove the As capping layer because desorption of the As passivation occurs at high temperatures [86]. Then, the substrates were allowed to cool to ambient temperature, prior to film deposition.

3.1.2 Polycrystalline Cobalt Multilayers

Polycrystalline materials have a microstructure that is composed of many small single crystals, or grains, with different orientations. These small crystals are joined at interfaces which are called grain boundaries. Thin polycrystalline materials can have preferred orientations of the crystals, called texture.

In this work, two sets of polycrystalline Co thin-films with Co thicknesses from 2 nm up to 55 nm were deposited onto Si/SiO_2 substrates by a combination of DC and RF magnetron sputtering at deposition rates of ~ 0.02 nm/s in Ar atmosphere for a UHV base pressure. The thin-films were deposited onto Ta/Cu seed layers, which promote consistently strong fcc(111) and hcp(0001) texture in the Co film for all thicknesses [87]. Both film series were capped with either Cu or Ir overlayers to observe the effects of spin-orbit coupling strength in AMR and FMR experiments associated with the interface to different NM layers. Both thin-film series were immediately capped with a Ta layer to prevent oxidization. All metal layer thicknesses, except the Co layer were fixed to 3 nm. A schematic illustration of the thin-film structures are shown in Fig. 3.2 (a).

3.1.3 Amorphous CoFeB:Ta Thin-Films

Ferromagnetic crystalline CoFe alloys have a high saturation magnetization and are widely used as soft magnetic materials in various applications [88]. The only alloying element which increases both T_C and the M_S for Fe is Co [17]. $Co_{50}Fe_{50}$ has low anisotropy and high permeability, but has a long-range order which makes the alloy brittle [17]. Amorphous materials may be produced by rapid cooling of magnetic alloys, which prevents the formation of the crystalline state. They are known as “metallic glasses” due to their random atomic structure, which results also in high electrical resistance.

Alloying of a dilute metalloid element, such as B, C, Si or N, into the ferromagnetic metal produces an amorphous ferromagnetic material. For example, the addition of $\sim 20\%$ B with the ferromagnetic transition metal alloy, such as CoFe, reduces the T_C and M_S relative to CoFe film, but this alloying prevents long-range crystal order [86]. Amorphous ferromagnetic alloys have nearly isotropic properties, and no magnetocrystalline anisotropy energy. The absence of any easy/hard magnetization directions leads amorphous material to have high permeability, low hysteresis losses and low coercivity [17].

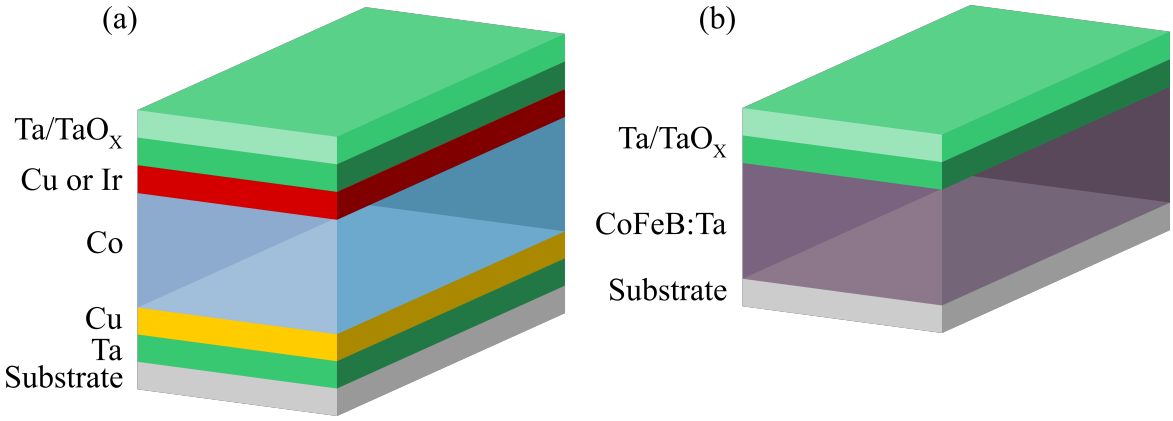

Fig. 3.2 Schematic illustrations of (a) polycrystalline Co thin-films with Cu and Ir overlayers, and (b) amorphous CoFeB:Ta thin-films deposited on Si/SiO_2 and GaAs(001) substrates.

CoFe alloy has a bcc crystal structure which displays cubic anisotropy. The addition of $\sim$ 10% B to CoFe converts its structure to an amorphous metallic glass [89], and slightly reduces the T_C from 1100°C to 900°C. When CoFeB thin-films are deposited on a III-V(001) semiconductor substrate, they display an interface induced volume uniaxial magnetic anisotropy (UMA) [90]. The only mechanism consistent with the volume magnetic anisotropy observed in amorphous CoFeB is bond orientation anisotropy (BOA) [91]. The BOA refers to an anisotropic distribution of atomic bonds caused by anelastic deformations due to growth dynamics and/or strain effects.

In alloys deposited by sputtering at a temperature below their T_C, spontaneous magnetization and domain formation allow BOA to arise in the material. However, by producing an alloy with a T_C which is below the growth temperature, BOA will not arise due to the absence of spontaneous magnetization during deposition. In order to reduce T_C, $Co_{40}Fe_{40}B_{20}$ sample was diluted with 30% Ta to achieve a $T_C \sim 100$ K. The addition of a transition metal to an CoFe-based amorphous alloy, Ta in this case, reduces both T_C and the magnetic moments per Co/Fe atom. This reduction in the magnetic moments was explained as a result of charge transfers from the transition metal atoms to fill holes in the *d* states of Fe [92]. When the sample is cooled below T_C the only remaining magnetic anisotropy for the CoFeB:Ta samples, deposited at room-temperature, should be in-plane interfacial UMA.

In this work, amorphous CoFeB:Ta thin-films were deposited at room-temperature using DC magnetron co-sputtering from Co(40%)Fe(40%)B(20%) and Ta sputtering targets for neutron scattering experiments. The nominal composition of the amorphous CoFeB:Ta thin-films was 28:28:14:30 [93]. Films with thickness of 10 nm were deposited onto 2 inch diameter Si/SiO_2 and GaAs(001) wafer substrates. To prevent oxidation the CoFeB:Ta layers

were capped with 3 nm Ta. The schematic illustration of amorphous CoFeB:Ta thin-films are shown in Fig. 3.2 (b).

3.1.4 DC-Magnetron Sputtering

Sputtering is one of the main techniques for the deposition of high quality metallic films, used in microelectronics fabrication [94]. It was first discovered by W. R. Grove [95] in 1852, and has become widely used in thin-film deposition. This technique has several advantages over other metal deposition techniques like thermal evaporation, such as better step coverage, less radiation damage and it is easier to deposit layers of compound materials and alloys. A schematic illustration of a typical sputtering system is shown in Fig. 3.3.

The sputtering mechanism involves the bombardment of a material target by highly energetic ions, typically Argon (Ar), to eject the individual target atoms from its surface by transferring sufficient momentum to the target atoms. These ejected atoms travel from the sputtering target and some will travel to the substrate surface, which is mounted above the target material, and start to condense into a film. As more atoms condense, they bind to each other to form build up a layer.

In the DC-magnetron sputtering system, a DC voltage is applied between the metal target (cathode) and substrate (anode). Ar atoms are ionized by this electric field and creating a

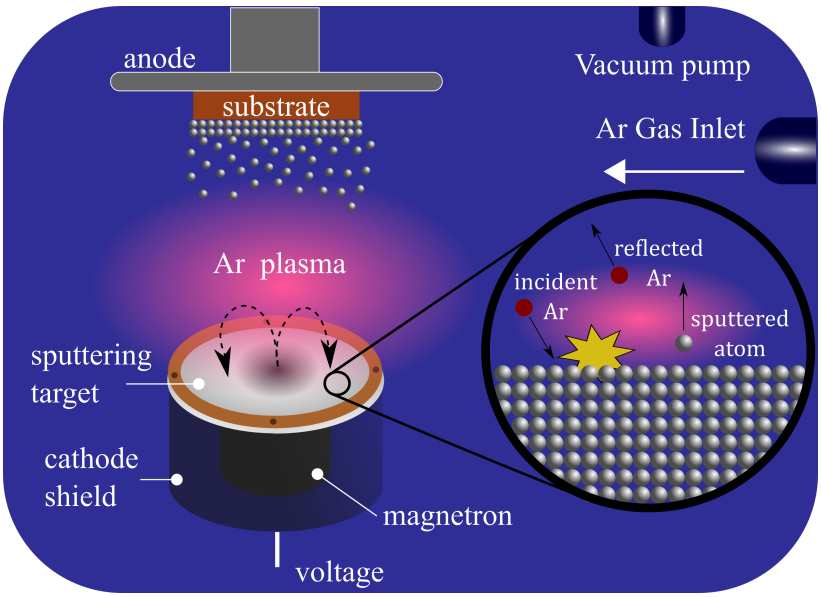

Fig. 3.3 Schematic illustration of DC-magnetron sputtering deposition system, where the energetic ions sputter materials from the target, which diffuse through the plasma towards the substrate

phase consisting of ions and electrons, called a plasma. A set of permanent magnets are positioned near the sputtering targets to create a strong magnetic field parallel to the target surface. This field is perpendicular to the electric field, and leads to Lorentz force to act on the electrons and ions in the plasma. Electrons are trapped close to the target surface by the Lorentz force, resulting in electron-atom collisions which produce further Ar ionization near the target surface, which tends to generate a stable plasma with a high density of Ar ions. These charged ions are accelerated to the target by the applied voltage, and eject target atoms from the surface. Electrons, released during the ionization, travel through the substrate, and collide with additional argon atoms which creates more ions.

Thin-films were deposited using a Mantis QPrep^{TM} magnetron sputtering system. The UHV system includes a load-lock chamber and 5 water-cooled magnetron sources, which are mounted in the vacuum chamber. DC sputtering is suitable for conducting target materials, while RF sputtering allows to deposit non-conducting materials, like dielectrics. Each magnetron source includes a gas line for the formation of a uniform high density plasma at the target surface. The growth rate for each target was monitored in-situ using a Quartz Crystal Microbalance (QCM) prior to film deposition, where the QCM measures the growth rate. The magnetron sources have a shutter plate to prevent any contamination of the other targets during deposition processes. The vacuum system has a base pressure $\sim 10^{-9}$ Torr, which is monitored by a mass spectrometer. This vacuum level is achieved by roughing the main chamber using rotary pump to reach the pressure around 10 mTorr, then switching to a turbo molecular pump to reach the base pressure. The samples in the turbo-pumped load-lock chamber were transferred to the main chamber with a magnetically coupled load transfer arm. The calibration of film thickness was done by deposition of relatively thick-film of material, typically ~ 50 nm. The thickness is determined by x-ray reflectivity, which enables to estimate of the sample film thickness with high accuracy and precision.

3.2 Magnetic Measurements (SQUID)

The magnetization measurements in this thesis were performed in Nottingham University and ISIS R53 Materials Characterization Lab using a SQUID (Superconducting Quantum Interference Device) magnetometer, the Quantum Design Magnetic Property Measurement System (MPMS) XL-7. This technique is one of the most effective and sensitive ways for measuring magnetic properties of thin-films, making it ideal for monitoring very small changes in magnetic flux as a function of temperature and magnetic field. The magnetometer

is capable of measuring magnetic properties of samples as a function of temperature (1.9 K - 400 K) and magnetic field (up to 7 Tesla).

A schematic illustration of SQUID magnetometer is shown in Fig. 3.4 (a). The SQUID magnetometer consists of two superconductors, separated by a thin insulating layers to form two parallel Josephson junctions in a superconducting loop which operates at a constant DC supply. The sample travels longitudinally through the superconducting detection coils, and the change of magnetic flux of the sample induces an electric current in the detection coils, according to Faraday's Law of electromagnetic induction. Fig. 3.4 (b) shows the variation of the SQUID voltage as a magnetic sample moved through the detection coils. The system works as an extremely sensitive current to voltage converter, the variations in the magnetic flux are then measured by the pick-up coils as a voltage response. The voltage variations from the SQUID detector is measured at a number of sample positions along the scan length, providing a highly accurate measurements of the magnetic moment [96].

There are four turns in the detection coil, as shown in Fig. 3.4 (a). Two turns are in the center of the system and a counter-wound turn at the top and the bottom of the wire to act as a second-derivative flux gradiometer. Any noise due to fluctuations in the magnet, which are picked up by the two turns in the center, will be canceled by the turns at the top and the bottom of the coil. The entire system is enclosed in a superconducting magnetic shield, which protects the SQUID from the large magnetic fields produced by the superconducting magnet.

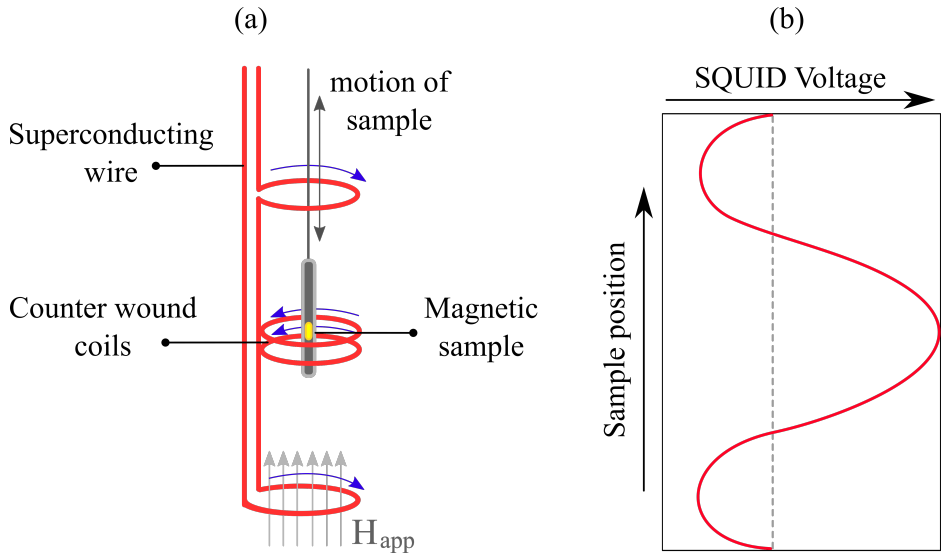

Fig. 3.4 (a) Schematic representation of SQUID magnetometer placed in a magnetic field. (b) The variation in SQUID voltage as a function of sample position.

The sample holder is usually the largest source of background signal. Samples for magnetic measurements were cut into 0.5 mm × 0.5 mm pieces and inserted in a polycarbonate capsule. They are sandwiched with two short pieces of drinking straws into the outer plastic straw to minimize background contribution where the plastic straw is weakly diamagnetic and thin-walled, hence it does not induce additional flux change in the pickup coils. Then the straw has attached on the end of the non-magnetic sample rod, which is centered within the superconducting coil, and initially field cooled at 200 Oe to 5 K to put them in a saturated magnetic state. The samples were kept at 5 K for around 5 minutes to stabilize the sample temperature within the sample space, which was filled with liquid helium. Fig. 3.5 shows examples of (a) a hysteresis loop and (b) a temperature dependent magnetization curve of magnetic thin-films, using SQUID magnetometry. The temperature scans were recorded at 100 Oe applied magnetic field. The T_C of the samples was found, as shown in Fig. 3.5 (b) and hysteresis loops were recorded above and below the T_C.

The temperature dependent measurements of magnetization can be performed in two different methods. The first method is done by cooling the sample to the lowest-temperature in the absence of a magnetic field. After it has stabilized, a magnetic field was applied to the sample, and the magnetic moment measured as a function of temperature. This process is called the zero-field cooled (ZFC) mode. However, in the field cooling (FC) process, the sample is cooled to the lowest-temperature with an applied magnetic field, and the magnetization is then measured during the change of the temperature. Before each measurement, the samples were field cooled at 200 Oe in order to make sure they were

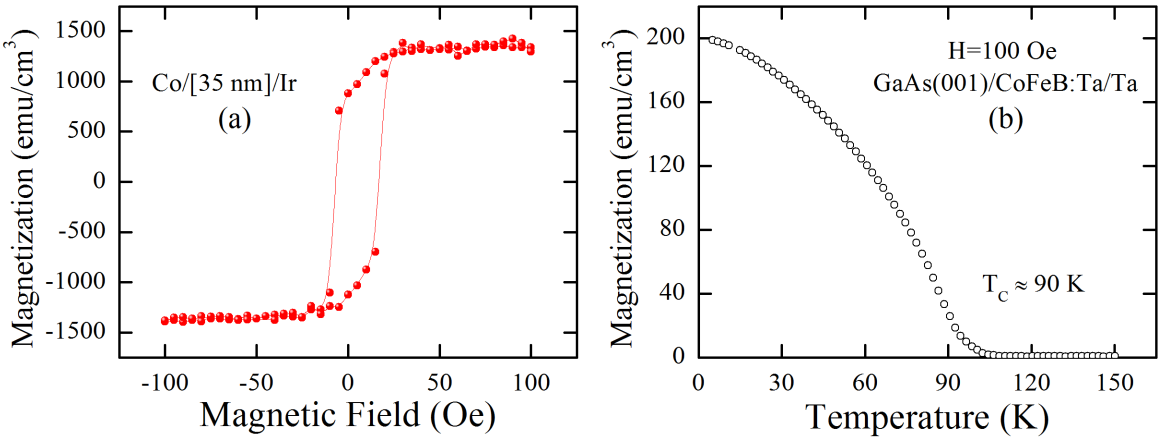

Fig. 3.5 (a) An example of SQUID hysteresis loop for Co[35 nm]/Ir thin-film. (b) Temperature dependent magnetization curve of 10 nm amorphous CoFeB:Ta thin-film on GaAs(001) substrate at 100 Oe magnetic field.

always in a saturated magnetic state. The magnetic response of the CoFeB:Ta film on both substrates was independent of the orientation of the sample within the SQUID coil.

3.3 X-ray Scattering

Structural characterization of magnetic thin-films was obtained using an x-ray diffractometer to measure high angle x-ray diffraction (XRD) and grazing incidence specular x-ray reflectivity (XRR) techniques. In this section, the production of laboratory-based x-rays and the experimental set-up of x-ray diffractometer are briefly outlined. More detailed discussion of x-ray scattering theory and fitting procedure of XRR data are discussed in Chapter 4.

Specular XRR is a surface-sensitive analytical technique to determine thin-film parameters, including layer thickness, density and surface/interface roughness with a high precision [97]. The penetration of x-ray beams into a thin-film allows subsurface layers and interfaces to be characterized. This technique is based on the measurements of the intensity of reflected x-rays from the thin-film as a function of incidence angle. XRR was first used by Parratt to determine the depth of oxidation in Cu films [98].

X-ray diffraction (XRD) is a powerful and a non-destructive technique for characterizing structural properties of materials. This technique provides useful information on crystal structures, preferred crystal orientation, grain size and crystal defects. X-rays have a similar wavelength in magnitude to the atomic spacing in most materials, hence x-ray beam can be diffracted by crystal lattices to reveal the nature of the lattice.

3.3.1 Laboratory X-rays

Laboratory X-ray sources are generated by two commonly used devices. Sealed-tube source which is the most widely used source, and rotating anode source [99]. In a sealed-tube source, an electron beam is generated on a hot filament (cathode), where the electron beam is accelerated using a high voltage between the cathode and the anode. A rotating anode works similar to the sealed-tube source, but the anode is made to rotate in order to reduce the heat load over a larger area [100].

X-rays are typically generated by bombarding a metal target (anode) in a vacuum tube with energetic high speed electrons produced by a filament, acting as a cathode [99]. When the electron beam collides and interacts with the target material, the high kinetic energy of the electrons is converted by deceleration into x-rays, produces Brehmsstrahlung, from the German for “braking radiation”, which generates x-ray photons with a continuous spectrum

of energy [101]. Characteristic x-rays are produced due to an interaction with electrons in the shells of the target material. If the bombarding high speed electrons have sufficient energy, they can eject an electron from a core shell of the target atom. Then electrons from outer shells drop down to fill the vacancy, with an emission of a single x-ray photon, called characteristic x-rays [99]. The production process is extremely inefficient, because more than 99% of the electron energy of the beam is converted into heat, and less than 1% of energy is converted to photons.

3.3.2 X-ray Diffractometer

Grazing incidence specular XRR and XRD measurements were performed at room-temperature using Rigaku SmartLab diffractometer with a copper anode tube source. The Smartlab is equipped with a 9 kW rotating copper anode X-ray generator, which produces a 0.4×8 mm x-ray beam with a ~ 1.54 Å wavelength, which is the characteristic wavelength of Cu-Kα radiation. These measurements were conducted with a filament current between 10 - 200 mA, and a high voltage between 20-45 kV to accelerate an electron beam towards a target. The x-ray source and the detector were placed on a 5-axis high resolution goniometer, which allows measurements for different scanning geometries. Multiple sample stages are available for tilting or translating the sample.

Soller slits, which contain a set of closely spaced thin metal plates, and an in-plane parallel slit analyzer (PSA) adapter were used to set the measurement resolution and collimate the x-ray beam for the polycrystalline thin-films measurements. The resolution of the incident x-ray beam was set using an incident PSA, and a 2-bounce Germanium (220) monochromator to achieve high resolution. The samples were mounted horizontally on a motorized high precision stage, and the height of the sample table can be adjusted between -4 to 1 mm with a 0.0005 mm step size. The detector is a NaI scintillation counter coupled with a photomultiplier with preamplifier. The x/y stage can be tilted in x and y direction between -5° to 5° with a step size of 0.002° for a perfect surface alignment. The instrument is controlled with the SmartLab Guidance Software, which guides the users through alignments and experimental setups, hence making the system very easy to use. The geometry of the experimental set-up is illustrated in Fig. 3.6.

Thin-films were aligned for structural measurements using the direct-beam half-cut alignment by scanning the thin-film along the z-axis to ensure the height of the film was placed half way in to the x-ray beam. Then, the thin-film was aligned over the ω axis, hence the maximum x-ray intensity is obtained by the critical angle of the reflectivity scan. Now, the sample can be considered to be parallel to the x-ray beam. In each measurement, the settings

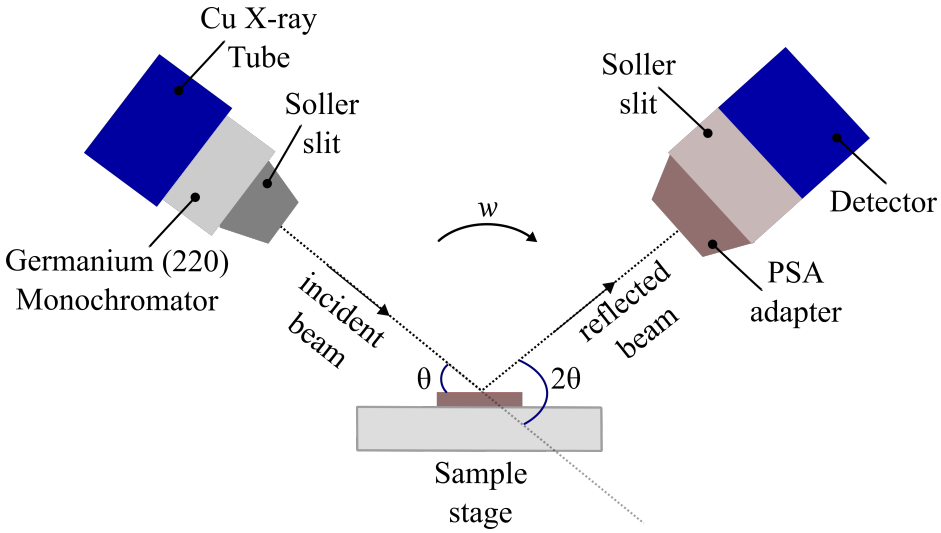

Fig. 3.6 X-ray geometry plan view of the x-ray diffractometer used for reflectivity measurements of FM thin-films.

of the instrument were chosen to maximize the x-ray signal yield around 2 hours per scan. The scanning times of the instrument depend on the speed of scan and step size. In order to obtain comparable measurements, the same scanning time was set for all measurements to allow peak intensities to be compared against each other.

In reflectivity scans the thin-films were aligned by carrying out a grazing incidence scan in order to obtain the 2θ angle of the total reflection from the sample surface. The ω scan which is often called "rocking curve" was measured to observe specular reflection of the sample where the measurement of rocking curve is important for accuracy of the measurements. ω was aligned to top of the rocking curve peak, and the sample tilt was varied using a mechanized sample stage. This process was repeated until the maximum signal was achieved for ω, which indicates the sample surface was aligned to the plane of the incident x-ray beam.

The reflectivity spectra of each sample was obtained using $2\theta - \theta$ scan over the low angle range $0^\circ - 5^\circ$, and the typical range for a diffraction measurement is between 20°-100° with a scan step of 1.5 deg/min and resolution of 0.0002°. X-ray reflectivity of thin-films has been fitted using the `GenX` software package [102] which calculates the electron density, thickness and roughness of the layers in a sample. The details of the fitting procedure are explained in Chapter 4.

3.4 Neutron Scattering

Polarized neutron reflectivity (PNR) has played an essential role for investigation of magnetic and structural properties of magnetic thin-films. In comparison to x-ray scattering, which is sensitive to the electron density, neutron scattering within a material is more complicated because neutrons can interact with the nuclei and the magnetic moments of the material, hence the scattering potential has two components; a neutron/nuclear and a neutron/magnetic term. Due to this complexity, the scattering theory of neutrons is not easy to formulate. A more detailed discussion of neutron scattering theory and fitting procedure of PNR data can be found in Chapter 4.

3.4.1 Production of Neutrons

Several nuclear reactions are capable of producing neutrons. Neutron beams can be produced by two fundamental mechanisms, either through nuclear fission in a research reactor or spallation in a accelerator-driven neutron source [103]. The former produces neutrons to use as microscopic probes by utilizing the fission chain reaction process. The latter creates neutrons through the use of an accelerator, and this was used to obtain the data recorded in Chapter 6.

Accelerator-driven spallation sources produce neutrons through collisions of high energy protons ($\sim$ 1 GeV) with a heavy metal target, such as W, Ta, or U. During this process, many sub-atomic particles such as neutrons, pions and protons are ejected from the highly excited nuclei in a process, which is called spallation [97]. These particles emerge from collisions with sufficient kinetic energy to collide again and they leave further excited nuclei, as illustrated in Fig. 3.7. For each spallation event, which is pulsed between 20 Hz and 60 Hz, there is an energy threshold of $\sim$ 20 MeV in a neutron production. In every collision, approximately 25 neutrons are released by evaporation, and these have an energy distribution similar to that from a fission reactor. One of the most powerful neutron spallation sources is situated at ISIS-STFC in UK, which provides a thermal neutron flux of over 10^{16} n/s/cm^2 with a pulse length of $\sim$ 50 μs.

The neutrons released by the reactor or spallation sources have very high kinetic energies and velocities. The energy of the neutrons should be around 25 meV with a wavelength close to 1 Å for most research applications. These higher energy neutrons need to be slowed to thermal energies (E $\sim$ meV). Hence, a hydrogenous moderator is used to slow the neutron down via inelastic collisions with light elements and has to be used around the target in order

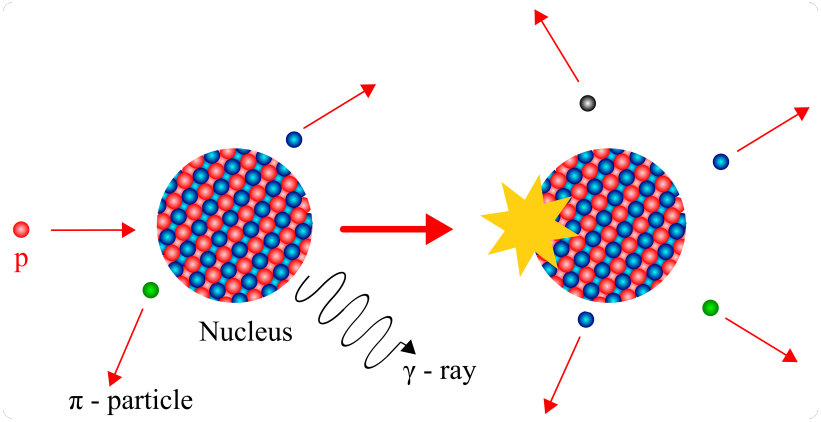

Fig. 3.7 A schematic illustration of the spallation mechanisms to produce neutrons.

to bring the neutron energy down to an energy suitable for scattering experiments. At ISIS, there are four moderators: two of them comprises water at room-temperature, one is liquid methane at 100 K and the other contains liquid hydrogen at 20 K, which provides a range of suitable neutron wavelengths. Each moderator reduces the energy of the neutron beam to make it suitable for a particular experimental beamline. The following section describes the experimental details of CRISP neutron reflectometers.

3.4.2 Polarized Neutron Reflectometry

The CRISP beamline is the polarized neutron reflectometry (PNR) at the ISIS spallation neutron source of the Rutherford Appleton Laboratory. Details of the experimental set-up can be found at [104, 105]. PNR measurements of amorphous 10 nm CoFeB:Ta thin-films, presented in Chapter 6, were made using this reflectometer. A schematic illustration of the reflectometer is shown in Fig. 3.8.

The principle of neutron reflectivity is to measure the specular reflection as a function of the perpendicular momentum transfer, $Q_Z = k_f - k_i$. The neutron beam has an incident wavelength range of 0.5-6.5 Å at the source frequency of 50 Hz. The instrument operates at a fixed angle of incidence, and allows for a range in Q_Z through the range of neutron wavelengths. The instrument uses a time-of-flight method in which the speed of the neutron is measured by timing its flight from the source to the detector.

The incident neutron beam is collimated by both coarse and adjustable fine collimating slits. The neutrons pass through a rotating variable disc chopper to select the wavelength range and pulse suppression is achieved by a nimonic chopper to remove the fast neutrons from the beginning of every pulse. Neutrons of very long wavelength which pass through the disc choppers are deflected by a frame overlap mirror, which reflect out the main beam

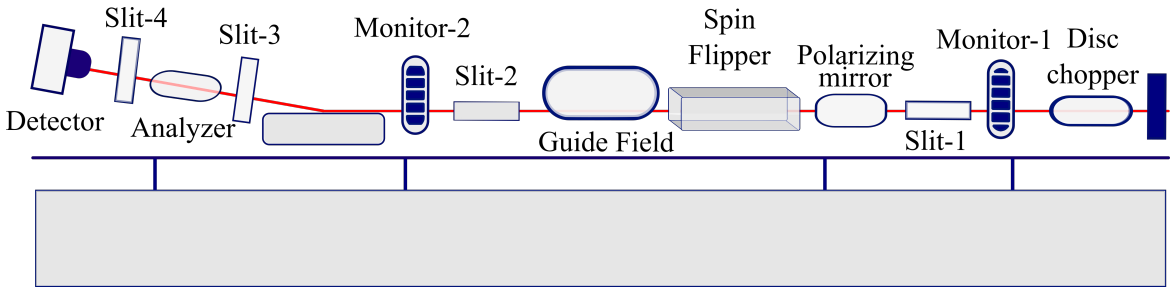

Fig. 3.8 A schematic illustration of the CRISP reflectometer. Red solid line show the path of the neutron beam through the detector.

wavelengths greater than 13 Å. The beam then passes through a ^{3}He detector which monitors the incident beam intensity, and is collimated by a slit, allowing a variable angular divergence (resolution) and beam size up to 40 mm in horizontal and up to 10 mm in vertical directions. As the scattered intensity is rapidly lost with increasing Q_Z, the reflectivity data were collected at several incident angle. To maintain a fixed Q_Z resolution of 4%, the instrument slits were modified at each angle. The neutrons are then polarized by the use of a polarizing supermirror, which has an efficiency of 99.9%. It produces neutron beams of polarized spin-up and spin-down neutrons by discarding neutrons of one particular eigenstate. A Drabkin type, two-coil non-adiabatic spin flipper is used to select the spin direction of the polarized neutron beam and the neutrons pass through a static guide field, which prevents the neutron beam from depolarizing on the way to the sample. The sample is positioned either directly onto a goniometer (sample stage) or in a continuous flow cryostat between the poles of the electromagnet which provides an in-plane reversible field of up to 10 kOe. The sample position is adjustable and designed to be vibrationally isolated from the rest of the experimental system. Low-temperatures can be achieved rapidly (∼1-2 hours) by the use of an Oxford Instruments continuous flow cryostat. Coarse sample alignment was an easy procedure using an optical laser system, set to travel a path identical to that of the neutrons. The sample height and angle are adjusted until the laser beam illuminates the slit at the back of the single detector slits. Fine alignment can then be obtained using the neutron beam.

The reflected neutron beam is collimated to remove non-specular scatter and detected by ^{3}He detector. Neutrons have no electrical charge, hence they cannot directly seen. The following nuclear reaction takes place for high efficiency neutron detection;

$$n + {}^3\mathrm{He} \rightarrow {}^3\mathrm{H}^+ + {}^1\mathrm{H}^+ + e^- + eV. \tag{3.1}$$

where both proton (^{1}H) and tritium (^{3}H) are directly detected using a proportional counter, and from them the presence of neutrons is deduced. Typical acquisition times were of the order of 12 hours for each temperature. Long counting times are required to provide sufficiently high quality data over the relatively large range of Q_Z employed. A more detailed theory of neutron scattering and polarized neutron reflectivity, as for investigations of amorphous CoFeB:Ta thin-films are provided in Chapter 4. In addition, it also explains a fitting procedure of CoFeB:Ta thin-films using `GenX` software [102].

3.5 Magnetoresistance of Thin-Films

Magnetoresistance measurements were performed using a room-temperature magnetoresistance system for angular dependent measurements. The sample was placed onto a motorized rotation stage in the center of an electromagnet which has a 1 kOe maximum field capacity connected to a Kepco power supply. A Hall probe was placed on one of the poles of the magnet to measure the applied magnetic field. The rotation stage is covered with an electrically and thermally shielded cover to minimize the background noise signal. This stage can be rotated with an angle of 0°-180° with respect to the applied field direction.

The electrical connection to the thin-films was made using a conventional linear four-point probe technique which is widely used for measuring sheet resistance of thin-films. Sheet resistance, denoted by $R_\square$, is an extensive property of a material and depends on the thickness of the thin-film. This technique comprises four gold-plated bronze spring loaded metal contacts with a 1.3 mm diameter rounded tip, as shown schematically in Fig. 3.9 (a). The illustration of voltage and current contact geometries are given in Fig. 3.9 (b). These metal contacts were compressed to half the entire compression distance, then fastening tightly with a screw to ensure that a good mechanical (and hence electrical) contact was made with the thin-film. The four contacts were placed on a flat surface of the film with separation distances between inner and outer probes. The outer two probes have a $b = 12 \pm 0.05$ mm separation and supply constant current across the samples, while the resistance was measured by detecting the voltage drop through the inner two probes, with a separation of $a = 7.05 \pm 0.05$ mm, connected to a nanovoltmeter to measure the voltage.

The four-point probe technique was used in the measurements to eliminate the contribution from the resistance of the wiring and the contacts from the measurement of the sample. The sample substrates were scribed linearly with a large aspect ratio of approximate dimensions 15 mm $\times$ 2 mm to ensure that current flows uniformly through the entire film.

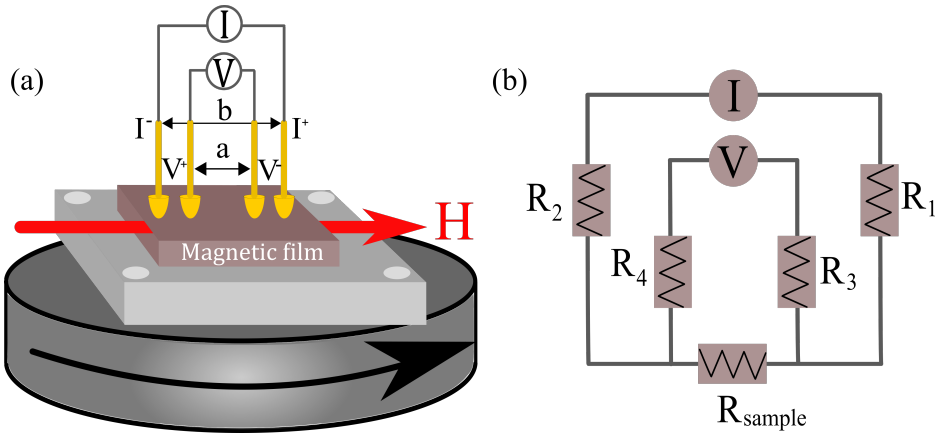

Fig. 3.9 (a) Schematic illustration of the voltage and current contact onto a motorized rotation stage for measurements of electrical resistance in thin-films using a four-point probe technique. (b) Illustration of voltage and current contact geometries for measurements of electrical resistance in thin-films.

An initial test-run was performed every time to ensure a proper contact when a new sample was loaded on the rotation stage.

An applied current of 1 mA was used to measure the resistance of thin-films. The magnetic field was applied to the sample in a wide range from -250 Oe to 250 Oe in increments of 0.5 Oe, where this small increment is to provide sufficient resolution to ensure all changes in resistance are observed. Large magnetic fields were not required to achieve saturation due to the relatively soft nature of the thin-films. A LABVIEW program was used to control the system and record the measured data.

3.6 Ferromagnetic Resonance of Thin-Films

Ferromagnetic resonance (FMR) spectroscopy is a very powerful technique to investigate the magnetization dynamics of ferromagnetic thin-films over a wide range of frequencies [106]. This was first demonstrated experimentally by Griffiths [107] in 1946 and the theoretical explanation of this phenomenon was provided by Kittel [51] in 1948. Since then, FMR spectroscopy has become one of the best-established techniques for the characterization of magnetic materials with respect to its effective magnetization and precessional damping. Several approaches exist for the measurement of magnetization dynamics in ferromagnetic thin-films [108]. Vector network analyzers (VNA) are mainly used for the investigation of high frequency (GHz) circuits. Since magnetization dynamics in thin-films occur in the microwave frequency range, the VNA is a powerful device for FMR experiments. FMR

measurements, presented in Chapter 7, were performed using a room-temperature broadband FMR with VNA, as illustrated schematically in Fig. 3.10 (a). This work was carried out at IN-IFIMUP, University of Porto, Portugal.

Due to the difficulties of measuring the total current and voltage at higher frequencies, *S*-parameters are used instead in a two-port measurement configuration. This involved measuring four *S*-parameters which consist of the two transmitted signals (S_{12}, S_{21}) and two reflected signals (S_{11}, S_{22}). The first subscript number is the port at which the outgoing wave is observed, and the second is the port at which the network is excited. These four parameters provide the elements of the scattering matrix S_{ij}, which is the ratio of the reflected voltage wave to the incident voltage wave amplitude; $S_{ij} = V_i/V_j$. This relation states that the incident waves which come from other ports are set to zero, except port j. The frequency is swept at a fixed applied magnetic field, and the complex transmission parameter S_{12} recorded as a function of the frequency. When the FMR condition is fulfilled the sample absorbs a part of the microwave signal, and changes the phase of the transmitted microwave signal. The resonance position and the FMR linewidth can be extracted by analyzing these changes in the measured transmission signal.

The main components of the experimental set-up are illustrated in Fig. 3.10 (a). The VNA serves as the source and the detector of the sinusoidal high frequency signal. It is connected

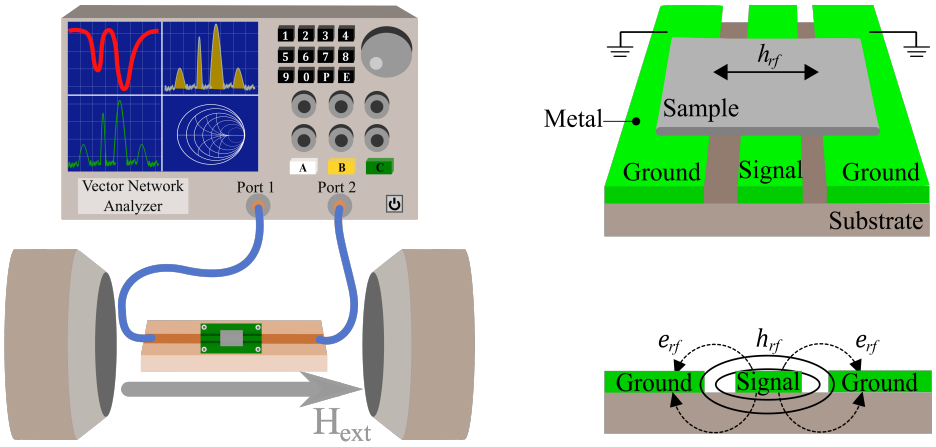

Fig. 3.10 (a) Schematic illustration of the VNA-FMR system. Microwave radiation is transmitted through a coplanar waveguide (CPW) placed in the center of an electromagnet. The sample is placed magnetic film side downwards on the CPW mounted in non-magnetic sample holder with goniometer between a set of magnetic coils. (b) Cross sectional diagram of CPW showing the configuration of rf field (h_{rf}) which is parallel to the plane of the CPW. The lower figure indicates the magnetic (solid lines) and electric (dashed lines) field lines winding around the signal conductor.

to a coplanar waveguide (CPW), having a characteristic impedance of 50 Ω using phase stable non-magnetic coaxial cables and microwave probes which is placed in the center of an electromagnet. The CPW excites the precession of the magnetization, which in turn induces a microwave voltage in the CPW. The resonance behaviour of the sample is investigated as a function of an externally applied magnetic field using a Rosenberger CPW, as shown in Fig. 3.10 (b). It has a central strip conductor of 3 cm length and 450 μm width surrounded by co-planar ground planes in each side. The gap between the central line and the ground planes is 300 μm.

Typical FMR data, obtained from VNA-FMR measurement, of polycrystalline Co thin-film are given in Fig. 3.11 as a function of applied magnetic field at 15 GHz. The linewidth of the samples are extracted from the FMR curves in Fig. 3.11 (a) by fitting to a Lorentzian peak function as shown by the solid line. Resonance frequency as a function of the magnetic field is given in Fig. 3.11 (b). The red solid line represents a fit to the Kittel equation.

The VNA sweeps the frequency of the outgoing signal across a specified range, from 45 MHz to 18 GHz, for the employed model (Anritsu 37247D). The static magnetic field is provided by a Bruker DC electromagnet ER-200D with water cooling system. The magnetic field was monitored using a Hall probe placed between the pole pieces, and it was calibrated using a Lakeshore-425 gaussmeter at the sample position. The static magnetic field was perpendicular to the microwave magnetic field, and can apply both in-plane and out-of-plane fields to the sample using the sample holder with goniometer. The calibration procedure and measurement process are fully automated using a LABVIEW software.

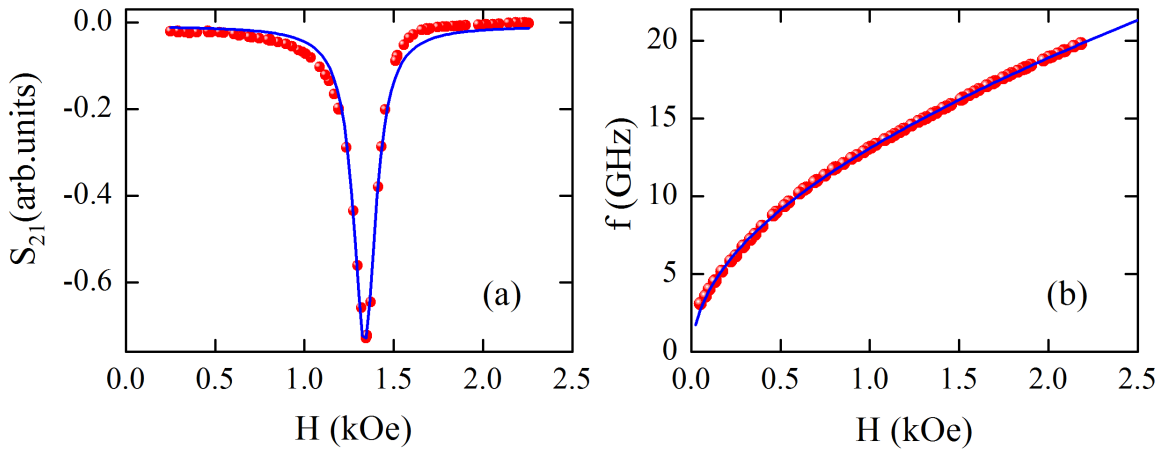

Fig. 3.11 (a) An example of the microwave transmission parameter S_{21} as a function of magnetic field for the Co[55 nm]/Ir sample. (b) An example of resonance frequency as a function of magnetic field for the same sample and a fit to the Kittel formula.

4

Theory of Scattering and Fitting Procedure

The purpose of this chapter is to introduce the theoretical background of x-ray and neutron scattering needed to understand the present work. The discussion starts with the interactions of x-rays with matter including; absorption, refraction and scattering mechanisms. In the following section, scattering geometry is explained with specular, off-specular and rocking scan types. Reflection from a homogeneous layer and multilayered films, and reflectivity from non-ideal interfaces, such as topologically rough and chemically graded interfaces, are introduced to understand reflectivity of thin-films in this work.

The physical principles of x-ray diffraction are also discussed briefly to aid the explanation of crystallographic phase transitions. Finally, the basic concepts of neutron scattering, including the fitting procedure of temperature dependent PNR data are discussed to express magnetic depth profiles of thin-films.

4.1 X-ray Interactions with Matter

X-rays were discovered by W. C. Röntgen [109] over a hundred years ago. Since that time they have become one of the major tools for the structure analysis of the matter because the wavelengths of x-rays are of the order of atomic spacing. This section presents the fundamental aspects of the x-ray interaction with matter which is needed to explain the principles of x-ray reflectivity and diffraction. The interaction between x-ray and matter depends on the characteristic of the material and the properties of the radiation. X-rays which meet with matter can undergo one of the three different mechanisms; absorption, refraction, and scattering. The following sections describe these mechanisms in detail.

4.1.1 Absorption

The absorption of x-rays for an element is governed by the linear absorption coefficient, μ, where μdz is the attenuation of the x-ray beam of the intensity I, after traveling a distance z through the material. The absorption is defined by;

$$I = I_0 \, e^{-\mu z} \tag{4.1}$$

where z is the depth from the surface, I_0 is the initial intensity and μ is the ratio of the beam intensities with and without the material. Absorption of a neutron by matter occurs via a different mechanism to that of x-rays. A nucleus within matter absorbs the neutron, which leads a reaction that causes fission, or the expulsion of a proton, an α particle or a γ-ray.

4.1.2 Refraction

The interaction of x-rays with a material have been considered at the atomic level. However, refraction should be expected at interfaces between different material layers because x-rays are electromagnetic waves. The scattering of x-rays can be regarded as reflection and refraction at the interfaces between two materials where each material has its own refractive index, n. This causes a change in the direction of the x-rays, as illustrated in Fig. 4.1. The refractive index is defined as the ratio of the speed of light in a vacuum c, to the speed of light in a medium v, where $n = c/v$. In general, the refractive index of a medium for x-rays and neutrons is complex;

$$n = 1 - \delta - i\beta \tag{4.2}$$

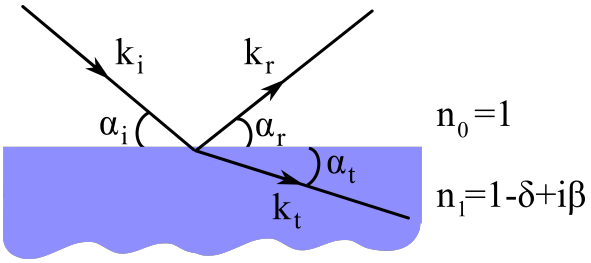

Fig. 4.1 Schematic illustration of the reflection and transmission at an ideal interface between two materials of different refractive index n_0 and n_1.

where δ is the dispersion coefficient, which is of the order of 10^{-5} in solids and $\sim 10^{-8}$ in air. The imaginary part, β, is the absorption coefficients, which is much smaller than δ. For x-rays, both coefficients are small positive numbers, yielding a refractive index less than unity. When x-rays are passing through an interface between two materials, the transmitted beam is refracted away from the surface normal. This is described by using Snell's law;

$$n_0 \cos\alpha_i = n_1 \cos\alpha_t \tag{4.3}$$

where n_0 and n_1 are the refractive indices of the two materials and α_i and α_t are the incident and transmitted grazing angles, respectively. As the incident angle α_i increases, the transmitted angle α_t also increases. When x-rays enter from one medium to different medium at a low incidence grazing angle, total external reflection occurs when the angle of incidence is less than the critical angle, α_c. When the angle of incidence is larger than the critical angle, x-rays penetrate into the material. If the wave is incident from vacuum, the critical angle can be expressed from Snell's law;

$$\alpha_c = \sqrt{2(1-n_1)} = \sqrt{2\delta} \tag{4.4}$$

where δ is the real part of the refractive index, and it is related to dispersion effects. For angles greater than α_c, x-rays or neutrons penetrate into the material. The reflection and transmission of electromagnetic waves which travel between media of different refractive indices is described by Fresnel's law. These are given in angular terms as;

$$r = \frac{n_0\alpha_{i,r} - n_1\alpha_t}{n_0\alpha_{i,r} + n_1\alpha_t} \qquad t = \frac{2n_0\alpha_{i,r}}{n_0\alpha_{i,r} + n_1\alpha_t} \tag{4.5}$$

where r is the amplitude of reflectivity and t is the amplitude of transmittivity. The corresponding intensities from reflection and transmission are $R = |r|^2$ and $T = |t|^2$ where $r^2 + t^2 = 1$ indicates the energy conserved at the boundary. Below α_c, only the reflected

component exist. As the angle is increased above the α_c, transmission increases, and the reflectivity drops sharply as α_i^{-4}.

4.1.3 Scattering

The final process is the so called scattering or diffraction mechanism when x-rays and neutrons interact with a matter. In this work the discussion is limited to the classical description of scattering events in which the wavelengths of the incident wave are the same as that of the scattered waves. This is elastic scattering, which is also called Thomson scattering. In this section, all interactions are assumed to be elastic. In general, this assumption is not true in quantum mechanics where the scattered photon has a lower energy relative to that of the incident energy. This inelastic scattering process is called Compton effect. This section includes scattering theory for x-rays with the interaction of a single electron and an atom. In this section the discussion of scattering theory for x-rays starts with the interaction of an x-ray with a single electron and develops through the consideration of the scattering from an atom.

The scattering of x-rays by a single electron can be considered in terms of dipole oscillations. The electron, being charged, is forced to vibrate by the electromagnetic interaction of an incident x-ray beam. This vibrating electron then radiates a spherical waves as a dipole which is described using Maxwell's equations. The radiated electric field at a point r is given by;

$$E_{rad}\ (r,t) = -\left(\frac{e^2}{mc^2}\right)\left(\frac{1}{r}\right)E_0 \exp[2\pi i(k.r - wt)] \tag{4.6}$$

where E_0 is the amplitude of the incident electric wave. The first term ($r_0 = e^2/mc^2 = 2.82 \times 10^{-13}$Å) is defined as the Thomson scattering length or classical radius which represents the scattering power of the free electron. Here, the minus sign is due to the π-phase shift. The number of scattered photons collected per second in detector of area A at solid angle from incident direction is defined by [99];

$$I_S = I_0 \triangle\Omega \left(\frac{d\sigma}{d\Omega}\right) \tag{4.7}$$

where I_0 is the strength of the incident flux, which is the number of photons passing through unit area per second, $\triangle\Omega$ is the unit solid angle, and $d\sigma/d\Omega$ is the differential scattering cross-section. Thus, the efficiency, I_S/I_0, of the scattering process can be measured by the differential cross-section.

In the previous section, the discussion was based on the Thomson scattering of a free electron, where its position was fixed. However, it is known that the electrons do not scatter with the same phase. The intensity of the scattered radiation from an atom is defined by the atomic scattering factor which is the ratio of the amplitude of the x-ray scattered by the atom to the amplitude of that scattered by a single free electron. There are Z electrons in an atom which are spread over its volume:

$$Z = \int_V \rho(r) dV. \tag{4.8}$$

The scattering ability of these electrons is summed up in the scattering factor f which can be written using Fermi's Golden rule as a Fourier transform of the electron density [99, 110];

$$f = \int_V \rho(r) \exp(2\pi Q r) dV \tag{4.9}$$

where ρ is the number of electron per unit volume and r is the radius. Here $\rho(V)\, dV$ is the probability that an electron exists in volume dV.

4.2 Scattering Geometries

The scattering geometry for a typical experiment is shown in Fig. 4.2 (a) and its reciprocal space equivalent in Fig. 4.2 (b). The incident beam strikes to the sample surface at an angle θ and reflected beam intensity can be measured as a function of θ. For specular reflectivity studies the z-component of the scattering vector, Q_Z is parallel to the z-axis, which is perpendicular to the sample surface. The scattering vector, which is the reciprocal direction of the scattering, is described as;

$$Q = k_f - k_i = \frac{4\pi}{\lambda} \sin\theta \tag{4.10}$$

where λ is the wavelength and k_i is the incident wavevector at an angle θ_i to the sample surface. After scattering through an angle θ_f, the reflected beam is defined by the wavevector k_f. For elastic scattering, the magnitude of these wavevectors are the same, hence;

$$|k_i| = |k_f| = |k| = \frac{1}{\lambda}. \tag{4.11}$$

The out-of-plane, Q_Z and in-plane Q_X components of the scattering vector can be expressed in terms of k_f and k_i. The transformations are;

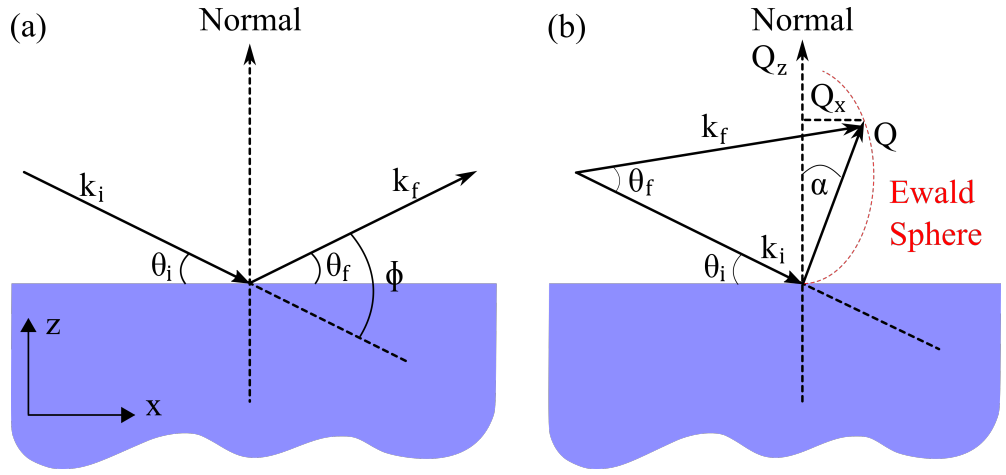

Fig. 4.2 Schematic illustration of a vector map showing the relation between (a) real and (b) reciprocal space.

$$Q_Z = \frac{2\pi}{\lambda}\Big[\sin(\phi-\theta)+\sin(\theta)\Big] \quad \text{and} \quad Q_X = \frac{2\pi}{\lambda}\Big[\cos(\phi-\theta)-\cos\theta\Big] \tag{4.12}$$

where $\theta = \theta_i$ and $\phi = \theta_f + \theta_i$ are the sample and the detector angles, respectively. These two equations can be expressed in terms of α and ϕ;

$$Q_Z = \frac{4\pi}{\lambda}\Big[\sin\big(\frac{\phi}{2}\big)\cos\alpha\Big] \quad \text{and} \quad Q_X = \frac{4\pi}{\lambda}\Big[\sin\big(\frac{\phi}{2}\big)\sin\alpha\Big] \tag{4.13}$$

where $\alpha = \theta - (\phi/2)$. These equations state that reciprocal space can be probed in two dimensions. Eq. 4.13 have a common factor, $(2/\lambda)\sin(\phi/2)$, which only depends on the detector angle, and the difference between the in-plane and out-of-plane terms that depend on α. These equations allow the determination of different types of grazing incident x-ray scans; specular, off-specular (longitudinal diffuse), and rocking scan (transverse).

In the specular condition, the angle of incidence is equal to the angle of reflectivity; $\theta_i = \theta_r$, hence $\alpha = 0$. Q_X disappears and the scattering is only sensitive to the out-of-plane component. In this scan, the sample and detector are coupled such that the detector moves twice the rate of the sample, $\theta = \phi/2$. Thus the specular condition is maintained throughout the scan with Q_Z. The specular scan also contains forward diffuse scatter, hence it is required to perform an off-specular scan to obtain the true specular reflection by subtracting off this intensity from the measured specular reflectivity. The off-specular or longitudinal diffuse scan is essentially the same as the previous case, with a small offset angle. The in-plane diffuse scatter can be measured in the Q_X direction by fixing the detector angle 2θ, and then

sweeping the sample angle θ from 0 to ϕ. This scan type is called rocking or transverse scan which provides information on the lateral length scale. Although there is a slight variation to the out-of plane component during rocking scan, it is typically negligible at small angles.

4.3 X-ray Diffraction

Diffraction of x-rays is one of the most important method of studying the structural investigations of materials. X-ray diffraction is the interference of x-rays which are scattered coherently from periodically arranged groups of electrons. When the incident wave interacts with a crystal lattice, each atom re-radiates a spherical wavefronts. The simplest mathematical construction of diffraction mechanism is described by Bragg [111] in 1913. In a crystalline solid which has parallel planes of ions and separated by the interplanar distance d, Bragg diffraction occurs when the incident x-rays are scattered from lattice planes at certain angles. Fig. 4.3 shows schematic illustration of Bragg condition for the constructive interference of waves. This condition is satisfied by;

$$n\lambda = 2d_{hkl} \sin\theta \tag{4.14}$$

where λ is the wavelength of the radiation used, n is a positive integer, d_{hkl} is the interplanar spacing and θ is the angle between the incident x-ray and the relevant lattice planes. This is called Bragg's law [111] which explains the interference pattern of x-rays scattered by a crystal lattice. Fig. 4.3 shows first and second waves are in phase each other. The condition of these waves to stay in phase after reflection is that the path length of CB and BD is $n\lambda$.

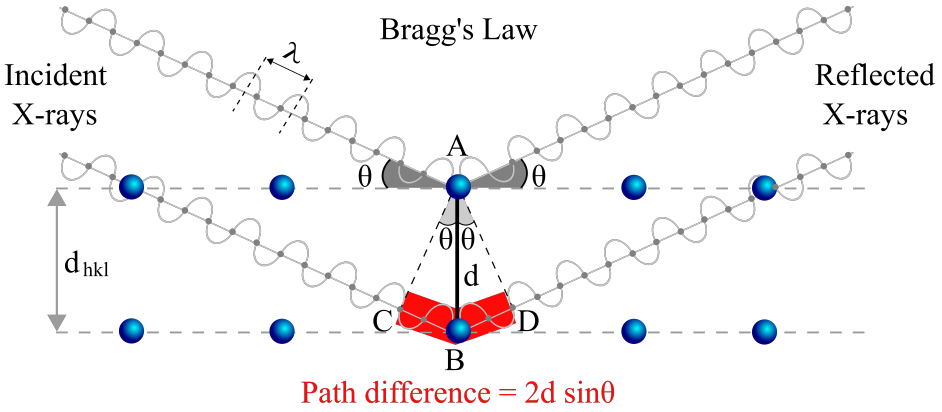

Fig. 4.3 Schematic representation of the derivation of Bragg's law with reflection of two incident waves from lattice planes. The path difference is highlighted in red.

Here, CB and BD are equal to each other, $CB = BD = d\sin\theta$. Bragg's law states that the scattered x-rays interfere constructively when difference between the path lengths of two waves is $n\lambda = 2d\sin\theta$. The diffraction pattern can be obtained by measuring the intensity of scattered waves as a function of the scattering angle. In the diffraction pattern, a strong intensity is obtained at the points when the scattering angles satisfy the Bragg condition.

4.4 Reflection from a Homogeneous Layer

Consider a single layer of finite thickness, grown onto an infinitely thick substrate, exposed to monochromatic x-rays at grazing incidence, as shown schematically in Fig.4.4. There are three media, that x-ray experiences before and after the scattering. These are the air n_0, the material n_1 and the substrate n_2. At the surface of the layer, the incidence beam in air with refractive index n_0, will be partially reflected onto a single layer, r_{10}, and transmitted, t_{01} into a medium with refractive index n_1. The transmitted x-ray travels through to the next interface, and they will be partially reflected and transmitted again. This process will continue until the x-rays reach the substrate surface with refractive index n_2. The x-rays transmitted into the substrate dies off and the reflected x-ray reaches to the another part of the surface and is again partially transmitted to the next layer. When all possible pathways of the x-ray beam are considered, the total reflectivity of a single layer is given in terms of the transmission and reflection coefficients;

$$\begin{aligned} r_{total} &= r_{10} + t_{01}r_{21}t_{10}\,p^2 + t_{01}r_{21}r_{10}r_{21}t_{10}\,p^4 + \ldots\ldots \\ &= r_{10} + t_{01}r_{21}t_{10}\,p^2 \sum_{m=0}^{\infty} (r_{01}r_{21}\,p^2)^m \end{aligned} \tag{4.15}$$

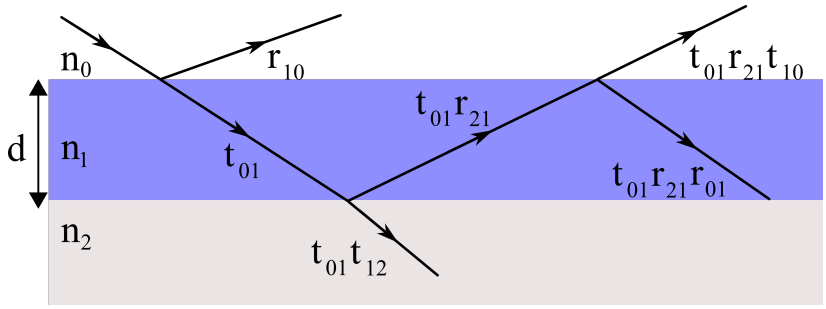

Fig. 4.4 Schematic illustration of reflection and transmission of incident x-rays from a thin-slab of thickness d with refractive index n_1 on a infinitely thick substrate with refractive index n_2. Reflection and transmission are denoted by r and t, respectively.

where p^2 is the phase factor of the x-ray which is reflected from the top and bottom sides of the layer, and it is given by $p^2 = \exp(iq_1 d)$ where $q_1 = 2k_1 \sin\alpha_1$ is the scattering vector with incident wavevector k_1 and thickness d. The summation of the total reflectivity is simplified using Fresnel's equation, Eq. 4.5, and then it is given by;

$$r_{Total} = r_{10} + \frac{t_{01} r_{21} t_{10}\, p^2}{1 + r_{10} r_{21} p^2}. \tag{4.16}$$

The oscillations of the reflected intensity are called Kiessig fringes and result from interference between various reflections of x-rays from the top and the bottom of the layer. Fig. 4.5 (a) shows the simulated reflectivity profile of a 6 nm Co thin-film with Ir overlayer, showing the Kiessig fringes and the critical angle, and Fig. 4.5 (b) shows the incident angle when it is lower or higher than critical angle. These fringe numbers depend on the total film thickness where they increase with increasing film thickness and they are related to the thickness of the layer with an equation $\triangle\theta = \lambda/2d$ [112]. Here, the reflected intensity shows a sharp drop at the critical angle, which means that the x-rays begin to penetrate through the material, and distinct fringes begin to appear. For a single film, the separation of the two consecutive fringes m and $m+1$ are given by;

$$d = \frac{\lambda}{\theta_{m+1} - \theta_m} \tag{4.17}$$

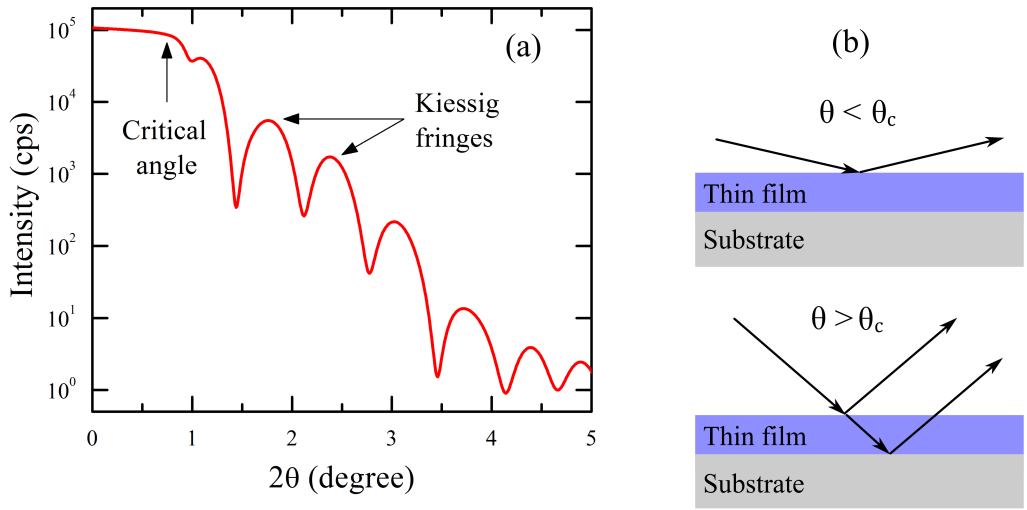

Fig. 4.5 (a) Simulated specular reflectivity for 6 nm Co layer with Ir overlayer on Si/SiO_2 substrate. The Kiessig fringes and the critical angle are clearly shown. (b) Schematic illustration of x-ray reflectivity for cases when the incident angle, θ, is lower and higher than critical angle θ_c.

where θ_m is the location of the m^{th} fringe. This shows that the layer thickness based on the angular position of the fringes where the separation between two fringes increases with decreasing layer thickness. The amplitude of the fringes depends on the difference in electron density between the layers, grading and roughness of the interfaces. The decay in the intensity shows the roughness of the interfaces where reflected x-rays decrease more rapidly with a large surface roughness [112].

4.5 Reflection from a Multilayered Films

Throughout this work, the thin-film samples contain bilayers and multilayers, hence the reflectivity for these structures has to be taken into account. The reflectivity of multilayered structures is more complicated than for the single layer. More transmission and reflection of the x-ray beam from sub-layers and interfaces may affect the total reflectivity. A general method to measure the reflectivity of multilayered system extends from the reflectivity of a single layer to include the multiple reflections and refraction effects. For multilayered structures, the reflectivity is described by a recursive relation, developed by Parratt [98]. This method includes refraction and multiple scattering events for a stack on top of a thick substrate.

Fig. 4.6 shows a multilayer stack consisting of N layers, where each layer has a thickness d_j, and refractive index $n_j = 1 - \delta_j + i\beta_j$. Here the layers are numbered from the surface towards the substrate. The wavevector transfer becomes $Q_j = 2k_j \sin\alpha_j = 2k_{z,j}$ where;

$$k_{z,j}^2 = (n_j k)^2 - k_{x,j}^2. \tag{4.18}$$

In the x direction the wavevector component is constant throughout the multilayer stack. The wavevector transfer for each layer becomes;

$$Q_j^2 = Q^2 - 8k^2\sigma_j + 8ik^2\beta_j. \tag{4.19}$$

The reflectivity from the top of the j'th layer can be calculated using the Fresnel relations, Eq. 4.16, as;

$$r_{j-1,j} = \frac{r_{j-1,j} + r_{j,\infty}\, p_j^2}{1 + r_{j-1,j}\, r_{j,\infty}\, p_j^2}. \tag{4.20}$$

The reflectivity at the next interface can be calculated in a similar way until the total reflectivity amplitude, r_{10}, is obtained at the interface between the first layer n_1 and the vacuum n_0.

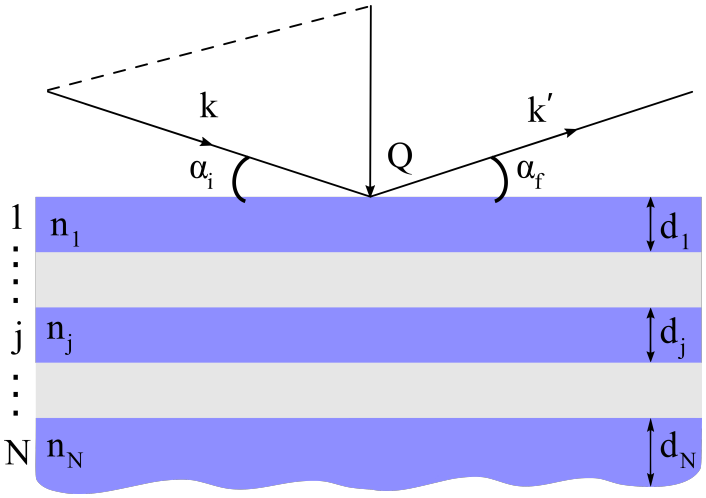

Fig. 4.6 A schematic illustration of a multilayer consisting of N layers with refractive indices, n and layer thicknesses, d.

Using this equation, the reflected intensity from the top of the stack to the bottom is obtained for a multilayered structure which contains smooth interfaces between layers. However, multilayers do not always comprise perfect interfaces, hence this must be taken into account. During deposition of thin-films, the interdiffusion of target atoms into other layers is possible depending on the energetics of the sputtering process and the relative difference in size between atoms and diffusivity. Thus, it is required to consider a mechanism, during the fitting procedure, in order to account for a graded interface, which causes the fluctuations in the density profile of the layers. Besides, the layers in a multilayer system are unlikely to be flat, which is called interfacial topological roughness. Hence, this must also be considered within the calculations for vertical changes in the layer thickness.

4.6 Reflection on non-ideal interfaces

The scattering in the previous section has been described for perfectly sharp and flat interfaces. However, in real thin-film systems most of the structures have topologically rough and chemically graded interfaces, hence it is necessary to extend the scattering formalism to take into account these interfaces. A specular reflectivity measurement is sensitive only to the average change in the electron density as a function of layer depth, hence it can quantify only the total interface width.

Fig. 4.7 shows examples of (a) topologically rough and (b) chemically graded interfaces where the interface is blurred due to the intermixing of two different atomic species. In reality,

a mixture of these two is expected in thin-films. In the first case of a topologically rough interface, the heights of layers at different positions are uncorrelated, hence the roughness can be considered by varying the index of refraction. This is a method which is proposed by Nevot and Croce [113]. This model shows that x-ray reflection from an interface exhibits a Gaussian roughness distribution, where it has a standard deviation σ. The root mean square roughness (RMS) can be extracted from reflectivity data using this model. When a wave of x-ray incident onto a rough surface, it is scattered through different angles by the various facets, as shown in Fig. 4.7 (a). If these are distributed in a Gaussian with a standard deviation σ, the reflectivity of a rough interface is given by;

$$R(Q) = R_F(Q)e^{-(Q_Z^2\sigma^2)} \tag{4.21}$$

where Q_Z is the out-of-plane components of the scattering vector, σ is the width of interfacial region and R_F is the Fresnel reflectivity. The reflectivity of a multilayer with chemically graded interfaces is the product of the intensity from a multilayer R_F and a factor which determines a change in the density across the layer interface. In this case, a new model is used for grading profile at an interface with an error function to define the roughness at the interface;

$$f(z) = \mathrm{erf}\Big(\frac{z}{\sigma\sqrt{2}}\Big). \tag{4.22}$$

The derivative of the error function is a Gaussian, and the Fourier transform of a Gaussian gives another Gaussian. Hence, this allows the intensity for the reflectivity of graded interface;

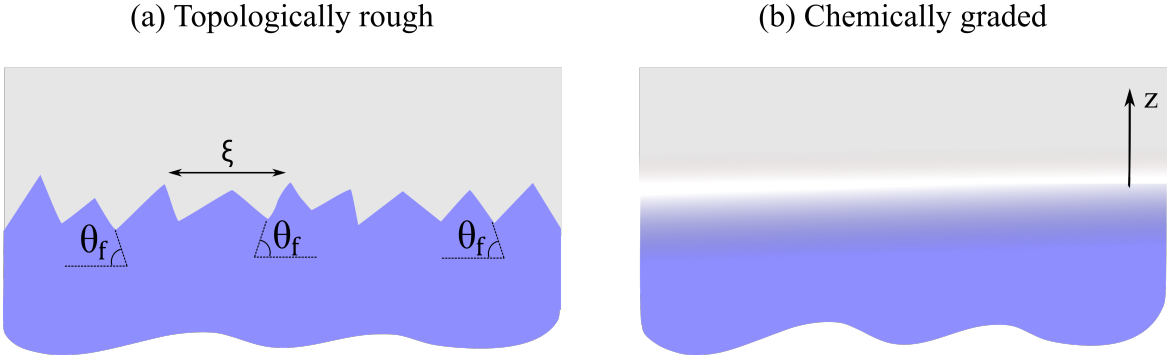

Fig. 4.7 Examples of the type of transition that can exist at an interface between two layers (a) topologically rough defined by correlation lengths ξ and facet orientations, θ_F, and (b) chemically graded, but perfectly flat surface.

$$R(Q) = R_F(Q)e^{-(Q^2\sigma^2)}. \tag{4.23}$$

The topologically rough interface is oriented locally in different directions, as shown in Fig. 4.7 (a), and the reduction in specular scatter reveals through diffuse scatter out of the specular direction. In contrast, the chemically graded interface is parallel to the film surface and perpendicular to the scattering vector. Thus, changes in the specular scatter due to composition variation arises from coherent effects [112].

4.7 Neutron Scattering

Neutrons were discovered by J. Chadwick [114] in 1932, and neutron scattering has been proven to be a useful technique to understand the properties of materials. The wavelength of neutrons is similar to the spacing between atoms, which makes neutrons an ideal technique to study structure with atomic resolution. The scattering of neutrons is analogous to the scattering of x-rays, hence the scattering theory in the previous sections for x-rays is also applicable to neutrons. Both x-ray and neutrons are used to study condensed matter systems, the mechanism behind neutron scattering is more complex in comparison to x-ray scattering. Neutrons are of course charge neutral and can be described by their wavevector k and their spin σ, which results in a magnetic moment, therefore they interact with unpaired electrons of magnetic atoms. This makes neutrons an ideal tool to study magnetic fluctuations and structural properties of magnetic materials. Charge neutrality allows neutrons to penetrate deeply into material better than charged particles. Similar to x-rays, neutrons show interference effects in the case of scattering from ordered systems. Hence, it is possible to analyze the crystal structure of a sample from nuclear and magnetic interactions.

4.7.1 Properties of Neutrons

The fundamental properties of a free neutron are summarized in Table 4.1. Neutrons consist of one up and two down quarks, thus they have a total charge of zero. Neutrons with a de Broglie wavelength ~ 2 Å are referred as thermal neutrons. This wavelength is of the same order of magnitude of interatomic distances in materials. The wavelength of a neutron is given by the de Broglie relation;

$$\lambda = \frac{h}{mv} \tag{4.24}$$

Table 4.1 Basic properties of a free neutron

Mass	1.675×10^{-27} kg
Spin	1/2
Charge	0
Magnetic dipole moment	-1.913 μ_N
Gyromagnetic ratio	8.5161×10^8 rad/s T
Nuclear magneton μ_N	5.051×10^{-27} J/T
Free neutron decay	$n \rightarrow p + e^- + \tilde{\nu}_e$
β-decay lifetime	885.8 ± 0.9 s

where m is the mass of the neutron and v is the velocity. The energy of a neutron using kinetic energy is given by;

$$E = \frac{1}{2}\, mv^2. \tag{4.25}$$

The energy of the neutron is also related to the wavelength, and the temperature T via the Boltzmann constant, k_B = 1.381×10^{-23} JK^{-1};

$$E = k_B T = \frac{1}{2} mv^2 = \frac{h^2}{2m\lambda^2} = \frac{\hbar^2 k^2}{2m}. \tag{4.26}$$

Neutrons can be classified as hot, cold and thermal depending of the moderator. The wavelengths of x-rays and thermal neutrons are of the order of 1 Å, but their energies show huge difference. For example, a neutron with a 1 Å wavelength has an 0.08 eV energy, an x-ray with the same wavelength has an energy of 12.400 eV. In a neutron scattering experiment, a neutron beam with momentum $\hbar k_i$ and energy E_i is incident on a sample and scatters from the sample at an angle θ with a momentum $\hbar k_f$ and energy E_f. Due to the conservation of the energy and momentum, the scattering process is expressed by;

$$Q = k_i - k_f \quad \text{and} \quad Q^2 = k_i^2 + k_f^2 - 2k_i k_f \, cos(2\theta) \tag{4.27}$$

$$\hbar\omega = E_i - E_f = \frac{\hbar^2 k_i^2}{2m} - \frac{\hbar^2 k_f^2}{2m} = \frac{\hbar^2 (k_i^2 - k_f^2)}{2m} \tag{4.28}$$

where m is the mass of neutron, Q denotes the wavevector transfer and $\hbar\omega$ is the energy transferred to the sample. Initial and final wavevectors are given as k_i and k_f, respectively. In

the case of elastic scattering, there is no energy transfer from neutron to the sample, hence $\hbar\omega = 0$, $|k_i| = |k_f|$ and the wavevector transfer become $Q = 2|k|\sin\theta$. For inelastic scattering, both momentum and energy are transferred from the neutron to the sample and $\hbar\omega \neq 0$ and $|k_i| \neq |k_f|$. The wavevector values are achieved by varying the scattering angle.

4.7.2 Scattering of Neutrons

Two different interactions occur between a neutron and the atoms in a crystal. They are the interaction of neutron/nuclear and the interaction of neutron-magnetic, which the latter is the interaction between the neutron magnetic moment and any magnetic moment of atom. There is a very strong interaction between neutrons and nuclei which bind the nucleus together. The scattering mechanisms of neutrons are given in Fig. 4.8 for (a) structural and (b) magnetic scattering. In general, the interaction between an incident neutron at position r and the j^{th} atomic nucleus positioned at r_j is described within the Born approximation by;

$$V(r) = \frac{2\pi\hbar}{m}\, b_j\, \delta(r - r_j) \tag{4.29}$$

where $V(r)$ is the Fermi pseudopotential, m is the mass of the neutron, r is the position of the neutron relative to the nucleus and b_j is the bound scattering length. In a similar way to x-ray scattering, the atomic scattering factor can be defined as;

$$f_n(q) = \frac{m}{2\pi\hbar^2}\Big[\int_{Vol} V(r)\; exp(2\pi i(q.r))\; dV\Big]. \tag{4.30}$$

This equation shows the different scattering potentials between neutrons and x-rays where the scattering potential for x-rays is the electron density. The radius of the nucleus ranges between 1 fm for a single nucleon, up to 7 fm for the heaviest nuclei, where it is smaller than the wavelength of the neutron with ~ 1 Å. Hence, by assuming the fermi pseudopotential is negligible outside of the nucleus with radius r_0, and a constant a, within it then: $0 < a < r_0$ the integral in Eq. 4.30 can be carried out. Then the atomic scattering factor for neutrons can be expressed as;

$$f_n = \frac{m}{2\pi\hbar^2}\, a\, \left(\frac{4}{3}\pi r_0^3\right) \tag{4.31}$$

where f_n is a constant and denoted as b, which is the nuclear scattering length. Since scattering is originated by a point source (unlike x-rays), f_n has no q dependence. Now, the similarity between neutron and x-ray scattering breaks down, and it becomes difficult to

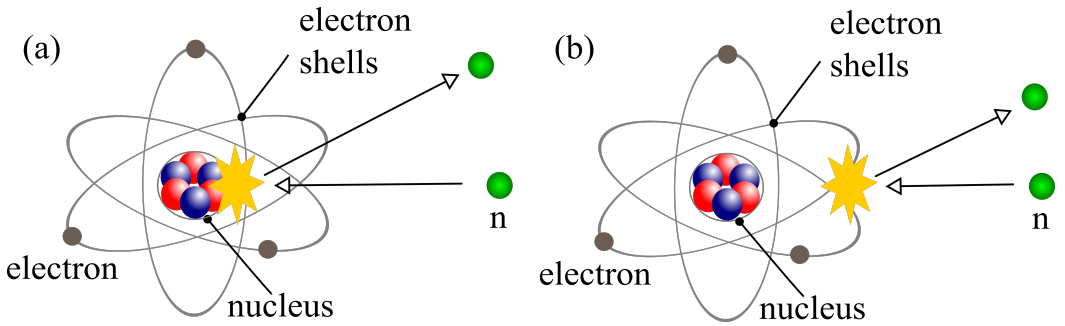

Fig. 4.8 The scattering mechanisms of neutrons for (a) structural and (b) magnetic scattering.

compare neutron with x-ray scattering. At this point Fermi's golden rule helps the differential cross section to be introduced by its wavevector k and spin σ with;

$$\left(\frac{d\sigma}{d\Omega}\right)_{k_0,\sigma_0\to k_1,\sigma_1} = \left(\frac{m}{2\pi\hbar^2}\right)^2 |\langle k_1,\sigma_1|V|k_0,\sigma_0\rangle|^2. \tag{4.32}$$

Here, the initial and final states are defined in terms of their spin and wavevector. Neutrons have a magnetic moment which can interact with the internal magnetic field of the atom. This interaction is the consequence of the energy associated with the magnetic moment of neutron, μ_N, in the internal magnetic field, H from any unpaired electrons within the atom.

If an incident neutron enters in a magnetic material, it interacts with the magnetization of the sample, which is aligned at an angle θ to an axis perpendicular to the moment of the neutron, and experiences a magnetic potential V_{mag};

$$V_{mag}(z) = -\mu_N.H(z) = -\frac{2\pi\hbar^2}{m}\, b_{mag}(z)\sin\theta. \tag{4.33}$$

The total scattering of a neutron is the sum of the nuclear and magnetic components (the Zeeman interaction), $b_{total} = b_{nuc} + b_{mag}$. If the incoming neutron is polarized (up/down) with respect to the magnetization, V_{mag} changes its sign. Hence, the total scattering length is different for spin-up and spin-down neutrons;

$$V_{\pm} = V_{nuc} \pm V_{mag} = \frac{2\pi\hbar^2}{m} N\left(b_{nuc} \pm b_{mag}\right) \tag{4.34}$$

where N denotes the atomic density. The first term in the equation results from the interaction of neutron with the nucleus, and the second term results from the interaction of the neutron with the sample magnetization. A schematic illustration of the SLDs for spin-up and spin-downs are sketched in Fig. 4.9. Here, Nb_{nuc} is the nuclear scattering length density (SLD), which is directly related to the elements and their isotopes within the material. The magnetic

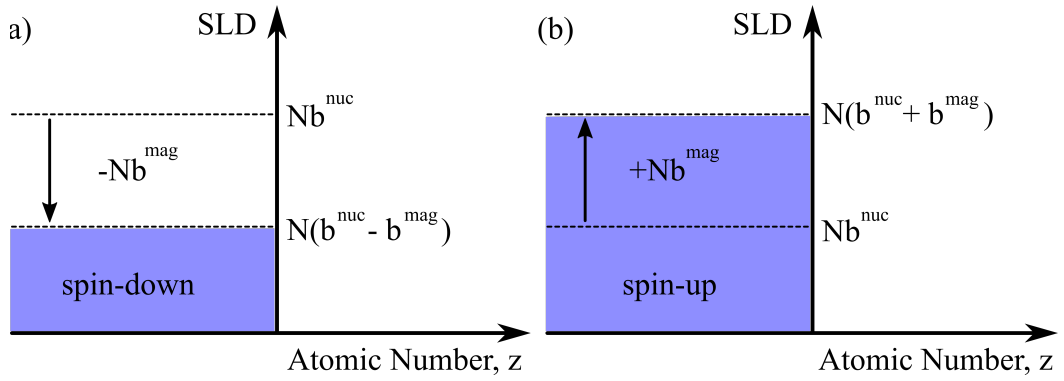

Fig. 4.9 Scattering length density for (a) spin-down neutrons and (b) spin-up neutrons. Scattering density profile is the sum of a nuclear and a magnetic component. Reproduced from [115].

component of the scattering length density is Nb_{mag}, is proportional to the magnetization of the sample. This equation also shows that the total scattering length is dependent on the neutron polarization. Here, plus/minus sign corresponds to a neutron beam which is polarized parallel/perpendicular to the magnetization direction. PNR is very sensitive to the magnetic structure of materials because both nuclear and magnetic SLDs are of the same order of magnitude. The nuclear and magnetic SLDs of bulk Fe are Nb_{nuc} = 801.9 μm^{-2}, Nb_{mag} = 498.5 μm^{-2}, respectively.

4.8 Data Modeling Procedure

The best fitting simulations of both the XRR and PNR reflectivities were obtained by simulating a sample structure and calculating the reflectivity, which provides the nuclear and magnetic profiles in the out-of plane direction. The freely available `GenX` [102] simulation code, which uses Parratt's recursion formalism [98], was used for the modeling of reflectivity curves. The reflectivity data can be simulated using a set of parameters including each layer thicknesses, magnetic moments, densities and each interface roughnesses, which determine the physical nature of the thin-films. The structural depth profiles are obtained from room-temperature PNR and XRR reflectivities. The data was modeled using layer stacks of substrate/CoFeB:Ta/Ta cap, where the thin-films were deposited on Si/SiO_2 and GaAs(001) substrates. A thin oxidized Ta layer was added to the models to take into account oxide formation of the Ta cap. The density of each layer is transformed from kg/m^3 to formula units $\mathring{A}^3$, where the relative atomic mass u is defined by;

$$\begin{aligned} 1u &= 1.66054 \times 10^{-27} kg \\ \rho[kg/m^3] &= 1.66054 \times 10^3 \times \rho[u/\mathring{A}^3] \end{aligned} \tag{4.35}$$

The densities of each layer was calculated using this way and summarized in Table 4.2. The magnetization depth profiles of the CoFeB:Ta thin-films were obtained by consistently fitting the low-temperature reflectivities using the structural parameters obtained at room-temperature. During fitting, room-temperature structural parameters were fixed, and only the magnetic parameters including layer thickness, interfacial roughness and magnetic moments were allowed to vary as a function of temperature. It is required to generate different models for best fit parameters of reflectivities and corresponding spin-asymmetries at different temperatures.

First of all, a simple model was introduced including substrate/uniform CoFeB:Ta/Ta capping layer. This is called "1-Layer model" because the FM layer is comprised of a uniform CoFeB:Ta layer with a thickness of 10 nm. To indicate the MDL formations at interfaces, a new model with subdivided CoFeB:Ta thin-slabs is required because there is only one magnetically active layer. However, other models can provide magnetically inactive layers at the interfaces. The second model is called the "2-Layers model", where the CoFeB:Ta layer in the structure was divided into two thin-slabs with different parameters. The following simulations were "3-Layers" and "4-Layers" models, where the CoFeB:Ta layers are divided into three and four thin-slabs to provide a realistic description of the magnetic structure of the thin-films. A schematic illustration of the CoFeB:Ta thin-films divided into various thin-slabs are outlined in Fig. 4.10. Each model gives a reduced chi-squared values at the end of fitting the data, where the goodness of fit of these simulations can be compared using these chi-squared values. This procedure assists in deciding the agreement of the model with the PNR data. In this investigation, the 3-Layers model for the structure on Si/SiO_2 and the 4-Layers model for the structure on GaAs(001) gave the lowest chi-squared values for both

Table 4.2 Calculated densities of each layers used in the models.

Layer	Density	Substrate	Density
Ta_2O_5	0.0111	SiO_2	0.0254
Ta	0.0554	Si	0.0499
CoFeB:Ta	0.0755	GaAs(001)	0.0222

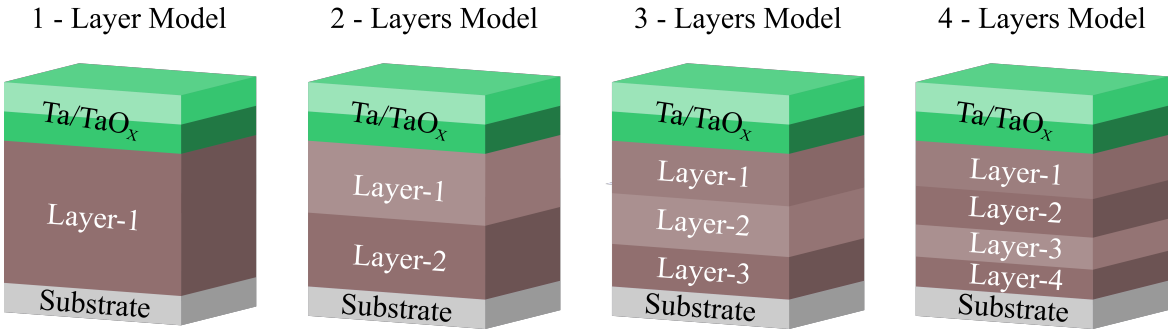

Fig. 4.10 A schematic illustration of CoFeB:Ta layers divided into various thin-slabs.

temperatures, as adding further subdivisions to the model gave no improvement to the quality of the fits. This modeling procedure for amorphous CoFeB:Ta thin-films was used to define temperature dependent MDL formations at interfaces in Chapter 6.

The figure of merit is the fitting function of reflectivity curves that compares how well the simulation matches with the measured reflectivities. In the fitting procedure, an absolute logarithmic difference "log" of the figure of merit was used to fit the reflectivity curves. The modeled structure can be modified to minimize the difference between the theoretical curves and experimental reflectivities, where these minimizations provide values of reduced chi-squared, χ^2, for the specular reflectivity.

5

Interfacial Origin of Thickness Dependent In-plane Anisotropic Magnetoresistance

Magneto-transport phenomena in ferromagnetic (FM) thin-films, such as anisotropic magnetoresistance (AMR) [42–44] have attracted considerable attentions in a wide variety of applications in the emerging field of spintronics [116]. The interest in anisotropic magnetotransport effects has become important again due to the discoveries of the tunnelling AMR (TAMR) which results from strong spin-orbit interaction (SOI) in a single FM semiconductors [117] and metals [118], spin-Hall magnetoresistance (SHMR) [119] originating from concerted actions of the direct and inverse spin Hall effect, and "hybrid" magnetoresistance [120] which appears in a metal in close proximity with a FM layer. In addition to these anisotropic effects, conventional AMR in FM thin-films continues to present its unexplained behaviour [121] including a possible interfacial AMR for perpendicularly magnetized Co thin-films [122].

AMR was first observed by William Thomson [44] and, a detailed understanding of the mechanism underpinning the AMR continues to emerge [122, 123]. In ferromagnetic (FM) thin-films the AMR is a prominent manifestation of the anisotropic scattering of conduction electrons due to the SOI [42, 43] within the bulk of the FM thin-films. Almost all materials exhibit magnetocrystalline anisotropy, hence they also exhibit AMR [121]. The AMR is very small for most materials, usually a few percent, even at high applied magnetic fields and rarely exceeds 5% at room-temperature for strong magnetic materials. Large AMR ratios

have been reported in MBE-grown Co/Ni multilayers where it reaches up to 8.2% at 4.2 K. AMR has been observed in FM thin-films and bulk materials where the change is smaller in thin-films than bulk materials. Several AMR studies in FM thin-films showed that the magnitude depends on the thickness of FM layer, grain size and the thin-film deposition parameters [43, 45, 62].

Recently, an interfacial contribution to the AMR in a perpendicular geometry where magnetization rotated out of the plane of the layers, has been found in Pt/Co/Pt structures [122] and Co/Pd multilayers [124]. This anisotropic interface magnetoresistance has been explained in terms of a hybrid magnetoresistance resulting from induced magnetic moments near the interfaces with an FM material in contact with a Pt layer [120]. However a recent study disagrees [125] where the observed magnetoresistance in Pt/$CoFe_2O_4$ hybrid interfaces cannot be attributed to proximity-induced magnetic moments at Pt. The observed magnetoresistance is dominated by either bulk or interface SOI related effects [125].

There has been significant interest in Rashba-torque effects which originates in interfacial SOI. The Rashba-torque in FM thin-films with structural inversion asymmetry [126, 127] may be thought of as the converse of the AMR. Recently, AMR in Rashba and Dresselhaus spin-orbit splitting systems with polarized magnetic impurities has been studied theoretically by Trushin *et al.* [128]. They have shown that the Rashba SOI produces an in-plane AMR in the FM layer with the same sign as conventional non-crystalline AMR. Recently an unconventional angular dependence of AMR was discovered experimentally [120, 122] in an adjacent non-magnetic layer with strong SOI which may also arise due to Rashba SOI.

In this chapter, the structural, magnetic and magnetoresistance behaviour of polycrystalline Co thin-films with Cu and Ir overlayers are investigated using several techniques. The detailed structural analysis of thin-films using specular x-ray reflectivity are discussed to confirm the layer thicknesses and interface roughness of each layer. Magnetic characterizations of all thin-films using SQUID magnetometer at room-temperature are performed to analyze interfacial magnetic dead layer formation within the structures. Thickness dependence of resistivity and in-plane AMR are studied in polycrystalline Co thin-films with different overlayers. The chapter concludes with a discussion that shows interfacial contribution to the in-plane AMR in a single FM layer.

5.1 Structural Analysis of Cobalt Multilayers

Grazing incidence XRR measurements of polycrystalline Co thin-films with Cu and Ir overlayers for magneto-transport and magnetization dynamics experiments are performed at room-temperature to determine layer thicknesses and interface roughnesses. The structures consist of Si/SiO_2/Ta[3 nm]/Cu[3 nm]/Co[t_{Co}]/Cu or Ir[3 nm]/Ta[3 nm] with Co thicknesses ranging from 2 nm to 55 nm. All reflectivity simulations were performed by starting with the nominal structure of the as-deposited thin-films, including the thermally grown oxidized layer on the silicon substrate. To improve the quality of XRR data fitting, a thin oxide layer with a thickness up to a few nanometers was added onto the Ta capping layer (TaO_x). In the simulation model, a number of free structural parameters were required to achieve an acceptable fit.

Grazing incidence XRR data and the corresponding best-fitting simulations are presented in Fig. 5.1 for (a) Co[2.5 nm]/Ir and (b) Co[15 nm]/Ir thin-films. Here the solid lines correspond to best-fit simulated reflectivity curves calculated using `GenX` simulation code [102] for thin-films. The multi-periodic Kiessig fringes observed in the reflectivity profiles are due to the interference from x-rays reflecting off interfaces within the sample structure. For each layer the thickness and interfacial roughness parameters were obtained from the best-fitting simulations of XRR for the Cu and Ir overlayered thin-films with various Co thicknesses. Full results are provided in Appendix A.

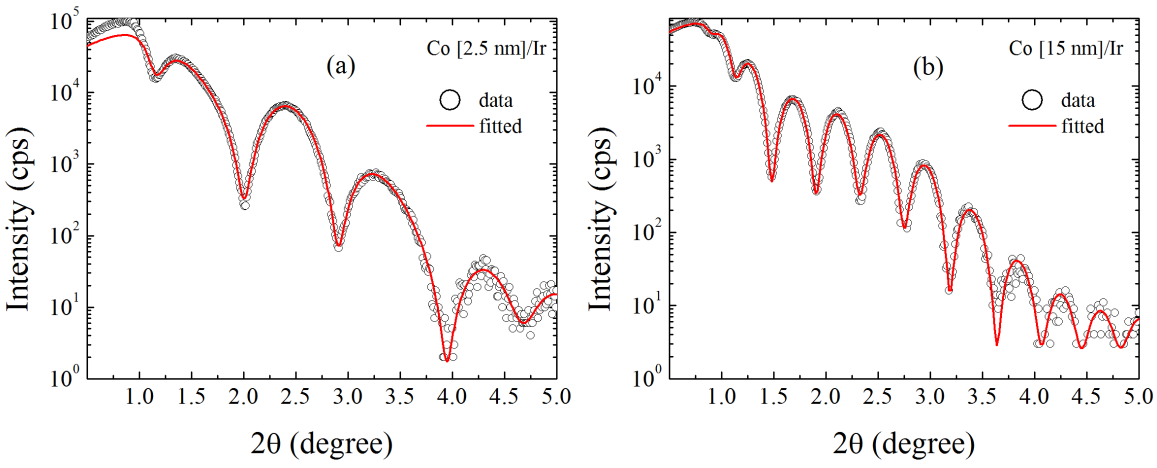

Fig. 5.1 Measured and best-fitting simulated specular reflectivity curves calculated for (a) Co[2.5 nm]/Ir and (b) Co[15 nm]/Ir thin-films. Red solid lines are best-fit simulations of thin-films.

5.2 Magnetic Properties of Cobalt Multilayers

In this section, investigation of the magnetic properties of polycrystalline Co thin-films was performed to understand and support the experimental results of magneto-transport measurements. Magnetic characterizations were performed using the SQUID magnetometer at Nottingham University. Both series of thin-films were measured and showed in-plane magnetization for the entire range of Co thicknesses.

The presence of an interfacial magnetic dead layer in FM thin-films is important for AMR studies due to loss of FM thickness. To investigate any magnetic dead layer formation in these thin-films the saturation magnetic moments per unit area of the thin-films was determined as a function of Co film thickness as shown in Fig. 5.2 (a). A linear increase in magnetic moment with Co film thickness was observed here for both structures, which is expected from a SQUID measurement because it provides a direct measure of the magnetic response of the entire structure. The intersection point between the linear fit and the Co thickness gives an estimated magnetic dead layer thickness, whereas the slope of the linear fit enables determination of the bulk saturation magnetization of the Co films. From the slopes of the fits

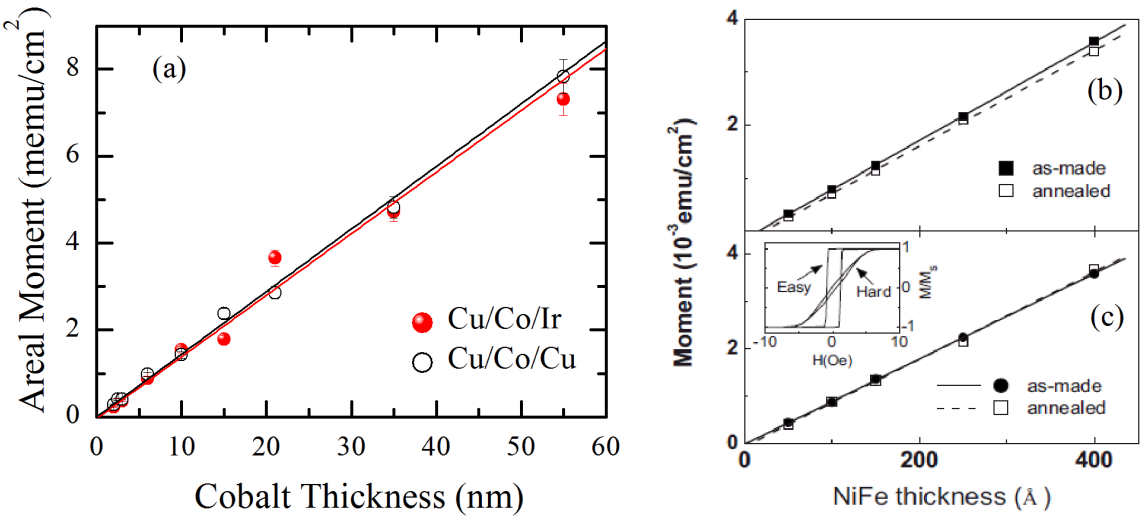

Fig. 5.2 (a) Dependence of areal magnetic moment on polycrystalline Co thickness of Cu and Ir overlayered thin-films. Black and red solid lines represent linear fits of Cu and Ir overlayered films, respectively where the slopes give saturation magnetization of Co thin-films. Both linear fits pass through the origin within experimental error, which suggests no magnetic dead layer formation through the entire Co film thickness. (b) Dependence of areal magnetic moment on NiFe thickness for films with the structures of (b) Ta/NiFe/Ta and (c) Ta/[Pt]/NiFe/[Pt]/Ta, measured by [123]. The solid lines are linear fits of the data.

presented in figure are found to be 1400 $\pm$ 100 emu/cm^3 where obtained for Cu overlayered and 1400 $\pm$ 70 emu/cm^3 for Ir overlayered thin-films, which are in good agreement with the bulk saturation magnetization of Co 1400 emu/cm^3 [129]. Also, it is shown here that both linear fits pass through the origin within experimental error which indicates no loss of magnetic moment through the structure. Thus, these zero intercepts suggesting no magnetic dead layer formation associated with interfaces between polycrystalline Co layers with Cu and Ir overlayers.

Magnetic dead layer formation also can be suppressed using Pt layers at the FM/Ta interfaces, which can contribute the enhancement of the AMR ratio. Liu *et al.* [123] showed a dead layer formed at Ta/NiFe/Ta structure with a thickness of 13 $\pm$ 2 Å, as shown in Fig. 5.2 (b). In contrast, the insertion of a thin Pt layer at NiFe/Ta interface eliminate the interfacial magnetic dead layer formation to 2 Å, which is within the experimental error, as shown in Fig. 5.2 (c). Such interfacial magnetic dead layers should affect the AMR by reducing $\Delta\rho$ due to the loss of FM volume where $\Delta\rho$ is directly related to the magnetic layer of the structure. However there is no significant change in $\rho_\perp$ which is dominated by interfacial scattering. Although this can account for the enhanced AMR ratio in Ta/[Pt]/NiFe/[Pt]/Ta structures with Pt layers inserted [123], no such magnetic dead layers are expected to form at the Co/Cu or Co/Ir interfaces here. Thin Pt layers, as studied in [122, 123], are strongly magnetically polarized by proximity exchange enhancement with an adjacent FM layer. This may potentially enhance the effective FM volume [130] and lead to hybrid proximity magnetoresistance [120]. Unlike Pt, both Cu and Ir exhibit at most only a weak oscillatory polarization, so they cannot significantly modify the total FM volume [131–134]. Neither interfacial magnetic dead layers nor proximity polarization account for the enhanced AMR in Co/Ir structure observed here.

5.3 Thickness Dependence of Resistivity

A schematic illustration of the studied thin-film structure is shown in Fig. 5.3. Polycrystalline Co thin-films with various thicknesses were deposited onto seed layers that promote strong fcc(111) and hcp(0001) texture in the Co layers for all thicknesses [87]. This isolates any interfacial contribution to AMR from effects due to variations in the film microstructure and/or texture between pairs of samples with different overlayers. Structures with overlayers of either Cu or Ir were used here to isolate the contribution to the AMR from a single designed interface. The electronic band-structure of Cu and Co are similar, hence the structures

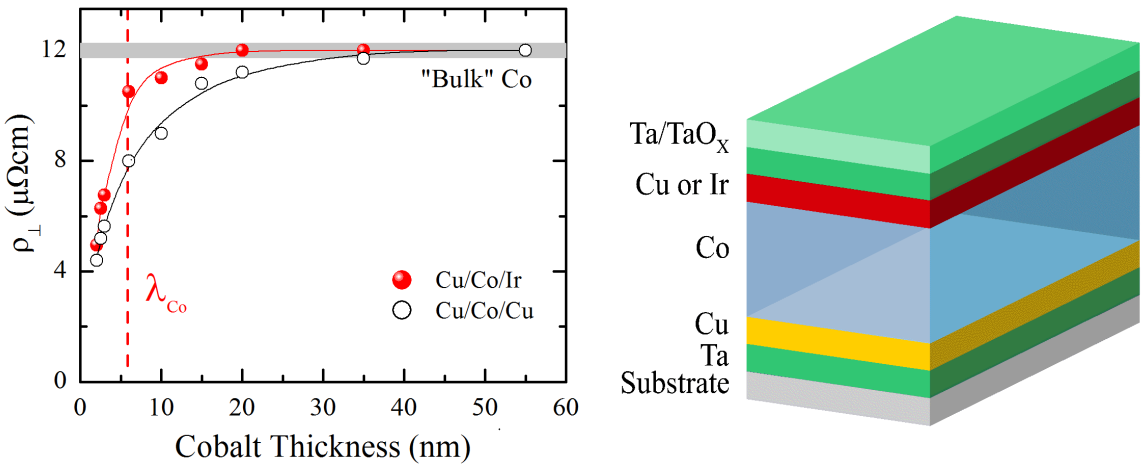

Fig. 5.3 Dependence of the transverse resistivity, $\rho_\perp$ on Co film thickness in structures with Cu and Ir overlayers. The shaded area represent the bulk resistivity of Co. The solid lines through the data are a guide to the eye. A schematic illustration of the thin-film structure is given on the right.

with Cu overlayers have electrically transparent interfaces, and with the Cu seed layers preserve structural inversion symmetry. However, the electronic band-structure of Ir and Co are different to each other. This means that Co thin-films with Ir overlayers have more electrically opaque interfaces and broken structural inversion symmetry. Also Ir has strong SOI due to its larger atomic number, which should enhance any Rashba contribution to the AMR. In the bulk limit essentially all of the current flows through the Co layer, and that as the Co thickness decreases this approximation will become less valid. These structures allow the isolation of the in-plane AMR contribution due to scattering at an electrically opaque interface using the Co/Ir interface as an illustrative model system. More details of thin-films are given in Section 3.1.2.

The Co thickness dependence of the transverse resistivity, $\rho_\perp$, for structures with Cu and Ir overlayers are shown in Fig. 5.3. Both data sets follow similar trends where the resistivity increases sharply as Co thickness increases and saturates at larger Co thicknesses. In both overlayered structures the electrical resistivity for large Co thickness corresponds to the bulk room-temperature resistivity of Co, ~ 12 $\mu\Omega$cm. This value is typical for a sputtered polycrystalline material whereas the "textbook" value for the bulk resistivity of single crystal Co is ~ 6 $\mu\Omega$cm [110]. The higher resistivity of the sputtered Co thin-films compared to bulk Co is attributed to the effect of grain boundaries, high defect density of the film, and grain size [135]. The bulk mean free path of electrons (λ) in Co layers at room-temperature is calculated using the Drude equation, Eq. 2.8, to be $\lambda_{Co} \sim 6$ nm, as

indicated in Fig. 5.3 by the dashed vertical line. At the smallest Co thickness, it is found that $\rho_\perp$ tend toward the resistivity of sputtered Cu thin-film, $\sim 2\ \mu\Omega$cm. This behavior indicates the increasing of current shunting through the Cu seed and overlayer for Cu/Co/Cu structure, where increasing thickness of Cu layer enhances the current shunting, and leads to reduction of AMR ratio [123]. In this case, the thickness of Cu layer (3 nm) is thicker than smallest Co layer (2 nm), hence current shunting is dominant. Similar case applies for Cu/Co/Ir structure where $\rho_\perp$ decreases due to current shunting through the Cu seed layer and less through Ir overlayer because Co/Ir is an opaque interface.

It is important to note that a simple parallel resistor model for individual layers in the multilayer structure cannot be used here in order to describe either the Co thickness dependence of ρ or $\Delta\rho$. This dependence of resistivity on Co thickness also makes a simple Fuchs-Sondheimer (F-S) analysis inappropriate as it offers no useful information on the interface scattering. The expressions derived by Sondheimer [41] which are most commonly-used are valid only in the limiting cases $t_{\mathrm{Co}} \ll \lambda_{\mathrm{Co}}$ and $t_{\mathrm{Co}} \gg \lambda_{\mathrm{Co}}$, but these are not the case. In perfect specular reflection on the boundaries, the resistivity is always equal to the bulk resistivity [136]. Since $\rho_\perp$ for the Ir overlayered thin-films is close to the bulk Co resistivity until $t_{\mathrm{Co}} \sim 6$ nm ($\sim \lambda_{\mathrm{Co}}$), while $\rho_\perp$ for Cu overlayered thin-films start to fall below $t_{\mathrm{Co}} \sim 30$ nm, it is suggested that such a variation in the Co thickness dependence which may indicate a higher degree of electronic specular reflection at the Co/Ir interface compared to the Co/Cu interface [136].

Fig. 5.4 presents $\rho_\perp t_{\mathrm{Co}}$ as a function of Co thickness in order to determine the bulk resistivity of the Co films with Cu and Ir overlayers, the solid straight lines are corresponding linear fits to the data. As given in Eq. 2.10, for thicker Co film limit where $t >> \lambda_0$, the Fuchs-Sondheimer expression has a dependence on inverse Co film thickness. This is the case for most of the samples, hence it is a reasonable first approximation. With that expression, it is the easiest way to show such a relationship. Both linear fits exhibit a linear dependence of $\rho_\perp t_{\mathrm{Co}}$ on Co thickness. Also, there is a non-zero intercept for both series of thin-films which may a signature of current shunting. The current flows mostly through the Co layer for most of the Co thicknesses except for the thinnest Co layer because for most of the thin-films studied the thickness of Co layer is thicker than both overlayers and underlayers of the structure. Therefore, the electrical resistance of the Co layer is lower than other layers. The slopes of the linear fits yield estimates of room-temperature values for the bulk resistivity of the Co films. Such an analysis gives values of the bulk resistivity for Co thin-films $\rho_{\mathrm{bulk}} = (12.3 \pm 0.01)\ \mu\Omega$cm with Cu overlayers and $\rho_{\mathrm{bulk}} = (12.4 \pm 0.01)\ \mu\Omega$cm with Ir overlayers, where both bulk resistivities are consistent with reported values in literature.

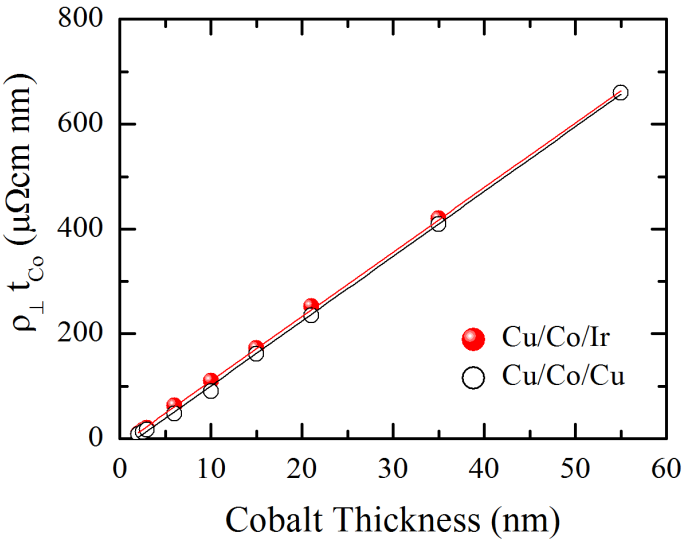

Fig. 5.4 Dependence of $\rho_{\perp} t_{Co}$ as a function of Co film thickness. The solid lines are linear fits to the data where the slopes enable to calculate the bulk resistivity of Co films with Cu and Ir overlayers.

5.4 Thickness Dependence of AMR

The variation of magnetoresistance at room-temperature is given in Fig. 5.5 with the magnetic field oriented parallel and perpendicular to the current for Co[35 nm]/Cu thin-film. The coercive field H_C, and the resistivity at H_C depend on the relative orientation of current and magnetic field. This indicates a weak magnetic anisotropy due to its low coercive field and results in an angular dependence of H_C. As shown in Fig. 5.5, the resistivity in the demagnetized state at zero external field is given by $\rho_0 = (1/3)\rho_{||} + (2/3)\rho_{\perp}$, where $\rho_0 = 13.55$ $\mu\Omega$cm. This is very close to the value of resistivity at the $H_C \sim 13.53$ $\mu\Omega$cm. There is a sharp switching behaviour in electrical resistivity, obtained in both parallel and perpendicular orientations at applied magnetic fields close to the zero. These correspond to the rotating of the effective magnetization within the Co layer until it saturates, and provides information on the coercivity of the thin-films.

The Co thickness dependence of $\Delta\rho$, the difference between longitudinal $\rho_{||}$ and transverse $\rho_{\perp}$ resistivities for Co thin-films with Cu and Ir overlayers are shown in Fig. 5.6. Here it is seen that $\Delta\rho$ exhibits a slight thickness dependence for Co films thicker than 20 nm for both series of thin-films. However, as film thickness decreases, $\Delta\rho$ falls rapidly with and tends toward zero for Co thicknesses less than 6 nm for both series of thin-films. Also, $\Delta\rho$

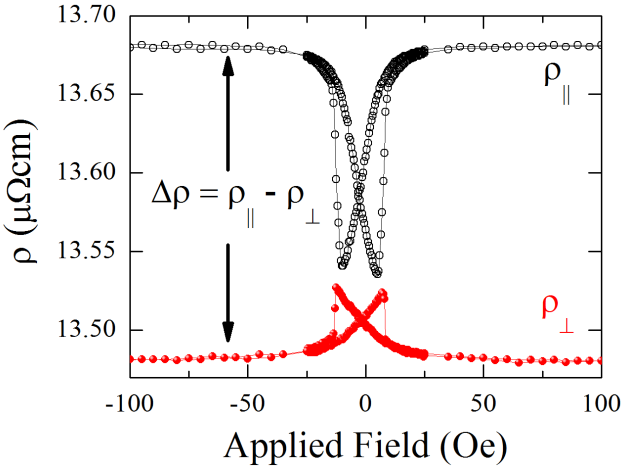

Fig. 5.5 Representative applied field dependent resistivity for Co[35 nm]/Cu thin-film. The current orthogonal to the magnetization direction results in a lower resistance ($\rho_{\perp}$, $\theta = \pi/2$), whereas a higher resistance is obtained when the current and magnetization direction are parallel to each other ($\rho_{||}$, $\theta = 0$). The differences in resistivities at magnetic saturation are labeled as $\Delta\rho$. The solid lines through the data are a guide to the eye.

remains larger for the Co/Ir thin-films than the Co/Cu thin-films with the exception of the thinnest Co thickness.

The Co thickness dependence of the AMR ratio is presented in Fig. 5.7 for both thin-film series. The AMR ratio for films with the largest Co thickness corresponds to the "bulk" Co AMR [122], and indicated by the shaded region. Similar to the thickness dependence of $\Delta\rho$,

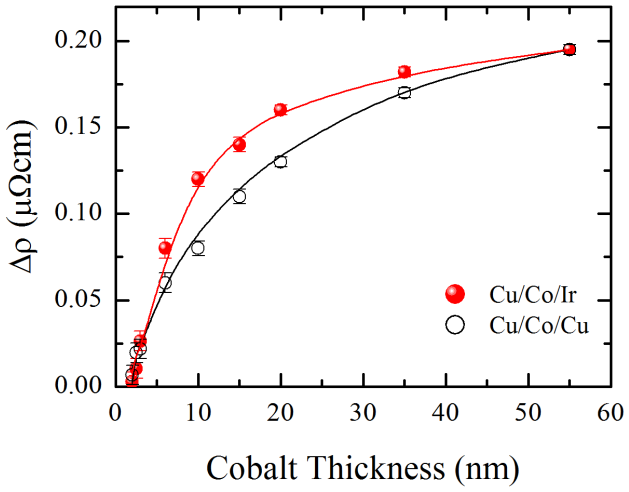

Fig. 5.6 Dependence of the resistivity change, $\Delta\rho = \rho_{||} - \rho_{\perp}$ on Co film thickness in structures with Cu and Ir overlayers. The error-bars are smaller than the data markers. The solid lines through the data are a guide to the eye.

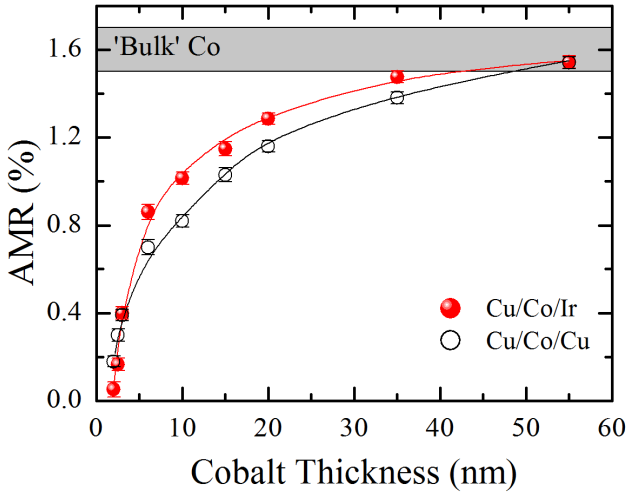

Fig. 5.7 Dependence of the AMR ratio, $\Delta\rho/\rho_{\perp}$, on Co film thickness in structures with Cu and Ir overlayers where AMR ratio for "bulk" Co is indicated at top. The error-bars are smaller than the data markers. The solid lines through the data are a guide to the eye.

the AMR ratio reduces as the Co film thickness decreases. It is also important to note that the divergence from the bulk values for both AMR and $\Delta\rho$ start at the same Co thicknesses. However, this divergence starts at different Co thickness for the case of $\rho_{\perp}$, as shown in Fig. 5.3. This suggests that the Co thickness dependence of the AMR is related to $\Delta\rho$, instead of $\rho_{\perp}$, as noted by [46, 47].

The standard explanation for the reduction in AMR is that the resistivity increases at low film thickness due to F-S boundary scattering [40, 41], but $\Delta\rho$ being independent of FM film thickness (bulk scattering) [43], as shown in Fig. 5.8 (a). In contrast to this explanation, it is also shown that $\Delta\rho$ actually depends on FM film thickness where there is a very strong trend toward zero for NiFe films [46], as shown in Fig. 5.8 (b). The mechanism for the film thickness dependence of the AMR, in particular the thickness dependence of $\Delta\rho$, remains unknown. In a recent article, it is shown that in some single-film systems this may be related to an enhanced spin-flip magnon scattering in ultra thin-films [47]. The decrease in both $\Delta\rho$ and the AMR ratio with decreasing FM film thickness is seen in single films [46, 47] and multilayers [123], and is not entirely due to current shunting through under/overlayers at smaller FM thicknesses [124], contrary to the suggestion in [122].

A recent study of AMR enhancement in Ta/[Pt]/NiFe/[Pt]/Ta multilayers has been suggested by Liu *et al.* [123] as shown in Fig. 5.9. They observed that the insertion of 1.5 nm thin Pt layers at the Ta/NiFe/Ta interfaces causes a significant enhancement of the AMR ratio. This study is similar to that shown here for Co/Ir thin-films in Fig. 5.7. They attribute this large AMR ratio enhancement for thin NiFe films to strong electron spin-orbit scattering

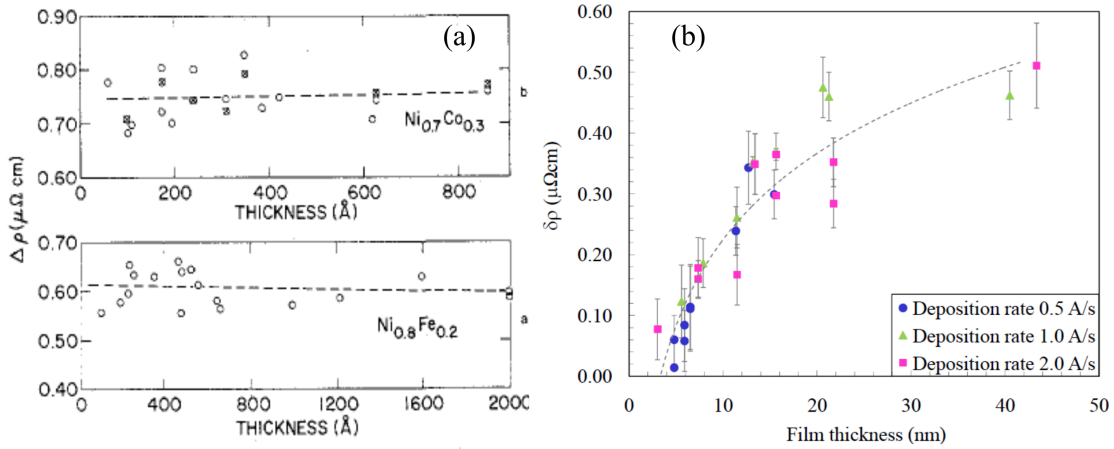

Fig. 5.8 (a) Dependence of $\Delta\rho$ on film thickness for $Ni_{70}Co_{30}$ and $Ni_{80}Fe_{20}$, measured by [43]. Here $\Delta\rho$ is constant with decreasing FM film thickness. (b) Dependence of $\Delta\rho$ on $Ni_{81}Fe_{19}$ film thickness, measured by [46]. The dashed line is a guide to the eye.

at NiFe/Pt interfaces. Unlike any proximity induced polarization for Ta/[Pt]/NiFe/[Pt]/Ta multilayers, it was confirmed that there is no proximity polarization in Cu or Ir layers using SQUID magnetometry. This is essential in order to isolate any interfacial contributions to AMR. However, their study did not include NiFe thin-films below 5 nm. Here, an advantage is that the insertion of Ir layer only above the Co layer causes no microstructural modification, unlike the insertion of a Pt layer below NiFe [123]. The in-plane AMR in a single FM ultra-thin-film may have a previously unconsidered interfacial contribution, as a result of anisotropic interface scattering and/or interfacial SOI.

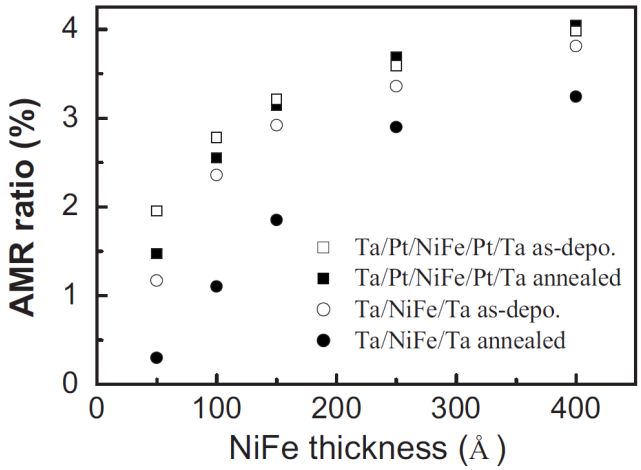

Fig. 5.9 Dependence of AMR ratio on NiFe film thickness for films with the structures of Ta/NiFe/Ta and Ta/[Pt]/NiFe/[Pt]/Ta before and after annealing, measured by Liu *et al.* [123].

The variation of the thin-film resistivity and AMR as a function of thickness are calculated theoretically by Dieny *et al.* [136], as given in Fig. 5.10 for various specularity parameters p. As shown in Fig. 5.10 (a), the thin-film resistivity is equal to the bulk resistivity for perfect specular reflection ($p = 1$) on surface boundaries. When the specular reflection coefficient decreases, the thickness dependent resistivity is more important due to diffuse scattering on outer boundaries, hence thinner films have larger increase on resistivity. Boltzmann transport analysis with non-specular interface scattering, where the AMR is included via an anisotropic bulk mean free path, suggests that $\Delta\rho$ diverges with decreasing thin-film thickness. However, this divergence is slower than that of ρ, resulting in the observed reduction in AMR at low film thickness [136]. Neither of these suggested explanations for the thickness dependence of AMR can apply in the present case where ρ and $\Delta\rho$ can not diverge, due to current shunting. However, AMR still reduces with decreasing Co film thickness in a similar fashion to other observations. A new description is required in order to explain the thickness dependence of the AMR. Here, this data shows that the AMR ratio in the ultra thin-film limit is determined predominantly by the thickness-dependence of $\Delta\rho$ rather than $\rho_\perp$ (or ρ_0).

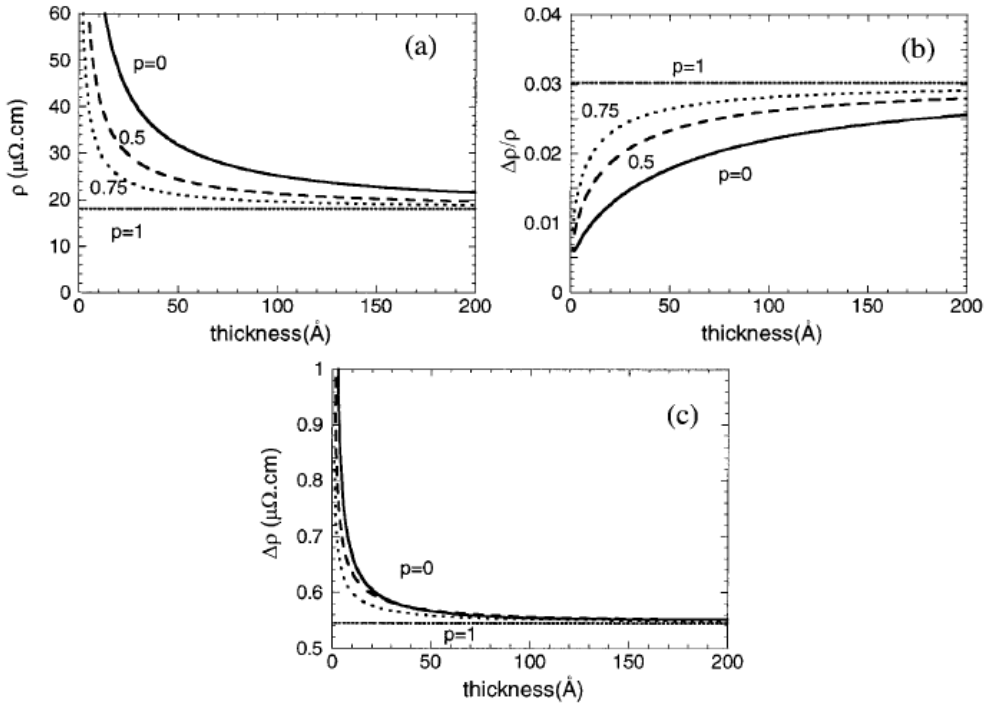

Fig. 5.10 (a) Theoretical calculation of the resistivity and AMR expressed in terms of (b) relative change or (c) absolute change of resistivity as a function of film thickness for various values of specular reflection coefficients on outer boundaries. Adapted from [136].

Within this investigation, the thin-film resistivities of polycrystalline Co thin-films for perpendicular orientation of current and magnetization, the resistivity change and the AMR ratio are summarized in Table 5.1 for Co thin-films with Cu and Ir overlayers.

Table 5.1 Transverse $\rho_\perp$ resistivity, the resistivity change $\Delta\rho$ and AMR ratio for polycrystalline Co thin-films with Cu and Ir overlayers.

Overlayer	t_{Co} (nm)	$\rho_\perp$ ($\mu\Omega$cm)	$\Delta\rho$ ($\mu\Omega$cm)	AMR Ratio (%)
Cu	2	4.39 ± 0.04	0.01 ± 0.002	0.18 ± 0.03
	2.5	5.19 ± 0.04	0.02 ± 0.003	0.31 ± 0.03
	3	5.63 ± 0.04	0.02 ± 0.005	0.39 ± 0.02
	6	8.10 ± 0.04	0.06 ± 0.003	0.66 ± 0.03
	10	9.10 ± 0.03	0.08 ± 0.002	0.85 ± 0.04
	15	10.80 ± 0.03	0.11 ± 0.004	1.04 ± 0.03
	21	11.20 ± 0.02	0.13 ± 0.004	1.20 ± 0.02
	35	11.80 ± 0.02	0.17 ± 0.005	1.40 ± 0.02
	55	12.00 ± 0.02	0.20 ± 0.003	1.55 ± 0.03

Overlayer	t_{Co} (nm)	$\rho_\perp$ ($\mu\Omega$cm)	$\Delta\rho$ ($\mu\Omega$cm)	AMR Ratio (%)
Ir	2	4.95 ± 0.09	0.01 ± 0.003	0.06 ± 0.01
	2.5	6.27 ± 0.09	0.01 ± 0.004	0.23 ± 0.03
	3	6.76 ± 0.09	0.03 ± 0.004	0.39 ± 0.03
	6	10.50 ± 0.09	0.08 ± 0.005	0.86 ± 0.04
	10	11.00 ± 0.07	0.12 ± 0.003	1.05 ± 0.03
	15	11.50 ± 0.06	0.14 ± 0.004	1.20 ± 0.03
	21	12.00 ± 0.05	0.16 ± 0.005	1.30 ± 0.02
	35	12.00 ± 0.04	0.18 ± 0.003	1.48 ± 0.03
	55	12.00 ± 0.04	0.20 ± 0.004	1.55 ± 0.02

5.5 Interfacial Contribution to AMR

To understand the interfacial contribution to the AMR the inverse Co thickness dependence of $\Delta\rho$ and the AMR ratio is plotted as shown in Fig. 5.11 for both thin-film series. These plots are commonly used in studies of interfacial contributions to magnetic anisotropy and magnetostriction [91, 138, 139]. The effective magnetocrystalline anisotropy K_{eff} in FM thin-films includes contributions from volume magnetocrystalline anisotropy, K_{vol}, and a contribution from the interfaces K_{int} which may arise in thin-films from the strain or SOI at the interface. The relation between these two anisotropy contributions can be written as;

$$K_{\text{eff}} = K_{\text{vol}} + K_{\text{int}}/t_{\text{FM}} \tag{5.1}$$

where t_{FM} is the FM film thickness. The magnetocrystalline anisotropy is dominated by the volume component in bulk systems. However, the interface term can become more important in thin-films when the film thickness becomes thinner, $t_{\text{FM}} \sim 2K_{\text{int}}/K_{\text{vol}}$. The reorientation of the magnetization from the sample plane to the normal is observed when the FM film thickness falls below a critical FM thickness t_{critical}. In this case the interfacial component, K_{int} has an opposite sign to the volume component, K_{vol}, where they cancel each other and resulting in a perpendicularly magnetized system. Such behaviour is found for perpendicular magnetic anisotropy where interface and volume terms cancel each other at a critical FM thickness of $\sim$ 1.3 nm [140].

The inverse Co thickness dependence of (a) $\Delta\rho$ and (b) AMR ratio are shown in Fig. 5.11 for both thin-film series. Interfacial effects show linear dependence on inverse thin-film thickness, as seen in Eq. 5.1. There are non-linear dependences of both $\Delta\rho$ and AMR on inverse film thickness for Co/Cu thin-films in comparison to Co/Ir thin-films. This non-linearity suggests that scattering at the Co/Cu interface does not play a dominant role in determining the Co thickness dependence. Current shunting dominates at the Co/Cu interface due to the transparency of the interfaces to the majority *s*-like states which primarily contribute to electrical conduction. Thin-films with Ir overlayer have a lower interface transparency for conducting states at the Co/Ir interface, and effect of current shunting on AMR reduces, hence AMR appears larger in these thin-films.

The exact contribution to the AMR of a single interface is difficult to determine experimentally. Systems can be designed with one dominant interface for studies of magnetic anisotropy [33, 86]. The thin-films with Ir overlayer (Cu/Co/Ir structure) provide an comparable system to determine a single dominant interfacial contribution to AMR. Any contribution

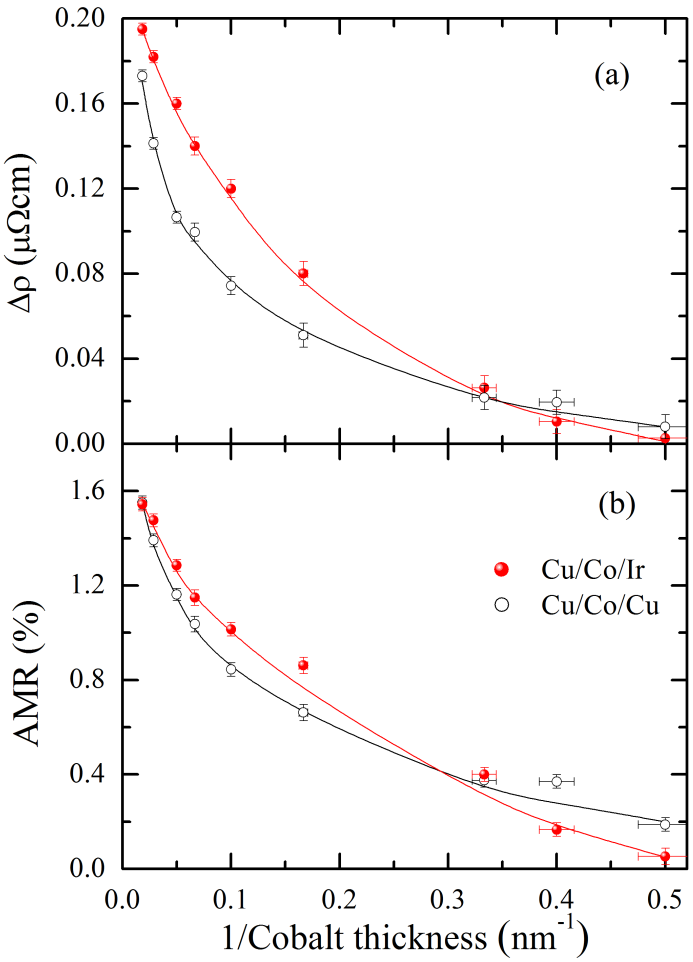

Fig. 5.11 Inverse Co thickness dependence of (a) $\Delta\rho$ and (b) AMR ratio for Co films with Cu and Ir overlayers. The solid lines through the data are a guide to the eye.

due to scattering at the Co/Cu interface or the current-shunting effect of the Cu seed layer must be accounted for to demonstrate the interfacial contribution. As shown in Fig. 5.12. this is done by effectively dividing the symmetric Cu/Co/Cu structure into two "half-structures" with Ta/Cu seed and Cu/Ta overlayers and equal Co thickness, as Ta/Cu/Co(t_{Co}/2) and Co(t_{Co}/2)/Cu/Ta. Then only one of these half-structures is considered with a single transparent Co/Cu interface. The data in Fig. 5.11 are analyzed using this approach in order to obtain $\rho_{\perp}$ and $\rho_{||}$ for these Cu overlayered half-structures using a simple parallel resistor model for the sheet resistances, $R_{\square\perp}$ and $R_{\square||}$. This approach is also applied for the asymmetric Ir overlayered structure by dividing into two "half-structures" which consist of one of the Ta/Cu/Co(t_{Co}/2) half-structure which is the same half-structure of Co/Cu thin-films, and a Co(t_{Co}/2)/Cu/Ta half-structure, as shown in Fig. 5.12. Using the parallel resistor model the AMR for half-structures containing a single Co/Ir interface is obtained by removing

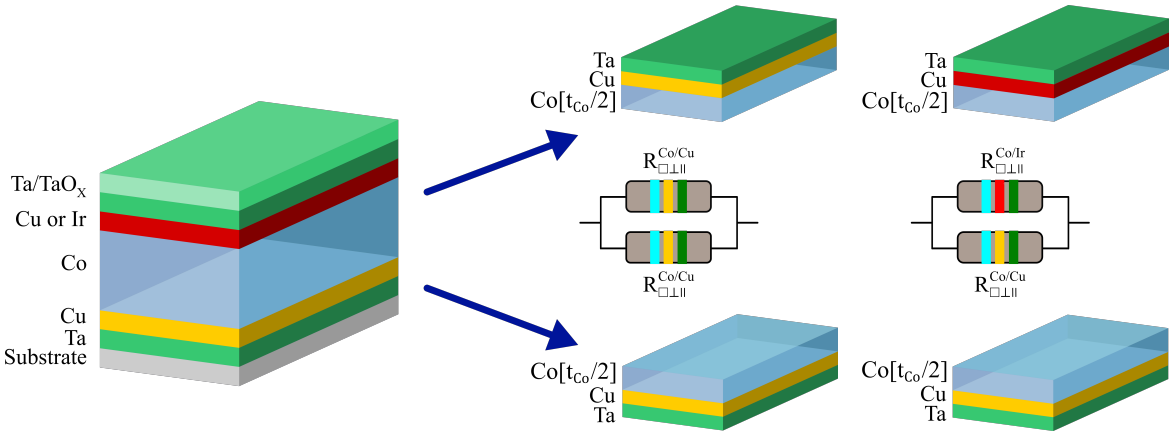

Fig. 5.12 A schematic view of the thin-film structure and measurement geometry. A schematic of Co/Cu and Co/Ir 'half-structures' are given with the corresponding parallel resistor models to extract the interfacial contribution to the AMR from Co/Ir interface.

the contribution of the Co/Cu "half-structure". This is equivalent to setting the Co/vacuum interface as specularly reflecting within the F-S type model [136]. Note that this approach does not consider differences in current distribution in the Co layer between Cu and Ir overlayered structures, which will differ increasingly as the Co film thickness decreases. More complex calculations within a F-S type model for such trilayers [122] do not yield physically meaningful results, since the F-S model for a single layer considering only bulk scattering anisotropy predicts the opposite behavior of $\Delta\rho$ to that found experimentally [136].

The inverse Co "half-film" thickness dependence of the AMR is shown in Fig. 5.13 (a) for Co/Ir "half-structures". There is a linear dependence on inverse Co "half-film" thickness which indicates an interfacial contribution to anisotropic scattering. This suggests that the interfacial scattering anisotropy for the interface is opposite to that of the volume contribution. This simple model breaks down for the lowest Co thickness due to current-shunting through the Cu seed and overlayers. The linear fit to the data, excluding the structure with 2 nm Co thickness, defines an approximate Co "half-film" thickness, $t_{Co}/2 = (1.2 \pm 0.02)$ nm, where the Co/Ir interfacial contribution to anisotropic scattering may be expected to cancel the Co volume contribution. This simple analysis provides an explanation for the interfacial contribution to the Co thickness dependence of the in-plane AMR which is a result not only of bulk anisotropic scattering, but also contains anisotropic interface scattering contributions. As the film thickness decreases the anisotropic interface scattering term becomes increasingly important until, at some critical thickness, $\Delta\rho$ and the AMR ratio vanish. Here, it is suggested that such interface scattering may prevent the divergence of $\Delta\rho$ at low thickness.

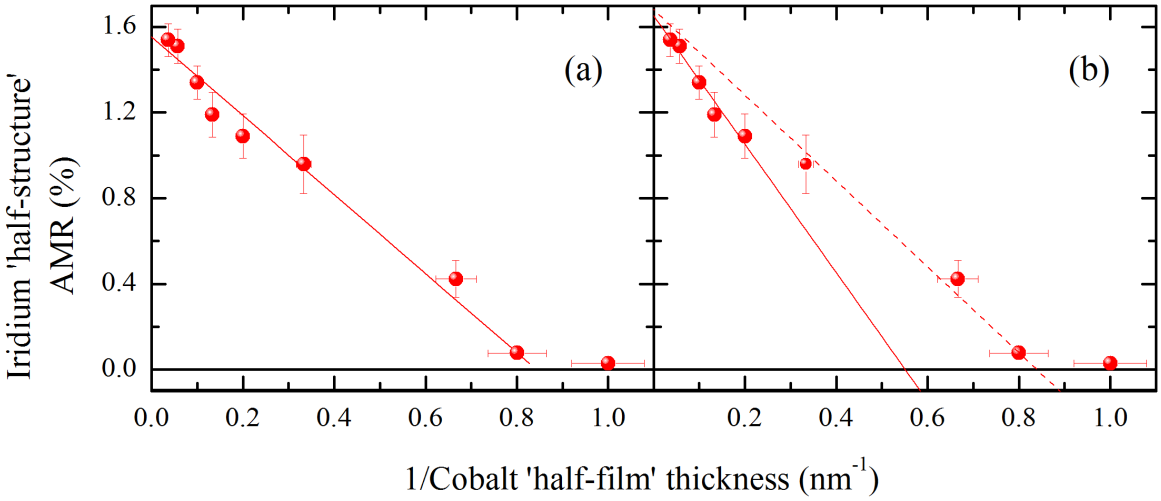

Fig. 5.13 (a) Inverse Co thickness dependence of AMR for a Co/Ir "half-structure" extracted from the parallel resistor model. The solid line is a fit excluding the sample with thinnest Co layer. The "characteristic" thickness for which volume and interfacial scattering terms may cancel falls within the region $t_{Co}/2 = (1.2 \pm 0.02)$ nm. (b) The same data for different thickness regimes. The solid line is a fit for $t_{Co} > 6$ nm, corresponding to hcp(0001) Co, and the dashed line is a fit excluding the sample with thinnest Co layer for $t_{Co} \leq 6$ nm, corresponding to fcc(111) Co.

Crystal structure of Co thin-films were studied in Section 7.1 using x-ray diffraction in order to observe the structural phase transition from fcc(111) to hcp(0001)-dominated structures as Co film thickness increases. To understand whether this interfacial contribution to AMR is interfacial structure dependent or not, Fig. 5.13 (a) is divided into two thickness regimes as fcc(111) Co and hcp(0001) Co, and fitted independently as shown in Fig. 5.13 (b). The solid line is a linear fit for Co thicknesses above 6 nm which corresponds to hcp(0001) Co, and the dashed line is a linear fit for Co thicknesses under 6 nm. This model again breaks down for the thinnest Co thickness, hence it was excluded from the fit.

The reliability of this fitting procedure is investigated by normalized residual analysis by combination of horizontal and vertical residuals. This analysis involves taking the difference between the measured value and the corresponding observed data points, and dividing by the each error bar. A good fit can be characterized by randomly distributed residuals. The residual analysis of Fig. 5.13 (a) and (b) are performed and shown in Fig. 5.14 to compare linear fits to the data for (a) entire thickness and (b-c) different thickness regimes. The dashed lines above and below the data indicate highest and lowest residuals. This analysis reveals that the residuals in Fig. 5.14 (b) and (c) are between the dashed lines and they behave similar to the residuals for entire Co thickness range. This analysis suggest that dividing Co

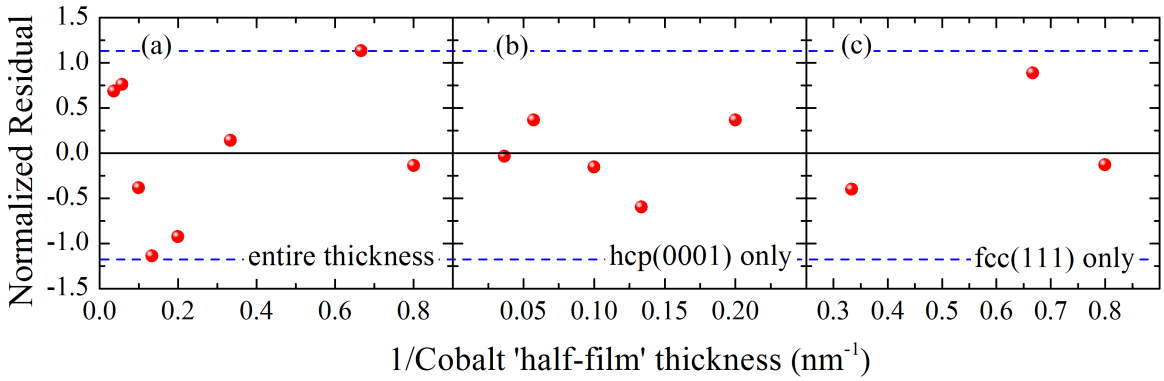

Fig. 5.14 Normalized residual analysis of Ir half-structure AMR as a function of inverse Co film thickness for (a) linear fits through entire Co thickness range, (b) linear fits for $t_{Co} > 6$ nm, and (c) linear fits for $t_{Co} \leq 6$ nm. This analysis does not include thinnest Co layer. The dashed lines above and below the data shows highest and lowest residual points.

thickness into two regimes and fitting them independently provides no significant benefit to define interfacial contribution to AMR for Co/Ir structure. However, the FMR data with the same thin-film series are analyzed with different thickness regimes in Chapter 7, but a more strong linear dependencies is obtained for each structural phase.

The Co/Cu interfacial transparency introduces a current-shunting contribution, producing a more rapid decrease in AMR with decreasing Co thickness for Co/Cu structures. The interfacial contribution to anisotropic scattering in the Cu/Co/Ir structure is made apparent by considering only the Co/Ir interface. The more electrically opaque Co/Ir interface behaves more like a film/vacuum interface (boundary) and does not result in significant current shunting. This strongly reflecting, electrically opaque, interface allows to show a previously unconsidered interface scattering contribution, which acts to diminish AMR as FM film thickness is reduced. The detailed origin of this anisotropic interface scattering is still unknown.

As a result of anisotropic interface scattering, the AMR may vanish at a critical FM film thickness, ~ 2.4 nm for the Co/Ir material system. Spin-polarized electrical transport is investigated in NiFe thin-films where the polarization extrapolates to zero at a film thickness ~ 2.3 nm [141]. Maintaining a high AMR ratio at low film thickness requires opaque interfaces to prevent current shunting and a materials combination which suppresses interfacial magnetic dead layer formation. The interfacial scattering contribution to the AMR presents a fundamental physical limit to scalability as, even under these conditions, the AMR diminishes as film thickness decreases.

5.6 Chapter Conclusion

The structural, magnetic and magnetoresistive behaviour of polycrystalline Co thin-films with Cu and Ir overlayers were investigated in this chapter using several techniques. Each layer thickness and interface roughness was determined using specular x-ray reflectivity analysis. Magnetic characterization was performed using SQUID magnetometry at room-temperature, where Co thin-films showed in-plane magnetization for the entire range of thickness studied. To determine any magnetic dead layer formations in these thin-films, the saturation magnetic moments per unit area of Cu and Ir overlayered thin-films with respect to Co film thickness was studied. The slopes of the linear fits which give bulk saturation magnetization, were extracted for both structures and these values were in good agreement with the bulk saturation magnetization of Co in literature. Both linear fits pass through the origin, indicating no magnetic dead layer formation present within the structures.

Electrical resistivity measurements of Co thin-films were studied for orientations of the structures with respect to the applied magnetic field where in-plane AMR are shown in Co thin-films. The AMR was observed to be dependent upon on Co film thickness and tends toward zero for thicknesses below 6 nm. The AMR decreases with decreasing of Co thickness, and the AMR with Ir overlayers is greater than with Cu overlayers due to interfacial conduction transparency. This decrease becomes steeper for thin Co films and it saturates to about 1.5 % for the thickest of Co films studied. The bulk resistivity of Co is found using the linear fit to be $\sim 12\ \mu\Omega$cm for both structures.

A simple model was used here in order to try to extract the contribution to the AMR from a single Co/Ir interface. The AMR ratio was shown to vary inversely proportional to the Co film thickness with a Co/Ir interface. This is an indication that the in-plane AMR is a consequence of anisotropic scattering with both volume and interfacial contributions. The interface scattering anisotropy opposes the volume scattering contribution, causing the AMR ratio to diminish as the Co film thickness is reduced. An intrinsic anisotropic interface scattering effect explains the significantly reduced AMR ratio in ultra thin-film thin-films; the explanation for which has remained a significant problem in understanding the electrical properties of magnetic thin-films. Also, the interfacial contribution to the AMR was analyzed for each thickness regimes and corresponding residual analyses are performed where the residuals in fcc(111) and hcp(0001) Co are very similar to the residuals for the entire Co thickness range.

6

Temperature Dependence of Magnetic Dead Layers in CoFeB:Ta Thin-Films

In the development of spintronic systems, ferromagnetic (FM) materials such as CoFeB thin-films have been widely used in a range of studies including tunneling magnetoresistance [142], current induced magnetization switching [143], and in commercial applications such as hard disk read heads and magnetic random access memories [144]. There have been several previous reports of CoFeB, CoFe, and Fe thin-films which provide evidence for a magnetically dead layer (MDL) at the interfaces in thin-films of a few monolayers thick [34, 145–147]. This dead-region may form during the deposition processes due to interfacial diffusion of target atoms into the substrate which causes the magnetic moment loss in the FM layer over a distance of the order of a few monolayers. An important point is that in these studies the MDL is inferred from magnetometry data, rather than being true magnetization depth profiles. The formation of these MDLs and their thickness depend on several parameters including the FM material, deposition conditions, and the material interface [28]. It is important to understand the formation of MDL in the thin-film structure as the MDL modifies not only the magnetic volume but also the magnetic anisotropy [34]. Also, as the dimensions of spintronic devices become smaller such effects become more important.

Interfacial effects influence the magnetic properties of magnetic thin-films; hence, MDLs have consequences for spintronic systems which depend on interfacial magnetism, such as

magnetic tunnel junctions and spin-injection devices [32, 33]. The anisotropy and thermal activation energies are reduced when the magnetic volume decreases, which causes thermal stability issues that are known to affect the performance of spintronic devices [34, 148].

FM thin-films deposited on III-V semiconductor (SC) wafer substrates, such as Fe/GaAs, have potential applications in hybrid spintronics, which is the combination of the functionalities of FM metals and SC devices [149, 150]. This requires efficient spin-polarized current injection from the FM layer into the SC substrate. Interfaces between FM metals and SC substrates generally feature intermixing resulting from the FM thin-film deposition [151, 152]. This frequently results in interfacial MDLs that act to prevent efficiency of spin-injection.

Finally, there is no information in literature about temperature dependence of these MDL thickness in a FM thin-film. As many spintronic devices work at elevated temperatures, understanding how temperature may influence MDLs becomes a crucial issue. The T_C of the FM materials used in spintronics devices are generally above 700 °C, it is not possible to investigate MDL formations at these temperatures corresponding to an appreciable fraction of T_C without promoting significant interdiffusion in the delicate thin-film structures.

In this chapter, the structural and magnetic properties of amorphous CoFeB:Ta thin-films deposited on Si/SiO_2 and GaAs(001) were investigated using several techniques. The amorphous CoFeB:Ta alloy used in this study was designed to have a T_C below room-temperature in order that the temperature dependence of the MDL thickness could be easily studied without causing further interfacial diffusion. The structural investigations of thin-films using specular x-ray reflectivity (XRR) and polarized neutron reflectometry (PNR) are discussed to confirm the layer thicknesses and interface roughnesses. Temperature dependent magnetic characterizations of amorphous CoFeB:Ta thin-films were performed in order to extract T_C of both thin-film structures, which suggest a slight compositional variation between those structures. PNR has been used to study interface magnetism and MDLs in amorphous CoFeB:Ta thin-films with T_C below room-temperature. The magnetization depth profiles of the thin-films were obtained by consistently fitting the low-temperature neutron reflectivities using the structural parameters obtained from room-temperature PNR and XRR. During fitting of low-temperature reflectivities, only the magnetic parameters were allowed to vary as a function of measurement temperature.

6.1 Structural Analysis of CoFeB:Ta Thin-Films

An investigation of the structural properties of 10 nm amorphous CoFeB:Ta thin-films deposited on Si/SiO_2 and GaAs(001) wafer substrates is presented based on room-temperature measurements using a Rigaku Smartlab reflectometer, as described in Section 3.3.2, in order to determine layer thicknesses and interface roughnesses. All reflectivity measurements were interpreted by fitting the measured specular reflectivity data using the `GenX` simulation code [102] which utilizes the Parratt recursion formula for simulating specular reflectivity.

The structure of the layer stacks was Si/SiO_2/CoFeB:Ta(10 nm)/Ta(3 nm)/TaO_x and GaAs(001)/CoFeB:Ta(10 nm)/Ta(3 nm)/TaO_x. X-ray reflectivity scans were performed by scanning θ - 2θ from 0° to 5° with a step size of 0.02°. All reflectivity simulations were performed by starting with nominal thicknesses of each layer of the as-deposited thin-films, and adding a thin tantalum oxide layer to model oxide formation on the Ta cap, with a thickness up to a few nanometers. A thermally oxidized SiO_2 layer on the Si substrate was also added to give a better description of the measured data. This procedure improved fitting quality of the XRR data and gave a lower figure of merit which provides an estimate of the goodness of the simulation fit [102].

Measured grazing incidence XRR and the corresponding best fit simulations for 10 nm CoFeB:Ta thin-films are presented in Fig. 6.1. Here, red and blue solid lines represent simulated fits of specular reflectivity data for structures on (a) Si/SiO_2 and (b) GaAs(001)

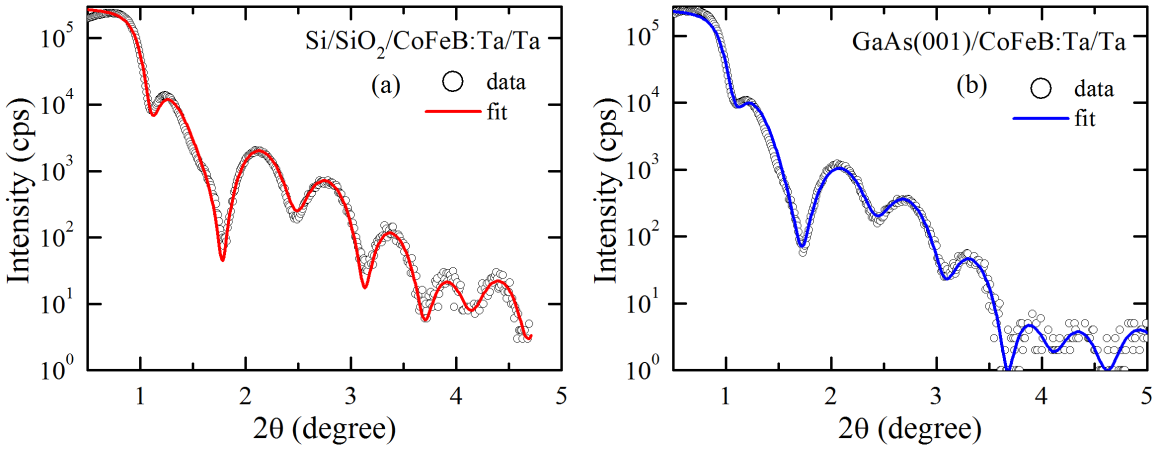

Fig. 6.1 Specular reflectivity data and corresponding simulated reflectivity calculated using `GenX` simulation software for amorphous 10 nm CoFeB:Ta thin-films deposited on (a) Si/SiO_2 and (b) GaAs(001) substrates. Red and blue solid lines represent best-fit simulations for structures on Si/SiO_2 and GaAs(001) substrates, respectively.

substrates, respectively. The layer thicknesses and roughnesses from these simulations of the XRR are summarized in Appendix A. As shown in the figure, the position of the critical angle appears at the same angle of around 0.7°, which suggests that x-rays penetrate inside the material beyond this angle for both structures. The reflectivities of the first dip in both XRR occur at the similar intensity, $\sim$ 100 cps. This suggests x-rays reach the CoFeB:Ta layer at similar intensities for both structures. The decay in the reflectivity is determined by the roughness of the interfaces. For rough interfaces the reflectivity drops faster than for sharp interfaces [112]. Here, the reflectivity dies off sharply for CoFeB:Ta thin-film on GaAs(001) due to interface roughness. The number of Kiessig fringes increases with increasing thin-film thickness. There are equal number of fringes, which suggests the layer thicknesses are nearly identical.

6.2 Magnetic Properties of CoFeB:Ta Thin-Films

In this section, temperature dependent magnetic characterization of amorphous CoFeB:Ta thin-films, as introduced in Section 3.1.3, deposited on Si/SiO_2 and GaAs(001) substrates were performed in order to extract T_C for both structures. The magnetic response of CoFeB:Ta thin-films were measured at Durham, and at ISIS R53 Materials Characterization Laboratory. Thin-films were loaded and initially field cooled at 200 Oe to 5 K in order to put CoFeB:Ta thin-films in a saturated magnetic state for temperature dependent magnetization measurements. Then, they were left at 5 K around 10 minutes to allow the temperature of the thin-films to stabilize within the sample space. Temperature scans were performed from 5 K to 150 K at 100 Oe applied field, where an estimate of T_C was extracted from these scans. Then, a number of hysteresis loops were recorded around T_C. The magnetic response is independent of the orientation of the samples within the SQUID coil for CoFeB:Ta thin-film deposited on Si/SiO_2. However, for structures on GaAs substrates, two magnetization measurements were performed with the applied field oriented along the easy and hard axes.

The temperature, (a) and (c), and applied magnetic field dependent (b) and (d) magnetization measurements for CoFeB:Ta thin-films are presented in Fig. 6.2 using SQUID magnetometry in the temperature range from 5 K to 150 K. The hysteresis data spans the critical region which bounds the steep decrease in magnetic response. In the hysteresis data it can be seen clearly that CoFeB:Ta thin-films experience a phase transition through T_C, where it saturates to a large magnetization below T_C and exhibits a weaker paramagnetic response above T_C. The temperature dependent magnetization $M(T)$ of a FM material can be fitted at

low-temperatures, up to around $T_C/3$ using the spin-wave model and follows the Bloch $T^{3/2}$ power law;

$$M(T) = M(0)\left[1 - \left(\frac{T}{T_C}\right)^{3/2}\right] \tag{6.1}$$

where the solid line through the data is a fit to this equation, and $M(0)$ is the spontaneous magnetization at zero temperature. T_C values are estimated from the fit of the experimental data as $T_C \sim 110$ K, and $T_C \sim 90$ K for CoFeB:Ta films on Si/SiO_2 and GaAs(001) substrates, respectively. As explained in Section 3.1.3, doping of Ta to CoFeB during co-sputtering

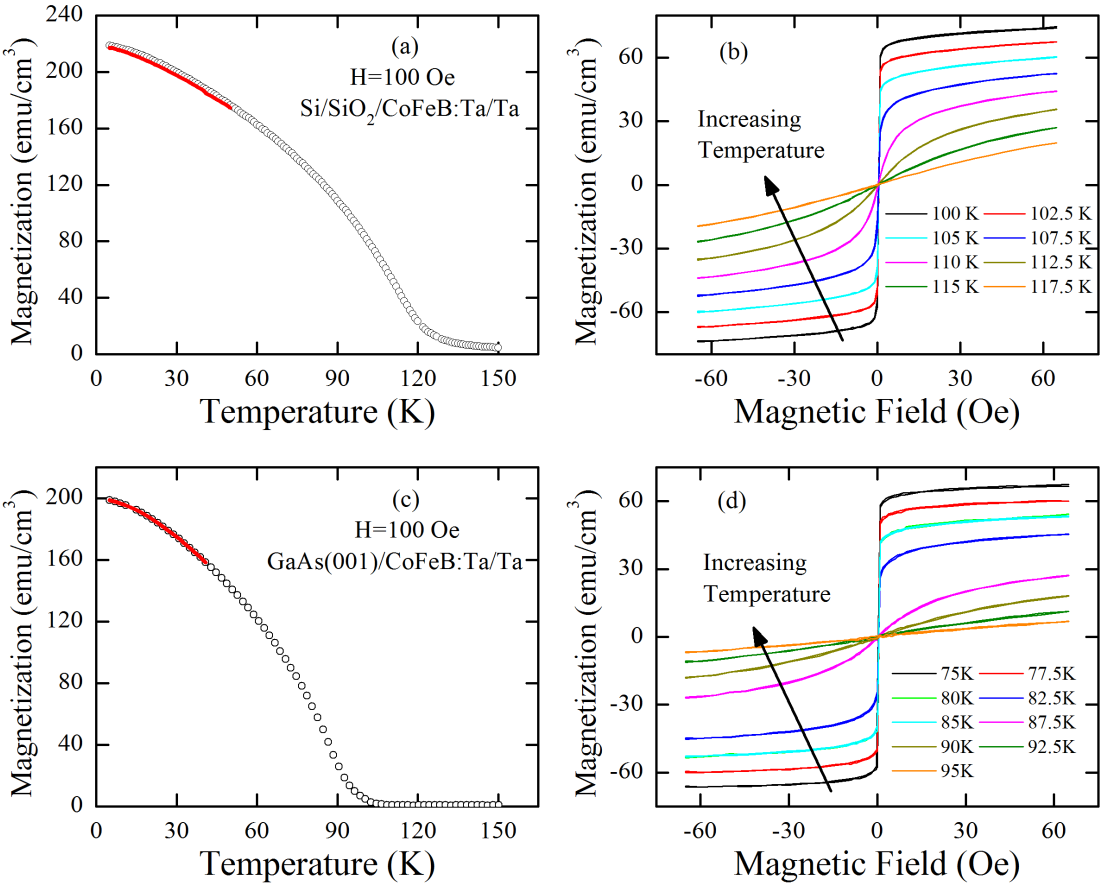

Fig. 6.2 Temperature dependent magnetization of 10 nm CoFeB:Ta thin-film on (a) Si/SiO_2 and (c) GaAs(001) substrates measured in a 100 Oe applied field. The solid lines are the fit curve according to Eq. 6.1. (b) Hysteresis loops between 100 K - 117.5 K for CoFeB:Ta thin-film on Si/SiO_2. (d) Hysteresis loops between 75 K - 95 K for CoFeB:Ta thin-film on GaAs(001) measured in a 100 Oe applied field oriented along the easy axis. The apparent lack or remanence is due to the very small coercivity and magnetic field step resolution of the SQUID. The magnetometry data was collected from [93].

dilutes the local magnetization and reduces the local T_C [92]. The difference in T_C for both thin-film structures is attributed here to a slight sample-to-sample compositional variation in the co-deposition process between those films.

6.3 PNR Measurements of CoFeB:Ta Thin-Films

This section describes the depth dependence of the magnetic structure of CoFeB:Ta thin-films deposited on Si/SiO_2 and GaAs(001) substrates at different measurement temperatures using CRISP reflectometer at the ISIS spallation neutron source, as described in Section 3.4.2. The amorphous CoFeB:Ta alloy which has a reduced T_C due to addition of Ta [92], allows investigation of interface magnetism and MDL formations at measurement temperatures close to the T_C. Such studies are not possible using conventional $3d$ transition metal FM as the high temperatures required promote interdiffusion and destroy the thin-film device structure. The main reason for using PNR is the presence of a dimensionality crossover from three-dimensional system to two-dimensional magnetism at low thin-film thickness, because MDL reduces the magnetic volume. This makes the conventional approach for obtaining MDL thickness at interface using SQUID magnetometry inappropriate. Also, the CoFeB:Ta layers are not homogeneous, hence it is required to obtain true magnetization depth profiles of the structures.

Room-temperature PNR measurements were performed to extract the structural parameters under a large magnetic field $\mu_0 H = 0.3$ T in order to investigate structural sensitivity to possible residual magnetization at this temperature. However, no magnetic signal was observed for structures at room-temperature.

Low-temperature measurements were made for both structures at temperatures of $\sim 0.1\ T_C$ (10 K for both structures) and $\sim 0.6\ T_C$ (55 K for the structure on GaAs(001) and 70 K for the structure on Si/SiO_2 substrate). These measurements were performed in a magnetic field of $\mu_0 H = 0.02$ T. This magnetic field was sufficient in order to saturate the magnetization of CoFeB:Ta. Over the studied temperature range the expected variation of thin-film thickness due to thermal expansion/contraction was around 0.03 % [153], which is far below the resolution ($\sim 4\%$) of the PNR measurements and so was neglected. XRR and PNR reflectivities were fitted using the `GenX` simulation code [102]. The magnetization depth profiles of the two CoFeB:Ta structures on Si/SiO_2 and GaAs(001) were obtained by consistently fitting the low-temperature reflectivities using the structural parameters obtained from room-temperature PNR and XRR. During fitting low-temperature reflectivities, only the magnetic parameters

were allowed to vary as a function of temperature. The magnetization depth profiles for the CoFeB:Ta layers were extracted as depth-resolved magnetic scattering length density (SLD) profiles.

The spin-asymmetry gives purely magnetic information through the sample thickness, which can lead to an accurate determination of reflectivity curves. A best-fitting to the reflectivity data provides a good correspondence of the derived spin-asymmetry. It is also important to note that the spin-asymmetry cannot be fitted, instead it is derived from the corresponding reflectivities;

$$\mathrm{SA} = \frac{\mathrm{R}^{+} - \mathrm{R}^{-}}{\mathrm{R}^{+} + \mathrm{R}^{-}} \tag{6.2}$$

where R^{+} and R^{-} are spin-up and spin-down reflectivities. In the next sections, the PNR data of CoFeB:Ta thin-films were analyzed using "various layer" models consisting of substrate/CoFeB:Ta/Ta, where the fitting procedure of PNR data is explained in Section 4.8. Here, the model names are given according to the subdivided CoFeB:Ta layers, where the 1-Layer model is comprised of 3 layers including substrate/uniform CoFeB:Ta layer/Ta capping layer. The two, three and four layers models have a similar structure, but CoFeB:Ta layers are divided into various thin-slabs. This modeling procedure is shown to provide a realistic description of the magnetic structure of the thin-films.

6.3.1 1-Layer Model

This section describes the PNR measurements to extract magnetic depth profiles using 1-Layer model for CoFeB:Ta thin-films on both substrates. This model comprises of a oxidized Ta surface layer and a uniform CoFeB:Ta layer. Fig. 6.3 shows x-ray and neutron reflectivities of CoFeB:Ta thin-films on (a) Si/SiO_2 and (b) GaAs(001) substrates at room-temperature to extract structural parameters where these parameters are then used for fitting low-temperature PNR. PNR measurements and corresponding spin-asymmetries using this model for CoFeB:Ta films on both substrates are shown in Fig. 6.4.

It is shown that the low-temperature PNR data and their fits are not described well for the structure on Si/SiO_2 substrate in Fig. 6.4 (a) and (c). Thus, the derived spin-asymmetries, indicated by red solid lines in Fig. 6.4 (b) and (d) do not pass through the data. The calculated chi-squared values are χ^2 = 11 at 0.1 T_C and χ^2 = 15.6 at 0.6 T_C, which shows the quality of the fits. Greater differences between expected and actual data produce a larger chi-squared value. If the the chi-squared value is large, then the observed and expected values are not close and the model is a poor fit to the data. This model does not provide a realistic

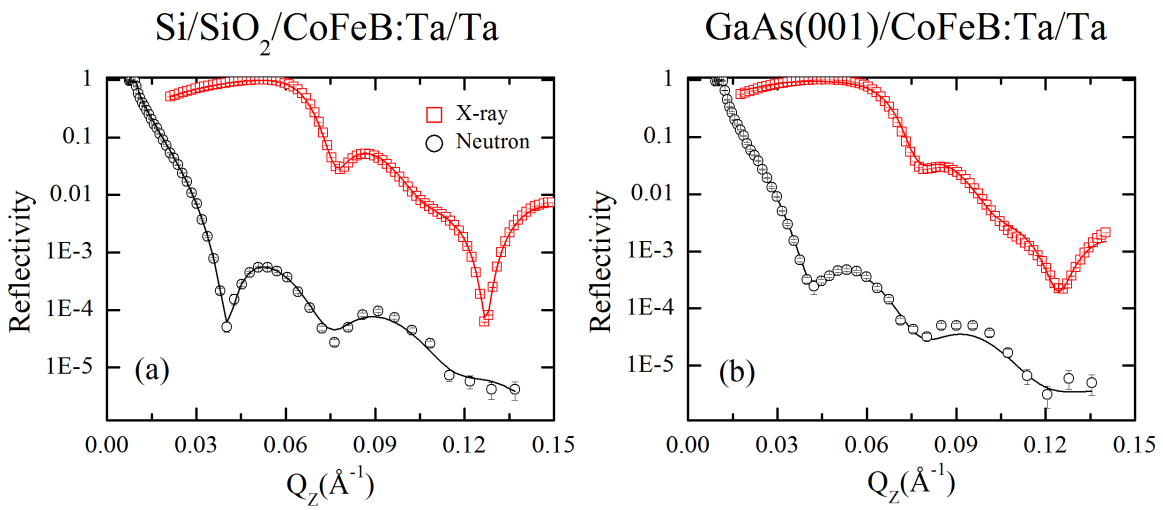

Fig. 6.3 Measured x-ray and polarized neutron reflectivities of CoFeB:Ta films on (a) Si/SiO_2 and (b) GaAs(001) substrates at room-temperature using 1-Layer Model. The solid lines in reflectivity plots are the best fit calculations for the model.

description of the magnetic structure of the sample on Si/SiO_2 due to the high values of chi-squared. Hence a new model for the structure on Si/SiO_2 is required to improve the fit quality. In contrast, the low-temperature PNR data for structure on GaAs(001) substrate are described better compared to the structure on Si/SiO_2, as shown in Fig. 6.4 (e) and (g). The derived spin-asymmetries for both temperatures indicate a behavior similar to the structure on Si/SiO_2. Here, red solid lines pass through the spin-asymmetries until $Q_Z = 0.075$ Å^{-1}, then they start to deviate above the spin-asymmetries. The lower chi-squared values are $\chi^2 = 11.1$ at 0.1 T_C and $\chi^2 = 9.6$ at 0.6 T_C. A new model is also required for this structure to improve the quality of PNR fits.

Fig. 6.5 show the real part of the SLD profiles extracted from the fits using 1-Layer model for structures on (a) Si/SiO_2 and (e) GaAs(001) substrates. The corresponding schematics of the sample structures with uniform CoFeB:Ta layer are given above. The structural SLD profiles for both structures varied from bulk values in the CoFeB:Ta layers close to the Ta capping layer interfaces. This suggests that compositionally-graded layers are formed in the region of these interfaces, between bulk CoFeB:Ta and the Ta capping layer. The CoFeB:Ta/substrate interface width appears relatively broad for the structure on Si/SiO_2. This is attributed to the diffuse interface between the Si substrate and the thin native SiO_2 layer.

The magnetic SLD profiles are shown in Fig. 6.5 for structures on (c) Si/SiO_2 and (g) GaAs(001) substrates. For each structure, the magnetic SLD decreases across the CoFeB:Ta

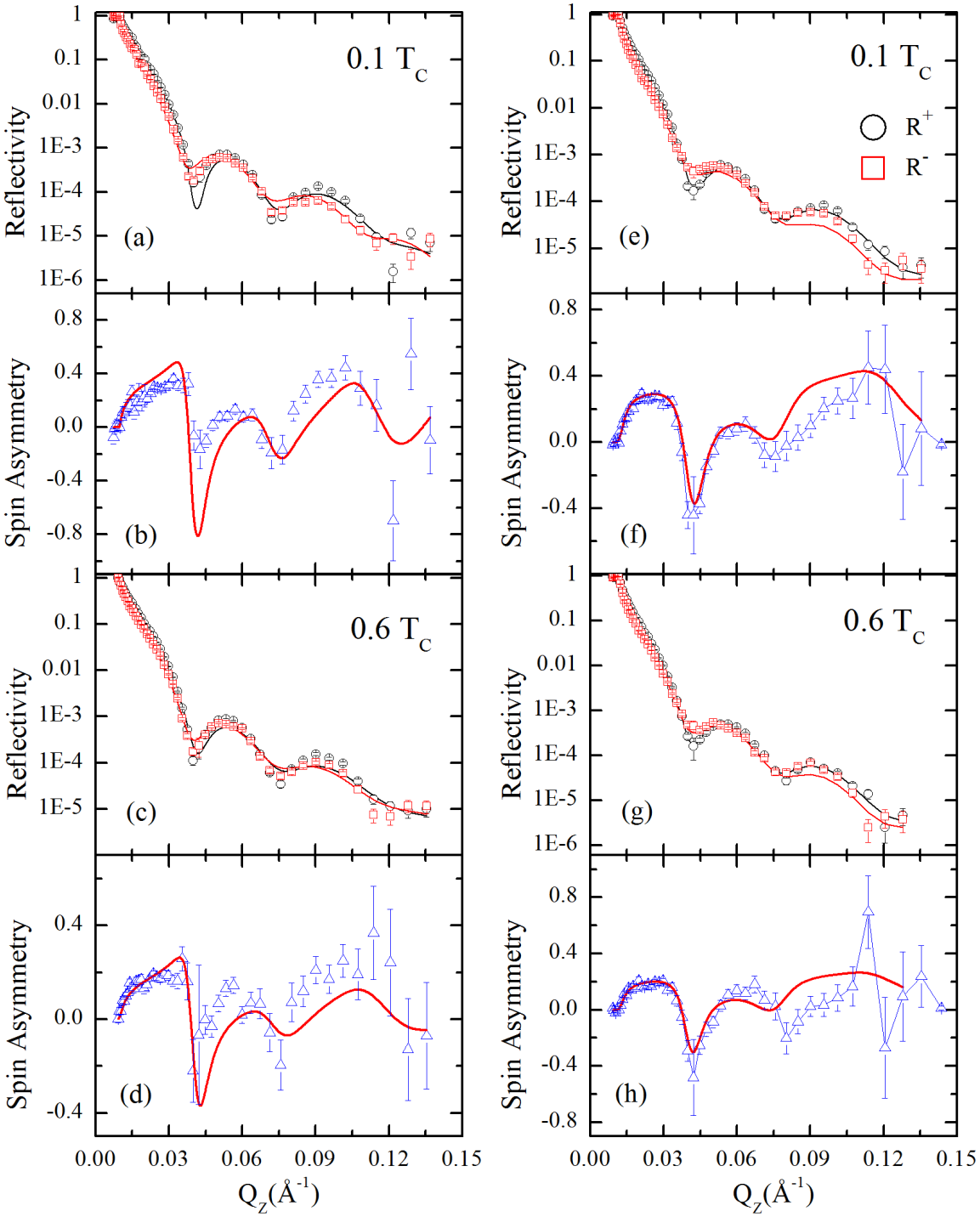

Fig. 6.4 Measured polarized neutron reflectivity and derived spin-asymmetry of CoFeB:Ta films on (a-d) Si/SiO_2 and (e-h) GaAs(001) substrates measured at 0.1 T_C and 0.6 T_C using 1-Layer model. The solid lines in reflectivity plots are the best fit calculations for the models, from which the corresponding spin-asymmetry are derived.

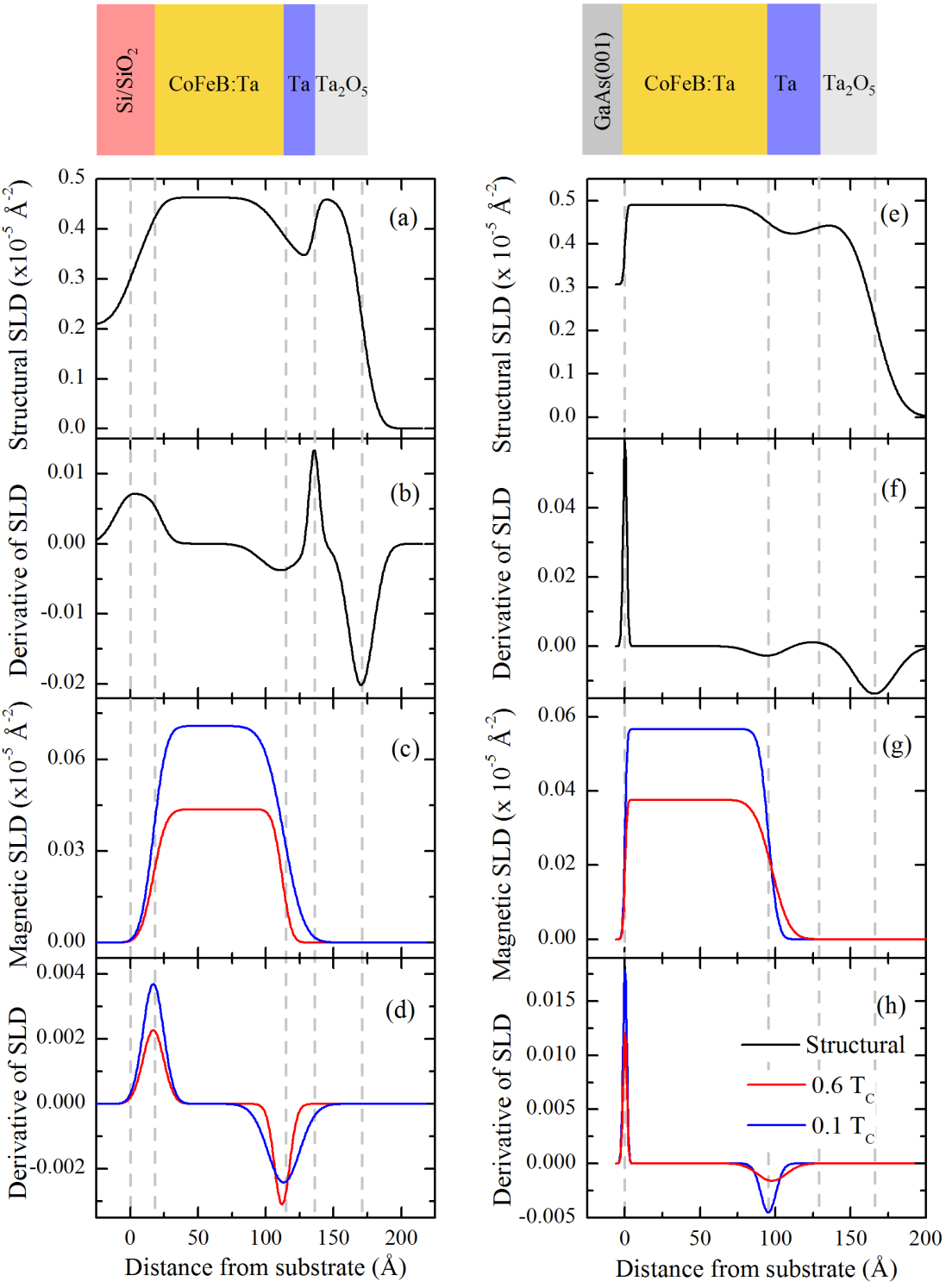

Fig. 6.5 Structural scattering length density (SLD) profiles for CoFeB:Ta films deposited on (a) Si/SiO_2 and (e) GaAs(001) substrates using 1-Layer model. The derivative of the structural SLDs are shown in (b) and (f). Magnetic SLD profiles and their derivatives at temperatures corresponding to 0.1 T_C and 0.6 T_C are shown in (c-d) and (g-h). The vertical dashed lines correspond to the positions of the layer interfaces in the model structures; the layer structures are shown schematically at the top of the figure.

thin-film thickness with increasing temperature, as expected. Also, the magnetic SLD profiles show that magnetizations are roughly constant within the volume of the CoFeB:Ta layers because the CoFeB:Ta layer is a uniform layer in this model. The magnetic SLDs reduce toward the interfaces with the Ta capping layers due to the compositional grading observed in the structural SLD profiles. Here, the magnetic SLD increases sharply at GaAs(001)/CoFeB:Ta interface and remains constant within the CoFeB:Ta volume. At CoFeB:Ta/Ta interface, the magnetization drops sharply at 0.1 T_C, compared to 0.6 T_C which suggests the magnetic roughness is higher at 0.6 T_C.

The derivatives of the structural and magnetic SLD profiles were plotted in order to more accurately visualize positions of the structural and magnetic interfaces in these structures. These derivatives enable to point layer interfaces in the model structures, indicated by peaks and dips. The vertical dashed lines correspond to the positions of the layer interfaces in the model structures. Fig. 6.5 (b) and (d) show the derivative of the structural and magnetic SLD profiles for the structure on Si/SiO_2. In the derivative of magnetic SLDs the peaks are overlapped for both temperatures at a depth of 1.8 nm which indicates the thickness of SiO_2 layer. Beyond this depth, the magnetization starts to increase and split with temperature. Fig. 6.5 (f) and (h) show the derivative of the structural and magnetic SLD profiles for the structure on GaAs(001). A sharp peak appears in both figures which indicates the sharp GaAs(001)/CoFeB:Ta interface. In the derivative of the magnetic SLDs, the dip $\sim$ 10 nm indicates CoFeB:Ta/Ta interface, where it is relatively broader for 0.6 T_C compared to the dip for 0.1 T_C.

As shown in these figures, this model does not provide a realistic description of the magnetic structure of the samples. Also, this model does not allow to study MDL formations at interfaces because CoFeB:Ta thin-film is a uniform layer. Thus, a new model is required with subdivided CoFeB:Ta layers into several thin-slabs.

6.3.2 2-Layers Model

This section describes the PNR modeling to extract magnetic depth profiles for CoFeB:Ta thin-films on both substrates using 2-Layers model. This model comprises a CoFeB:Ta layer that is subdivided into two slabs, where it provides better reflectivity fits to the PNR data compared to 1-Layer model. Fig. 6.6 show x-ray and neutron reflectivities of CoFeB:Ta films on (a) Si/SiO_2 and (b) GaAs(001) substrates at room-temperature to extract structural parameters. The low-temperature PNR measurements and corresponding spin-asymmetries using these structural parameters are shown in Fig. 6.7.

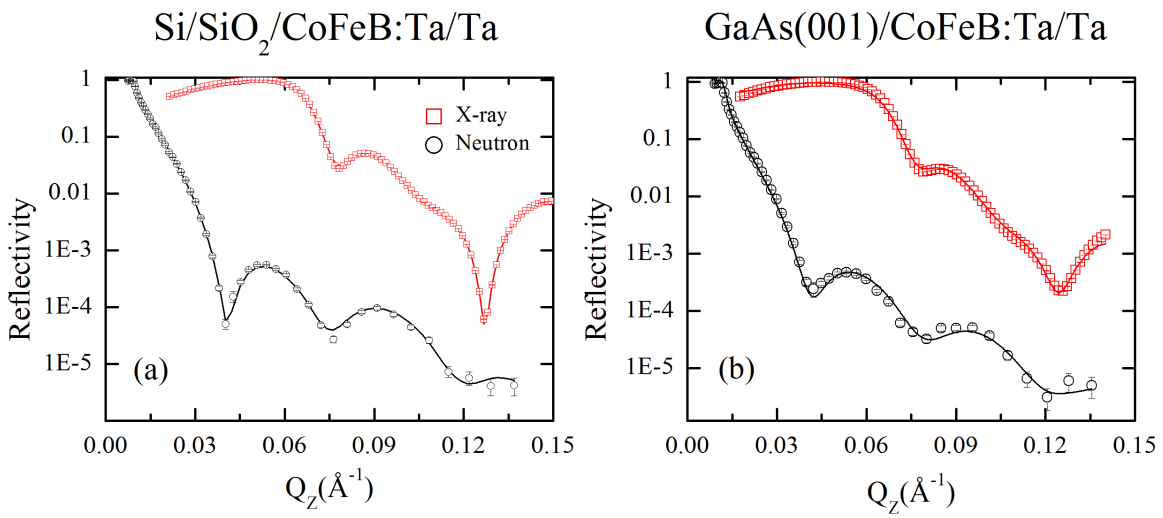

Fig. 6.6 Measured x-ray and polarized neutron reflectivities of CoFeB:Ta films on (a) Si/SiO_2 and (b) GaAs(001) substrates measured at room-temperature using 2-Layers model. The solid lines in reflectivity plots are the best fit calculations for the model.

Again, it is shown that the low-temperature PNR data and their fits do not match well for structure on Si/SiO_2 substrate, as shown in the derived spin-asymmetries in Fig. 6.7 (b) and (d). In this model, the chi-squared values are $\chi^2 = 9$ at 0.1 T_C and $\chi^2 = 11$ at 0.6 T_C for the structure on Si/SiO_2 substrate, which are still high. The low-temperature PNR data for the structure on GaAs(001), as given in Fig. 6.7 (f) and (h), are described better compared to structure on Si/SiO_2. In this model the derived spin-asymmetry at 0.1 T_C is well described until $Q_Z = 0.075$ Å^{-1}, then it starts to deviate. However, PNR data at 0.6 T_C fitted well and has a good correspondence with the derived spin-asymmetry entire Q_Z range. The chi-squared values are $\chi^2 = 9.4$ at 0.1 T_C and $\chi^2 = 8.5$ at 0.6 T_C.

Fig. 6.8 show the real part of the SLD profiles extracted from the fits using 2-Layers model for the structures on (a) Si/SiO_2 and (e) GaAs(001) substrates. The corresponding schematics of the sample structures with two CoFeB:Ta slabs are given at top. In this model the bulk CoFeB:Ta layer is divided into two thin-slabs; hence, the structural SLD shows variations in the main CoFeB:Ta layer for both structures. As similar to the previous model, the CoFeB:Ta/substrate interface width appears relatively broad for the structure on Si/SiO_2 due to the diffuse interface between the Si substrate and the thin native SiO_2 layer. The structural SLD profiles for the structure on Si/SiO_2 shows a drop in the CoFeB:Ta layer close to the Ta capping layer interface, which suggests a sharp CoFeB:Ta/Ta interface. The structural SLD profile varied from bulk values in the CoFeB:Ta layers close to the Ta capping

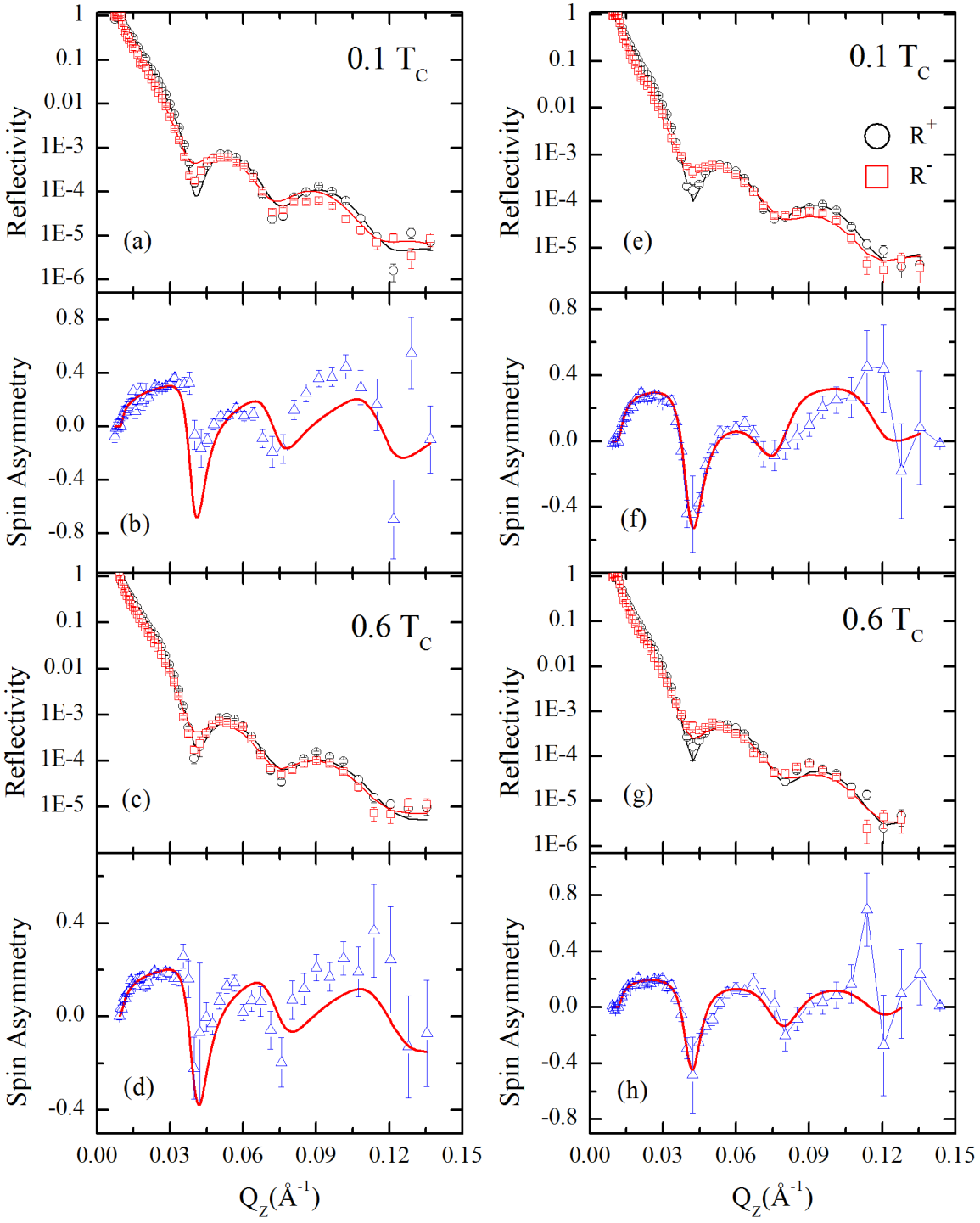

Fig. 6.7 Measured polarized neutron reflectivity and derived spin-asymmetry of CoFeB:Ta films on (a-d) Si/SiO_2 and (e-h) GaAs(001) substrates using 2-Layers model measured at 0.1 T_C and 0.6 T_C. The solid lines in reflectivity plots are the best fit calculations for the models, from which the corresponding spin-asymmetry are derived.

layer interfaces for the structure on GaAs(001) due to compositionally-graded layers at CoFeB:Ta/Ta interface.

The magnetic SLD profiles are shown in Fig. 6.8 for structures on (c) Si/SiO_2 and (g) GaAs(001) substrates. In both structures, the magnetic SLDs decrease across the CoFeB:Ta thin-film thickness with increasing temperature. The magnetic SLDs reduce toward the interfaces with the Ta capping layer for both structures due to the compositional grading. For the structure on GaAs(001), the magnetic SLD profile at 0.1 T_C show that magnetizations are roughly constant within the volume of the CoFeB:Ta layers, but the magnetic SLD profile at 0.6 T_C reduce toward the interfaces with the Ta capping layer. These magnetic SLD profiles for the structure on GaAs(001) show limited ability to describe the model.

Again, the derivative of the (b) structural and (d) magnetic SLDs are given in Fig. 6.8 to determine the positions of the structural and magnetic interfaces for CoFeB:Ta thin-film on Si/SiO_2 substrate. In the derivative of the structural SLD the first dip is located at 10.5 nm, which shows the sharp CoFeB:Ta/Ta interface. As similar to the previous model, the peaks with different temperatures are overlapped at a distance of 1.5 nm in the derivative of the magnetic SLDs where this distance corresponds to SiO_2 layer. Here, the broad dips which correspond to CoFeB:Ta/Ta interface are behind the dip in the derivative of the structural SLD, as shown by dashed vertical line. This indicates the evidence of MDL formation at CoFeB:Ta/Ta interface. Also, the dip for 0.6 T_C is behind the dip for 0.1 T_C.

Significantly, this suggests the position of magnetic interfaces is temperature dependent. Even this model enables to extract MDL formation at top interface, due to the limited ability to describe the low-temperature PNR data and corresponding spin-asymmetries, a new model is required with addition of a thin CoFeB:Ta slab to the model. Fig. 6.5 (f) and (h) show the derivative of the structural and magnetic SLDs for CoFeB:Ta thin-film on GaAs(001) substrate. In the derivative of the magnetic SLD, the peaks are located at the same position, and the dips are slightly shifted to lower CoFeB:Ta depth with increasing temperature. The PNR fits and corresponding spin-asymmetries are described well, but the SLD profiles do not represent actual magnetic depth profiles. Thus, this model is not suitable to extract MDL thicknesses at interfaces.

This model provides a better description of the magnetic structure of the samples on both substrates compared to the previous model, but there are still some issues to obtain best-fitting. However, chi-squared values for low-temperature PNR are too high to understand the magnetic depth profiles, Hence a further model is required that adds further subdivisions of CoFeB:Ta to the model to improve the quality of the best-fitting low-temperature PNR simulations.

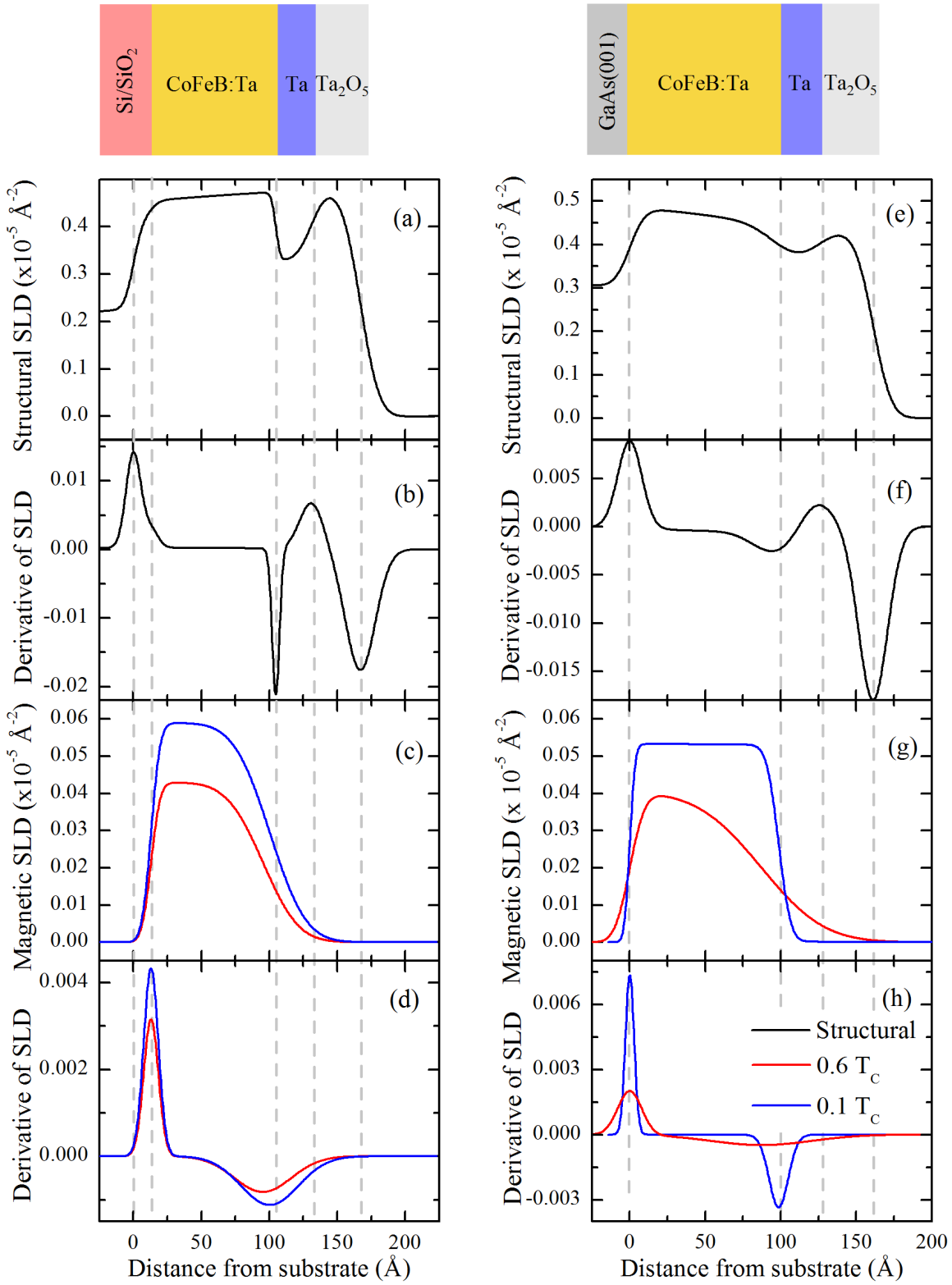

Fig. 6.8 Structural scattering length density (SLD) profiles using 2-Layers model for CoFeB:Ta films deposited on (a) Si/SiO_2 and (e) GaAs(001) substrates. The derivative of the structural SLDs are shown in (b) and (f). Magnetic SLD profiles and their derivatives at temperatures corresponding to 0.1 T_C and 0.6 T_C are shown in (c-d) and (g-h). The vertical dashed lines correspond to the positions of the layer interfaces in the model structures; the layer structures are shown schematically at the top of the figure.

6.3.3 3-Layers Model

The PNR measurements fitted using 3-Layers model are described in this section for CoFeB:Ta thin-films on both substrates. This model comprises of a CoFeB:Ta layer that is subdivided into three slabs. This model provides better reflectivity fits to the PNR data compared to previous models. Also, the best fits to the PNR data and corresponding spin-asymmetries for the structure on Si/SiO_2 are obtained using this model. Thus, the low-temperature PNR data and SLD profiles for both structures are analyzed separately in this section to indicate MDL thicknesses clearly. Fig. 6.9 show x-ray and neutron reflectivities of CoFeB:Ta films on (a) Si/SiO_2 and (b) GaAs(001) substrates at room-temperature to extract structural parameters.

The low-temperature PNR measurements and corresponding spin-asymmetries using this model are shown in Fig. 6.10 for the structure on Si/SiO_2. The spin-asymmetries show several prominent dip features indicated by dashed vertical lines. The first dip, at around $Q_Z = 0.04$ Å^{-1} shows no significant shifts with temperature within Q_Z resolution. However, the second dip shifts to higher Q_Z as the temperature increases. This indicates a reduction of the effective magnetic depth. In this model, the chi-squared values are $\chi^2 = 3.1$ at 0.1 T_C and $\chi^2 = 4.9$ at 0.6 T_C for the structure on Si/SiO_2 substrate, where these values are lower than the values for other models.

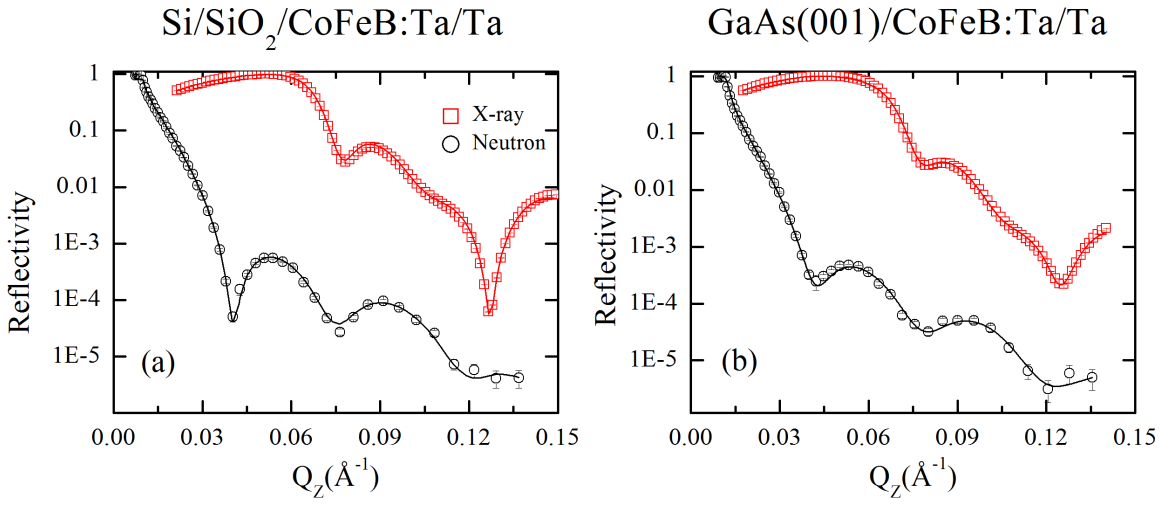

Fig. 6.9 Measured x-ray and polarized neutron reflectivities of CoFeB:Ta films on (a) Si/SiO_2 and (b) GaAs(001) substrates measured at room-temperature using 3-Layers model. The solid lines in reflectivity plots are the best fit calculations for the model.

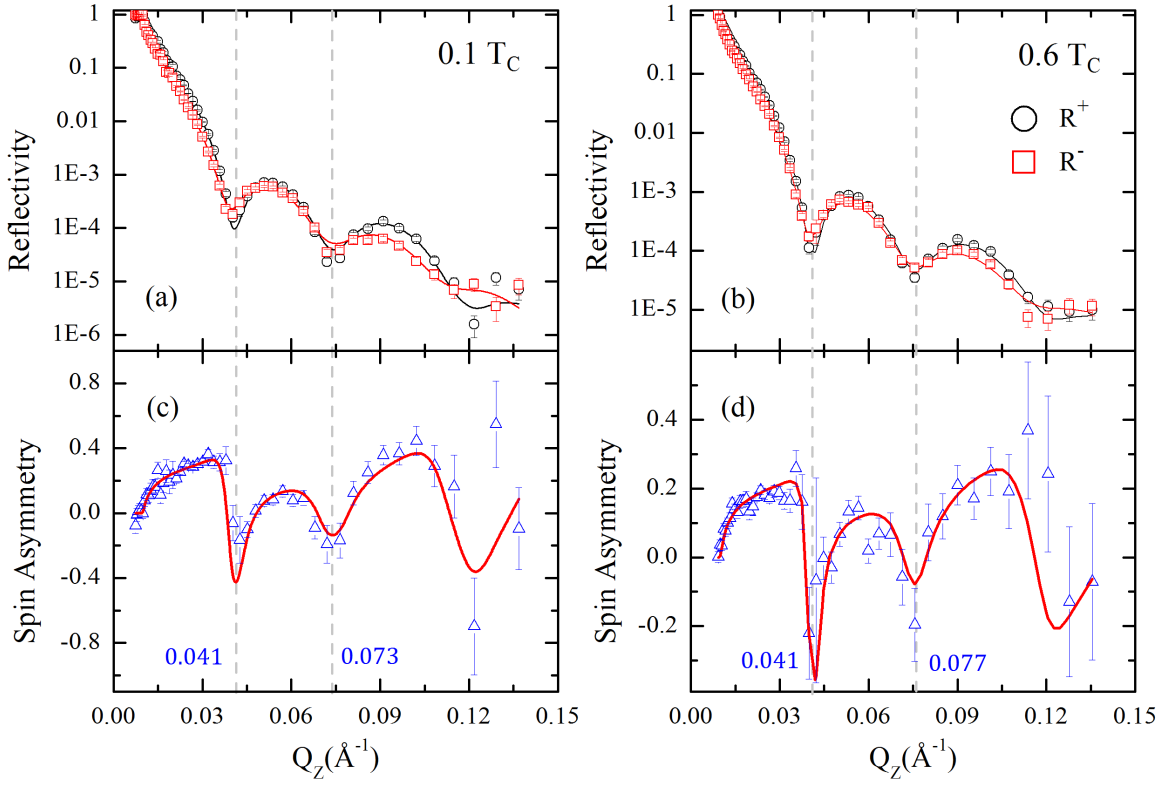

Fig. 6.10 Measured polarized neutron reflectivity and derived spin-asymmetry of CoFeB:Ta thin-film on Si/SiO_2 using 3-Layers model measured at (a-c) 0.1 T_C and (b-d) 0.6 T_C. The solid lines in reflectivity are the best fit calculations for the model, from which the corresponding spin-asymmetry are derived.

Structural and magnetic SLD profiles at temperatures corresponding to 0.1 T_C and 0.6 T_C using 3-Layers model are given in Fig. 6.11 for the structure on Si/SiO_2. The corresponding schematics of the sample structure with three CoFeB:Ta thin-slabs are given at top. As similar to the previous models, the CoFeB:Ta/substrate interface width appears relatively broad due to the diffuse interface between the Si substrate and the thin native SiO_2 layer $\sim$ 1–2 nm. Even the bulk CoFeB:Ta layer comprises of three thin-slabs, the structural SLD is constant across the thin-film depth. Fig. 6.11 (b) shows the magnetic SLDs which decrease with increasing temperature across the thin-film depth, as expected. The magnetic SLDs show that magnetizations are roughly constant within the volume of the CoFeB:Ta layers, and reduce toward the interfaces with the Ta capping layers due to the compositional grading suggested in the structural SLDs. A small region close to the interface with the substrate shows enhancement of the magnetic SLD. The structural SLDs in this region are comparable to the volume of the CoFeB:Ta thin-film, indicating that this enhanced magnetization is not due to a local reduction in Ta concentration. This locally enhanced magnetization may be a

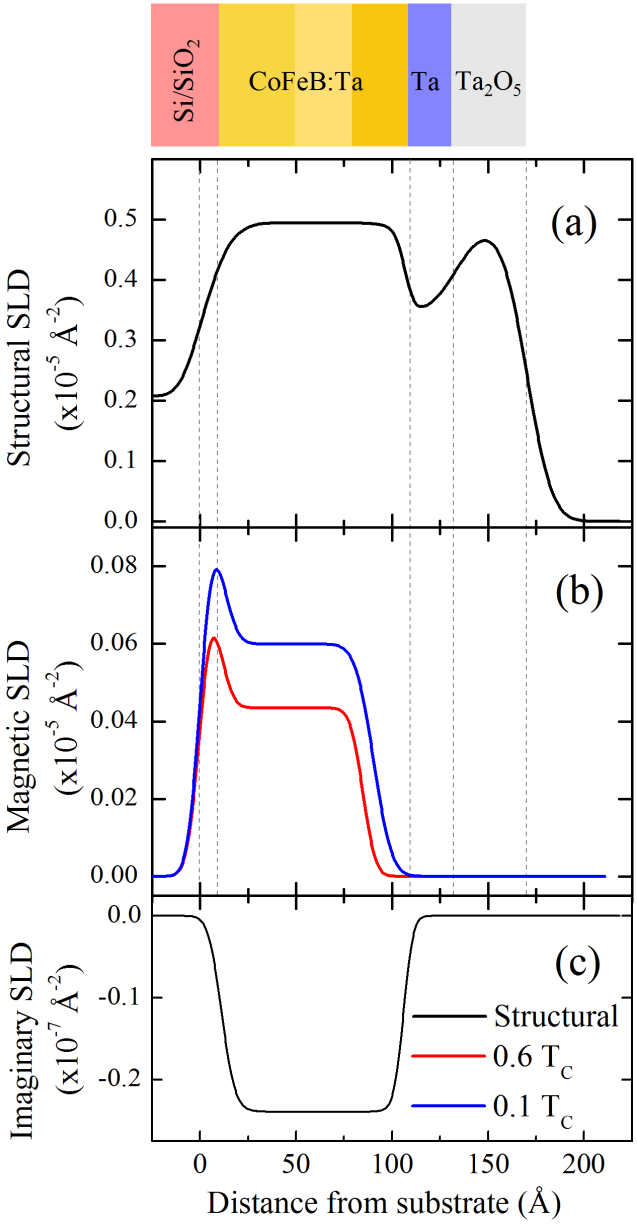

Fig. 6.11 (a) Structural and (b) magnetic scattering length density (SLD) profiles at temperatures corresponding to 0.1 T_C and 0.6 T_C using 3-Layers model for CoFeB:Ta thin-film deposited on Si/SiO_2 substrate. The corresponding imaginary parts of the structural SLDs are given in (c). The vertical dashed lines correspond to the positions of the layer interfaces in the model structure. The layer structures are shown schematically at the top of the figure.

result of charge transfer due to interface bonding [90, 154], which may differ for bonding at the sharp oxide-metal SiO_2/CoFeB:Ta interface. The imaginary part of the structural SLD profile, as shown in Fig. 6.11 (c) is sensitive only to boron, and shows the expected uniform CoFe-to-B composition through the CoFeB:Ta layer.

The derivative of the structural and magnetic SLDs for the structure on Si/SiO_2 are given in Fig. 6.12. The vertical dashed lines correspond to the positions of the layer interfaces in the model structures, and the shaded regions show MDL formations at CoFeB:Ta/Ta interface. Here it is observed that in addition to a broad peak indicating a diffuse substrate/oxide

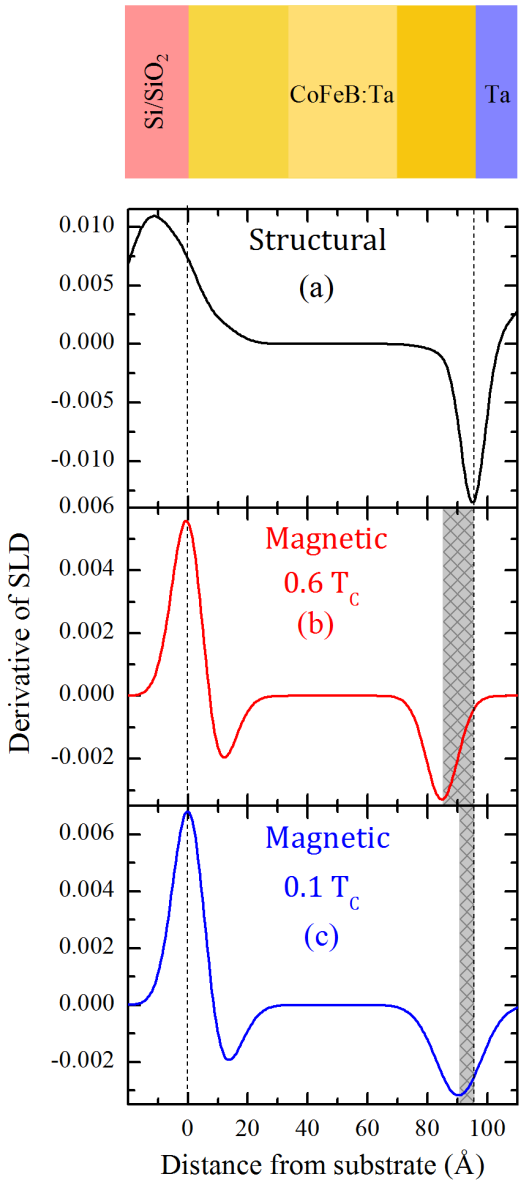

Fig. 6.12 The derivative of (a) room-temperature structural and magnetic scattering length density profiles for (b) 0.6 T_C and (c) 0.1 T_C to extract layer interfaces are shown for CoFeB:Ta films deposited on Si/SiO_2 using 3-Layers model. The vertical dashed lines correspond to the positions of the layer interfaces in the model structures. The shaded regions show magnetically dead layers. The layer structure is shown schematically at the top of the figure.

interface and a dip indicating the film/capping-layer interface, there is also an inflection corresponding to the interface between the SiO_2 native-oxide layer and magnetic CoFeB:Ta film. From the derivatives of the magnetic SLDs here the CoFeB:Ta thin-film deposited on Si/SiO_2 shows that the peaks which indicate the CoFeB:Ta/substrate interface is co-located with the structural interface for both measurement temperatures in the ferromagnetic phase. This means that no MDL arises at the SiO_2/CoFeB:Ta interface. However, previous studies using conventional magnetometry have suggested a 0.5 nm-thick MDL is found at the SiO_2/CoFeB interface, due to interdiffusion [147].

In contrast, the dips indicate the CoFeB:Ta/Ta magnetic interface is shifted to lower depth with increasing temperature, as shown by shaded regions. This indicates that there is a MDL at the CoFeB:Ta/Ta interface and the MDL thickness increases with increasing temperature, which means that the effective FM depth of the thin-film reduces with increasing temperature. This also explains the shift of features in the PNR spin-asymmetries shown in Fig. 6.10. Diffusion of Ta into the CoFeB:Ta layer from the Ta capping layer explains the broad CoFeB:Ta/Ta cap structural interface in Fig. 6.12. This also explains why the interfacial MDL thickness increases with increasing temperature, where the local T_C of this compositionally-graded region determines the position of the effective magnetic interface. Here, the upper magnetic interface is shifted (5.6 ± 0.4) Å into the volume of the CoFeB:Ta thin-film at 0.1 T_C, and (9 ± 1) Å into the thin-film at 0.6 T_C. This is consistent with studies of room-temperature MDL formation in nominally un-doped CoFeB/Ta interfaces, which have shown that deposition of a Ta capping layer on CoFeB creates a 0.6 nm thick MDL at the CoFeB/Ta interface at room-temperature, corresponding to $T \sim 0.4\ T_C$ [29], due to the diffusion of Ta into CoFeB [29, 147, 155].

The low-temperature PNR measurements and corresponding spin-asymmetries using this model are shown in Fig. 6.13 for the structure on GaAs(001). This model provides a better description of the magnetic structure of the samples compared to the previous models. There are three thin slabs in this model, where the thin-slabs at upper and lower interfaces are magnetically dead. Also, this model fitted well to the reflectivity data and has good correspondence with the derived spin-asymmetries. The chi-squared values are $\chi^2 = 8.2$ at 0.1 T_C and $\chi^2 = 7.3$ at 0.6 T_C for the structure on GaAs(001) substrate, which are still similar to the values for other models.

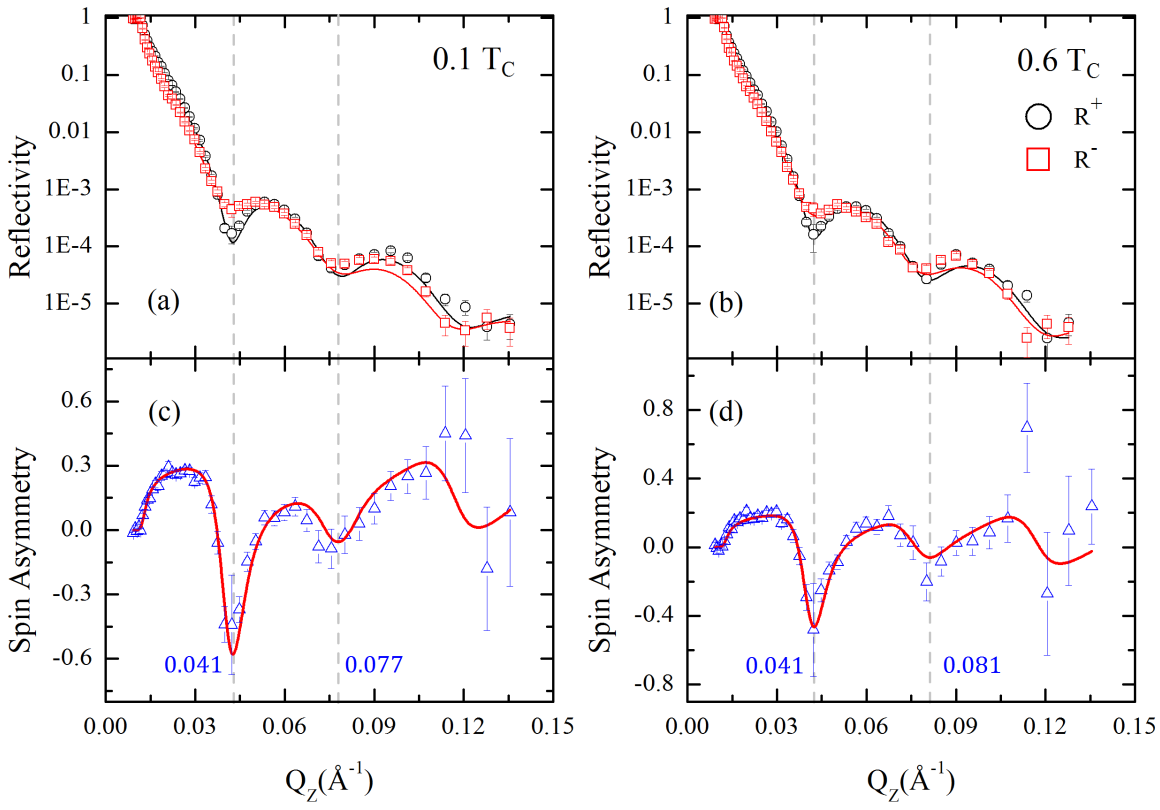

Fig. 6.13 Measured polarized neutron reflectivity and derived spin-asymmetry of CoFeB:Ta films on GaAs(001) using 3-Layers model measured at (a-c) 0.1 T_C and (b-d) 0.6 T_C. The solid lines in reflectivity plots are the best fit calculations for the models, from which the corresponding spin-asymmetry are derived.

Structural and magnetic SLD profiles at temperatures corresponding to 0.1 T_C and 0.6 T_C and their derivatives using this model are given in Fig. 6.14 for the structure on GaAs(001). For the bulk CoFeB:Ta layer, comprising three thin-slabs in this model, the structural SLD behaves as a uniform layer. Hence it is constant across the CoFeB:Ta depth. Similar to the previous models, the structural SLD varies from bulk values in the CoFeB:Ta layer close to the Ta capping layer interface due to a compositionally-graded layer at CoFeB:Ta/Ta interface. The magnetic SLDs which decrease with increasing temperature across the thin-film depth, is given in Fig. 6.14 (b). The magnetic SLDs decrease across the CoFeB:Ta thin-film depth with increasing temperature. Again, the magnetizations are roughly constant within the volume of the CoFeB:Ta layers, and reduce toward the CoFeB:Ta/Ta interface due to the compositional grading observed in the structural SLDs. As shown in Fig. 6.14 (d), the derivative of the magnetic SLDs at GaAs(001)/CoFeB:Ta interface are slightly shifted from the origin to the higher CoFeB:Ta depth with increasing temperature, as shown by the vertical solid line.

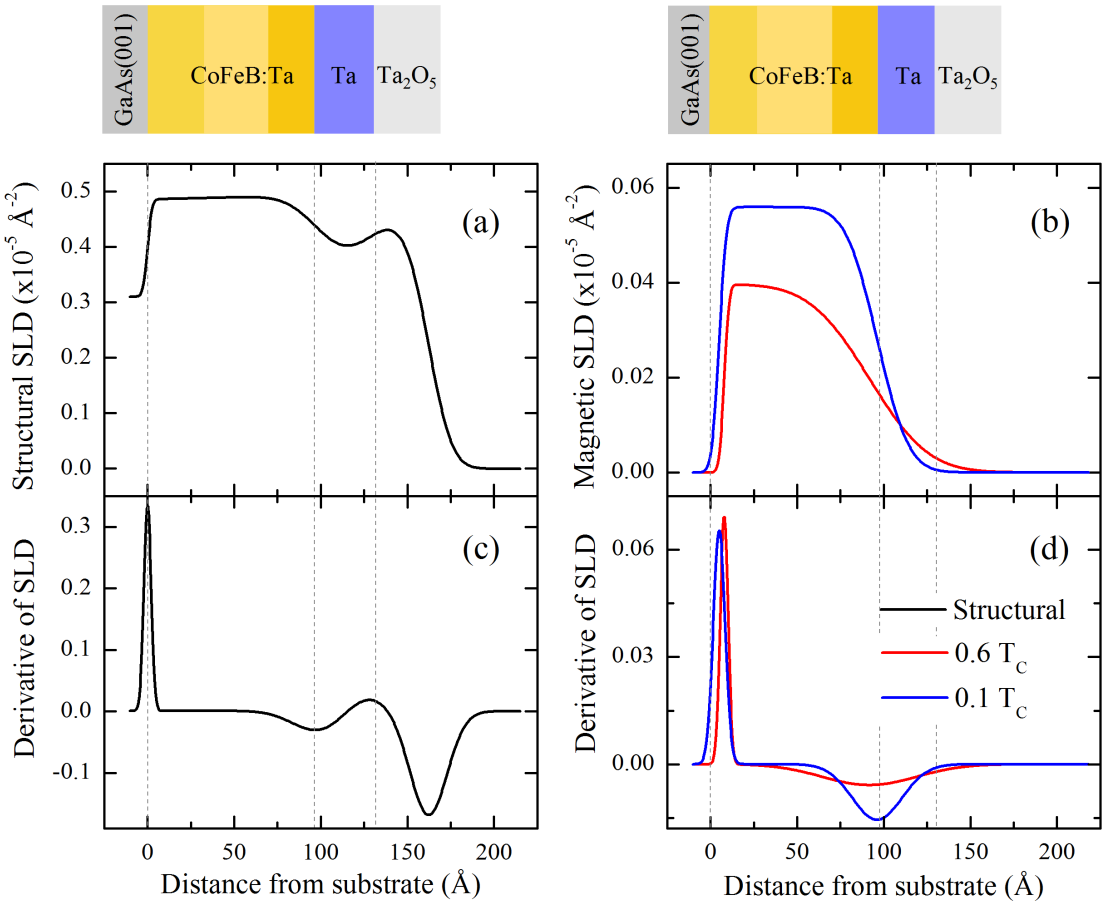

Fig. 6.14 Structural (a) and magnetic scattering length density profiles (b) at temperatures corresponding to 0.1 T_C and 0.6 T_C and (c-d) their derivatives using 3-Layers model for CoFeB:Ta thin-film deposited on GaAs(001) substrate. The vertical solid line in (b) and (d) represent GaAs(001)/CoFeB:Ta interface. The layer structure is shown schematically at the top of the figure.

Similar behaviour is observed at CoFeB:Ta/Ta interface, where the broader dip at 0.6 T_C is behind the sharp dip at 0.1 T_C. These indicate the evidence of temperature dependent MDL formations at these interfaces.

This model provides the best description of the magnetic structure for the structure on Si/SiO_2. Hence adding further subdivisions to the model for this structure resulted in no further improvement of the fit quality. In this model there is only one magnetically active thin-slab in the core region for the structure on GaAs(001) due to MDL formations at top and bottom interface. However, there are two magnetically active thin-slabs in this model for the structure on Si/SiO_2, where MDL is formed at top interface. Therefore adding another thin-slab to the model for the structure on GaAs(001) may result in a better description of the magnetic structure.

6.3.4 4-Layers Model

The PNR measurements were analyzed for CoFeB:Ta thin-films on GaAs(001) using a 4-Layers model. This model comprises of subdivision of the CoFeB:Ta layer into 4 thin-slabs. There are two interfacial regions at upper and lower interfaces and two fully magnetized thin-slabs in the core region where the magnetization was allowed to vary from the bulk value. This model provides a realistic description of the magnetic structure of the samples, and fitted very well to the reflectivity data and has very good correspondence with the derived spin-asymmetries. Adding further subdivisions to the model resulted in no further improvement of the fit quality. Fig. 6.15 show x-ray and neutron reflectivities of CoFeB:Ta thin-film on GaAs(001) measured at room-temperature to obtain structural parameters. The magnetization depth profiles of the CoFeB:Ta on GaAs(001) were obtained by consistently fitting the low-temperature reflectivities using the structural parameters obtained from room-temperature PNR and XRR.

PNR measurements and derived spin-asymmetries for the structure on GaAs(001), measured at (a-c) 0.1 T_C and (b-d) 0.6 T_C are shown in Fig. 6.16. The spin-asymmetries show several prominent dip features indicated by dashed vertical lines. The first dip, at around $Q_Z = 0.04$ Å^{-1} show no significant shifts with temperature within Q_Z resolution. However,

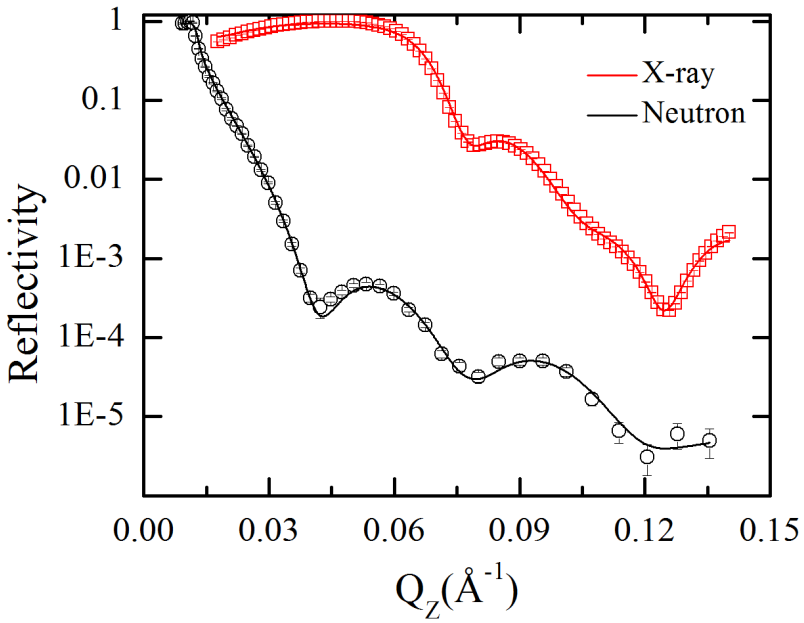

Fig. 6.15 Measured x-ray and polarized neutron reflectivities of CoFeB:Ta films on GaAs(001) at room-temperature using 4-Layers model. The solid lines in reflectivity plots are the best fit calculations for the model.

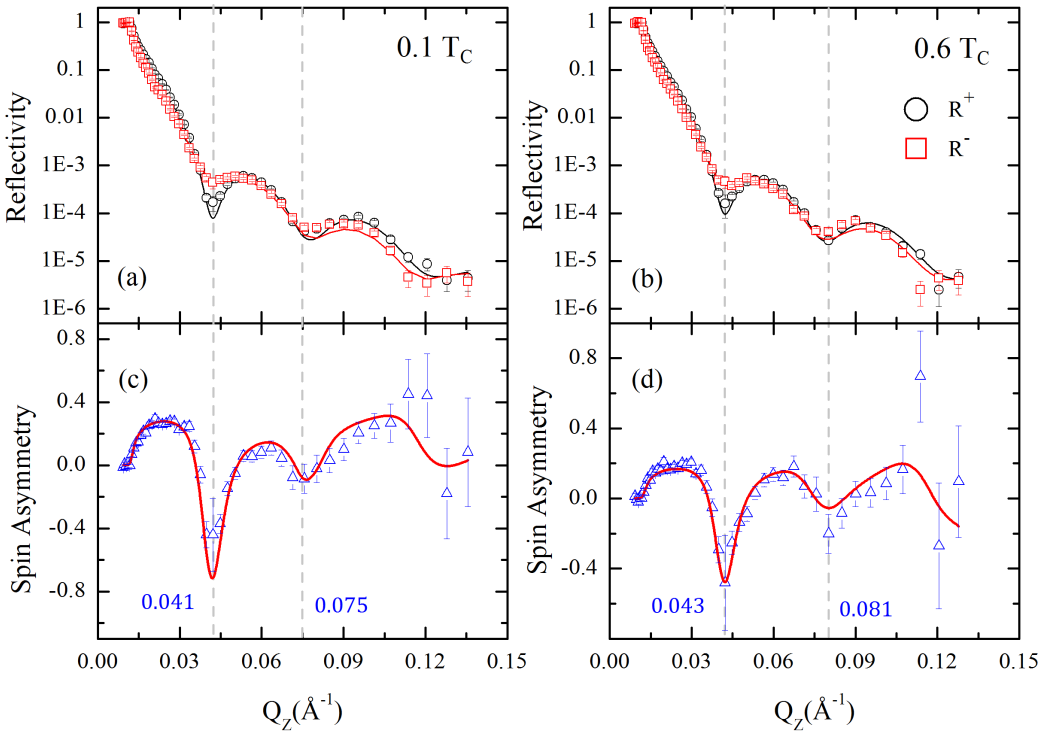

Fig. 6.16 Measured polarized neutron reflectivity and derived spin-asymmetries of CoFeB:Ta thin-films on GaAs(001) using 4-Layers model measured at (a-c) 0.1 T_C and (b-d) 0.6 T_C. The solid lines in reflectivity plots are the best fit calculations for the models, from which the corresponding spin-asymmetry are derived.

the second dip shifts from $Q_Z = 0.075$ Å^{-1} to $Q_Z = 0.081$ Å^{-1} as the temperature increases. This indicates a reduction of the effective magnetic depth. The shift is larger for the CoFeB:Ta thin-film on GaAs(001) than for the thin-film on Si/SiO_2, as given in Fig. 6.10 (c) and (d). In this model, the chi-squared values are $\chi^2 = 4.9$ at 0.1 T_C and $\chi^2 = 4.7$ at 0.6 T_C for the structure on GaAs(001).

The real part of the SLD profiles extracted from the PNR fits are shown in Fig. 6.17 (a) for the structure on GaAs(001). The structural SLD profile varied from bulk values in the CoFeB:Ta layer close to the capping layer interfaces. Again, this suggests that compositionally-graded layer is formed in the region of these interfaces, between bulk CoFeB:Ta layer and the Ta capping layer, with spatially varying Ta doping concentration. The structural SLD profile for the film on Si/SiO_2 is slightly larger than that for the film on GaAs(001) substrate. This indicates that the film on Si/SiO_2 has a slightly lower Ta concentration comparing to the film on GaAs(001) substrate due to sample-to-sample variation in the co-deposition process. This also indicates the reason of differences in T_C for both thin-film structures, as given in Section 6.2.

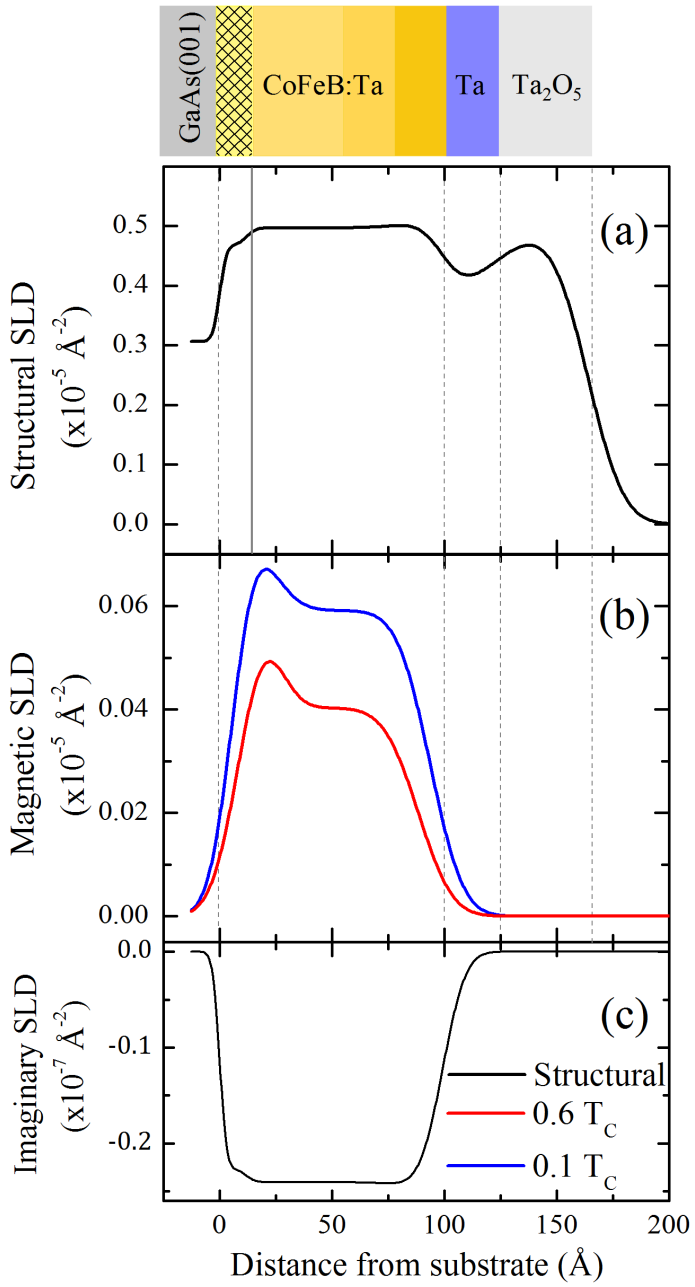

Fig. 6.17 Structural (a) and magnetic scattering length density (SLD) profiles (b) at temperatures corresponding to 0.1 T_C and 0.6 T_C and (c-d) their derivatives using 4-Layers model for CoFeB:Ta thin-film deposited on GaAs(001). The corresponding imaginary parts of the structural SLDs are given in (c). The vertical dashed lines correspond to the positions of the layer interfaces in the model structure. The solid line in (a) represent a thin-layer with intermediate SLD at the the CoFeB:Ta/substrate interface due to interfacial interdiffusion. The layer structure is shown schematically at the top of the figure.

As shown by solid vertical line, the structural SLD shows a clear layer with an intermediate SLD over a depth of $\sim$ 1.5 nm at the CoFeB:Ta/substrate interface, which is likely due to interfacial interdiffusion. Such interdiffusion produces various inter-metallic alloys of Fe, Ga and As at GaAs/Fe interfaces [149, 156, 157], Co_2GaAs at the GaAs/Co interfaces [146], and $(CoFe)_3GaAs$ at GaAs/CoFe interfaces [158]. This interfacial alloying appears irrespective of growth temperature, substrate orientation, and substrate reconstruction, and remains poorly understood.

The magnetic SLDs are shown in Fig. 6.17 (b) for the structure on GaAs(001). The two sets of magnetic SLDs, for the structure on Si/SiO_2 and GaAs(001) substrates, are qualitatively similar. Here, increasing temperature causes the magnetic SLD to decrease across the thin-film depth. As observed for the structure on Si/SiO_2, the magnetic SLD show that magnetization is roughly constant within the volume of the CoFeB:Ta layers, and reduces toward the interfaces with the Ta capping layer due to the compositional grading observed in the structural SLD. Again, a small region close to the interface with the substrate shows enhancement of the magnetic SLD. This enhancement is greater for the structure on Si/SiO_2 than for the structure on GaAs(001). The structural SLDs in this region are comparable to the volume of the film, indicating that this enhanced magnetization is not due to a local reduction in Ta concentration. This locally enhanced magnetization may be a result of charge transfer due to interface bonding [90, 154], which may differ for bonding at the sharp oxide-metal SiO_2/CoFeB:Ta interface compared to that at the intermixed semiconductor-metal GaAs/CoFeB:Ta interface. Again, the imaginary part of the structural SLD is shown in Fig. 6.17 (c), which shows the expected uniform CoFe-to-B composition through the CoFeB:Ta layer.

The derivative of the structural and magnetic SLD profiles were analyzed to determine the structural and magnetic interfaces for the structure on GaAs(001) as shown in Fig. 6.18. In these derivatives, layer interfaces in the model structures are indicated by peaks and dips. There is an additional peak in the derivative of the structural SLD near the CoFeB:Ta/substrate interface, as shown by solid vertical line, which indicates the interface between the intermixed CoFeB:Ta-GaAs interfacial region and CoFeB:Ta thin-film. Here, compositional grading and a corresponding temperature-dependent MDL are observed at the CoFeB:Ta/Ta interface, although the interface is slightly broader in this structure.

From the derivatives of the magnetic SLDs, Fig. 6.18 (b) and (c), there is also evidence of a MDL at the lower magnetic interface of the CoFeB:Ta thin-film, which shows the position of this magnetic interface is temperature dependent. The first dip indicates the magnetic interface between fully magnetized regions, and the second dip represents the CoFeB:Ta/Ta

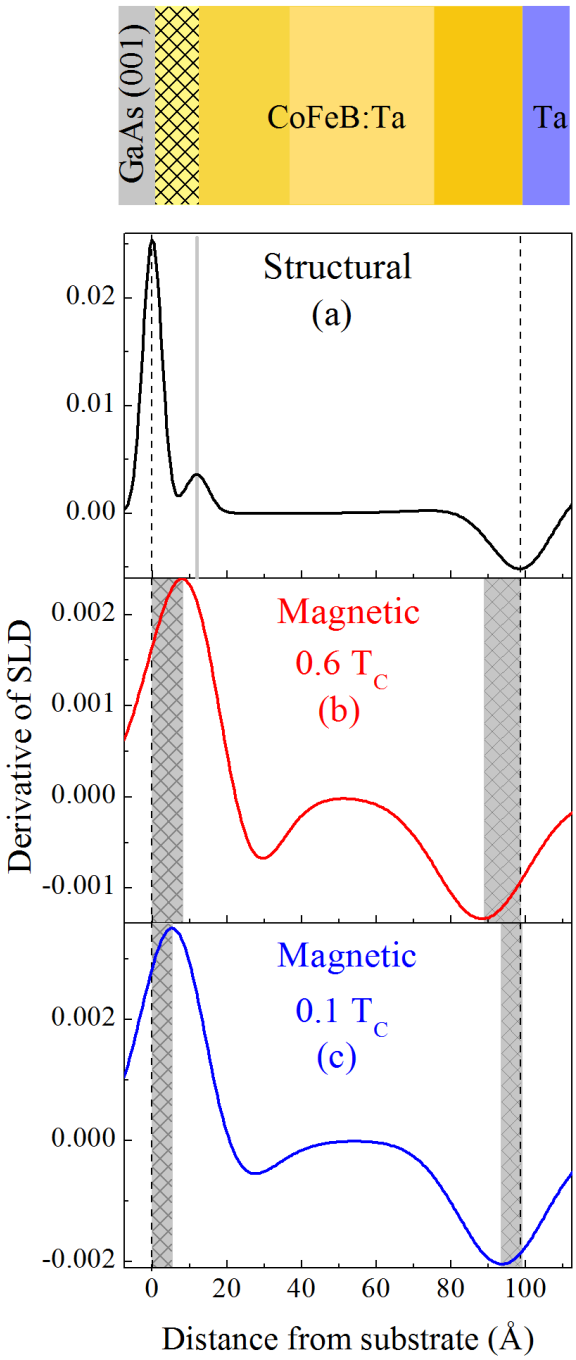

Fig. 6.18 The derivative of (a) room-temperature structural and magnetic scattering length density profiles for (b) 0.6 T_C and (c) 0.1 T_C to extract layer interfaces are shown for CoFeB:Ta thin-films deposited on GaAs(001) using 4-Layers model. The vertical dashed lines correspond to the positions of the layer interfaces in the model structures. The vertical solid line in (a) correspond to the interface between the CoFeB:Ta-GaAs interfacial region and CoFeB:Ta thin-film. The shaded regions in (b) and (c) show magnetically dead layers at top and bottom interfaces. The layer structure is shown schematically at the top of the figure.

magnetic interface, which is shifted to lower depth with increasing temperature. This shows that there is a MDL at the CoFeB:Ta/Ta interface and the thickness increases with increasing temperature. This also means that the effective ferromagnetic depth of the thin-film reduces with increasing temperature. The shift of features in the PNR spin-asymmetries shown in Fig. 6.16 (c) and (d) can be explained by the temperature dependence of the position of magnetic interfaces. The broad CoFeB:Ta/ Ta cap structural interface in Fig. 6.18 (a) can be explained due to Ta diffusion into the CoFeB:Ta layer from the Ta capping layer. It also explains why the interfacial MDL thickness increases with increasing temperature. The local T_C of this compositionally-graded region determines the position of the effective magnetic interface.

As indicated by the shaded regions, the upper magnetic interface is shifted (5.2 ± 0.4) Å into the volume of the CoFeB:Ta thin-film at 0.1 T_C, and (9.4 ± 0.9) Å into the thin-film at 0.6 T_C, as similar to the structure on Si/SiO_2. This indicates MDL thickness increases as temperature increases. The lower magnetic interface is also shifted (5.3 ± 0.4) Å into the volume of the CoFeB:Ta thin-film at 0.1 T_C, and (8.5 ± 1) Å into the thin-film at 0.6 T_C. As the MDL appears to be confined to the intermixed interfacial region it is likely that the MDL forms as a result of interfacial intermixing at the CoFeB:Ta/substrate interface. Magnetic depth profiles of CoFe/GaAs(001) using PNR have previously been reported [158], but only at room-temperature where this corresponds to $T \sim 0.4\ T_C$ for a CoFe alloy. The magnetic depth of the CoFe layer was found to be reduced from the structural depth by around 6 Å. This MDL thickness is compatible with what was found here at a similar reduced temperature. Such MDLs at SC/FM interfaces are detrimental for spin-injection applications where the FM material directly adjacent to the SC is no longer actually ferromagnetic.

The chi-squared values obtained from low-temperature measurements are given in Fig. 6.19 as a function of layer numbers for the structures on (a) Si/SiO_2 and (b) GaAs(001) substrates at 0.1 T_C and 0.6 T_C. In both figures, the χ^2 values are higher in 1-Layer model with a uniform CoFeB:Ta layer, and χ^2 values decrease with increasing layer numbers of CoFeB:Ta thin-films. For the structure on Si/SiO_2, 3-Layers model gives the best fit of the PNR data. Adding further subdivisions of CoFeB:Ta thin-film to the model was tried, and resulted no improvement of the fit quality. Similar procedure was followed for the structure on GaAs(001), where the more accurate magnetic depth profile was obtained using 4-Layers model. Again, further subdivisions was resulted in no improvement of the fit quality. This modeling procedure provides a realistic description of the magnetic structure of the CoFeB:Ta thin-films.

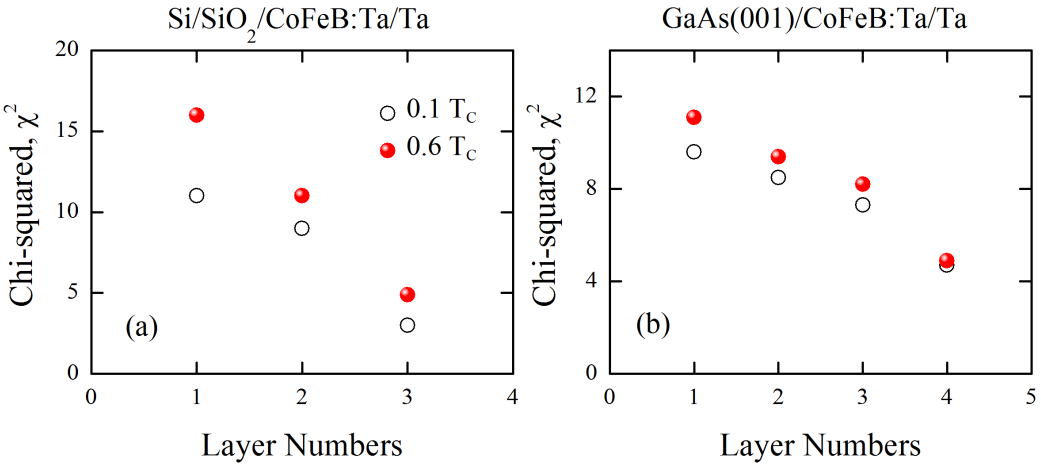

Fig. 6.19 The chi-squared, χ^2, values from low-temperature PNR measurements at 0.1 T_C and 0.6 T_C for the structure on (a) Si/SiO_2 and (b) GaAs(001) substrates.

6.4 Discussions in Literature

Interdiffusion is one of the most significant reason for MDL formations in FM thin-films. Incoming atoms with high kinetic energy penetrates into the adjacent layer, resulting in a reduction of magnetic moments of FM layer. Recently, the MDL formation in amorphous CoFeB layers with various top and bottom layers were investigated by Jang *et al.* [159], where the MDL thicknesses depend on the location of the adjacent NM layers, as shown in Fig. 6.21. The MDL thickness at Ru/CoFeB interface was found to be 0.20 nm, but 0.24 nm MDL formation has observed at CoFeB/Ru interface. Also, a 0.36 nm thick MDL at CoFeB/Ta interface was found, which is thicker than MDL at CoFeB/Ru interface. Since Ta (180.9 g) is heavier than Ru (101.1 g), Ta atoms can penetrate more deeply into the CoFeB.

The intermixing of both Ga and As in GaAs structures is a critical problem in spintronics devices. This appears unavoidable irrespective of the growth temperature, substrate orientation, and substrate reconstruction. During the deposition of Fe films on GaAs substrate at room-temperature, significant diffusion of Ga and As out from the substrate has been observed [160, 161]. In order to reduce diffusion effects low-temperature MBE growth of Fe on GaAs(001) has been used to enhance interface cleanliness by Lee *et al.* [162]. By reducing the GaAs substrate temperature, they could suppress both Ga and As out-diffusion from the substrate, and interfacial intermixing during Fe deposition.

Annealing is also a significant factor in MDL formation in FM thin-films. To measure the interface structure of Fe/AlGaAs(001) using high resolution TEM (HRTEM),

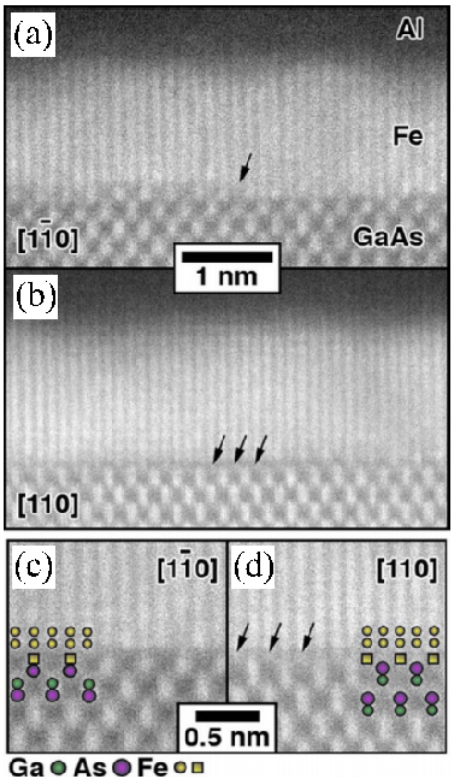

Fig. 6.20 High-angle annular-dark-field images of Fe/GaAs interface, viewed along (a) [1$\bar{1}$0] (b) [110]. Higher magnification images along [1$\bar{1}$0] and [110] are shown in (c) and (d), respectively. Adapted from [164].

Zega *et al*. [163] found that post-growth annealing of the structure results in a reduction of the intermixed interface width and an enhancement in spin injection. Lebeau *et al*. [164] extended this study for both GaAs(1$\bar{1}$0) and (110) directions to determine the interfacial structure of Fe/GaAs thin-film. They found As-terminated GaAs(001) and a partially-occupied, non-intermixed, interfacial Fe layer, terminating at the interface plane, after annealing as shown in Fig. 6.20.

The influence of thermal annealing on the Fe/GaAs(001) interface has shown that annealing temperatures between 400-450 °C promote the diffusion of both Fe into GaAs and Ga into Fe, resulting in $Fe_3Ga_{2-x}As_x$ alloy, because Fe is more weakly diffusive than Ga or As in this system [165]. Another study showed the formation of a MDL at the Co/GaAs interface due to Co_2GaAs formation. This inter-metallic layer causes decreasing Co magnetic moments due to the reaction of Co with the GaAs substrate [146]. Deposition of CoFe on GaAs substrate also showed an interface which consist of $(CoFe)_3GaAs$ magnetic alloy [158], where it is more pronounced in the Fe and Fe based alloys deposited on GaAs substrates which causes the formation of a MDL.

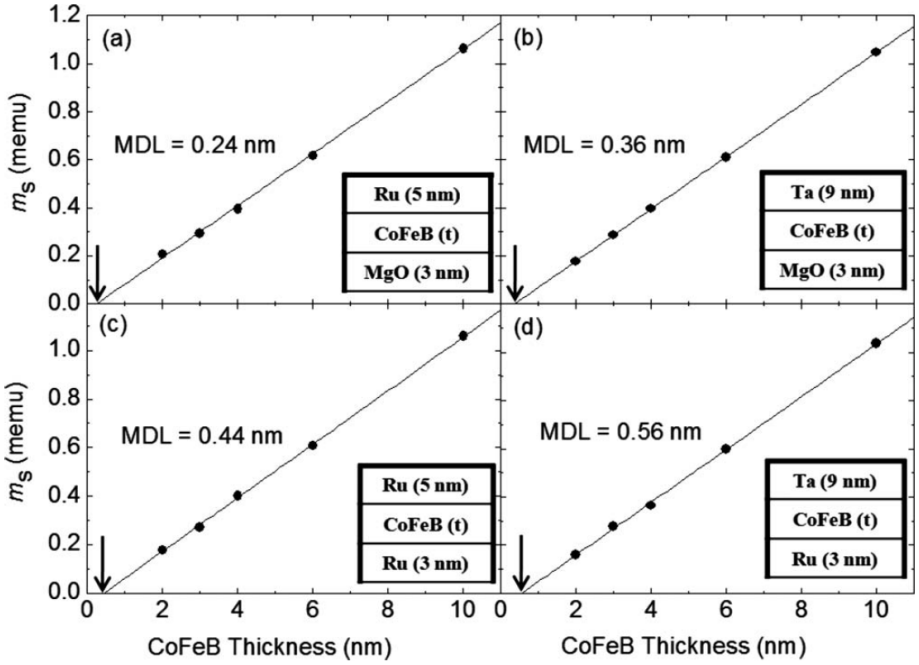

Fig. 6.21 Dependence of CoFeB thickness on the magnetization for different structures, measured by Jang *et al.* [159]. The magnetic dead layer thicknesses are indicated by arrows. The inset shows the stack structures.

Further studies on the influence of growth and annealing temperatures in epitaxially grown CoFe thin-films on GaAs(001) substrates have shown the thickest MDL at the CoFe/GaAs(001) interface occurs when the sample is grown at 95 °C, and the sharpest interface, when the sample is grown at −15 °C. Annealing for 1h at 250 °C produces an 11 Å interfacial MDL for samples grown at any temperature [166]. Another study has shown that after annealing at $T = 300$ °C, 0.2 nm thick TaB layer is formed at CoFeB/Ta interface which might be responsible for MDL formation which is due to out-diffusion of B atoms [167].

Most of the previous studies [147, 159] to determine MDL formations use conventional magnetometry, based on measuring magnetization as a function of ferromagnetic layer depth. Fitting the magnetization data with a straight line that passes through the origin is presented as evidence of the absence of MDL formation associated with the FM layer. However, if the fitting line passes from a certain FM layer thickness, the intercept shows the total MDL formation associated with the FM layer. Fig. 6.21 shows an example of MDL formations at CoFeB thin-films with various NM capping and seed layers using the method described above. Oguz *et al.* [147] studied MDL formations in CoFeB sandwiched with Ta layers, and they found 0.45 nm total MDL thickness from magnetometry data. In order to show MDL formation in each interface, they assumed the half of the total MDL thickness belongs to the

one interface, ~ 0.2 nm/interface. This approach to extract MDL thickness does not seem reliable because the MDLs depend on the location of the NM layer, as explained above. An important point is that these measurements are inferred from magnetometry data, rather than being true magnetization depth profiles. This unreliable method to indicate MDL formations at interfaces enhances the importance of our study presented here using PNR.

6.5 Chapter Conclusion

In this chapter, the depth-dependence of the magnetic structure in amorphous CoFeB:Ta/Ta thin-films on Si/SiO_2 and GaAs(001) substrates was studied using PNR as a function of measurement temperatures. An investigation of the structural properties of amorphous CoFeB:Ta thin-films were undertaken to confirm layer thickness and interface roughness. Then, temperature dependent magnetic characterization was performed in order to extract T_C of both structures. The PNR data of CoFeB:Ta thin-films were analyzed here using a "various layer" models where the model names are given according to subdivided CoFeB:Ta layers. This modeling procedure provided a realistic description of the magnetic structure of the samples. The amorphous CoFeB:Ta alloy has a reduced T_C due to addition of Ta. This allows investigation into interface magnetism and MDLs at temperatures close to the T_C. Such studies are not possible using conventional 3-d transition-metal ferromagnets as the high temperatures required promote interdiffusion and destroy the thin-film device structure.

The magnetic interface position corresponding to the CoFeB:Ta/Ta cap interface changes with temperature due to a compositional grading. This causes the local T_C of the interface to vary, where the magnetic depth varies with temperature. Onto both structures, a magnetic dead layer with ~ 5 Å thickness is formed at 0.1 T_C and the thickness increases to ~ 9 Å at 0.6 T_C. A dead-region forms at the GaAs(001)/CoFeB:Ta interface, where the depth of this region also varies with temperature, but is confined within an localized interfacial alloyed region. 5.3 Å dead-region forms at the GaAs(001)/CoFeB:Ta interface where increases to 8.5 Å with temperature, where such MDLs at III-V semiconductor/FM interfaces are detrimental for spin-injection applications. This shows the significant influence of subtle structural intermixing on magnetic thin-films where understanding of interfacial magnetism and MDL have critical importance for thin-film magnetic devices. As many spintronic devices work at elevated temperatures, these results show the influence of temperature on magnetic dead layer thicknesses.

7

Interfacial Structure Dependent Dynamical Properties of Cobalt Thin-Films

The generation of a spin-current in strongly spin-orbit coupled (SOC) materials continues to be extensively studied and may have a crucial importance due to its technological interest. Understanding of spin-currents, which traverse interfaces in ferromagnetic/non-magnetic (FM/NM) structures requires an understanding of the fundamental physics, and is required for applications of nanoscale magnetic systems in spintronics [2, 144, 168]. Precessional magnetization measurements have been widely used to access interfacial spin transport, where spin-current flows from the precessional motion of magnetization in a FM layer into an adjacent NM layer. Then, these pumped spin-currents in the NM layer are dissipated under the influence of the strong SOC which results in an enhancement of intrinsic damping in the FM layer [79]. This process is known as spin-pumping mechanism [66, 169].

In conventional spin-pumping theory [67, 78], the relaxation of spin-current in the NM layer is characterized by the interfacial spin-mixing conductance which is generally assumed to be a property of the NM material. However, a recent theoretical investigation by Liu *et al.* suggested a more complex picture of spin-pumping [81]. This investigation is based on a diffusion equation [170] which describes the enhancements of intrinsic damping for combinations of various materials [73]. In this model, the effective spin-mixing conductance consists of critical terms that quantify magnetic relaxation of the injected spin-current within the adjacent NM layers, and the ability of the spin-current to cross the FM/NM interface.

The latter is characterized by an effective specific interface spin-resistance, and the magnetic relaxation associated with crossing the FM/NM interface which is called spin memory loss parameter. Because of the interfacial spin-resistance and the spin memory loss details of the FM/NM interface structure have a significant impact in determining the contribution of magnetic damping due to spin-pumping mechanism [168, 171].

As the SOC plays a dominant role in magnetization dynamics, the nature of the atomic structure and crystallinity are also crucial factors for determining the magnetic properties of magnetic thin-films. The degree of texture and crystallite size present within thin-films are known to influence the magnetic behaviour of materials [87, 168]. To understand the role of texture on the dynamical properties the crystal structure of polycrystalline Co thin-films were investigated using high angle x-ray diffraction. This technique provides structural information on the out-of-plane crystal structure, average out-of-plane grain size, and any texture present within the layer, and was studied here as a function of Co film thickness.

In this chapter, the structural investigation of Co thin-films was discussed using x-ray diffraction pattern to derive crystal structure of thin-films. The intrinsic damping in polycrystalline Co thin-films of various thicknesses with Cu and Ir overlayers was investigated here to understand the role of local interface structure in spin-pumping mechanism. The key results relate to a deeper understanding of spin-mixing conductance, and they are compared with the other theoretical and experimental investigations.

7.1 Crystal Structure of Cobalt Multilayers

The structural characterization of polycrystalline Co thin-films with Cu and Ir overlayers was undertaken using x-ray diffraction (XRD) pattern which is described in this section to derive information on the nature of the crystal structure. Analysis of the crystalline structure of the polycrystalline thin-films provides crucial insight into material quality. Crystallinity and strain present within the film structure are significant in determining the magnetic properties of thin-films. Such structural properties of thin-films are sensitive to the film preparation technique and deposition rate [46].

Fig. 7.1 presents typical XRD patterns of Co[6 nm]/Ir thin-film scanned over a range of 2θ angles between 35° - 47° with CuKα x-rays. The diffraction pattern indicate four Bragg peaks located at $2\theta \sim 40°$, 42°, 43°, 44°. The shape of the diffraction peaks depends on the properties of the measured thin-film, i.e. defects, lattice strain, and grain size etc. Here, a broader peak located at $2\theta \sim 40°$ is the diffraction of x-rays from the amorphous Ta

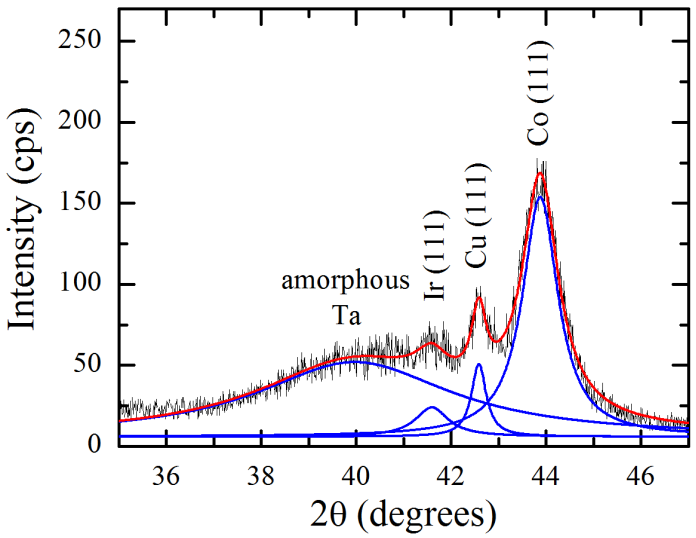

Fig. 7.1 X-ray diffraction pattern of 6 nm Co thin-film with Ir overlayer.

seed-layers and overlayers. From XRR analysis, a few nm thick Ta oxide layer is expected to form above Ta capping layer. Hence, this broadening of diffraction peak may be caused by an oxidized Ta layer. The diffraction peaks located at $2\theta \sim 42^\circ$ and 43° correspond to fcc(111) Ir peak above the Co layer, and fcc(111) Cu peak under the Co layer, respectively. The diffraction peaks of Co layers are discussed in detail in the next section.

Fig. 7.2 shows diffraction patterns of Co/Cu thin-films between 42.5° - 46° for various Co thicknesses. Here, the dashed and solid lines pass through in the middle of diffraction peaks of the thinnest and thickest Co films. The diffraction patterns indicate that Co peaks move away from the peak of Cu seed-layer with increasing Co layer thickness, where dislocations begin to nucleate, and this causes relaxation of epitaxial strain. Diffraction peak positions and FWHM were obtained by fitting the XRD patterns using Lorentzian peak functions. For each multilayer, Scherrer analysis revealed that the width of the diffraction peaks reduces with increasing Co layer thickness, which indicates increasing grain size as a function of Co thickness for both thin-films. The structural parameters including Bragg diffraction angle, *d*-spacing, and grain sizes using Scherrer analysis, and FWHM of polycrystalline Co thin-films with both overlayers are summarized in Table 7.1.

The inverse Co thickness dependence of the diffraction peak positions are shown in Fig. 7.3 for structures with both overlayers, where the diffraction peaks move in the same way for both overlayers. As this is relaxation of epitaxial strain from the Cu seed-layer, this justifies the inverse Co thickness dependence of diffraction peaks.

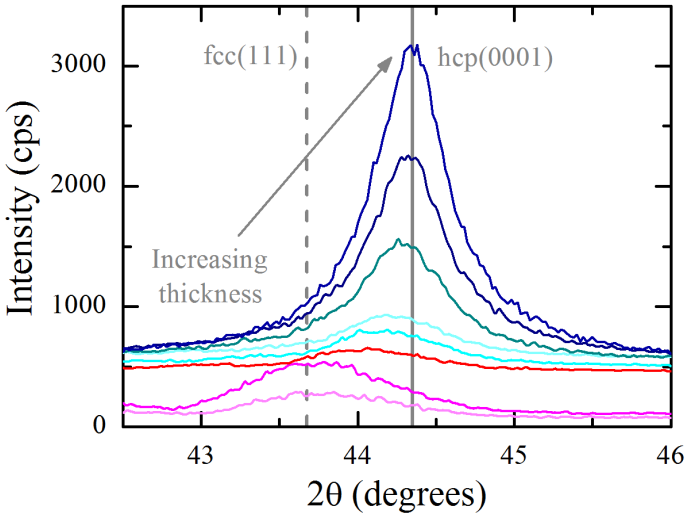

Fig. 7.2 X-ray diffraction pattern of polycrystalline Co/Cu thin-films with various Co thicknesses. X-ray diffraction peaks shift toward the higher 2θ angles with increasing Co thicknesses. The dashed and solid lines pass through in the middle of diffraction peaks of the thinnest and thickest Co films, respectively. The arrow indicates how diffraction peaks shift with increasing Co thickness.

Some materials may exist in several different phases with different crystal structures associated with each phase. The structure of Co on Cu(111) layer is a complicated structure, where the formation of Co is in either fcc or hcp structural phase. It is known that the initial

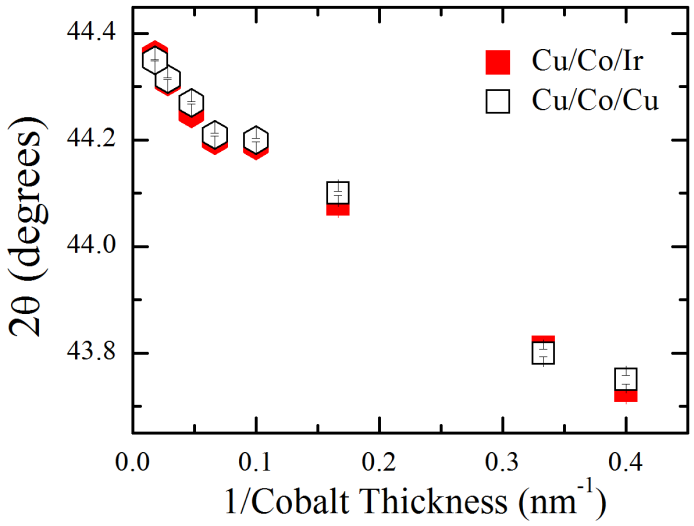

Fig. 7.3 Inverse Co thickness dependent diffraction peak points of polycrystalline Co thin-films with Cu and Ir overlayers. Squares and hexagons represent dominant fcc(111) and hcp(0001) texture in the Co layer, respectively. The vertical lines indicate the errors on the data points.

Table 7.1 Comparison of Bragg peak position, the d-spacing, average out-of-plane grain size deduced via the Scherrer analysis using FWHM values of polycrystalline Co thin-films with Cu and Ir overlayers.

Overlayer	t_{Co} (nm)	Diffraction angle (degrees)	d-spacing (nm)	FWHM (degrees)	Grain Size (nm)
Cu	2.5	43.75 ± 0.02	2.066 ± 0.001	1.05 ± 0.03	7.6 ± 0.2
	3	43.80 ± 0.01	2.064 ± 0.001	0.97 ± 0.02	8.1 ± 0.2
	6	44.10 ± 0.01	2.051 ± 0.001	0.90 ± 0.02	8.7 ± 0.2
	10	44.20 ± 0.01	2.047 ± 0.001	0.80 ± 0.02	9.8 ± 0.1
	15	44.21 ± 0.01	2.046 ± 0.002	0.78 ± 0.01	10.1 ± 0.3
	21	44.27 ± 0.01	2.044 ± 0.002	0.70 ± 0.01	11.3 ± 0.3
	35	44.32 ± 0.01	2.042 ± 0.001	0.63 ± 0.01	12.6 ± 0.3
	55	44.35 ± 0.01	2.040 ± 0.002	0.59 ± 0.01	13.4 ± 0.3
Overlayer	t_{Co} (nm)	Diffraction angle (degrees)	d-spacing (nm)	FWHM (degrees)	Grain Size (nm)
Ir	2.5	43.74 ± 0.02	2.068 ± 0.001	1.34 ± 0.03	5.9 ± 0.2
	3	43.81 ± 0.01	2.064 ± 0.001	1.11 ± 0.01	7.1 ± 0.2
	6	44.08 ± 0.01	2.052 ± 0.001	1.04 ± 0.03	7.6 ± 0.2
	10	44.19 ± 0.01	2.047 ± 0.001	0.91 ± 0.02	8.7 ± 0.1
	15	44.20 ± 0.01	2.047 ± 0.001	0.83 ± 0.02	9.5 ± 0.3
	21	44.25 ± 0.01	2.044 ± 0.001	0.72 ± 0.01	11.1 ± 0.3
	35	44.31 ± 0.01	2.042 ± 0.001	0.65 ± 0.01	12.2 ± 0.3
	55	44.36 ± 0.01	2.039 ± 0.001	0.59 ± 0.01	13.6 ± 0.3

stages of Co film deposited on Cu seed-layer are dominated by fcc(111) Co up to several nanometers, with a small fraction of stacking faults. As the Co layer thickness increases hcp stacking faults are introduced, and the subsequent Co film gradually transforms into hcp(0001) structure. Previous studies of Co/Cu thin-films have shown that for Co films less than 4 nm, a fcc Co structure is stable, and a mixture of fcc and the hcp crystal phases occur with increasing Co layer thickness [172]. To investigate this structural phase transition in the Co thin-films, XRD measurements were used to determine the thickness dependence of interplanar spacing.

The distance between two adjacent planes of atoms is called interplanar spacing or d-spacing. The d-spacing of structures with Cu and Ir overlayers as a function of inverse Co thickness are extracted from XRD measurements using Bragg's Law, see Section 4.3 for details, as shown in Fig. 7.4 (a). The corresponding bulk values for hcp Co along the

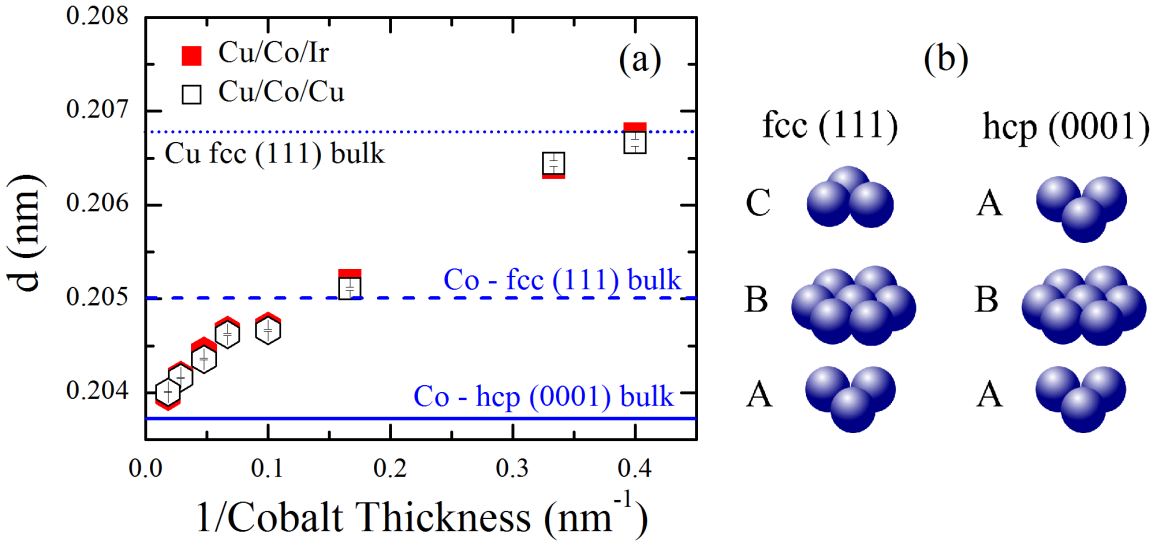

Fig. 7.4 (a) Inverse Co thickness dependence of the d-spacing of polycrystalline Co thin-films with Cu and Ir overlayers, extracted from XRD measurements using Scherrer relation. Squares and hexagons represent dominant fcc(111) and hcp(0001) texture in the Co layer, respectively. Solid line corresponds to d-spacing of bulk hcp(0001) Co, dashed and dotted lines correspond to d-spacing of bulk fcc(111) Co and fcc(111) Cu, respectively. (b) The representation of fcc(111) and hcp(0001) layer stacking sequence.

(0001) direction is 0.2035 nm (shown by solid line), and 0.205 nm (shown by dashed line) for fcc(111) Co [173], where the bulk value for fcc(111) Cu is shown by dotted line above. Here, squares and hexagons represent the dominant fcc(111) and hcp(0001) crystal structure in the Co layer, respectively. Thicker and thinner Co layers are separated from each other, which indicates the formations of hcp(0001) and fcc(111) structure in the Co layers. Structures with 6 nm Co layers are between thicker and thinner Co films. This suggest that increasing Co layer thickness beyond $t_{Co} \sim 6$ nm, hcp stacking faults occur, and a dominant hcp (0001) bulk-like structure develops. The d-spacing of thicker Co films are close to the hcp(0001) bulk value because these films have less strain and thus relax as the Co thickness increases to the bulk value. However, thinner Co films have d-spacing far above fcc(111) bulk of 0.205 nm, where strain develops at the initial Co layers, and close to the fcc(111) bulk of Cu layer. This is because the value for the perpendicular d-spacing for thinner Co films which conserves the unit-cell volume when the in-plane lattice parameter is matched with Cu.

In crystallography, a disruption of the long-range stacking sequence produces a crystal defects, called stacking faults. They occur in many crystal structures, but mostly appear at the close-packed structures. The representations of fcc and hcp layer sequence are given in Fig. 7.4 (b). A change of local region in crystal by removing/introducing external layers

produces stacking faults which destroy the perfection of the ideal structure. It is well-known that fcc structures differ from hcp only in stacking order, where both of them have close packed planes. In the fcc(111) lattice structure, the pattern consists of an ABCABC layer stacking sequence, and the pattern consists of an ABAB layer stacking sequence for hcp(0001) lattice structure. As shown in Fig. 7.4 (b), the first two layers arrange themselves identically as "AB" arrangements in both structures. A stacking fault appears in an fcc structure as one of the "C" planes missing, where the pattern would become ABC**ABAB**CAB. The placing of a plane in the "A", rather than "C" position results in a thin layer of hcp-like material. The difference between hcp and fcc Co crystal phases is that the atomic layer stacking sequence within the Co film differs moving away from the interface. Considering the final atomic plane of the Co layer to be the "A" lattice place, the crystal structure near to the interface may appear for fcc(111)-Co as **ABCA**/fcc(111)-NM, whereas for hcp(0001)-Co it would appear **BABA**/fcc(111)-NM. The importance of this subtle difference is shown to have a significant influence on dynamic magnetic properties.

The average grain size in the crystal was calculated from XRD pattern using the Scherrer relation [174] which gives an expression for broadening of diffraction peaks. Fig. 7.5 shows the variation of grain size as a function of Co thickness for thin-films with Cu and Ir overlayers. Here, it is observed that the increase of Co film thickness increases the diffraction peak intensity as expected, and which results in an increase in grain size of both thin-films. The increase of grain size as a function of Co thickness can be also attributed to the improved crystallinity of the films structure, where growth onto the seed-layer causes the film to grow coherently. Also, thin-films with Cu overlayers have larger grain size than thin-films with Ir overlayers. This is believed due to the higher lattice mismatch between Co and Ir overlayers ($\sim$8%) [133], compared to Co and Cu ($\sim$1.8%) [175]. Thus, Co/Cu interface appears as a single grain to the diffraction measurement due to the similar lattice parameters, whereas Co/Ir interface appears as a clear grain-boundary as the atomic registry across the Co/Ir interface is poor.

A schematic illustration of lattice match, lattice mismatch, and strain relaxation between two layers are also given in Fig. 7.5. Perfectly matched lattices are desired for many applications of spintronics to minimize defects between deposited layers. If the lattice mismatch between those is larger, the film may strain to form the lattice structure on the substrate surface during the initial stages of the deposition. Thin film deposition can proceed by several growth modes, as explained in Section 3.1. The Stranski-Krastanov growth mode is the most common mode for polycrystalline materials, where these thin-films would be grown as layer-plus-island mode. Here, Co layers are initially grown on the Cu surface as

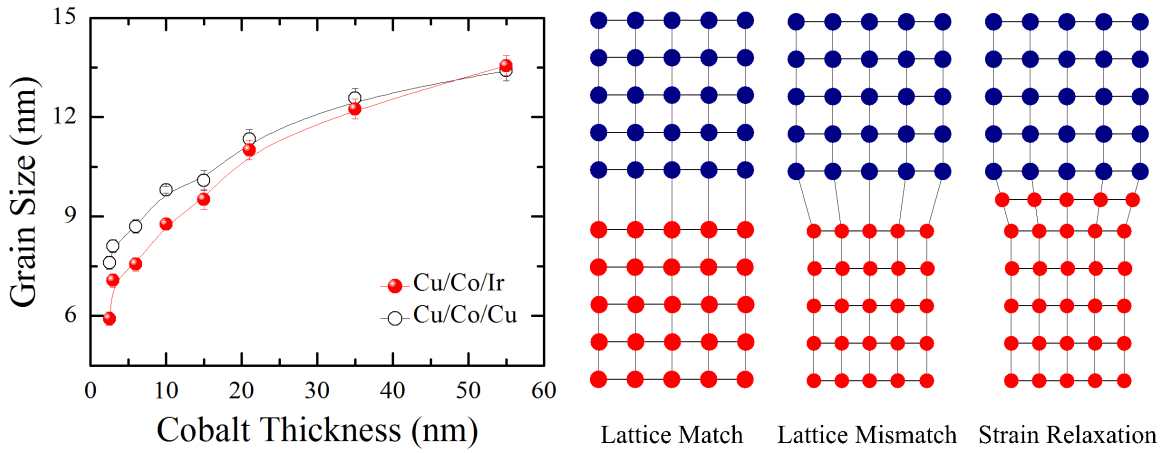

Fig. 7.5 Average out-of plane crystal grain size within Co thin-films with Cu and Ir overlayers. The grain size was calculated from FWHM of fits to diffraction peak using Lorentzian fit. The solid lines are guide to the eye. (Right) The representation of lattice match, lattice mismatch and strain relaxation at FM/NM interface.

layer-by-layer mode up to several monolayers, where strain energy accumulates in initial Co layers. Then layer relaxation starts, which results in switching of the growth mode to island like epitaxy formation. Beyond a critical Co thickness these layers have less strain from the Cu seed-layer.

7.2 Thickness Dependence of Magnetic Parameters

This section explains the extraction of the magnetic parameters from ferromagnetic resonance (FMR) measurements. The resonance condition for a polycrystalline FM thin-film, which is magnetically saturated in the film plane, can be described from fitting the FMR spectrum using the Kittel relation, Eq. 2.25, as given in Section 2.8.1. An example of FMR spectra and a best-fit to the Kittel equation for a Co[55 nm]/Ir sample are shown in Fig. 7.6 (a) to extract saturation magnetization M_S, the perpendicular surface magnetic anisotropy constant K_S and g-factor.

For a continuous polycrystalline thin-film of thickness t_{FM}, the effective demagnetization field, $4\pi M_{eff}$, is given in Eq. 2.26 with M_S and K_S. It has been shown previously that interfacial effects can show a linear dependence on inverse of the FM layer thickness [91, 138, 139]. In most FMR analysis, the $4\pi M_{eff}$ data as a function of inverse FM thickness is fitted linearly for entire FM thickness range. However, the data are not well described using this approach, as shown in Fig. 7.7 (a), where there is some noticeable difference between

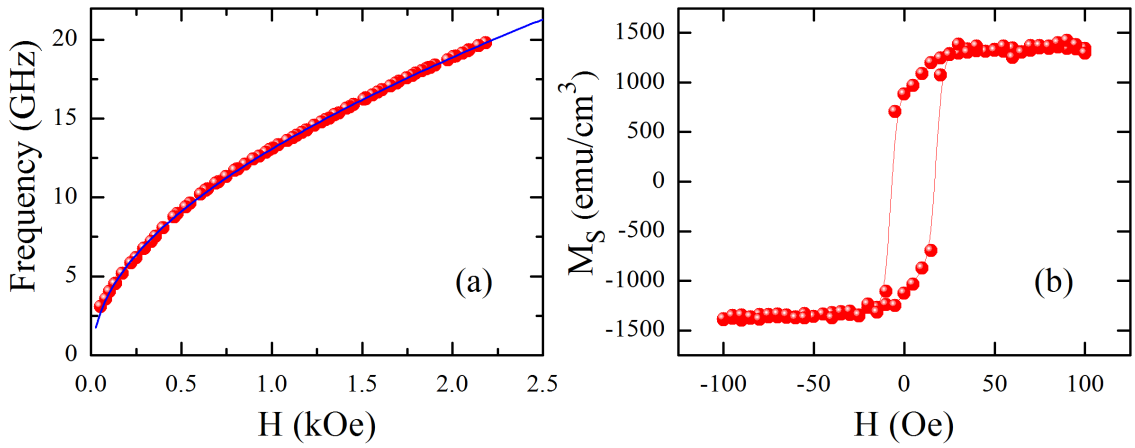

Fig. 7.6 (a) An example of resonance frequency as a function of magnetic field for Co[55 nm]/Ir thin-film and a fit to the Kittel formula [110]. (b) An example of hysteresis loop for Co[55 nm]/Ir thin-film.

thin and thick Co films. This is the main reason why XRD measurements are investigated in this work to determine the interplanar spacing, as explained in Section 7.1.

Instead of this conventional method, a new approach is required to describe magnetic properties of FM thin-films more accurately. In doing so, the data are divided into two categories defined as the thin and thick Co film regions, and each thickness region has been analyzed independently using Eq. 2.26 to determine the magnetic parameters of each dominant region. The inverse Co thickness dependence of $4\pi M_{\text{eff}}$ for structures with Cu and Ir overlayers are shown in Fig. 7.7 (b). $4\pi M_{\text{eff}}$ has the same value for structures with the same Co thickness but different overlayers. This indicates that the Cu and Ir overlayers do not significantly influence the anisotropy field or M_S. Previously, this was found for Pt/Co/Ir multilayers [176], where the anisotropy mostly emerges from Pt/Co not the Co/Ir interface.

In each thickness regime, as shown in Fig. 7.7 (b), there is a clear Co thickness dependence of $4\pi M_{\text{eff}}$, where it decreases linearly with increasing inverse Co thickness. This indicates that these variations are linked to crystalline state. Here, the dashed line is the best fit to films with Co thickness less than or equal to 6 nm, and the solid line is a fit to the thicker Co films. The best fit to the experimental data enables extraction of the bulk M_S and K_S of Co thin-films with fcc(111) and hcp(0001) structural phases. Bulk M_S values are taken to be size independent in most studies, it is shown that bulk M_S values show variations in each crystal phase.

In hcp(0001)-dominated structures saturation magnetization is found as $M_S = 1470 \pm 40$ emu/cm^3 and $M_S = 1470 \pm 60$ emu/cm^3, and in fcc(111)-dominated structures saturation magnetization is $M_S = 1100 \pm 100$ emu/cm^3 and $M_S = 1200 \pm 200$ emu/cm^3 for structures

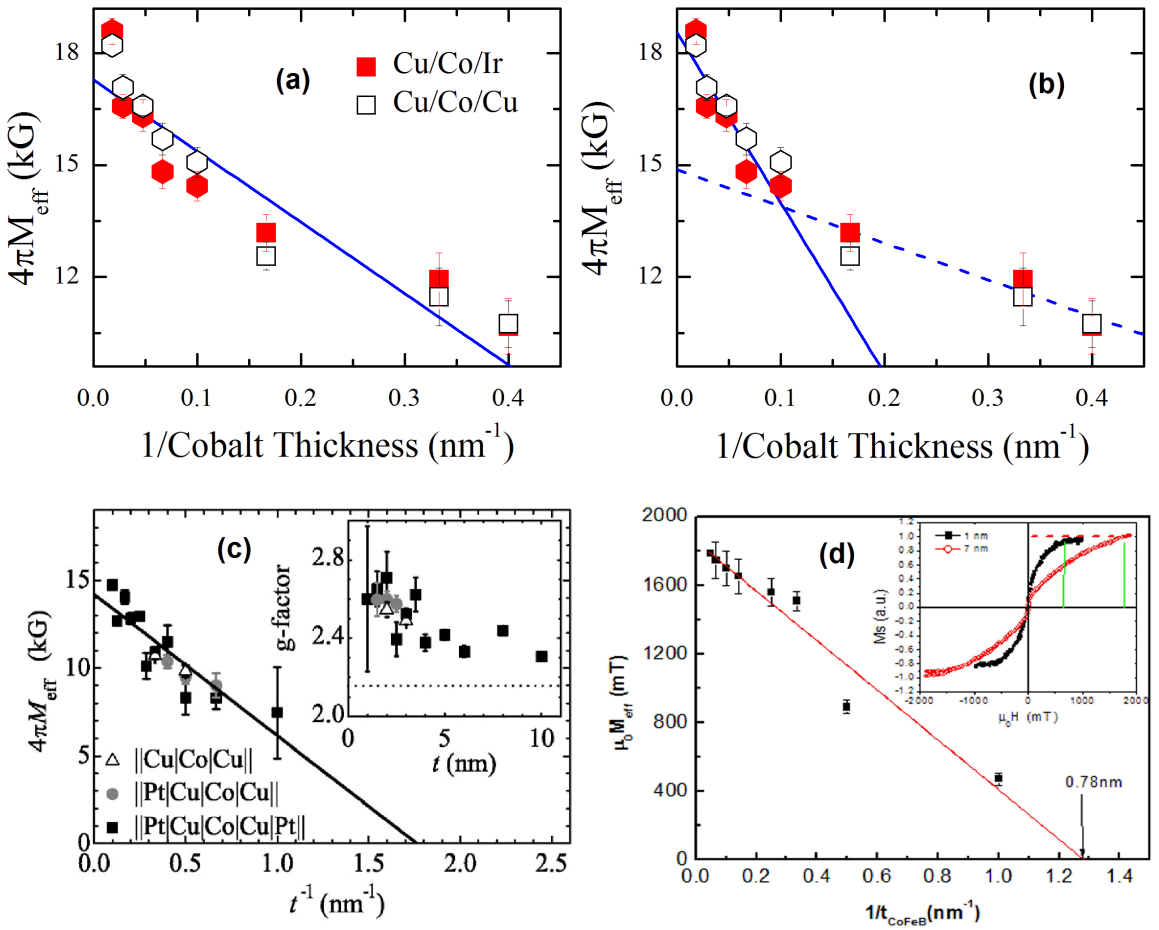

Fig. 7.7 (a) Inverse Co thickness dependence of the effective demagnetization field, $4\pi M_{\text{eff}}$. All data are fitted linearly (solid line) using standard approach for entire Co thickness range. (b) Here, the data are divided into thin and thick films where the solid and dashed lines are representative linear fits to Co thicknesses greater and less than 6 nm. Squares and hexagons in (a) and (b) represent dominant fcc(111) and hcp(0001) texture in the Co layer, respectively. (c) Inverse Co thickness dependence of $4\pi M_{\text{eff}}$ where the solid line is the best fit based on Eq. 2.26, measured by Beaujour *et al.* [52]. The inset shows the Co thickness dependence of the g-factor, where the dotted line shows the reported $g_{\text{bulk}} = 2.15$ for fcc Co films [177]. (d) Inverse CoFeB thickness dependence of $4\pi M_{\text{eff}}$ measured by Liu *et al.* [178].

with Cu and Ir overlayers, respectively. These values are consistent with the bulk hcp Co magnetization density $M_S \sim 1400$ emu/cm^3 [129], as shown in Fig. 7.6 (b). The surface anisotropy constant for hcp(0001)-dominated structures are $K_S = -2.8 \pm 0.4$ erg/cm^2 and $K_S = -3.3 \pm 0.5$ erg/cm^2 for structures with Cu and Ir overlayers, respectively. These values are the same within experimental error. This large surface anisotropy arises from the volume of the hcp phase, where the c-axis of the hcp Co is perpendicular to the plane of the film. The surface anisotropy constant K_S for fcc(111)-dominated structures are

$K_S = -0.42 \pm 0.05$ erg/cm^2 and $K_S = -0.56 \pm 0.06$ erg/cm^2 for structures with Cu and Ir overlayers, respectively. These values are not identical within experimental error, but close to each other. Here, the negative sign of surface anisotropy constant reflects a perpendicular component of the magnetic anisotropy. All extracted values are of Co thin-films with fcc(111) and hcp(0001) structural phases are given in Table 7.2, and are comparable to those found in the literature [179–181].

There are several FMR studies in the literature that extract the magnetic properties of thin-films using the conventional method consisting of a single linear fit to the inverse thickness dependence data. An investigation of polycrystalline Co thin-films, similar to the structure studied here, was carried out previously by Beaujour *et al.* [52], where they obtained the magnetic parameters using the standard approach, as shown in Fig. 7.7 (c). The data are fitted across the entire Co thickness range using Eq. 2.26. The saturation magnetization of Co was extracted from the slope as M_S = 1131 emu/cm^3, which is much smaller than the magnetization density of bulk Co thin-films. However, the best fit does not describe most of the $4\pi M_{\text{eff}}$ data, thus the crystal phase of the structure should have been taken into account during data fitting. It needs to be pointed out that the Co crystal phase may be different depending on what material the Co is grown on, hence making the comparison between datasets is difficult. In another study, shown in Fig. 7.7 (d), the magnetic damping of CoFeB thin-films were measured by Liu *et al.*, and the linear fit of $4\pi M_{\text{eff}}$ does not describe the thinnest three data points. Hence, the reliability of conventional method needs to be reconsidered because these experimental results are crucial for magnetization dynamics.

The determination of the g-factor (or spectroscopic g-factor) in FMR investigations is sometimes difficult in thin-film limit as a function of layer thickness due to larger uncer-

Table 7.2 Parameters extracted from spin-pumping measurements: saturation magnetization, M_S; surface magnetic anisotropy constant, K_S; and bulk g-factor, g_{bulk} showing comparison with relevant literature values. The literature value for K_S quoted for comparison from Ref. [177] is taken as negative due to a difference in sign convention.

Spin-pumped interface(s)	M_S (emu/cm^3)	K_S (erg/cm^2)	g_{bulk}
hcp(0001)-Co/Cu/Ta	1470 ± 40	-2.8 ± 0.4	2.07 ± 0.01
fcc(111)-Co/Cu/Ta	1100 ± 100	-0.42 ± 0.05	2.19 ± 0.02
hcp(0001)-Co/Ir/Ta	1470 ± 60	-3.3 ± 0.5	2.09 ± 0.01
fcc(111)-Co/Ir/Ta	1200 ± 200	-0.56 ± 0.06	2.21 ± 0.02
Ta/Cu/Co/Cu/Pt – Ref. [177]	1456	-1.04	2.15
Pt/Cu/Co/Cu/Pt – Ref. [52, 180]	1131	-0.46 ± 0.04	2.49 ± 0.14

tainties [182]. To determine the g-factor spectroscopic data was used, thus the correct term for the g-factor is the spectroscopic g-factor, rather than Landé g-factor [183]. The term Landé g-factor is only correct in an isolated atom where the spin-orbit coupling is well defined. The g-factor, as explained in Section 2.1, is determined from γ values extracted from fitting of the FMR spectra with Eq. 2.25. The common assumption in the literature is to describe the bulk g-factor, based on fitting the data linearly for the entire thickness range. Also, obtaining a weighted average value of g-factor is another way to estimate the bulk g-factor [180], where it is found as g_{bulk}= 2.25 [184] and $g_{\text{bulk}} = 2.49 \pm 0.14$ for sputtered Co thin-films, as shown inset of Fig. 7.7 (c). This is significantly larger than the reported value for fcc Co films (g_{bulk} = 2.15 [177]), as shown by a dotted horizontal line. The thickness and crystal structure of polycrystalline thin-films should be considered in order to determine these magnetic parameters of thin-films. The g-factor relates the spin and orbital components of atomic moments where $g = 2 + (2m_L/m_S)$. Here m_L is normally quenched toward zero by the crystal field breaking rotational symmetry. When the crystal is truncated, this quenching is reduced and m_L increases.

In Fig. 7.8 (a), the data are fitted linearly for entire Co thickness range using the conventional method to describe bulk g-factor, it is clear that most of data points are not described well by this fit. Contrary to the standard approach in the literature, it is shown here that the data are clearly not independent of Co thickness. Again, after dividing the Co thin-films

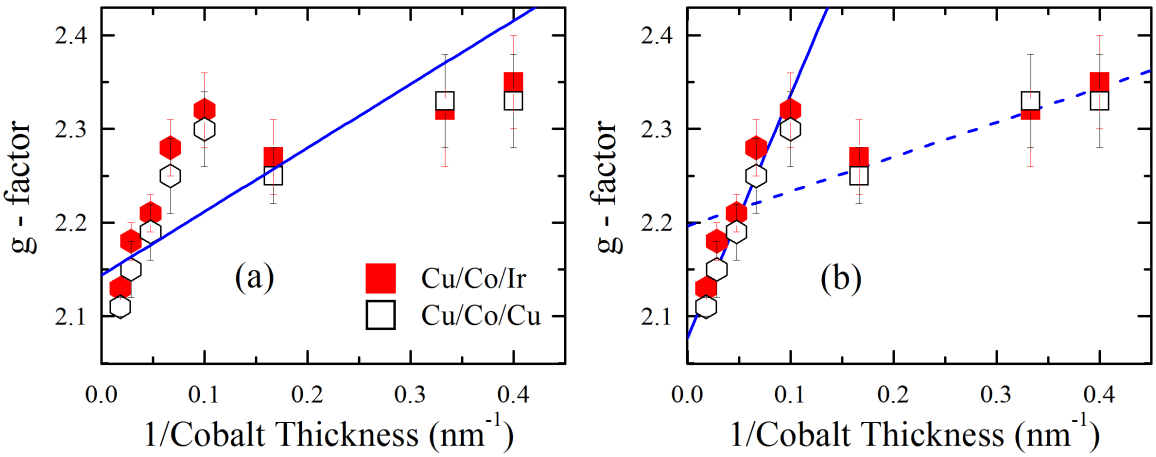

Fig. 7.8 Inverse Co thickness dependence of the g-factor for polycrystalline Co thin-films with Cu and Ir overlayers. (a) The data are fitted linearly using conventional method for entire Co thickness range. (b) The data are divided into thin and thick Co films where the solid (dashed) lines are representative linear fits to thicknesses greater (less) than 6 nm. Squares and hexagons represent dominant fcc(111) and hcp(0001) texture in the Co layer, respectively.

into two thickness regimes, as fcc(111) and hcp(0001) Co, it is observed that there are linear dependencies on inverse Co thickness for each phase, as shown in Fig. 7.8 (b). This is indicative of crystallographic effects with different behaviour for Co films in the thinner and thicker regimes. Also, in most of the samples, the g-factor for Co/Ir thin-films appears to be slightly larger than for Co/Cu thin-films. The standard explanation of a larger g-factor in Co/Ir thin-films would be due to a difference of spin-orbit interactions (SOI). This may be a result of a non-local SOI across the FM/NM interface [90, 185], which may be expected to appear in the magnetic anisotropy, g-factor, and the relative orbital and spin components of magnetic moments.

From the intercepts of the linear fits, bulk g-factors, g_{bulk} were estimated. For the fcc(111)-dominated structures the bulk g-factors obtained were $g_{\text{bulk}} = 2.07 \pm 0.01$ and $g_{\text{bulk}} = 2.09 \pm 0.01$, and in the hcp(0001)-dominated structures $g_{\text{bulk}} = 2.19 \pm 0.02$ and $g_{\text{bulk}} = 2.21 \pm 0.02$ for structures with Cu and Ir overlayers, respectively. The g-factor for both thin-films shows a Co thickness dependence due to crystal phases, where it decreases slightly with increasing Co thickness in both thickness regimes. The bulk values are similar to the values found elsewhere [52, 186]. In bulk Co, the orbital magnetic moment is largely quenched, however this quenching may be reduced at the interfaces, where the crystal symmetry is broken. A slight increase in orbital magnetic moment may enhance the g-factor due to reduced quenching of orbital moments at the interfaces. This explains the linear reduction in the g-factor, when the inverse Co film thickness reduces.

The films with larger g-factor may have larger magnetic anisotropy, which should be related to enhanced orbital moments at the Co/NM interfaces. Thus, Co thin-films with larger g-factor should also have larger interface anisotropy. However, comparing the $4\pi M_{\text{eff}}$ data in Fig. 7.7 (b), where the anisotropy is given by the slopes for each crystal phase, with g-factor in Fig. 7.8 (b), it is clear that there is no particular correlation between the g-factor, via enhanced orbital moments and surface anisotropy constant.

7.3 FMR Linewidth of Cobalt Multilayers

This section describes the investigation of FMR linewidth for Co thin-films with Cu and Ir overlayers. The lineshape of the FMR absorption is a typical Lorentzian shape. The FMR linewidth was used mostly as a measure of the magnetization relaxation rate, which is related to the magnetic damping of the system. The FWHM of the absorption curve, from fitting to a Lorentzian peak function, defines the FMR linewidth and includes significant information

about the magnetic relaxation of the structure. Fig. 7.9 shows an example of the measurement transmission parameter S_{21} as a function of applied magnetic field at microwave frequency of 15 GHz for the Co[55 nm]/Ir thin-film and the best-fitting Lorentzian peak function, as indicated by the solid line.

The frequency dependence of the in-plane FMR linewidth, ΔH, is shown in Fig. 7.10 for structures with (a) Ir and (b) Cu overlayers as a function of Co thicknesses. This shows a clear increase in ΔH on reducing the Co thickness, as indicated by arrows. For both thin-films with Co thicker than 6 nm, ΔH increases linearly with frequency over the entire experimental frequency range. However, for Co thickness equal to or thinner than 6 nm, ΔH becomes increasingly non-linear as a function of frequency, although there is less non-linearity of ΔH in the Co/Cu thin-films compared to the Co/Ir thin-films. Two-magnon scattering, which comes from coupling between the uniform FMR mode and degenerate spin waves, may be the reason for this non-linear behaviour, where this mechanism leads to an additional magnetic relaxation channels [187].

There are two different mechanisms to describe FMR linewidth as given in Eq. 2.28. The first term here is the so called extrinsic linewidth, ΔH_0, defined as zero-frequency intercept of the frequency dependence of the linewidth. It represents the linewidth broadening resulting from magnetic inhomogeneities such as local fluctuations of the magnetization and magnetic anisotropy, and polycrystallinity, which is assumed to be independent of the frequency. The

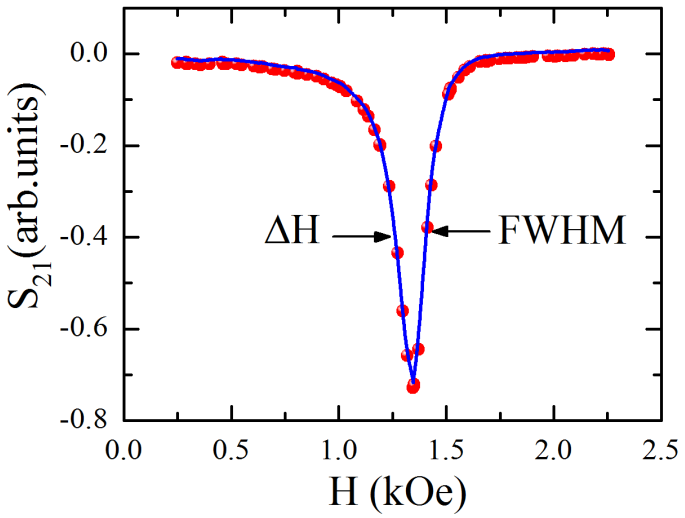

Fig. 7.9 An example of the experimental microwave transmission parameter S_{21} as a function of magnetic field at 15 GHz for the Co[55 nm]/Ir thin-film. FWHM of the curve enables to estimate FMR linewidth of the thin-film.

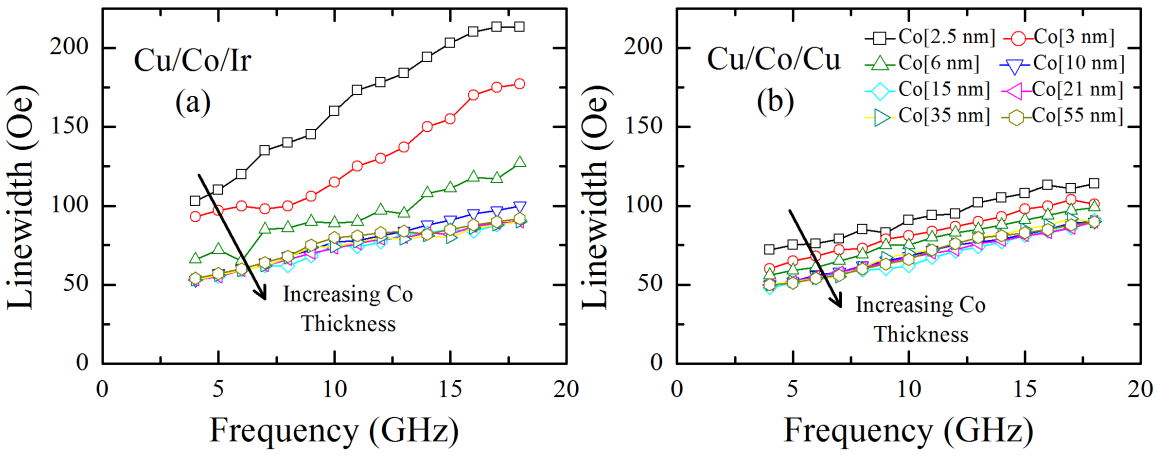

Fig. 7.10 Frequency dependence of FMR linewidth for polycrystalline Co thin-films with (a) Ir and (b) Cu overlayers. The arrows denote increasing Co thickness. Datamarkers represent the same Co thickness for (a) and (b).

second mechanism is known as intrinsic damping of the magnetization which enables to define the true Gilbert damping parameter.

In polycrystalline materials, stacking faults result in magnetic inhomogeneity (e.g. local variation in demagnetization and magnetocrystalline anisotropies) which appears as an inhomogeneous linewidth broadening. The dependence of inhomogeneous line broadening, ΔH_0, as a function of Co thickness is shown in Fig. 7.11 (a), where it increases with reducing Co thickness for both thin-films. Here, ΔH_0 is largely independent of Co thickness for thicknesses above 6 nm. However, for Co thickness of 6 nm and below, ΔH_0 increases strongly with reducing Co thickness for both overlayers. Also, ΔH_0 is smaller for Cu overlayers than for Ir overlayers for all Co thicknesses. FMR linewidth for polycrystalline Co films sandwiched between Cu/Pt layers exhibit similar thickness dependence of ΔH_0, and it approaches to zero for Co layers thicker than 6 nm. This reflects the good quality of these layers [52].

Fig. 7.11 (b) shows ΔH_0 as a function of the inverse Co thickness for both thin-films, where the slope and the intercept of ΔH_0 give volume and interfacial components. Here, there is a slight difference in the slope between Co films with Cu and Ir overlayers. This difference may be attributed to an increased density of stacking faults at the Co/Ir interface in comparison to Co/Cu interface, due to the larger lattice-mismatch between Co and Ir ($\sim$8%) [133] compared to Co and Cu ($\sim$1.8%) [175]. However, the exact origin of the small but significant difference in intercept between the two sets of thin-films, relating to slight differences in "bulk" structural and magnetic defects in the polycrystalline Co film with Cu and Ir overlayers, is presently unclear.

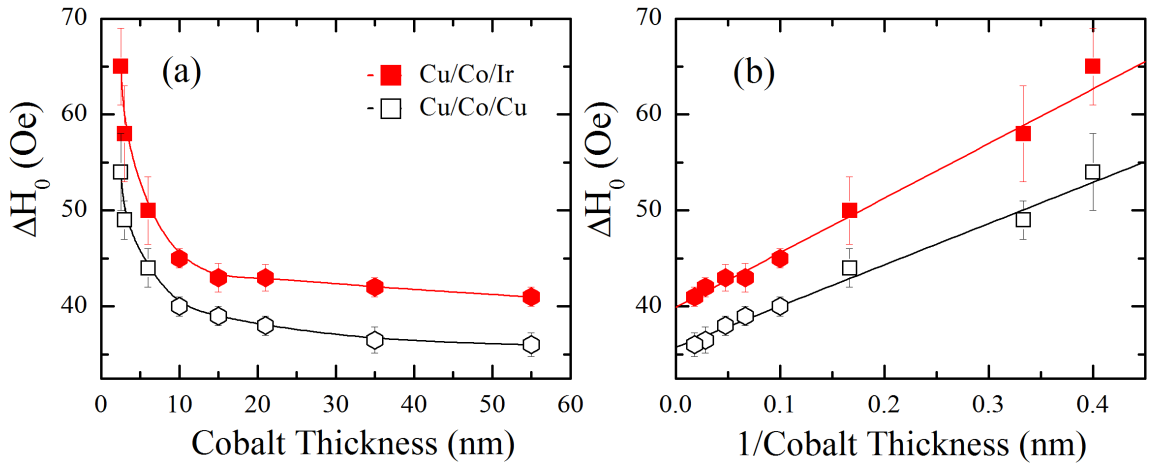

Fig. 7.11 (a) Dependence of Co thickness on the extrinsic linewidth ΔH_0 for structures with Cu and Ir overlayers. The solid lines are guide to the eye. (b) Inverse Co thickness dependence of the extrinsic linewidth for both thin-films. The solid lines are linear fits to the data. Squares and hexagons represent dominant fcc(111) and hcp(0001) texture in the Co layer, respectively.

7.4 Spin-Pumping in Complex Heterostructures

This section describes the multilayered sample structure used in this work to describe the spin-pumping mechanism. Here, a Co layer is sandwiched between NM layers in symmetric (Ta/Cu underlayers and Cu/Ta overlayers) and asymmetric (Ta/Cu underlayers, Ir/Ta overlayers) structures in order to demonstrate the role of local interface structure in spin-pumping mechanism. In this work, Cu was used here due to its poor sink property for the pumped spins (less SOI), and Ir was chosen because it is a good spin absorber (strong SOI). Fig. 7.12 shows a schematic illustration of the thin-film structures and possible spin-currents.

The precession of the magnetization in the Co layer, $M(t)$, generates spin-currents $J^{\mathrm{L}}_{\mathrm{s\ pump}}$ and $J^{\mathrm{R}}_{\mathrm{s\ pump}}$ which can traverse from the Co layer into both adjacent NM layers, $\mathrm{NM}^{\mathrm{L}}_1$ and $\mathrm{NM}^{\mathrm{R}}_1$. This mechanism provides two parallel channels for energy dissipation. In the steady state, this injected spin-current may relax within the $\mathrm{NM}^{\mathrm{L}}_1$ and $\mathrm{NM}^{\mathrm{R}}_1$ layers, where it may generate spin accumulation in $\mathrm{NM}^{\mathrm{L}}_1$ and $\mathrm{NM}^{\mathrm{R}}_1$ layers, which would then scattered back as spin-current into the Co layer as J^{L}_{s1} and J^{R}_{s1}; and/or it may reach the outer $\mathrm{NM}^{\mathrm{L}}_2$ and $\mathrm{NM}^{\mathrm{R}}_2$ (Ta) layers as J^{L}_{s2} and J^{R}_{s2} [67].

Since Cu is a poor spin sink in this structure, Co thin-films with Ta/Cu underlayers and Cu/Ta overlayers do not exhibit a significant enhancement in magnetic damping. Most of the

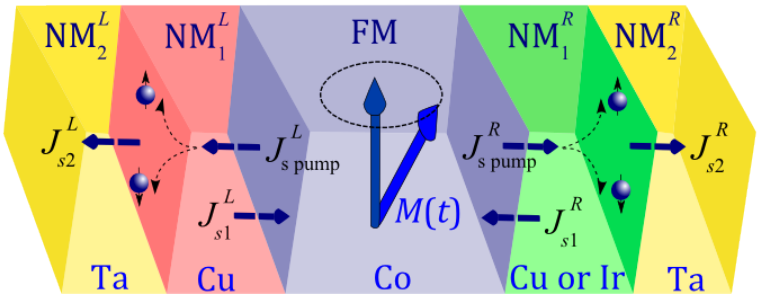

Fig. 7.12 A schematic of the sample structures used in this study, and examples of possible spin-currents generated by spin-pumping. The precession of the magnetization in Co layer, $M(t)$, generates spin-currents $J^{\mathrm{L}}_{\mathrm{s\ pump}}$ and $J^{\mathrm{R}}_{\mathrm{s\ pump}}$ from the Co layer into both adjacent NM layers. The spin accumulation in $\mathrm{NM}_1^{\mathrm{L}}$ and $\mathrm{NM}_1^{\mathrm{R}}$ either flows back into the Co layer as spin-current J^{L}_{s1} and J^{R}_{s1}, relaxes in $\mathrm{NM}_1^{\mathrm{L}}$ and $\mathrm{NM}_1^{\mathrm{R}}$ layers or reach to the $\mathrm{NM}_2^{\mathrm{L}}$ and $\mathrm{NM}_2^{\mathrm{R}}$ layers as spin-current J^{L}_{s2} and J^{R}_{s2}.

spins injected into the Cu films are scattered back and relax into the Co layer, because both Cu layers are 3 nm thick which is much thinner than its spin diffusion length, $\lambda_{\mathrm{sd}}^{\mathrm{Cu}} \sim 350$ nm [76] at room-temperature, hence it does not contribute to spin-flip. Also, the effective specific interface spin-resistance between $\mathrm{NM}_1^{\mathrm{L,R}}$ (Cu/Ir) and $\mathrm{NM}_2^{\mathrm{L,R}}$ (Ta) should be high [73, 81], so it is expected that $J_{s2}^{\mathrm{L,R}} \sim 0$. The spin back-flow $J_{s1}^{\mathrm{L,R}} \approx J_{\mathrm{s\ pump}}^{\mathrm{L,R}}$, thus the damping enhancement in these layers should be negligible. However, for Co thin-films with Ta/Cu underlayers and Ir/Ta overlayers, the damping enhancement from Ta/Cu underlayers is again negligible, as explained above. Ir is a good sink due to its strong SOI and is also 3 nm thick which is much thicker than its spin diffusion length, $\lambda_{\mathrm{sd}}^{\mathrm{Ir}} \sim 0.5$ nm [75]. Hence, $J^{\mathrm{R}}_{\mathrm{s\ pump}}$ may rapidly relax within the Ir layer. Now, J^{R}_{s1} is almost equal to zero, again $J^{\mathrm{R}}_{s2} \sim 0$, and the precessional magnetization should be enhanced in the structure with Ir overlayer.

7.5 Intrinsic Damping in Cobalt Multilayers

To investigate whether the intrinsic magnetic damping is influenced by Cu or Ir overlayers, Co thickness dependence of phenomenological damping parameter is estimated from the slope of the frequency dependence of ΔH using Eq. 2.28. The intrinsic damping parameter α, which encapsulates all of the intrinsic precessional damping contributions for both thin-films are shown in Fig. 7.13 (a). Here, it is clearly shown that the intrinsic damping increases with reducing Co thickness for both thin-film series. This enhancement comes from the spin-pumping, which is an interface effect via the spin-mixing conductance. For Co thicknesses greater than ~ 6 nm the intrinsic damping of Co/Ir thin-films are slightly higher than Co/Cu

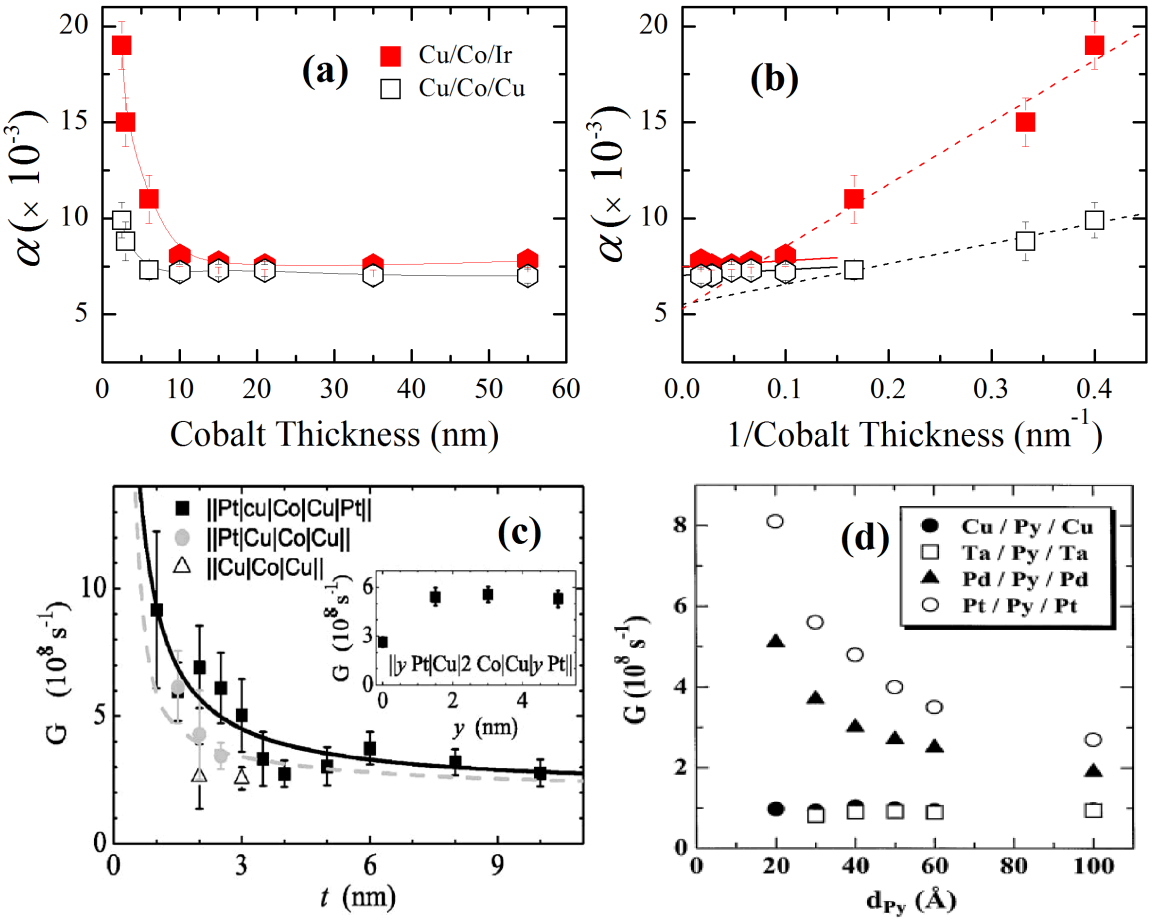

Fig. 7.13 (a)Dependence of Co thickness on the Gilbert damping parameter α for both sets of thin-films. The solid lines are guide to the eye. (b) The inverse Co thickness dependence of the Gilbert damping parameter for both sets of films. The solid and dashed lines are linear fit to the structures with different overlayer and dominant Co crystal phase. Squares and hexagons represent dominant fcc(111) and hcp(0001) texture in the Co layer, respectively. (c) Dependence of Co thickness on the magnetic damping for different structures, measured by Beaujour *et al.* [52]. The inset shows how intrinsic damping changes as a function of Pt layer thickness. (d) Dependence for NiFe of the Gilbert damping term for NM/NiFe/NM with various NM metals, measured by Mizukami *et al.* [73].

thin-films, and largely independent of Co thickness, where it saturates at a value of about ~ 0.007. In contrast, below 6 nm of Co, structures with Cu overlayers show only a small increase in $\alpha \sim 0.01$ for the thinnest Co/Cu film. However, structures with Ir overlayers show a more dramatic increase in α, where it reaches up to ~ 0.02 for the thinnest Co/Ir film, which is about 2 times larger for the thinnest Co/Ir thin-film than for the Co/Cu thin-film. The broadening of the FMR linewidth for structures with Ir overlayers causes a contribution

to the extrinsic damping, which is due to the strong spin-flip scattering through the increased structural disorder due to lattice mismatch and interfacial stacking faults at the Co/Ir interface.

The dependence of the intrinsic damping on the inverse Co thickness is shown in Fig. 7.13 (b), with linear fits to Eq. 2.35 for each overlayer and dominant Co crystal-phase combination. As shown in the figure, it is again clear that a single linear fit for entire FM thickness range is inappropriate. Here, the solid lines correspond to the thicker Co films with hcp(0001)-dominated structure, and the dashed lines are fits to the thinner Co films with fcc(111)-dominated phase for structures with Cu and Ir overlayers. The bulk damping parameters, α_0, are extracted from the intercepts for each structural phases where $\alpha_0 \sim (7 \pm 0.2) \times 10^{-3}$ for hcp(0001)-dominated structures and $\alpha_0 \sim (5 \pm 0.3) \times 10^{-3}$ for fcc(111)-dominated structures. These experimental results are summarized in Table 7.3 and agree well with literature values for bulk hcp-Co [188] and a recent theoretical prediction for bulk fcc-Co [189], where fcc-Co is not a stable bulk phase, hence there is no experimental value.

Fig. 7.13 (c) shows the Co thickness dependence of the magnetic damping for similar structures to this work [52]. The magnetic damping of Co films sandwiched between Cu layers is independent of the Co thickness, where no damping enhancement is expected due to small SOI of Cu contacts. The addition of a Pt contact under Cu seed-layer shows an enhancement of the damping parameter compared to Cu/Co/Cu structure, which indicates how a single Pt layer influences the damping parameter. The addition of a second Pt layer on top of the structure again shows a dramatic increase in Gilbert damping parameter, where it is about two times larger than the Co films without Pt contacts. Pt layer thickness dependence of the magnetic damping with a 2 nm Co layer was also performed, as shown inset of Fig. 7.13 (c), where the damping enhances sharply and it saturates beyond 1.5 nm Pt layer. The evolution of magnetic damping in Co bilayers with Pt and Au capping layers was studied as a function of NM layer thickness [190]. Here, a large enhancement of magnetic damping was observed for Co thin-film with Pt contact, however no significant enhancement was observed for Co film with Au capping layer, due to the different localized SOI related to intermixing and $d-d$ hybridization of Co/Pt and Co/Au interfaces.

An investigation of room-temperature FMR linewidth of NiFe magnetic thin-films sandwiched between different NM layers were carried out by Mizukami *et al.* [73], as shown in Fig. 7.13 (d). The Gilbert damping was found to be consistent with the spin-pumping mechanism, where it showed an enhancement as a function of NiFe thickness, when the NiFe thin-film was in contact with certain heavy metals. For NM, such as Pt and Pd, the top and bottom interface of NiFe experience a strong SOI of Pt and Pd atoms, hence an

enhancement of the intrinsic damping is expected due to the strong spin-flip scattering at NiFe/NM interface. This enhancement means that an additional torque is acting on the NiFe layer, thus transfer of angular momentum occurs at the NiFe interfaces with certain NM contacts. Also, the damping enhancement shows an inverse thickness dependence of the NiFe layer with Pt and Pd contacts. This indicates an interfacial effect where the interface is a larger fraction for thinner NiFe film, hence interfacial effects would be enhanced. However, the intrinsic damping is independent of NiFe thickness, when NiFe is sandwiched between Cu and Ta layers.

7.6 Spin-Mixing Conductance in Cobalt Multilayers

The efficiency of spin-current transfer across the FM/NM interface is governed by the interfacial spin-mixing conductance which is a crucial parameter to determine the efficiency of magnetization dynamics in such systems. The intrinsic damping under the influence of spin-pumping is related to the total effective spin-mixing conductance in units of spin channels per unit area for the multilayer structure, $g_{\uparrow\downarrow}^{\mathrm{T,eff}}$, by [67, 81, 189];

$$\alpha = \alpha_0 + \frac{\mathrm{g}\mu_{\mathrm{B}}}{4\pi M_{\mathrm{s}} t_{\mathrm{FM}}} g_{\uparrow\downarrow}^{\mathrm{T,eff}}. \tag{7.1}$$

In principle, the slope of the linear fits shown in Fig. 7.13 (b) enables to extract $g_{\uparrow\downarrow}^{\mathrm{T,eff}}$ in fcc(111) and hcp(0001) dominated crystal phases for structures with Cu and Ir overlayers. Here, it is clear that $g_{\uparrow\downarrow}^{\mathrm{T,eff}}$ shows not only the expected dependence on overlayer material, but there is also a strong dependence on the crystal phase of the Co film directly below the FM/NM interface. This simple analysis for $g_{\uparrow\downarrow}^{\mathrm{T,eff}}$ cannot include Co thickness dependence of g-factor, as shown in Fig. 7.8. Instead, using the α_0 values extracted for each thin-film series from the data in Fig. 7.13 (b), the inverse Co thickness dependence of a quantity $4\pi M_{\mathrm{S}}(\alpha - \alpha_0)/\mathrm{g}\mu_{\mathrm{B}}$, as shown in Fig. 7.14, enables directly to calculate $g_{\uparrow\downarrow}^{\mathrm{T,eff}}$ which is related to parallel dissipation of angular momentum in both underlayers and overlayers.

To extract the individual $g_{\uparrow\downarrow}^{\mathrm{eff}}$ for each Co/NM interface, it is useful to recall the four film structures;

- Ta/Cu/fcc(111)-Co/fcc(111)-Co/**Cu**/Ta Ta/Cu/fcc(111)-Co/hcp(0001)-Co/**Cu**/Ta
- Ta/Cu/fcc(111)-Co/fcc(111)-Co/**Ir**/Ta Ta/Cu/fcc(111)-Co/hcp(0001)-Co/**Ir**/Ta

Here, the thinnest Co films with Cu overlayers are symmetric. From this symmetric structure the $g_{\uparrow\downarrow}^{\mathrm{eff}}$ for a single fcc(111)-Co/Cu interface can be extracted as half that found for

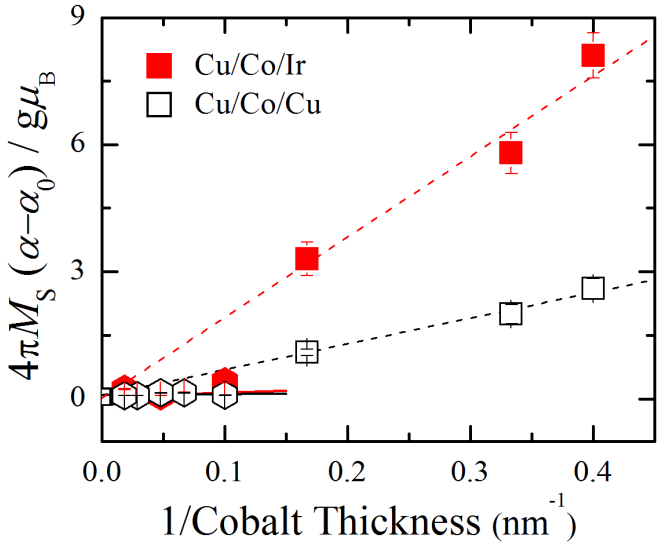

Fig. 7.14 The gradient of the inverse Co thickness dependence of $4\pi M_S\,(\alpha-\alpha_0)\,/g\mu_B$ directly yields spin-mixing conductances of Co/Cu and Co/Ir thin-films with dominant fcc-Co and hcp-Co crystal phases. The solid and dashed lines are linear fits to the hcp(0001)- and fcc(111)-dominated structures, respectively.

the full structure [67]. The lower Co interface in all samples has this exact Ta/Cu/fcc(111)-Co structure, hence the $g^{\text{eff}}_{\uparrow\downarrow}$ for the various other Co/NM combinations can be similarly extracted. The upper Co/NM interface of the remaining three sets of structures are comprised of hcp(0001)-Co/Cu/Ta, fcc(111)-Co/Ir/Ta, and hcp(0001)-Co/Ir/Ta, as listed above. Structures including Pt layers have higher $g^{\text{eff}}_{\uparrow\downarrow}$ than found in this work with Ir layer due to the stronger SOI in Pt. The values of $g^{\text{eff}}_{\uparrow\downarrow}$ for each Co/NM interface combination are given in Table 7.3 with literature values for some similar works quoted for comparison with this study.

The key result of this work is that the effective interfacial spin-mixing conductance for both Co/Ir and Co/Cu interfaces depends strongly on structural details of the local crystal phase of the Co layer directly adjacent to the NM interface. Here, $g^{\text{eff}}_{\uparrow\downarrow}$ is found as $g^{\text{eff}}_{\uparrow\downarrow} = 9.1 \pm 0.5\ \text{nm}^{-2}$ for fcc(111)-Co/Ir and $g^{\text{eff}}_{\uparrow\downarrow} = 0.6 \pm 0.1\ \text{nm}^{-2}$ for hcp(0001) - Co/Ir which is ~ 15 times smaller. Also, $g^{\text{eff}}_{\uparrow\downarrow} = 1.8 \pm 0.1\ \text{nm}^{-2}$ for fcc(111)-Co/Cu and $g^{\text{eff}}_{\uparrow\downarrow} = 0.4 \pm 0.1\ \text{nm}^{-2}$ for hcp(0001)-Co/Cu, which is ~ 4 times smaller. However, these experimental results are incompatible with a recent theoretical model of Chen and Zhang [191] where this model, in conjuction with these results, completely destroys the idea that Rashba interaction is primary mechanism for spin-pumping. The Rashba effect is an interaction of the spin and the momentum of electrons induced by the SOI in surface/interface states. Here, $g^{\text{eff}}_{\uparrow\downarrow}$ of fcc(111)-Co/Cu (weak SOI - no symmetry breaking) has greater than $g^{\text{eff}}_{\uparrow\downarrow}$ of hcp(0001)-Co/Ir (strong Rashba effect due to inversion symmetry breaking), despite far stronger SOI in Ir

Table 7.3 Parameters extracted from spin-pumping measurements: bulk Gilbert damping, α_0; and effective spin-mixing conductance, $g^{\text{eff}}_{\uparrow\downarrow}$, showing comparison with relevant literature values.

Spin-pumped interface(s)	$\alpha_0(\times 10^{-3})$	$g^{\text{eff}}_{\uparrow\downarrow}$ ($\times 10^{18}$ m^{-2})
hcp(0001)-Co/Cu/Ta	(7.1 ± 0.2)	(0.4 ± 0.1)
fcc(111)-Co/Cu/Ta	(5.5 ± 0.3)	(1.8 ± 0.1)
hcp(0001)-Co/Ir/Ta	(7.5 ± 0.2)	(0.6 ± 0.1)
fcc(111)-Co/Ir/Ta	(5.2 ± 0.3)	(9.1 ± 0.5)
Co/Pt – Quoted from Ref. [192]		80
Ta/Cu/Co/Cu/Pt – Ref. [177]	8.5	7.3
Pt/Cu/Co/Cu/Pt – Ref. [52, 180]		0.89 ± 0.12

compared to Cu. These suggests spin memory-loss is not the dominant mechanism here due to interfacial Rashba SOI. Theoretical works about spin-mixing conductance are not at the point to allow any further comments on the details of this scattering mechanism.

Due to the different atomic-scale arrangement of atoms, the electronic structure of the Co/NM interface should be different between fcc and hcp structures. This may result in differences in the effective specific interface spin-resistance, R^*, and/or spin-memory loss, δ. An observed enhancement of $g^{\text{eff}}_{\uparrow\downarrow}$ in fcc(111)-Co is over that for hcp(0001)-Co suggests three factors; (i) R^* is smaller for the fcc(111)-Co/NM interface than for the hcp(0001)-Co/NM interface, where injected spin-current is more easily able to enter NM layer from fcc(111)-Co structure, (ii) δ is larger for the fcc(111)-Co/NM interface than for the hcp(0001)-Co/NM interface, where spin-flip scattering is enhanced at the FM/NM interface with fcc(111)-Co structure, (iii) a combination of these two factors.

Increased spin memory loss, larger δ, is mainly attributed to interfacial intermixing between FM and NM layers [192]. From XRR measurements, as given in Appendix A, no evidence is found for increased intermixing of fcc(111)-Co/NM in comparison to hcp(0001)-Co/NM films. This suggests that the R^* plays the dominant rôle here. This effect is dominated by R^* as the electronic structure differs more across hcp(0001)-Co/fcc(111)-NM interfaces than across fcc(111)-Co/fcc(111)-NM interfaces, likely resulting in enhanced interface scattering.

Recently, interfacial $g^{\text{eff}}_{\uparrow\downarrow}$ was studied for $CoFe_2O_4$/Pt films using spin-Hall magnetoresistance, where the experimental results suggest a different interfacial spin-mixing conductance depending on the crystallographic orientation of $CoFe_2O_4$ [168]. Also, in another recent report [171], the voltage generated due to the combination of spin-Seebeck and inverse

spin-Hall effect, governed by the interfacial $g^{\text{eff}}_{\uparrow\downarrow}$, was found to enhance significantly when a $Fe_{70}Cu_{30}$ layer was inserted between Pt and YIG layers. This suggests that the interfacial $g^{\text{eff}}_{\uparrow\downarrow}$ may be tunable with an understanding of the properties of magnetic materials.

7.7 Chapter Conclusion

In this chapter, the primary motivation was to understand not only the spin-pumping mechanism in complex structures, but also how this mechanism works in different crystal phases. For this reason, the magnetization dynamics under FMR was studied here using a thin-film structure with polycrystalline Co thin-films sandwiched between NM layers in symmetric (Ta/Cu underlayers and Cu/Ta overlayers), and asymmetric (Ta/Cu underlayers, Ir/Ta overlayers) structures to demonstrate how local interface structure is influenced in spin-pumping mechanism. In order to obtain structural details of Co thin-films, X-ray diffraction measurements were performed, where structural phase transitions were observed from fcc(111) to hcp(0001)-dominated structures as a function of Co layer thickness. Instead of using the conventional method to describe the magnetic parameters, both $4\pi M_{\text{eff}}$ and the g-factor were determined by a new approach using structural information of Co thin-films. It is shown that the magnetic parameters exhibit a significantly different behaviour for thicker and thinner Co films. The combined thickness and crystal structure dependence of the g-factor has not previously been considered.

From FMR linewidth measurements, the intrinsic damping of Co thin-films with different NM overlayers were described, where the magnetic damping for Co thicknesses above 6 nm is weakly dependent on Co thickness for structures with both overlayers, and below 6 nm of Co structures with Ir overlayers show higher damping enhancement compared to structures with Cu overlayers; which is attributed to strong SOI via spin-pumping mechanism, but seems to be linked also to Co crystal phase.

The magnetization dynamics of Co thin-films also depends on subtle details of the local crystal structure of the FM layer close to the NM interface, where the precessional damping is influenced by both the NM overlayer and the local interfacial structure. Hence, this allows to determine the spin-pumping contribution to the intrinsic damping from individual interfaces with different local atomic-scale structures. The interfacial spin-mixing conductance is also significantly enhanced in structures where both Co and Ir overlayers have fcc(111) structure, in comparison to those where the Co layer has subtly different hcp(0001) texture at the interface.

8

Concluding Remarks and Future Work

8.1 Conclusions

The research work presented in this thesis has focused on the several experimental studies of interfacial effects in polycrystalline Co thin-films with Cu and Ir overlayers, and amorphous CoFeB:Ta thin-films deposited on Si/SiO_2 and GaAs(001) substrates. In this context, the influence of adjacent material layers on the magnetization, dynamics, and transport properties of thin ferromagnetic (FM) films has been explored.

The structural, magnetic and magnetoresistive behaviour of polycrystalline Co thin-films were investigated in Chapter 5 using several techniques. Structural analysis was performed to confirm layer thicknesses and interface roughnesses using x-ray reflectivity. Magnetic characterization of thin-films was performed using SQUID magnetometry at room-temperature. These measurements revealed that Co thin-films showed in-plane magnetization for the entire range of Co thickness studied. Also to determine any magnetic dead layer formations in these thin-films, the saturation magnetic moments per unit area of both thin-films with respect to the Co film thickness was studied, and showed that no magnetic dead layer formation present within these structures. Electrical resistivity measurements of Co thin-films were studied for orientations of the structures with respect to the applied magnetic field. The AMR was observed to be dependent upon on Co film thickness and it tends toward zero for Co thicknesses below 6 nm. The AMR decreases with decreasing of Co thickness,

and the AMR of structures with Ir overlayers is greater than structures with Cu overlayers due to interfacial conduction transparency of Co/Ir. To extract the contribution to the AMR from a single Co/Ir interface, a simple model was used in this study, where the AMR ratio was shown to vary inversely proportional to the Co film thickness with a Co/Ir interface. This suggested that the in-plane AMR was a consequence of anisotropic scattering with both volume and interfacial contributions. Such interfacial contribution to the in-plane AMR has not previously been considered.

The depth-dependence of the magnetic structure in amorphous CoFeB:Ta/Ta thin-films on Si/SiO_2 and GaAs(001) substrates was studied in Chapter 6 using PNR as a function of measurement temperatures. The PNR data of CoFeB:Ta thin-films were analyzed using "various layer" models, as described in Chapter 4, where this modeling procedure provided a realistic description of the magnetic structure of the thin-films. The amorphous CoFeB:Ta alloy has a reduced T_C due to addition of Ta which enables investigation into interface magnetism and magnetic dead layers at temperatures close to the T_C. The magnetic interface position corresponding to the CoFeB:Ta/Ta cap interface shifts with measurement temperature due to a compositional grading where $\sim$ 6 Å magnetic dead layer is formed at 0.1 T_C and this thickness increases to $\sim$ 9 Å at 0.6 T_C. Also 5.3 Å dead-region forms at the GaAs(001)/CoFeB:Ta interface where the thickness increases to 8.5 Å with increasing temperature, but this dead layer thickness is confined within an localized interfacial alloyed region. This indicates the significant influence of subtle structural intermixing on magnetic thin-films.

The final experimental chapter of this thesis has been devoted to the study of the magnetization dynamics with FMR, using a vector network analyzer system in a thin-film sandwiched between non-magnetic (NM) layers in order to demonstrate how local interface structure influences the spin-pumping mechanism. X-ray diffraction measurements were performed in order to obtain structural details of Co thin-films, where structural phase transitions were observed from fcc(111) to hcp(0001)-dominated structures as a function of Co layer thickness. Instead of using the conventional method for describing the magnetic parameters, both $4\pi M_{eff}$ and the g-factor were determined using a new approach using the details of structural information of these thin-films, where these magnetic parameters exhibit a significantly different behaviour in thicker and thinner film regimes. Furthermore, the combined thickness and crystal structure dependence of the g-factor has not previously been considered. The intrinsic damping of Co thin-films with different NM overlayers were described from FMR linewidth measurements. It is found that the magnetic damping for Co thicknesses above 6 nm is weakly dependent on Co thickness and below 6 nm of Co structures with Ir overlayers show

higher damping enhancement compared to structures with Cu overlayers. This difference was attributed to not only a strong SOI via spin-pumping mechanism, but also linked to Co crystal phase. The magnetization dynamics of Co thin-films also depends on structural details of the crystal structure of the Co layer close to the overlayer interface. The Gilbert damping is influenced by both the NM overlayer and the local interfacial structure which allows determination of the spin-pumping contribution to the intrinsic damping from individual interfaces with different local atomic-scale structures. The role of NM/FM interface is of substantial importance in spin-pumping. The efficiency of generation of spin-current in NM from a precessing magnetization is quantified by spin-mixing conductance of the FM/NM interface, where the enhancement of spin-mixing conductance in FM/NM interface leads to enhancement in the amount of spin-current. The interfacial spin-mixing conductance was extracted from damping measurements which is significantly enhanced when both Co and Ir overlayers have fcc(111) structure, in comparison to those where the Co layer has different hcp(0001) texture at the interface. Thereby, this work does not only contribute to a deeper understanding of the involved interfacial effects, but it also gives a guideline to the development of new approaches to determine magnetic parameters of thin-films.

Regarding the interfacial contribution to damping via Fermi surface breathing, in order to definitively determine this would require further investigation of overlayer/underlayer thickness dependence and the change in the FM Fermi surface (and hence breathing) is determined by only the interface with NM and therefore should be independent of NM thickness. To confirm that variations in the damping parameter are due to spin pumping, it is also necessary to measure a transverse voltage due to spin-pumping and inverse spin-Hall effect to definitively characterize as spin-pumping.

8.2 Future work

The studies presented in this thesis developed a deeper understanding of the interfacial effects in FM thin-films. These have led to novel findings, however, further scientific investigation is still required. This section highlights some possible areas of research that could be continued and may lead to further advances in the fundamental understanding of the interfacial effects.

The study of the magneto-transport measurements have focused on Co thin-films with Cu and Ir overlayers, which shows the importance of interface transparency. It would be interesting to study other material systems to confirm interfacial contributions to AMR. X-ray

diffraction measurements demonstrated the crystal structure of Co layers, where interfacial contribution to AMR showed no crystal phase dependences. Similar analysis with different crystallographic structures may provide beneficial information of interfacial effects.

In this study, amorphous CoFeB:Ta thin-films were used for the depth-dependence of the magnetic structure. Further investigation in other systems, such as Ni- or Fe-based alloys, may be beneficial for temperature dependence of magnetic dead layer thicknesses. Amorphous CoFeB:Ta thin-film were deposited onto GaAs(001) semiconductor substrate, however, temperature dependence of magnetic dead layers using different semiconductor substrate, such as GaSb, or single crystal substrates, such as MgO or Al_2O_3 (sapphire), also need to be investigated. The amorphous CoFeB:Ta alloy has a reduced $T_C \sim 100$ K due to addition of Ta, hence the measurement temperature is limited. However, addition of less Ta enables to have a CoFeB:Ta alloy with a high T_C which allows to study in a broad temperature range. For a complete understanding of the temperature dependent magnetic dead layers measured at more temperatures need to be explored further. Amorphous CoFeB:Ta was used in this work as a FM layer, however, for completeness it would also be interesting to examine different amorphous materials or crystalline systems to identify magnetic dead layer formations at interfaces. The magnetization depth-profiles obtained from measurements on 10 nm CoFeB:Ta films inform future studies on thinner films may enable understanding of how two-dimensional ordering arises at finite film thickness.

To understand in more details the influence of interface structure in spin-pumping mechanism, again different material systems or crystallographic structures can be considered. The combined thickness and crystal structure dependence of the g-factor has not previously been considered, thus these dependencies of g-factor need to be studied in other material systems. The difference in crystal structure at interface is important for pure spin-current, however, spin polarized currents show no clear dependence in AMR measurements. Further experimental and theoretical studies need to be performed to verify these results.

It is my sincere hope that this work would provide some useful insights for interfacial effects in thin FM films.

References

[1] R.P. Feynman. Miniaturization. *Reinholds, New York*, 1961.

[2] S. S. P. Parkin, M. Hayashi, and L. Thomas. Magnetic domain-wall racetrack memory. *Science*, 320(5873):190–194, 2008.

[3] J.M. Slaughter, R.W. Dave, M. DeHerrera, M. Durlam, B.N. Engel, J. Janesky, N.D. Rizzo, and S. Tehrani. Fundamentals of mram technology. *J. Supercond.*, 15:19, 2002.

[4] M.N. Baibich, J.M. Broto, A. Fert, F.N. Van Dau, and F. Petroff. Giant magnetoresistance of (001)Fe/(001)Cr magnetic superlattices. *Phys. Rev. Lett.*, 61:2472, 1988.

[5] G. Binasch, P. Grünberg, F. Saurenbach, and W. Zinn. Enhanced magnetoresistance in layered magnetic structures with antiferromagnetic interlayer exchange. *Phys. Rev. B*, 39:4828, 1989.

[6] M. Julliere. Tunneling between ferromagnetic films. *Phys. Lett. A*, 54:225, 1975.

[7] Everspin. Everspin debuts first Spin-Torque MRAM for high performance storage systems, http://www.everspin.com/pdf/st-mram press release.pdf. 2012.

[8] Toshiba. Toshiba's new STT-MRAM memory element promises world's best power consumption and to outperform SRAM, http://www.toshiba.co.jp/about/press/2012 12/pr1001.htm. 2012.

[9] MRAM-Info. TDK to present a 8-mbit STT-MRAM prototype, plans to commercialize the technology in 3-5 years, http://www.mram-info.com/tdk-present-8-mbit-stt-mram-prototype-plans-commercializetechnology-3-5-years. 2014.

[10] J. A. Katine, F. J. Albert, R. A. Buhrman, E. B. Myers, and D. C. Ralph. Current-driven magnetization reversal and spin-wave excitations in Co /Cu /Co pillars. *Phys. Rev. Lett.*, 84:3149–3152, Apr 2000.

[11] M. Tsoi, A. G. M. Jansen, J. Bass, W.-C. Chiang, M. Seck, V. Tsoi, and P. Wyder. Excitation of a magnetic multilayer by an electric current. *Phys. Rev. Lett.*, 80:4281–4284, May 1998.

[12] L. Berger. Emission of spin waves by a magnetic multilayer traversed by a current. *Phys. Rev. B*, 54:9353–9358, Oct 1996.

[13] J.C. Slonczewski. Current-driven excitation of magnetic multilayers. *J. Magn. Magn. Mater.*, 159(1):L1 – L7, 1996.

[14] S. Mangin, D. Ravelosona, J.A. Katine, M.J. Carey, B.D. Terris, and E.E. Fullerton. Current-induced magnetization reversal in nanopillars with perpendicular anisotropy. *Nat. Mater.*, 5(3):210–215, 2006.

[15] N. Nishimura, T. Hirai, A. Koganei, T. Ikeda, K. Okano, Y. Sekiguchi, and Y. Osada. Magnetic tunnel junction device with perpendicular magnetization films for high-density magnetic random access memory. *J. Appl. Phys.*, 91(8):5246–5249, 2002.

[16] G. E. Uhlenbeck and S. Goudsmit. Spinning electrons and the structure of spectra. *Nature*, 117:264–265, 1926.

[17] C. D. Cullity, B. D. & Graham. Introduction to magnetic materials, 2nd edition. *John Wiley & Sons*, 2009.

[18] N. A. Spaldin. Magnetic materials : fundamentals and applications (2nd ed.). *Cambridge University Press*, 2010.

[19] D. Hanneke, S. Fogwell, and G. Gabrielse. New measurement of the electron magnetic moment and the fine structure constant. *Phys. Rev. Lett.*, 100:120801, Mar 2008.

[20] P. Weiss. La variation du ferromagnetisme du temperature. *Compt. Rend.*, 143:1136, 1906.

[21] W. Heisenberg. Zur theorie des ferromagnetismus (on the theory of ferromagnetism). *Zeitschrift für Physik A*, 49:619–636, 1928.

[22] E. C. Stoner. Collective electron ferromagnetism. *Proc. R. Soc. London A*, 165(922):372–414, 1938.

[23] J. C. Slater. The ferromagnetism of nickel. *Phys. Rev.*, 49:537–545, Apr 1936.

[24] Robert C. O'Handley. Modern magnetic materials, principles and applications. *John Wiley & Sons*, 2000.

[25] S. Blundell. Magnetism in condensed matter. *Oxford University Press*, 2001.

[26] I. M. Miron, K. Garello, G. Gaudin, P.-J. Zermatten, M. V. Costache, S. Auffret, S. Bandiera, B. Rodmacq, A. Schuhl, and P. Gambardella. Perpendicular switching of a single ferromagnetic layer induced by in-plane current injection. *Nature*, 476(7359):189–193, 2011.

[27] M. Weinert and J. W. Davenport. Chemisorption of H on magnetic Ni(001). *Phys. Rev. Lett.*, 54:1547–1550, Apr 1985.

[28] J. S. Claydon, Y. B. Xu, M. Tselepi, J. A. C. Bland, and G. van der Laan. Direct observation of a bulklike spin moment at the Fe/GaAs(100)- 4×6 interface. *Phys. Rev. Lett.*, 93:037206, Jul 2004.

[29] Y-H. Wang, W-C. Chen, S-Y. Yang, K-H. Shen, C. Park, M-J. Kao, and M-J. Tsai. Interfacial and annealing effects on magnetic properties of CoFeB thin films. *J. Appl. Phys.*, 99(8), 2006.

[30] L. N. Liebermann, D. R. Fredkin, and H. B. Shore. Two-dimensional "Ferromagnetism" in iron. *Phys. Rev. Lett.*, 22:539–541, Mar 1969.

[31] L. Liebermann, J. Clinton, D. M. Edwards, and J. Mathon. "Dead" layers in ferromagnetic transition metals. *Phys. Rev. Lett.*, 25:232–235, Jul 1970.

[32] G. A. Prinz. Hybrid ferromagnetic-semiconductor structure. *Science*, 250(4984):1092–1097, 1990.

[33] G. Wastlbauer and J. A. C. Bland. Structural and magnetic properties of ultrathin epitaxial Fe films on GaAs(001) and related semiconductor substrates. *Adv. Phys.*, 54(2):137, 2005.

[34] S. Y. Jang, C-Y. You, S. H. Lim, and S. R. Lee. Annealing effects on the magnetic dead layer and saturation magnetization in unit structures relevant to a synthetic ferrimagnetic free structure. *J. Appl. Phys.*, 109(1), 2011.

[35] A. Ernst, M Lueders, W. M. Temmerman, Z. Szotek, and G. van der Laan. Theoretical study of magnetic layers of nickel on copper; dead or alive? *J. Phys.: Condens. Matter*, 12(26):5599, 2000.

[36] P. Drude. Zur elektronentheorie der metalle. *Annalen der Physik*, 1:566, 1900.

[37] N. F. Mott. The electrical conductivity of transition metals. *Proc. R. Soc. London A*, 153(880):699–717, 1936.

[38] P.L. Rossiter. The electrical resistivity of metals and alloys. *Cambridge University Press*, 1987.

[39] J. J. Thomson. *Proc. Cambridge Philos. Soc.*, 11(120), 1901.

[40] K. Fuchs. The conductivity of thin metallic films according to the electron theory of metals. *Proc. Cambridge Philos. Soc.*, 34:100, 1938.

[41] E. H. Sondheimer. The mean free path of electrons in metals. *Advances in Physics*, 1(1):1–42, 1952.

[42] J Smit. Magnetoresistance of ferromagnetic metals and alloys at low temperatures. *Physica*, 17:612, 1951.

[43] T. McGuire and R. Potter. Anisotropic magnetoresistance in ferromagnetic 3d alloys. *IEEE Trans. Mag.*, 11(4):1018, 1975.

[44] W. Thomson. On the electro-dynamic qualities of metals: Effects of magnetization on the electric conductivity of nickel and of iron. *Proc. R. Soc. London*, 8:546, 1857.

[45] M. Tondra, D. K. Lottis, K. T. Riggs, Y. Chen, E. D. Dahlberg, and G. A. Prinz. Thickness dependence of the anisotropic magnetoresistance in epitaxial iron films. *J. Appl. Phys.*, 73(10):6393–6395, 1993.

[46] L. K. Bogart. *An Investigation of the Structure, Pinning and Magnetoresistance of Domain Walls in $Ni_{81}Fe_{19}$ Planar Nanowires*. PhD thesis, Durham University, 2010.

[47] R. M. Rowan-Robinson, A. T. Hindmarch, and D. Atkinson. Enhanced electron-magnon scattering in ferromagnetic thin films and the breakdown of the Mott two-current model. *Phys. Rev. B*, 90:104401, Sep 2014.

[48] M. Tokaç, M. Wang, S. Jaiswal, A. W. Rushforth, B. L. Gallagher, D. Atkinson, and A. T. Hindmarch. Interfacial contribution to thickness dependent in-plane anisotropic magnetoresistance. *AIP Advances*, 5(12), 2015.

[49] L. Landau and E. Lifshitz. On the theory of the dispersion of magnetic permeability in ferromagnetic bodies. *Phys. Z. Sowjetunion.*, 8:153, 1935.

[50] T.L. Gilbert. A lagrangian formulation of the gyromagnetic equation of the magnetization field. *Phys. Rev.*, 100:1243, 1955.

[51] C. Kittel. On the theory of ferromagnetic resonance absorption. *Phys. Rev.*, 73:155–161, Jan 1948.

[52] J-M. L. Beaujour, J. H. Lee, A. D. Kent, K. Krycka, and C-C. Kao. Magnetization damping in ultrathin polycrystalline Co films: Evidence for nonlocal effects. *Phys. Rev. B*, 74:214405, Dec 2006.

[53] J.A.C. Bland and B. Heinrich. Ultrathin magnetic structures iii. *Springer-Verlag*, pages 143–210, 2005.

[54] D.L. Mills and S.M. Rezende. Spin dynamics in confined magnetic structures-II. *Springer-Verlag*, 2003.

[55] H. Suhl. Theory of the magnetic damping constant. *IEEE Trans. Mag.*, 34(4):1834–1838, Jul 1998.

[56] B. Heinrich, D. Fraitová, and V. Kamberský. The influence of s-d exchange on relaxation of magnons in metals. *physica status solidi (b)*, 23(2):501–507, 1967.

[57] R. J. Elliott. Theory of the effect of spin-orbit coupling on magnetic resonance in some semiconductors. *Phys. Rev.*, 96:266–279, Oct 1954.

[58] F Schreiber, J Pflaum, Z Frait, Th. Mühge, and J Pelzl. Gilbert damping and g-factor in Fe_xCo_{1-x} alloy films. *Solid State Communications*, 93(12):965 – 968, 1995.

[59] V. Kamberský. On the landau-lifshitz relaxation in ferromagnetic metals. *Can. J. Phys.*, 48(24):2906–2911, 1970.

[60] S. M. Bhagat and P. Lubitz. Temperature variation of ferromagnetic relaxation in the 3*d* transition metals. *Phys. Rev. B*, 10:179–185, Jul 1974.

[61] M. Sparks, R. Loudon, and C. Kittel. Ferromagnetic relaxation. i. theory of the relaxation of the uniform precession and the degenerate spectrum in insulators at low temperatures. *Phys. Rev.*, 122:791–803, May 1961.

[62] C. E. Patton, C. H. Wilts, and F. B. Humphrey. Relaxation processes for ferromagnetic resonance in thin films. *J. Appl. Phys.*, 38(3):1358–1359, 1967.

[63] R. Arias and D. L. Mills. Extrinsic contributions to the ferromagnetic resonance response of ultrathin films. *Phys. Rev. B*, 60:7395–7409, Sep 1999.

[64] J. E. Hirsch. Spin hall effect. *Phys. Rev. Lett.*, 83:1834–1837, Aug 1999.

[65] M. Dyakonov and V. Perel. *Phys. Lett. A*, 35:459, 1971.

[66] Y. Tserkovnyak, A. Brataas, and G. E. W. Bauer. Spin pumping and magnetization dynamics in metallic multilayers. *Phys. Rev. B*, 66:224403, Dec 2002.

[67] Y. Tserkovnyak, A. Brataas, G. E. W. Bauer, and B. I. Halperin. Nonlocal magnetization dynamics in ferromagnetic heterostructures. *Rev. Mod. Phys.*, 77:1375–1421, Dec 2005.

[68] D. Qu, S. Y. Huang, Jun Hu, Ruqian Wu, and C. L. Chien. Intrinsic spin seebeck effect in Au/YIG. *Phys. Rev. Lett.*, 110:067206, Feb 2013.

[69] K. Uchida, H. Adachi, T. Ota, and Maekawa S. Nakayama, H., and E. Saitoh. Observation of longitudinal spin-seebeck effect in magnetic insulators. *Appl. Phys. Lett.*, 97(17), 2010.

[70] M. Weiler, M. Althammer, F. D. Czeschka, H. Huebl, M. S. Wagner, M. Opel, I.-M. Imort, G. Reiss, A. Thomas, R. Gross, and S. T. B. Goennenwein. Local charge and spin currents in magnetothermal landscapes. *Phys. Rev. Lett.*, 108:106602, Mar 2012.

[71] E. Saitoh, M. Ueda, H. Miyajima, and G. Tatara. Conversion of spin current into charge current at room temperature: Inverse spin-hall effect. *Applied Physics Letters*, 88(18), 2006.

[72] K. Ando and E. Saitoh. Observation of the inverse spin hall effect in silicon. *Nature Communications*, 3:629, 2011.

[73] S. Mizukami, Y. Ando, and T Miyazaki. Ferromagnetic resonance linewidth for NM/80NiFe/NM films (NM=Cu, Ta, Pd and Pt). *J. Magn. Magn. Mater.*, 226-230, Part 2:1640 – 1642, 2001. Proceedings of the International Conference on Magnetism (ICM 2000).

[74] S Mizukami, Y. Ando, and T. Miyazaki. The study on ferromagnetic resonance linewidth for NM/80NiFe/NM (NM=Cu, Ta, Pd and Pt) films. *Japanese Journal of Applied Physics*, 40(2R):580, 2001.

[75] W. Zhang, V. Vlaminck, J. E. Pearson, R. Divan, S. D. Bader, and A. Hoffmann. Determination of the pt spin diffusion length by spin-pumping and spin hall effect. *Appl. Phys. Lett.*, 103(24), 2013.

[76] F. J. Jedema, A. T. Filip, and B. J. van Wees. Electrical spin injection and accumulation at room temperature in an all-metal mesoscopic spin valve. *Nature*, 410:345–348, 2001.

[77] L. Berger. Influence of spin-orbit interaction on the transport processes in ferromagnetic nickel alloys, in the presence of a degeneracy of the 3d band. *J. Appl. Phys.*, 34(4):1360–1361, 1963.

[78] Y. Tserkovnyak, A. Brataas, and G. E. W. Bauer. Enhanced gilbert damping in thin ferromagnetic films. *Phys. Rev. Lett.*, 88:117601, Feb 2002.

[79] A. Brataas, Y. Tserkovnyak, G. E. W. Bauer, and B. I. Halperin. Spin battery operated by ferromagnetic resonance. *Phys. Rev. B*, 66:060404, Aug 2002.

[80] G. Woltersdorf. *Spin-pumping and two magnon scattering in magnetic multilayers*. PhD thesis, Simon Fraser University, 2004.

[81] Y. Liu, Z. Yuan, R. J. H. Wesselink, A. A. Starikov, and P. J. Kelly. Interface enhancement of gilbert damping from first principles. *Phys. Rev. Lett.*, 113:207202, Nov 2014.

[82] S. Babu and K. Moorthy. Thin film structures in energy applications. *Springer*, (16-18), 2015.

[83] H. Ibach. Physics of surfaces and interfaces. *Springer*, 2006.

[84] J. A. Venables. Introduction to surface and thin film processes. *Cambridge University Press*, 2003.

[85] G Guisbiers, O. Van Overschelde, M. Wautelet, Ph. Leclère, and R. Lazzaroni. Fractal dimension, growth mode and residual stress of metal thin films. *J. Phys. D: Appl. Phys.*, 40(4):1077, 2007.

[86] A. T. Hindmarch. Interface magnetism in ferromagnetic metal-compound semiconductor hybrid structures. *Spin*, 1(1):45, 2011.

[87] M. Tokaç, S. A. Bunyaev, G. N. Kakazei, D. S. Schmool, D. Atkinson, and A. T. Hindmarch. Interfacial structure dependent spin mixing conductance in cobalt thin films. *Phys. Rev. Lett.*, 115:056601, Jul 2015.

[88] R.M. Bozorth. Ferromagnetism. *John Wiley & Sons*, 1951.

[89] C. L. Platt, N. K. Minor, and T. J. Klemmer. Magnetic and structural properties of fecob thin films. *IEEE Trans. Mag.*, 37(4):2302–2304, Jul 2001.

[90] A. T. Hindmarch, C. J. Kinane, M. MacKenzie, J. N. Chapman, M. Henini, D. Taylor, D. A. Arena, J. Dvorak, B. J. Hickey, and C. H. Marrows. Interface induced uniaxial magnetic anisotropy in amorphous CoFeB films on AlGaAs(001). *Phys. Rev. Lett.*, 100(11):117201, 2008.

[91] A. T. Hindmarch, A. W. Rushforth, R. P. Campion, C. H. Marrows, and B. L. Gallagher. Origin of in-plane uniaxial magnetic anisotropy in CoFeB amorphous ferromagnetic thin films. *Phys. Rev. B*, 83:212404, June 2011.

[92] K. Fukamichi and R.J. Gambino. The curie temperature and magnetization of fe-base amorphous binary alloys containing transition metal. *IEEE Trans. Mag.*, 17(6):3059–3061, 1981.

[93] S. Horry. Critical phenomena in hybrid magnetic nanostructures. Master's thesis, Durham University, 2012.

[94] S.A. Campbell. The science and engineering of microelectronic fabrication. *Oxford University Press*, 2001.

[95] W.R. Groove. On the electrochemical polarity of gasses. *Philos Trans Faraday Soc*, 87:142, 1852.

[96] MPMS-XL. User's manual. *San Diego, CA, Quantum Design*.

[97] D.S. Sivia. Elementary scattering theory for x-ray and neutron users. *Oxford University Press*, 2011.

[98] L. G. Parratt. Surface studies of solids by total reflection of x-rays. *Phys. Rev.*, 95:359–369, Jul 1954.

[99] J. Als-Nielsen and D. McMorrow. Elements of modern x-ray physics, 2nd edition. *Wiley*, 2011.

[100] L. Ooi. Principles of x-ray crystallography. *Oxford University Press*, 2010.

[101] R. Guinebretière. X-ray diffraction by polycrystalline materials. *ISTE*, 2007.

[102] M. Björck and G. Andersson. *GenX*: an extensible X-ray reflectivity refinement program utilizing differential evolution. *J. Appl. Crystallogr.*, 40(6):1174–1178, Dec 2007.

[103] G.S. Bauer. Physics and technology of spallation neutron sources. *Nuclear Instruments and Methods in Physics Research A*, 463:505–543, 2001.

[104] D.G. Bucknall, S. Langridge, and R.M. Dalgliesh. Crisp instrument manual, http://www.isis.stfc.ac.uk/instruments/crisp/documents/crisp-instrument-manual6521.pdf. 2006.

[105] CRISP. Beamline webpage, http://www.isis.rl.ac.uk/largescale/crisp/crisp.htm.

[106] M. Farle. Ferromagnetic resonance of ultrathin metallic layers. *Rep. Progr. Phys.*, 61:755, 1999.

[107] J.H.E. Griffiths. Anomalous high-frequency resistance of ferromagnetic metals. *Nature*, 158:670, 1946.

[108] S. S. Kalarickal, P. Krivosik, M. Wu, C. E. Patton, M. L. Schneider, P. Kabos, T. J. Silva, and J. P. Nibarger. Ferromagnetic resonance linewidth in metallic thin films: Comparison of measurement methods. *J. Appl. Phys.*, 99(9), 2006.

[109] W.C. Röntgen. On a new kind of rays. *Nature*, 53:274, 1896.

[110] C. Kittel. Introduction to solid state physics. *John Wiley & Sons*, 2005.

[111] W. L. Bragg. The structure of some crystals as indicated by their diffraction of xrays. *Proc. R. Soc. London A*, 89:248–277, 1913.

[112] K.D. Bowen and B.K. Tanner. X-ray metrology in semiconductor manufacturing. *Taylor & Francis*, 2006.

[113] L. Névot and P. Croce. Characterization of surfaces by grazing x-ray reflection–application to study of polishing of some silicate-glasses. *Revue de Physique Appliquée*, 15:761–779, 1980.

[114] J. Chadwick. Possible existence of a neutron. *Nature*, 192:312, 1932.

[115] H. Fritzsche, Z. Yamani, R. Cowley, and R.C.C. Ward. Polarized neutron reflectometry as a unique tool in magnetization reversal studies of thin films and multilayers. *Physics in Canada*, 62(5):265–271, 2006.

[116] S. A. Wolf, D. D. Awschalom, R. A. Buhrman, J. M. Daughton, S. von Molnar, M. L. Roukes, A. Y. Chtchelkanova, and D. M. Treger. Spintronics: A spin-based electronics vision for the future. *Science*, 294:1488–1495, 2001.

[117] C. Gould, C. Rüster, T. Jungwirth, E. Girgis, G. M. Schott, R. Giraud, K. Brunner, G. Schmidt, and L. W. Molenkamp. Tunneling anisotropic magnetoresistance: A spin-valve-like tunnel magnetoresistance using a single magnetic layer. *Phys. Rev. Lett.*, 93:117203, 2004.

[118] L. Gao, X. Jiang, S-H. Yang, J. D. Burton, E. Y. Tsymbal, and S. S. P. Parkin. Bias voltage dependence of tunneling anisotropic magnetoresistance in magnetic tunnel junctions with MgO and Al_2O_3 tunnel barriers. *Phys. Rev. Lett.*, 99:226602, 2007.

[119] H. Nakayama, M. Althammer, Y.-T. Chen, K. Uchida, Y. Kajiwara, D. Kikuchi, T. Ohtani, S. Geprägs, M. Opel, S. Takahashi, R. Gross, G. E. W. Bauer, S. T. B. Goennenwein, and E. Saitoh. Spin hall magnetoresistance induced by a nonequilibrium proximity effect. *Phys. Rev. Lett.*, 110(20):206601, 2013.

[120] Y. M. Lu, J. W. Cai, S. Y. Huang, D. Qu, B. F. Miao, and C. L. Chien. Hybrid magnetoresistance in the proximity of a ferromagnet. *Phys. Rev. B*, 87(22):220409, 2013.

[121] R. Skomski. Simple models of magnetism. *Oxford University Press*, 2008.

[122] A. Kobs, S. Heße, W. Kreuzpaintner, G. Winkler, D. Lott, P. Weinberger, A. Schreyer, and H. P. Oepen. Anisotropic interface magnetoresistance in Pt/Co/Pt sandwiches. *Phys. Rev. Lett.*, 106:217207, 2011.

[123] Y. F. Liu, J. W. Cai, and L. Sun. Large enhancement of anisotropic magnetoresistance and thermal stability in Ta/NiFe/Ta trilayers with interfacial Pt addition. *Appl. Phys. Lett.*, 96(9):092509, 2010.

[124] J-C. Lee, C-H. Hsieh, C-C. Chang, L-W. Huang, L-K. Lin, and S-F. Lee. Comparison of anistropic interface magnetoresistance in Co/Pt and Co/Pd multilayers. *J. Appl. Phys.*, 113(17), 2013.

[125] M. Valvidares, N. Dix, M. Isasa, K. Ollefs, F. Wilhelm, A. Rogalev, F. Sánchez, E. Pellegrin, A. Bedoya-Pinto, P. Gargiani, L. E. Hueso, F. Casanova, and J. Fontcuberta. Absence of magnetic proximity effects in magnetoresistive $Pt/CoFe_2o_4$ hybrid interfaces. *Phys. Rev. B*, 93:214415, Jun 2016.

[126] Yu A. Bychkov and E. I. Rashba. Oscillatory effects and the magnetic susceptibility of carriers in inversion layers. *J. Phys. C*, 17(33):6039, 1984.

[127] Yu A. Bychkov and E. I. Rashba. Properties of a 2D electron gas with lifted spectral degeneracy. *JETP lett*, 39(2):78, 1984.

[128] M. Trushin, K. Výborný, P. Moraczewski, A. A. Kovalev, J. Schliemann, and T. Jungwirth. Anisotropic magnetoresistance of spin-orbit coupled carriers scattered from polarized magnetic impurities. *Phys. Rev. B*, 80(13):134405, 2009.

[129] A. Kharmouche. Thickness dependent magnetic and structural properties of Co_x Cr_{1-x} thin films evaporated on Si(100) and glass substrates. *J. Nanosci. Nanotechnol.*, 11:4757–4764, 2011.

[130] J. Geissler, E. Goering, M. Justen, F. Weigand, G. Schütz, J. Langer, D. Schmitz, H. Maletta, and R. Mattheis. Pt magnetization profile in a Pt/Co bilayer studied by resonant magnetic x-ray reflectometry. *Phys. Rev. B*, 65(2):020405, 2001.

[131] E.Y. Tsymbal and D.G. Pettifor. Perspectives of giant magnetoresistance. *Solid State Physics*, 56:113–237, 2001.

[132] H. Yanagihara, K. Pettit, M. B. Salamon, E. Kita, and S. S. P. Parkin. Magnetoresistance and magnetic properties of Co/Ir multilayers on MgO(110) substrates. *J. Appl. Phys.*, 81(8):5197, 1997.

[133] H. Yanagihara, E. Kita, and M. B. Salamon. A periodical oscillation of interlayer coupling in epitaxial Co/Ir(001) superlattices. *Phys. Rev. B*, 60:12957–12962, Nov 1999.

[134] Y. Luo, B. Pfeifer, A. Kaeufler, M. Moske, and K. Samwer. Structural, magnetotransport, and micromagnetic properties of sputtered Ir(111)/Co superlattices. *J. Appl. Phys.*, 87(5):2479, 2000.

[135] Osaka T. Schultze J. W. Datta, M. Microelectronic packaging. *CRC Press*, 2004.

[136] B. Dieny, M. Li, S. H. Liao, C. Horng, and K. Ju. Effect of interfacial specular electron reflection on the anisotropic magnetoresistance of magnetic thin films. *J. Appl. Phys.*, 88(7):4140–4145, 2000.

[137] L. Wang, J. Zhang, and L. Wang. Effect of nano-oxide layers on the magnetoresistance of ultrathin permalloy films. *Rare Met.*, 28(6):624–628, 2009.

[138] G. Bayreuther, M. Dumm, B. Uhl, R. Meier, and W. Kipferl. Magnetocrystalline volume and interface anisotropies in epitaxial films: Universal relation and Néel's model. *J. Appl. Phys.*, 93(10):8230, 2003.

[139] H. J. Hatton and M. R. J. Gibbs. Interface contributions to magnetostriction in transition metal based soft magnetic multilayers. *J. Magn. Magn. Mater.*, 156(1):67–68, 1996.

[140] M. T. Johnson, P. J. H. Bloemen, F. J. A. den Broeder, and J. J. de Vries. Magnetic anisotropy in metallic multilayers. *Rep. Progr. Phys.*, 59(11):1409, 1996.

[141] M. Haidar and M. Bailleul. Thickness dependence of degree of spin polarization of electrical current in permalloy thin films. *Phys. Rev. B*, 88(5):054417, 2013.

[142] D. D. Djayaprawira, K. Tsunekawa, M. Nagai, H. Maehara, S. Yamagata, N. Watanabe, S. Yuasa, Y. Suzuki, and K. Ando. 230inCoFeB/MgO/CoFeB magnetic tunnel junctions. *Appl. Phys. Lett.*, 86(9), 2005.

[143] H. Kubota, A. Fukushima, K. Yakushiji, T. Nagahama, S. Yuasa, K. Ando, H. Maehara, Y. Nagamine, K. Tsunekawa, D. D Djayaprawira, N. Watanabe, and Yoshishige S. Quantitative measurement of voltage dependence of spin-transfer torque in MgO-based magnetic tunnel junctions. *Nat. Phys.*, 4(1):37–41, 2008.

[144] J-M. Hu, Z. Li, Chen L.-Q., and C.-W. Nan. High-density magnetoresistive random access memory operating at ultralow voltage at room temperature. *Nat. Commun.*, 2:553, 2011.

[145] T. Ashraf, C. Gusenbauer, J. Stangl, G. Hesser, and R. Koch. Growth, structure and morphology of epitaxial Fe(001) films on GaAs(001)) c(4x4). *J. Phys.: Condens. Matter*, 27(3):036001, 2015.

[146] T. L. Monchesky and J. Unguris. Magnetic properties of Co/GaAs(110). *Phys. Rev. B*, 74:241301, Dec 2006.

[147] K. Oguz, P. Jivrajka, M. Venkatesan, G. Feng, and J. M. D. Coey. Magnetic dead layers in sputtered $Co_{40}Fe_{40}B_{20}$ films. *J. Appl. Phys.*, 103(7), 2008.

[148] J. K. Han, K. H. Shin, and S. H. Lim. Thermal stability of a nanostructured trilayer synthetic antiferromagnet. *J. Appl. Phys.*, 101(9):–, 2007.

[149] J. J. Krebs, B. T. Jonker, and G. A. Prinz. Properties of Fe single-crystal films grown on (100)GaAs by molecular-beam epitaxy. *J. Appl. Phys.*, 61(7):2596–2599, 1987.

[150] G. A Prinz. Magnetoelectronics. *Science*, 282(5394):1660–1663, 1998.

[151] Y. B. Xu, E. T. M. Kernohan, D. J. Freeland, A. Ercole, M. Tselepi, and J. A. C. Bland. Evolution of the ferromagnetic phase of ultrathin Fe films grown on GaAs(100)-4 $\times$ 6. *Phys. Rev. B*, 58:890–896, Jul 1998.

[152] Y. B. Xu, D. J. Freeland, E. T. M. Kernohan, W. Y. Lee, M. Tselepi, C. M. Guertler, C. A. F. Vaz, J. A. C. Bland, S. N. Holmes, N. K. Patel, and D. A. Ritchie. Ferromagnetic metal/semiconductor hybrid structures for magnetoelectronics. *J. Appl. Phys.*, 85(8):5369–5371, 1999.

[153] W. M. Haynes. Handbook of chemistry and physics. *CRC Press*, 2015.

[154] A. Y. Liu and D. J. Singh. General-potential study of the electronic and magnetic structure of FeCo. *Phys. Rev. B*, 46:11145–11148, Nov 1992.

[155] M. Frankowski, A. Żywczak, M. Czapkiewicz, S. Ziętek, J. Kanak, M. Banasik, W. Powroźnik, W. Skowroński, J. Chęciński, J. Wrona, H. Głowiński, J. Dubowik, J-P. Ansermet, and T. Stobiecki. Buffer influence on magnetic dead layer, critical current, and thermal stability in magnetic tunnel junctions with perpendicular magnetic anisotropy. *J. Appl. Phys.*, 117(22), 2015.

[156] A. Filipe, A. Schuhl, and P. Galtier. Structure and magnetism of the Fe/GaAs interface. *Appl. Phys. Lett.*, 70(1):129–131, 1997.

[157] C. J. Palmstrøm, C. C. Chang, A. Yu, G. J. Galvin, and J. W. Mayer. Co/GaAs interfacial reactions. *J. Appl. Phys.*, 62(9):3755–3762, 1987.

[158] S. Park, M. R. Fitzsimmons, X. Y. Dong, B. D. Schultz, and C. J. Palmstrøm. Magnetic degradation of an FeCo/GaAs interface. *Phys. Rev. B*, 70:104406, Sep 2004.

[159] S. Y. Jang, S. H. Lim, and S. R. Lee. Magnetic dead layer in amorphous CoFeB layers with various top and bottom structures. *J. Appl. Phys.*, 107(9), 2010.

[160] M. W. Ruckman, J. J. Joyce, and J. H. Weaver. Interdiffusion and reaction at the Fe/GaAs(110) interface. *Phys. Rev. B*, 33:7029–7035, May 1986.

[161] E. M. Kneedler, B. T. Jonker, P. M. Thibado, R. J. Wagner, B. V. Shanabrook, and L. J. Whitman. Influence of substrate surface reconstruction on the growth and magnetic properties of Fe on GaAs(001). *Phys. Rev. B*, 56:8163–8168, Oct 1997.

[162] J-M. Lee, S.-J. Oh, K. J. Kim, S.-U. Yang, J.-H. Kim, and J.-S. Kim. Kinetic stabilization of a pristine Fe film on (4×2)-GaAs(100). *Phys. Rev. B*, 75:125421, Mar 2007.

[163] T. J. Zega, A. T. Hanbicki, S. C. Erwin, I. Žutić, G. Kioseoglou, C. H. Li, B. T. Jonker, and R. M. Stroud. Determination of interface atomic structure and its impact on spin transport using z-contrast microscopy and density-functional theory. *Phys. Rev. Lett.*, 96:196101, May 2006.

[164] J. M. LeBeau, Q. O. Hu, C. J. Palmstrøm, and S. Stemmer. Atomic structure of postgrowth annealed epitaxial Fe/(001)GaAs interfaces. *Appl. Phys. Lett.*, 93(12), 2008.

[165] B. D. Schultz, C. Adelmann, X. Y. Dong, S. McKernan, and C. J. Palmstrøm. Phase formation in the thin film Fe/GaAs system. *Appl. Phys. Lett.*, 92(9), 2008.

[166] S. Park, M. R. Fitzsimmons, C. F. Majkrzak, B. D. Schultz, and C. J. Palmstrøm. The influence of growth temperature and annealing on the magnetization depth profiles across ferromagnetic/semiconductor interfaces. *J. Appl. Phys.*, 104(8), 2008.

[167] A. A. Greer, A. X. Gray, S. Kanai, A. M. Kaiser, S. Ueda, Y. Yamashita, C. Bordel, G. Palsson, N. Maejima, S.-H. Yang, G. Conti, K. Kobayashi, S. Ikeda, F. Matsukura, H. Ohno, C. M. Schneider, J. B. Kortright, F. Hellman, and C. S. Fadley. Observation of boron diffusion in an annealed Ta/CoFeB/MgO magnetic tunnel junction with standing-wave hard x-ray photoemission. *Appl. Phys. Lett.*, 101(20), 2012.

[168] M. Isasa, A. Bedoya-Pinto, S. Vélez, F. Golmar, F. Sánchez, L. E. Hueso, J. Fontcuberta, and F. Casanova. Spin hall magnetoresistance at Pt/$CoFe_2O_4$ interfaces and texture effects. *Appl. Phys. Lett.*, 105(14):–, 2014.

[169] S. Mizukami, Y. Ando, and T. Miyazaki. Effect of spin diffusion on gilbert damping for a very thin permalloy layer in Cu/permalloy/Cu/Pt films. *Phys. Rev. B*, 66:104413, Sep 2002.

[170] T. Valet and A. Fert. Theory of the perpendicular magnetoresistance in magnetic multilayers. *Phys. Rev. B*, 48:7099–7113, Sep 1993.

[171] D. Kikuchi, M. Ishida, K. Uchida, Z. Qiu, T. Murakami, and E. Saitoh. Enhancement of spin-seebeck effect by inserting ultra-thin $Fe_{70}Cu_{30}$ interlayer. *Appl. Phys. Lett.*, 106(8), 2015.

[172] A. M. Shukh, D. H. Shin, and H. Hoffmann. Dependence of giant magnetoresistance in Co/Cu multilayers on the thickness of the Co layers. *J. Appl. Phys.*, 76(10):6507–6509, 1994.

[173] C. Christides. Handbook of surfaces and interfaces of materials, magnetotransport properties of ultrathin metallic multilayers. *Academic Press*, page 1844, 2001.

[174] A.R. West. Solid state chemistry and its applications. *Wiley*, 1974.

[175] R. Clarke, D. Barlett, F. Tsui, B. Chen, and C. Uher. An alternate route to giant magnetoresistance in MBE grown Co/Cu superlattices (invited). *J. Appl. Phys.*, 75(10):6174–6177, 1994.

[176] A. Hrabec, N. A. Porter, A. Wells, M. J. Benitez, G. Burnell, S. McVitie, D. McGrouther, T. A. Moore, and C. H. Marrows. Measuring and tailoring the Dzyaloshinskii-Moriya Interaction in perpendicularly magnetized thin films. *Phys. Rev. B*, 90:020402, Jul 2014.

[177] A. Ghosh, J. F. Sierra, S. Auffret, U. Ebels, and W. E. Bailey. Dependence of nonlocal gilbert damping on the ferromagnetic layer type in Ferromagnet/Cu/Pt heterostructures. *Appl. Phys. Lett.*, 98(5), 2011.

[178] X. Liu, W. Zhang, M. J. Carter, and G. Xiao. Ferromagnetic resonance and damping properties of cofeb thin films as free layers in mgo-based magnetic tunnel junctions. *J. Appl. Phys.*, 110(3), 2011.

[179] C. H. Lee, H. He, F. J. Lamelas, W. Vavra, C. Uher, and R. Clarke. Magnetic anisotropy in epitaxial Co superlattices. *Phys. Rev. B*, 42:1066–1069, Jul 1990.

[180] J-M. Beaujour, W. Chen, A. Kent, and J. Z. Sun. Ferromagnetic resonance study of polycrystalline cobalt ultrathin films. *arXiv:cond-mat/0509036v1*, 2011.

[181] K. Nagano, K. Tobari, M. Ohtake, and M. Futamoto. Effect of magnetic film thickness on the spatial resolution of magnetic force microscope tips. *Journal of Physics: Conference Series*, 303(1):012014, 2011.

[182] Justin M. Shaw, Hans T. Nembach, T. J. Silva, and Carl T. Boone. Precise determination of the spectroscopic g-factor by use of broadband ferromagnetic resonance spectroscopy. *J. Appl. Phys.*, 114(24), 2013.

[183] C. Kittel. On the gyromagnetic ratio and spectroscopic splitting factor of ferromagnetic substances. *Phys. Rev.*, 76:743–748, Sep 1949.

[184] A.H. Morrish. The physical principles of magnetism. *Wiley-IEEE Press*, 2001.

[185] C. Andersson, B. Sanyal, O. Eriksson, L. Nordström, O. Karis, D. Arvanitis, T. Konishi, E. Holub-Krappe, and J. Hunter Dunn. Influence of ligand states on the relationship between orbital moment and magnetocrystalline anisotropy. *Phys. Rev. Lett.*, 99:177207, Oct 2007.

[186] J Pelzl, R Meckenstock, D Spoddig, F Schreiber, J Pflaum, and Z Frait. Spin-orbit-coupling effects on g-value and damping factor of the ferromagnetic resonance in Co and Fe films. *J. Phys.: Condens. Matter*, 15(5):S451, 2003.

[187] P. Landeros, R. E. Arias, and D. L. Mills. Two magnon scattering in ultrathin ferromagnets: The case where the magnetization is out of plane. *Phys. Rev. B*, 77:214405, Jun 2008.

[188] T. Devolder, P.-H. Ducrot, J.-P. Adam, I. Barisic, N. Vernier, Joo-Von Kim, B. Ockert, and D. Ravelosona. Damping of $Co_xFe_{80-x}B_{20}$ ultrathin films with perpendicular magnetic anisotropy. *Appl. Phys. Lett.*, 102(2), 2013.

[189] E. Barati, M. Cinal, D. M. Edwards, and A. Umerski. Gilbert damping in magnetic layered systems. *Phys. Rev. B*, 90:014420, Jul 2014.

[190] S. Azzawi, A. Ganguly, M. Tokaç, R. M. Rowan-Robinson, J. Sinha, A. T. Hindmarch, A. Barman, and D. Atkinson. Evolution of damping in ferromagnetic/nonmagnetic thin film bilayers as a function of nonmagnetic layer thickness. *Phys. Rev. B*, 93:054402, Feb 2016.

[191] K. Chen and S. Zhang. Spin pumping in the presence of spin-orbit coupling. *Phys. Rev. Lett.*, 114:126602, Mar 2015.

[192] J.-C. Rojas-Sánchez, N. Reyren, P. Laczkowski, W. Savero, J.-P. Attané, C. Deranlot, M. Jamet, J.-M. George, L. Vila, and H. Jaffrès. Spin pumping and inverse spin hall effect in platinum: The essential role of spin-memory loss at metallic interfaces. *Phys. Rev. Lett.*, 112:106602, Mar 2014.

A

X-Ray Reflectivity of Thin-Films

Grazing incidence X-Ray reflectivity was performed for polycrystalline Co thin-films with Cu and Ir overlayers and amorphous CoFeB:Ta thin-films deposited on Si/SiO_2 and GaAs(001) wafer substrates in order to confirm the layer thickness and estimate the roughness from each interface. Measurements were performed at room-temperature using Rigaku Smartlab reflectometer, as described in Section 3.3.2. All reflectivity measurements were interpreted by fitting the measured specular reflectivity data using the GenX simulation code [102] which utilizes the Parratt recursion formula for simulating specular reflectivity.

The parameters used to obtain the best fit simulations for Cu (left column) and Ir (right column) overlayered thin-films with various Co thicknesses, and amorphous CoFeB:Ta thin-films deposited on Si/SiO_2 and GaAs(001) wafer substrates are provided in Table A.1 and Table A.2, respectively.

Table A.1 Best fit parameters including thickness and roughness used in the simulation of specular reflectivity of polycrystalline Co thin-films with Cu and Ir overlayers.

t_{Co} (nm)	Layers	Thickness (nm)	Roughness (nm)	t_{Co} (nm)	Layers	Thickness (nm)	Roughness (nm)
2	Ta_2O_5	4.1 ± 0.6	0.9 ± 0.4	2	Ta_2O_5	2.9 ± 0.2	0.5 ± 0.1
	Ta	3.3 ± 0.5	0.3 ± 0.1		Ta	2.8 ± 0.2	0.5 ± 0.2
	Cu	3.1 ± 0.4	0.4 ± 0.2		Ir	2.9 ± 0.3	0.4 ± 0.1
	Co	2.1 ± 0.1	0.3 ± 0.1		Co	1.9 ± 0.1	0.3 ± 0.1
	Cu	2.9 ± 0.4	0.4 ± 0.2		Cu	3.3 ± 0.4	0.4 ± 0.2
	Ta	2.9 ± 0.3	0.3 ± 0.1		Ta	2.7 ± 0.2	0.3 ± 0.2
2.5	Ta_2O_5	3.3 ± 0.2	0.9 ± 0.1	2.5	Ta_2O_5	2.1 ± 0.4	0.6 ± 0.2
	Ta	2.9 ± 0.4	0.4 ± 0.1		Ta	3.3 ± 0.2	0.4 ± 0.1
	Cu	2.9 ± 0.2	0.3 ± 0.2		Ir	3.0 ± 0.2	0.4 ± 0.1
	Co	2.6 ± 0.4	0.2 ± 0.1		Co	2.7 ± 0.4	0.3 ± 0.1
	Cu	3.1 ± 0.4	0.6 ± 0.2		Cu	3.2 ± 0.5	0.4 ± 0.2
	Ta	2.7 ± 0.4	0.5 ± 0.2		Ta	2.5 ± 0.3	0.4 ± 0.1
3	Ta_2O_5	3.8 ± 0.3	1.2 ± 0.2	3	Ta_2O_5	2.4 ± 0.6	1.1 ± 0.1
	Ta	2.8 ± 0.4	0.3 ± 0.1		Ta	3.4 ± 0.5	0.4 ± 0.1
	Cu	3.3 ± 0.8	0.2 ± 0.1		Ir	3.1 ± 0.2	0.5 ± 0.2
	Co	3.1 ± 0.5	0.3 ± 0.1		Co	3.3 ± 0.4	0.3 ± 0.1
	Cu	3.4 ± 0.5	0.4 ± 0.2		Cu	2.8 ± 0.7	0.4 ± 0.1
	Ta	2.2 ± 0.4	0.6 ± 0.2		Ta	3.1 ± 0.4	0.8 ± 0.1
6	Ta_2O_5	4.1 ± 0.3	0.7 ± 0.2	6	Ta_2O_5	2.5 ± 0.2	0.6 ± 0.3
	Ta	2.7 ± 0.3	0.4 ± 0.2		Ta	2.7 ± 0.3	0.2 ± 0.1
	Cu	3.4 ± 0.7	0.3 ± 0.1		Ir	3.2 ± 0.5	0.3 ± 0.1
	Co	6.2 ± 0.3	0.3 ± 0.1		Co	6.4 ± 0.7	0.2 ± 0.1
	Cu	3.1 ± 0.5	0.5 ± 0.1		Cu	2.9 ± 0.4	0.4 ± 0.2
	Ta	2.7 ± 0.2	0.4 ± 0.2		Ta	2.8 ± 0.3	0.3 ± 0.1
10	Ta_2O_5	2.6 ± 1.2	0.6 ± 0.2	10	Ta_2O_5	3.3 ± 0.9	1.1 ± 0.1
	Ta	2.6 ± 0.2	0.7 ± 0.3		Ta	3.5 ± 0.6	0.6 ± 0.2
	Cu	3.1 ± 0.6	0.4 ± 0.1		Ir	3.4 ± 0.5	0.3 ± 0.1
	Co	10.3 ± 1.2	0.3 ± 0.1		Co	10.1 ± 1.3	0.2 ± 0.1
	Cu	3.4 ± 0.2	0.2 ± 0.1		Cu	3.1 ± 0.4	0.4 ± 0.2
	Ta	2.7 ± 0.4	0.4 ± 0.1		Ta	3.2 ± 0.6	0.3 ± 0.1

t_{Co} (nm)	Layers	Thickness (nm)	Roughness (nm)	t_{Co} (nm)	Layers	Thickness (nm)	Roughness (nm)
15	Ta_2O_5	3.8 ± 0.8	0.7 ± 0.1	15	Ta_2O_5	3.3 ± 1.2	1.4 ± 0.6
	Ta	2.9 ± 0.2	0.4 ± 0.2		Ta	3.5 ± 0.2	0.5 ± 0.3
	Cu	3.1 ± 0.5	0.5 ± 0.2		Ir	3.2 ± 0.2	0.4 ± 0.2
	Co	14.5 ± 0.6	0.4 ± 0.2		Co	14.8 ± 0.8	0.3 ± 0.1
	Cu	3.3 ± 0.2	0.2 ± 0.1		Cu	3.1 ± 0.5	0.5 ± 0.1
	Ta	2.8 ± 0.2	0.3 ± 0.1		Ta	2.7 ± 0.2	0.4 ± 0.1
21	Ta_2O_5	2.6 ± 0.3	2.1 ± 0.2	21	Ta_2O_5	2.1 ± 0.1	0.7 ± 0.1
	Ta	3.4 ± 0.2	0.5 ± 0.1		Ta	3.3 ± 0.2	0.5 ± 0.1
	Cu	2.9 ± 0.2	0.2 ± 0.1		Ir	2.8 ± 0.1	0.6 ± 0.1
	Co	21.7 ± 0.2	0.3 ± 0.2		Co	20.3 ± 0.5	0.2 ± 0.1
	Cu	3.2 ± 0.4	0.2 ± 0.1		Cu	3.2 ± 0.2	0.2 ± 0.1
	Ta	2.3 ± 0.1	0.2 ± 0.1		Ta	2.3 ± 0.2	0.5 ± 0.2
35	Ta_2O_5	2.8 ± 0.5	2.2 ± 0.3	35	Ta_2O_5	2.8 ± 0.9	3.4 ± 0.6
	Ta	3.3 ± 0.4	0.5 ± 0.2		Ta	3.3 ± 0.3	0.6 ± 0.2
	Cu	3.2 ± 0.5	0.7 ± 0.3		Ir	3.0 ± 0.5	0.5 ± 0.1
	Co	36.2 ± 1.2	0.3 ± 0.2		Co	34.4 ± 2.1	0.4 ± 0.2
	Cu	3.4 ± 0.6	0.4 ± 0.2		Cu	3.2 ± 0.5	0.2 ± 0.1
	Ta	2.9 ± 0.2	0.2 ± 0.1		Ta	2.7 ± 0.2	0.4 ± 0.2
55	Ta_2O_5	2.5 ± 0.5	2.4 ± 0.3	55	Ta_2O_5	2.1 ± 0.4	0.9 ± 0.2
	Ta	3.4 ± 0.5	0.7 ± 0.1		Ta	3.1 ± 0.4	0.5 ± 0.3
	Cu	3.5 ± 0.6	0.4 ± 0.2		Ir	2.8 ± 0.4	0.4 ± 0.1
	Co	54.6 ± 3.1	0.3 ± 0.1		Co	54.7 ± 2.7	0.4 ± 0.2
	Cu	3.4 ± 0.2	0.4 ± 0.2		Cu	3.2 ± 0.4	0.5 ± 0.2
	Ta	3.1 ± 0.2	0.3 ± 0.1		Ta	3.3 ± 0.5	0.6 ± 0.3

Table A.2 Best fit parameters including thickness and roughness used in the simulation of specular reflectivity of amorphous 10 nm CoFeB:Ta thin-films deposited onto Si/SiO_2 and GaAs(001) wafer substrates for PNR measurements CRISP Beamline.

Si/SiO_2 Substrate				GaAs(001) Substrate			
t_{FM} (nm)	Layers	Thickness (nm)	Roughness (nm)	t_{FM} (nm)	Layers	Thickness (nm)	Roughness (nm)
10	Ta_2O_5	3.4 ± 0.5	4.5 ± 0.8	10	Ta_2O_5	3.3 ± 0.4	4.2 ± 0.5
	Ta	2.2 ± 0.4	0.3 ± 0.2		Ta	2.4 ± 0.2	0.3 ± 0.2
	CoFeB:Ta	9.9 ± 0.5	0.2 ± 0.1		CoFeB:Ta	9.7 ± 0.6	0.3 ± 0.1